ISBN 978-82-326-3004-2 (printed version)
ISBN 978-82-326-3005-9 (electronic version)
ISSN 1503-8181

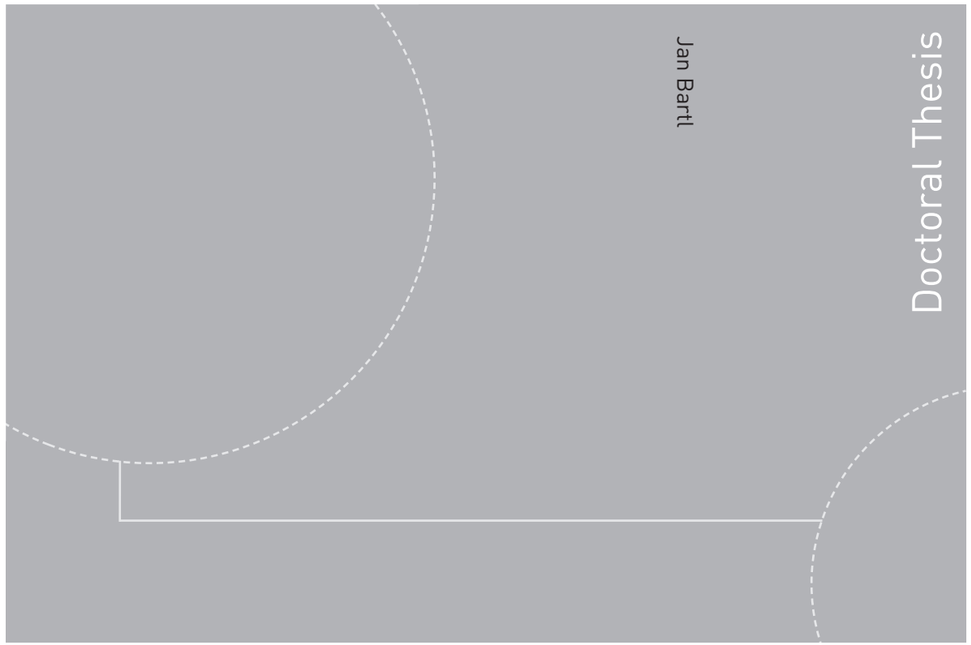

Doctoral theses at NTNU, 2018:107

Jan Bartl

Experimental testing of wind turbine wake control methods

NTNU
Norwegian University of
Science and Technology
Faculty of Engineering
Department of Energy and Process Engineering

NTNU
Norwegian University of
Science and Technology

Doctoral theses at NTNU, 2018:107

NTNU

NTNU
Norwegian University of
Science and Technology

Jan Bartl

Experimental testing of wind turbine wake control methods

Thesis for the degree of Philosophiae Doctor

January 2018

Norwegian University of Science and Technology
Faculty of Engineering
Department of Energy and Process Engineering

NTNU
Norwegian University of
Science and Technology

NTNU
Norwegian University of Science and Technology

Thesis for the degree of Philosophiae Doctor

Faculty of Engineering
Department of Energy and Process Engineering

ISBN 978-82-326-3004-2 (printed version)
ISBN 978-82-326-3005-9 (electronic version)
ISSN 1503-8181

Doctoral theses at NTNU, 2018:107

Printed by Skipnes Kommunikasjon as

Preface

This thesis is submitted in partial fulfillment of the requirements for the degree Philosophiae Doctor (PhD) at the Norwegian University of Science and Technology (NTNU). The work concludes a period of four years at the Fluid Mechanics Laboratory at the Department of Energy and Process Engineering.
The project was realized based on a strategic collaboration between NTNU and Technische Universität Berlin (TUB). The project was supervised by Professor Lars Roar Sætran at NTNU and co-supervised by Professor Paul-Uwe Thamsen at TUB.

January 2018 *Jan Bartl*

Acknowledgements

First of all, I would like to thank my family. All the unforgettable summers in Sweden and Norway were the initial spark for starting a student exchange and later a PhD in Norway. Thank you for your inexhaustible support throughout the years. Thanks to all my friends in Germany, Norway, Austria, Sweden and Australia for always being there and all the exceptional trips during the last years.

A special thank you goes out to Debbie, Ingrid, Anita, Wenche and everyone else at EPT's administration for your support in all kind of situations and many good conversations.

I am grateful to all the technical support by Arnt, Bård, Henning and Aslak in the wind tunnel lab. Your help in building wings and rotors, test rigs and finding solutions to all kind of problems was priceless. Thank you for your support and good vibes in the lab.

This thesis would not have been possible without the work of all the Master students, with whom I collaborated during the last four years. Many thanks to Paul, Szymon, Piotr, Clio, Andrea, Guro, Abdur, Sören, Nikolai, Maria, Marthijn, Kristian, John Magne, Julie, Lovisa, Mari, Jan and Felix. Many of you have produced outstanding Master theses, which were directly or indirectly contributing to the content of this PhD thesis. It was a great pleasure to work with all of you.

A major part of the work related to our wing model studies was done by Nikolai, who took the initiative in building the model, and Kristian, who performed all the numerical simulations. This project would not have successful without both your exceptional efforts. Thanks, Kristian, for proofreading the thesis and all the good times at the coffee machine and in the climbing gym.

A big thank you to all of my fellow colleagues and friends at EPT: Fabio, Tania, Luca, Pål-Egil, Lars Morten, Heiner, Thomas, Øyvind, Marin, Ehsan, Franz, Anna, Jørgen and everyone else in the ever growing bunch of PhD students. I had a superb time sharing an office with Ehsan and found a really good friend in you. Thanks, Øyvind, for all guidance in skiing and many good laughs at Gløshaugen, Oppdal, Brussels and Reykjavik.

I especially want to thank Fabio, Luca and Tania for many inspiring conversations, which already started during my time as a Master student. With your positive and down-to-earth attitudes you all were a main inspiration for me to start this PhD. Thanks to all of you for great collaborations and continuously guiding me through those years.
A great friend during the last years was Heiner. Thanks for many unforgettable coffee breaks on the roof and a lot of deep conversations about pathways to the future.
A very special thank you goes to Franz. It was an exceptional experience to closely collaborate with one of my best friends and actually produce some science. Without your remarkable skills in the lab and untiring ambition for our projects this work would be far from where it is now. Beyond our research, I thank you for your peerless friendship during good and difficult times.

This PhD work flourished on two international collaborations with experimental researchers in Ankara and Oldenburg. Thank you, Yashar, for shipping your turbines to Trondheim and many good times in and outside of the lab in Trondheim, Leuven, Copenhagen and Munich.
A very special thank you goes to Jannik. Your knowledge, ideas and good instincts were inspiring and greatly pushed the scientific quality of this work. Our very successful collaboration gradually transformed into a collaBROration with many unforgettable weekend trips around Trondheim, Oldenburg, Munich, Visby and Boulder.
Thank you to all the other friends and colleagues at ForWind for very good times in Oldenburg and many open and inspiring conversations during my visits.

Finally, I would like to express my gratitude to my supervisors Lars and Paul-Uwe for making this project possible and establishing a successful collaboration between NTNU and TU Berlin. Thank you, Paul-Uwe, for always having trust in me doing my thing here in Trondheim and many fruitful meetings. A special thanks also to all the staff at TU Berlin, with whom we established numerous thesis student exchanges and group visits within the course "Design of a wind turbine".

Lars, thank you for answering to an email of a naive engineering student, who was looking for mountain adventures and a Master thesis in Norway. Already our first collaboration during my Master was so outstanding that I decided to quit a very good job in Germany and come back to Trondheim to work with you on this PhD. I did not regret it. From the first minute you showed full confidence in me, which allowed me to develop as a researcher but beyond that also as a responsible person. You were a great role-model for me with your ever-positive attitude and open, down-to-earth personality. Your personal support was far beyond that of normal supervisor, both in good and in difficult times. I am incredibly grateful to have gotten the opportunity to have you as a scientific supervisor, mentor and good-old uncle Lars.

Abstract

In the light of the growing world-wide wind energy production, the optimization of wind farms has become an increasingly important field of research. Herein, the aerodynamic interactions between the single turbines through their wakes play a key role. The wake flow is characterized by lower velocities and increased levels of turbulence, causing power losses and fatigue loads on downstream turbines. Several different wind farm control concepts have been proposed, which are all based on the concept of reducing an upstream turbine's power extraction for the benefit of additional power available for a downstream turbine. In this experimental wind tunnel study the most promising three concepts are investigated on a setup of two or three model-scale wind turbines. Additionally, two model-scale reference experiments for computational simulation tools for wake and airfoil flow are presented.

A comparison of intentional control of the upstream turbine's tip speed ratio, blade pitch angle and yaw angle demonstrated the highest potential for overall power gains through yaw angle control. The wake flow behind a yawed turbine formed a curled shape at larger downstream distances and was observed to be slightly asymmetrical with respect to the upstream turbine yaw angle. However, the power surplus was observed to be penalized by increased yaw moments on both upstream and an aligned downstream turbine. For situations in which the turbines are laterally offset, an intentional yaw misalignment could steer the wake away from a downstream rotor, causing smaller loads and higher power. Moreover, it was demonstrated that a mitigation of yaw moments on the downstream rotor operated in a partial wake could be achieved by opposed yawing of the downstream rotor at a simultaneous increase of its power. For setups of tight inter-turbine spacing and full wake impingement tip speed ratio and pitch angle control might be applied for a reduction of upstream turbine thrust loads at an almost constant combined wind farm power. For higher turbine separation than $x/D \geq 3$, however, the additional kinetic energy added to the wake flow by tip speed ratio or pitch angle control was observed to diffuse into the freestream and could not be recovered by a downstream turbine anymore.

A comparison of external wake flow predictions by different computational models with experimental reference data confirmed the supremacy of Large Eddy Simulations combined with an Actuator Line rotor model as well as hybrid Detached Eddy Simulations in this field. Both modeling approaches mastered the challenges of a sheared inflow (blind test 4) and the complex interaction of a partial wake inflow to a downstream turbine (blind test 5) distinctively.

Contents

Part I

Summary

Introduction

1 Background

1.1 Developments in wind energy

We are confronted with a steadily increasing energy consumption around the world. According to the International Energy Agency (IEA), the global energy demand will grow by 30% by 2040 [38]. At the same time global carbon dioxide emissions are still seen to increase, implying severe consequences of climate change. In order to counteract these developments, carbon-free renewable energy technologies are taking over larger shares in today's electricity production worldwide. This development has led to falling costs and increasing investments in renewable energy technologies during the last decade. On a global level, China and India are predicted to develop the largest amount of renewable energy in the coming decades. In terms of newly installed capacity in the European Union (EU), renewable energy sources already account for 80% today [38]. Due to its applicability on land and offshore, wind energy is a key technology in this green energy shift. Based on today's growth rates, the IEA predicts wind energy to hold the biggest share of all energy producing sources in the EU from 2030 [38]. With its long and uninterrupted history of wind power utilization, Denmark holds the highest percentage of wind energy production with almost 40% [29]. In Europe, several countries continuously invest in wind energy, with Portugal, Ireland, Spain and Cyprus producing well over 20% of the countries' electricity. A noteworthy development has also taken place in Europe's largest economy Germany, which is today producing about 16% of its energy with wind power [29]. In Norway, wind energy still holds a relatively small share of only 1.4% of the total electricity production [62]. This is due to the dominating role of hydro power in Norway, which already provides around 96% of country's electricity needs with clean, renewable energy. Nevertheless, enormous potentials for wind energy production exist along Norway's long Atlantic coast, opening future perspectives as a green energy resource for a major part of northern and central Europe. A huge wind energy project recently began constructions at three sites in the county of Trøndelag. With a total capacity of about 1 GW, the project is announced as

Europe's biggest onshore wind farm cluster [57]. Moreover, major Norwegian company Statoil is currently pioneering the offshore wind energy sector. By realizing the world's first floating offshore wind farm "Hywind Scotland", previously unusable deep water offshore areas have suddenly become potential sites for wind energy production [74].
A limiting factor in wind energy production is its relatively large area usage, both onshore and offshore. Due to high costs for the electrical infrastructure and land, rather compact wind farm layouts are favorable. However, the interaction of densely installed wind turbines are facing the issue of wake losses. The wake is an area of lower kinetic energy downwind of a turbine, which has already extracted a significant amount of energy from the wind. The power total losses in a wind farm are estimated to range between 10 and 20% [5] depending on the site-specific wind conditions and farm layout. In addition to that, the interaction of the wind with the rotor generates a significant amount of turbulence in the wake. When a downstream turbine is impinged by the highly unsteady fluctuations in a wind turbine wake, it experiences higher fatigues loads on its blades and other turbine components. This leads to a decreased lifetime and higher maintenance costs [25].
Consequently, wind farm planners are challenged to find the most economically feasible wind farm configuration for a limited farm area. Besides an accurate prediction of wind resource statistics and terrain effects, the wake interactions between the single turbines need to be predicted as precisely as possible. This comprises the exact modeling of the mean and turbulent velocity field in the wake as well as the power output and fatigue loads on a downstream turbine operating in this wake. For this purpose simple analytical wake models were developed from the 1980s, being able to give a rough estimation of the mean velocity deficit in the wake. One of the first wake models was proposed by Jensen (1983) [40]. The velocity loss in the wake was calculated from a momentum balance and assumed to be constant over the entire wake area. In 1986, Katic et al. [43] further developed this model by adding a thrust dependency to the model, which resulted in today's most commonly used Jensen or PARK model. Several alternative models were proposed amongst others by Larsen (1988, 2009) [51, 52], Frandsen et al. (2006) [23] and Bastankhah and Porté-Agel (2014) [7].
An accurate prediction of the wake flow behind a turbine, however, is dependent on many parameters, which are not sufficiently modeled in simplified analytical wake models. Atmospheric parameters such as atmospheric stability, which is governing the large scale turbulence, wind shear and veer in the inflow to the wind turbine are for instance not included. With the rise in computational power in the 1990s, however, a more realistic representation of the wake flow was attempted to be modeled by applying computational fluid dynamics (CFD). Besides less expensive Reynolds-Averaged Navier Stokes (RANS) computations, which are dependent on additional turbulence closure models, more expensive time-resolved Large Eddy Simulations (LES) and hybrid Detached Eddy Simulations

(DES) became more popular. A comprehensive review of wake experiments and simulations was presented in 2003 by Vermeer et al. [77], who also addressed the need for increased research activities within wind turbine wake aerodynamics. This paper triggered a lingering wave of experimental and numerical wake studies during the last 15 years. Also at the Norwegian University of Science and Technology (NTNU) investigations on wind turbine wakes were initiated in the end of 2008. A model scale wind turbine rotor was designed by Krogstad and Lund (2012) [48] and tested in NTNU's slow-speed wind tunnel. In the following years, a number of mostly experimental wake studies then investigated the wake flow behind one and two model turbines in detail [1, 47, 18, 61]. Complementary to that, a series of blind test reference experiments was initiated, investigating the state of the art in computational wake modeling by comparing blind simulations of external expert groups with experimental wind tunnel data [49, 59, 50].

1.2 Wake control approaches

Along with growing knowledge about a wind turbine's wake characteristics, several approaches to control the wake flow emerged. Taking the mutual interactions between the single turbines through their wakes into account, the objective shifted towards an optimized control of an entire wind farm. The concept of coordinated wind farm control was originally proposed by Steinbuch et al. (1988) [75], aiming for a holistic optimization of a wind farm rather than a single turbine. They indicated the potential of an overall power increase by downrating the upstream turbine. Several different strategies have been proposed in the following years, most of which are summarized in papers by Knudsen et al. (2014) [45] and Gebraad et al. (2015) [27]. The common idea of these strategies is to reduce the energy extraction of an upstream turbine and thus leave more kinetic energy in the wake flow, which potentially can be extracted by downstream turbines. Besides the goal of wind farm power maximization, fatigue load mitigation on the individual turbines is another important objective of optimized wind farm control. For the purpose of minimizing the total Cost-of-Energy (CoE) a reduction of component failure and an increase in total lifetime are important objectives.

Wind farm control methods are in general classified in axial induction based control methods and wake deflection based control strategies. Axial induction based methods follow the concept of reducing the axial forcing by the rotor on the incoming wind. In other words, the thrust coefficient is intentionally decreased, in order to leave more kinetic energy in the wake. This can be realized by decreasing the rotor's rotational speed through the torque controller (λ-control) or changing the blade pitch angle through the pitch actuators (β-control). The second class of wind farm control strategies are wake redirection techniques, in which an uneven load distribution on an upstream rotor is applied to intentionally deflect the wake's trajectory away from a downstream rotor. This can be achieved

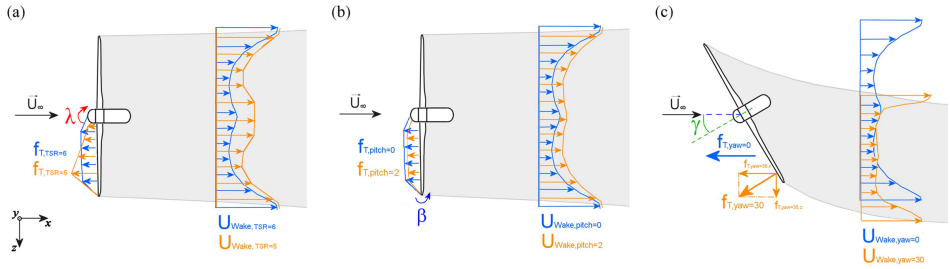

Fig. 1. Approximated rotor loads f_T and mean axial wake velocity distributions U_{wake} for **(a)** λ-control, **(b)** β-control and **(c)** γ-control. A top-down-view on the turbines is sketched.

by applying an intentional yaw or tilt angle on the upstream rotor or pitching the individual blades cyclically [19]. Herein, the method of intentional yaw misalignment of a turbine rotor (γ-control) is concluded to be the most promising. Figure 1 compares the three investigated concepts of λ-, β- and γ-control. A variation of the tip speed ratio λ from its optimum results in a radially uneven induction over the blade span as sketched in Figure 1 (a). Consequently, the velocity deficit in the wake also changes unevenly, making it possible to re-energize specific areas of the wake. A pitch angle variation, however, as sketched in Figure 1 (b) evenly reduces the angle of attack and the induction over the entire rotor area. Both concepts rise the kinetic energy level in the wake, which is then available for a potential downstream turbine. Figure 1 (c) outlines the basic principle of wake deflection by yaw misalignment (γ-control). Along with a reduction of the axial induction $f_{T,x}$ the misaligned rotor additional induces a lateral force component $f_{T,z}$ on the incoming flow. Consequently, the wake flow is laterally deflected, while the kinetic energy level in the wake is slightly increased due to a lower axial thrust component.

Axial induction based wake control

Axial induction based control methods are able to increase the kinetic energy level in the wake behind the downrated rotor. Whether a curtailment of the axial induction of an upstream turbine results in an increase of total power of a wind farm, is dependent on many parameters. Besides the specific rotor design and its operational characteristics, the wind farm layout, specifically the inter-turbine spacing, influences the velocity deficit in the wake impinging on a downstream turbine. With increasing downstream distance the kinetic energy losses in the wake recover due to an entrainment of higher kinetic energy fluid from the surrounding freestream. The wake recovery is strongly dependent on the ambient turbulence intensity in the atmospheric boundary layer, as shown by Barthelmie and Jensen (2010) [6] or Hansen et al. (2012) [34]. The intensity of atmospheric turbulence consequently also affects the potential for wind farm optimization. Wind farms

are observed to produce less energy for low turbulence intensities in a stable atmospheric stratification, due to stronger wakes. On the other hand, the potential for wind farm power optimization is larger in a stable stratifications as small changes in turbine control affect the wake properties to a higher degree than in a highly convective atmospheric boundary layer. Furthermore, the atmospheric parameters shear and veer, which describe the variation of wind speed and direction with height, are important influence factors on the wake characteristics and thus wind farm performance. As shown by Bromm et al. (2016) [10], inflow shear and veer created a strongly non-symmetrical skewed wake development, indicating the importance of these parameters for wind farm optimization studies. Obviously, also the directional distribution of the wind at a specific site, i.e. the wind rose, defines the frequency of situations in which the wakes of upstream turbines interact with downstream turbines.

Applying a mathematical simulation program Steinbuch et al. (1988) [75] obtained an efficiency increase of 4% by optimizing the tip speed ratios of a turbine array in a modeled wind farm. They furthermore emphasize the importance of wind farm control for rotor loads optimization. Another optimization study of an array of eight aligned wind turbines by Horvat et al. (2012) [36] found an increase of 2.85% in total wind farm power production. Applying an engineering wake model they slightly reduced the tip speed ratio of the first three turbines in the array, which resulted in a larger power increase of the last five turbines. A similar study was performed by Johnson and Fritsch (2012) [42], who applied a control algorithm on three aligned turbines. They found an increase in wind farm efficiency for low inflow turbulence by modeling the wakes applying the PARK wake model. Another theoretical study on axial induction control through pitch was performed by Lee et al. (2013) [53] on a layout of the Horns Rev wind farm. Based on an eddy viscosity model for the wake, a total efficiency increase by 4.5% was simulated. The power production of three in-line turbines was also modeled by Marden et al. (2013) [54] applying game theoretic methods. The application of a wake-model-free approach strongly simplified the underlying physics, but showed the potential for a total efficiency gain by optimized operation. Another control algorithm was implement in a model-framework based on the PARK wake model by Gonzalez et al. (2015) [30]. Controlling both the individual turbine's pitch angle and tip speed ratio a total wind farm power increase of 7.55% was calculated for aligned turbines. The application of simple engineering wake models for axial induction based wind farm optimization was recently challenged by Annoni et al. (2015) [4]. A comparison of high fidelity Large Eddy Simulations to a simpler engineering wake model framework was performed. A curtailment of the upstream turbine showed up clear over predictions in total efficiency by the simple engineering model, while the results of the high fidelity simulations indicated that the energy lost on an upstream turbine could not be fully recovered by a downstream turbine.

High-fidelity Large Eddy Simulations were recently performed by Nilsson et al. (2015) [56] on the tightly spaced Lillgrund offshore wind farm and the simulations results compared to real production data. After validating the simulations with measurement data, a pitch angle variation of the front row turbines was simulated. This curtailment strategy did however not result in an increased farm production. Another simulation based on an Eddy viscosity model for the wake was conducted by Kim et al. (2016) [44]. For a row of ten aligned turbines separated $x/D = 4$ the study found a wind farm power increase of 4.1% when the energy extraction of the upstream turbine was reduced to 82.5%. A recent computational study by Santhanagopalan et al. (2017) [64] focused on a combined performance and loads optimization for different incoming wind turbulence. The simulation based on a relatively fast RANS solver optimized the tip speed ratios of five aligned turbines, achieving a reduction of fatigue loads while the combined wind farm power was held stable. Only small power increases of about 1.3% were simulated for low background turbulence.

An early theoretical and experimental study on the power output and axial loads in a model wind farm was conducted by Corten and Schaak (2003) [14]. Their experiment consisted of a eight times three turbine model wind farm installed in a wind tunnel, in which the turbines' pitch angles could be adjusted. A variation of the front row turbines' pitch angle to 7.5° lead to a overall wind farm power increase of 4.5%. Corten and Schaak motivated their experiments on axial induction based wind farm control by an extension of the one-dimensional momentum theory to an array of two turbines. These considerations show that a reduction of an upstream turbine's induction results in a combined power increase for an array of two ideal wind energy converters. The detailed theory is therefore shortly revisited in the following section.

One-dimensional momentum theory

The one-dimensional momentum theory is well-known for one rotor and included in most wind energy textbooks, e.g. by Hansen (2013) [35]. The theory describes influence of a rotor on the axial momentum balance in the surrounding flow. For this purpose the axial induction factor a is introduced, which indicates the reduction of the inflow velocity to the wake velocity. The rotor is represented by an non-rotating actuator disc, meaning that the theory is by no means a physical representation of the energy extraction of a real wind turbine. It is important to mention that the wake flow is not recovering and thus neither the turbine separation distance nor turbulence characteristics play a role in these considerations. To begin with, the axial momentum theory for one rotor is recalled. After introducing the axial induction factor $a_{T1} = 1 - \frac{u_{T1}}{u_0}$, the theoretical power coefficient can be obtained from Eq. 1.

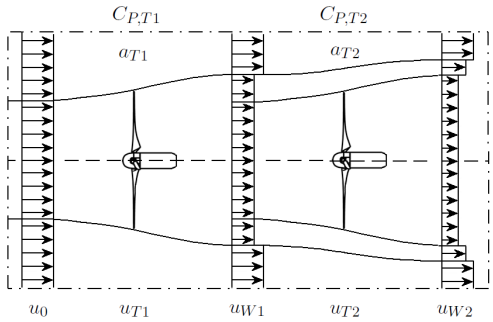

Fig. 2. One-dimensional axial momentum theory: sketch of the wake velocity levels behind one and two aligned wind turbines.

$$C_{P,T1} = 4a_{T1}(1 - a_{T1})^2 \tag{1}$$

The induction factor at which the power is maximum is obtained by derivating Eq. 1 $\frac{dC_{P,T1}}{da_{T1}} = 0$ and finding its maximum.

$$a_{T1}(C_{P,T1,max}) = \frac{1}{3} \tag{2}$$

Inserting this induction factor into Eq. 1 the maximum possible power to be extracted by a wind turbine is calculated to be 59.3%, which is commonly known as the Betz-limit.

$$C_{P,T1,max} = \frac{16}{27} \approx 59.3\% \tag{3}$$

The objective is here to investigate the potential for a total power increase of an array of two wind turbines by a reduction of the upstream turbine's axial induction. For this purpose the one-dimensional momentum theory is expanded to two in-line turbines. A sketch of two aligned wind turbine rotors is shown in Figure 2, defining the locations of the different velocity levels. The velocities are defined to decrease from the left to the right as the two actuator discs extract kinetic energy from the flow (see Figure 2).

$$u_0 > u_{T1} > u_{W1} > u_{T2} > u_{W2} \tag{4}$$

A second axial induction factor for the downstream turbine T2 is defined accordingly.

$$a_{T2} = 1 - \frac{u_T 2}{u_{W1}} \tag{5}$$

Under the assumption that $u_{T1} = \frac{1}{2}(u_0 + u_{W1})$ the total efficiency of the two aligned turbines can be expressed as

$$C_{P,tot} = C_{P,T1} + (\frac{u_{W1}}{u_0})^3 \cdot C_{P,T2} \tag{6}$$

Expressing the velocity ratio $\frac{u_{W1}}{u_0} = 1 - 2a_{T1}$ as a function of the induction factor a_{T1}, the total efficiency can then be expressed as

$$C_{P,tot} = C_{P,T1}(a_T 1) + (1 - 2a_{T1})^3 \cdot C_{P,T2}(a_{T2}) \tag{7}$$

In a traditional control approach, at which each turbine extracts the maximum possible power from the wind, the upstream turbine and the downstream turbine would be operated at $a_{T1} = \frac{1}{3}$. This would result in a total power of the turbine array of

$$C_{P,tot}(a_{T1} = \frac{1}{3}) = \frac{448}{729} \approx 61.5\%. \tag{8}$$

The maximum combined power of both turbines is found by $\frac{dC_{P,tot}}{da_{T1}} = 0$. The following expression is found, which is still dependent on both induction factors a_{T1} and a_{T2}.

$$6(1 - 2C_{P,T2}(a_{T2})) \cdot a_{T1}^2 - 4(2 - 3C_{P,T2}(a_{T2})) \cdot a_{T1} + (2 - 3C_{P,T2}(a_{T2})) = 0 \tag{9}$$

Given that $C_{P,T2,max} = C_{P,T2}(\frac{1}{3}) = \frac{16}{27}$ simplifies Eq. 9 to a quadratic equation only depending on a_{T1}.

$$5a_{T1}^2 + 4a_{T1} - 1 = 0 \tag{10}$$

Solving the quadratic equation for a_{T1} gives the positive solution $a_{T1} = \frac{1}{5}$ for the optimum induction of the first turbine in a two turbine in-line array. For this induction factor the maximum extractable power of the upstream turbine T1 would reduce to

$$C_{P,T1,max}(a_{T1} = \frac{1}{5}) = \frac{64}{125} \approx 51.2\%. \tag{11}$$

The maximum total power of the two turbine array, however, would then amount

$$C_{P,tot} = C_{P,T1}(a_{T1} = \frac{1}{5}) + (1 - 2a_{T1})^3 \cdot C_{P,T2}(a_{T2}) = \frac{16}{25} = 64.0\% \tag{12}$$

This combined power extraction for a curtailed upstream turbine of 64.0% is higher than the power found for the traditional control approach of 61.5% in Eq. 8, meaning that a reduction of upstream turbine axial induction factor a_{T1} from $\frac{1}{3}$ to $\frac{1}{5}$ in theory leads to an combined power increase of 4.1%. However, this is based on a number of simplifications, which are deemed not to reflect the real physics. Nevertheless, a deeper experimental investigation of this strategy should give more insight into the physical processes in the wake behind a curtailed rotor.

Deflection-based wake control

A different approach for optimized wind farm control are deflection based wake control methods. A similarity to the previously discussed axial induction based control methods is the intentional load reduction on the upstream turbine in deflection based control for the benefit of a downstream turbine. The load reduction in deflection based methods is however not symmetrically distributed over the rotor area, as a lateral forcing of the flow is intentionally created in order to deflect the wake flow (see Figure 1 (c)). By deflecting the low kinetic energy wake partly or entirely away from a potential downstream rotor, the downstream turbine is able to extract more energy from the wind. Due to increased asymmetrical loads on the rotors, a detailed assessment of these loads and their impact on component fatigue has to be taken into account when optimizing a wind farm's control strategy. Three different wake deflection mechanisms have been compared in a computational study by Fleming et al. (2014) [19]. The techniques (1) individual pitch angle control, (2) tilt angle variation and (3) yaw angle actuation were discussed with regards to added power in the wake and rotor loads. Individual pitch control was observed to cause higher structural rotor loads, while most turbine designs do not feature a degree of freedom in tilt direction. Yaw angle control is easily implementable due to available yaw actuators on all modern turbines and therefore concluded to be a promising wind farm control technique.

The aerodynamics of a yawed rotor are much more complex than those of a non-yawed rotor. In the course of a rotation a blade experiences significant load variations. The angle of attack on the blades varies cyclically, which is causing instationary flow on the blades. For high yaw angles the cyclic variation can even cause dynamic stall as stated in a detailed theoretical description of rotor aerodynamics in yaw by Schepers (2012) [69]. Measured axial blade forces and velocities for different azimuth angles of a turbine operated in yaw were compared to a number of simulations by Schepers et al. (2014) [70] in the Mexnext project. Besides an assessment of the simulations tools' capability of to model flow and forces correctly, the measurement showed up some complex unsteady flow phenomena around the blades during yaw.

A number of experimental and computational studies on the wake behind a yawed rotor have been conducted in the past two decades. An early set of experimental wind tunnel studies on vortex tracking in the wake of a yawed turbine was reported from Grant et al. (1997) [31] and Grant and Parkin (2000) [32]. The tip vortices behind a model turbine were tracked by the means of optical methods, which allowed them to estimate the wake deflection. In a follow-up study the wake circulation was measured for positive and negative yaw angles by phase-locked particle image velocimetry (PIV) indicating clear asymmetries between positive and negative yaw angles. Similar observations were reported by Haans et al. (2005) [33], who measured asymmetric locations of the tip vortices behind a yawed

model turbine. A full vector field in the wake behind a yawed model turbine was measured by Medici and Alfredsson (2006) [55]. A cross-stream flow component was observed in the center of the wake laterally deflecting the flow. A prediction model for the wake deflection at different yaw angles was later developed by Jiménez et al. (2010) [41], which was derived from large eddy simulations (LES) on a yawed actuator disc. Measurement in the near wake have also been reported by Krogstad and Adaramola (2012) [47], who showed that the wake deflection varies significantly for different tip speed ratios of the rotor. The far wake behind a yawed drag disc was measured by Howland et al. (2016) [37]. The study described the formation of a curled wake shape by a large-scale vortex pair at higher downstream distances. An comprehensive contribution to the field of yawed rotor wakes was recently made by Bastankhah and Porté-Agel (2016) [8]. In their experimental and theoretical work they developed a new analytical model for the far wake from full field wind tunnel measurements. Many features of the wake are such as the formation of a counter-rotating vortex pair are explained by conservation laws. All these studies confirmed a lateral deflection of the wake behind a yawed rotor. The deflection results are observed to vary significantly due to different quantification methods, modeling approaches and turbine models used. However, the wake deflection for high yaw angles of $\gamma = 30°$ is observed to converge to a value of roughly half a rotor diameter in the far wake. This implies that the wake cannot be fully deflected away from a downstream turbine located directly behind the yawed upstream turbine rotor.

Moreover, recent research investigated the potential of intentional wake steering through yaw misalignment for a potential wind farm power gain. A wind tunnel investigation by Adaramola and Krogstad (2011) [1] demonstrated a combined power gain on two aligned model wind turbines with increasing upstream turbine yaw angle. A maximum power gain of 12% compared to a non-yawed reference case was found for a yaw angle of $\gamma = 30°$. A similar experimental study was performed by Schottler et al. (2016) [71], who measured an increase in array power of about 4.0% when the upstream turbine was yawed to $\gamma = -18°$. The combined power output of the two turbines was found to be clearly asymmetric with respect to the upstream turbine's yaw angle. The study confirmed computational results reported by Fleming et al. (2015) [20], who found a similarly asymmetric profile for the combined power. Their simulation found a maximum combined power increase of 4.8% for an upstream turbine yaw angle of $\gamma = 25°$. These studies all confirmed a gain in combined power output through upstream turbine yawing but also showed that the optimum yaw angle and the relative power gains are dependent on the rotor geometry and modeling approach. A recent model-scale experiment by Campagnolo et al. (2016) [11] investigated the combined power of three laterally offset turbines. A yaw-optimized configuration resulted in a combined power increase of 21% compared to a non-yawed reference case. This study indicates that power gains might be even larger for laterally offset turbine positions, in

which the biggest part of the wake can be deflected away from the downstream turbine. A yaw control and layout optimization study on a existing wind farm layout was recently conducted by Fleming et al. (2016) [21]. Optimizing the yaw control resulted in a performance increase of 7.5%, while a power density gain of 62% was calculated for combined layout and yaw control optimization. The first reported field test of wake steering in a real offshore wind farm was recently reported by Fleming et al. (2017) [22]. By demonstrating a good correlation of measured power data of two turbines with their prediction models, they demonstrated the applicability of wake steering in a full scale wind farm.

Despite the large potential for wind farm power gains, a yaw-misaligned upstream rotor experiences increased loads. As angle of attack varies through the course of a rotation, the blades are exposed to cyclic loads. Depending on the yaw angle and the specific rotor design these unsteady loads vary in magnitude. A simulation by Kragh and Hansen (2014) [46] quantified blade load variations for different inflow conditions. A recent study by Damiani et al. (2017) [16] describes which impact blade load variations can have on damage equivalent loads and extreme loads under yaw misalignment. The load distributions measured on a fully instrumented utility scale wind turbine turbine are observed to be dependent on the inflow for different yaw angle offsets. Another study by Schreiber et al. (2016) [72] describes a method to estimate the relative position of a partial wake impinging on the rotor and the strength of a sheared inflow by measurement of the azimuthal blade load variation. All of these studies underline the importance of an assessment of blade loads for wind farm optimization studies. An investigation of both loads and power of two turbines during yaw misalignment was modeled by van Dijk et al. (2017) [76] for different lateral turbine offsets. For this purpose a computational framework of a blade element momentum (BEM) code, wake model and gradient-based optimizer was used. Upstream turbine yaw misalignment was found to increase the combined power, while it was shown to also reduce blade loads in partial wake overlap situations. The study indicated that wind farm control though intentional yaw misalignment might only be beneficial for laterally offset positions of the downstream turbine.

2 Motivation and objectives

Wake control experiments

The main objective of this thesis is to investigate the effectiveness of three different wind farm control approaches with respect to power and loads optimization in model scale. For this purpose the effect of variations in tip speed ratio λ, blade pitch angle β and yaw angle γ on the mean and turbulent wake flow behind the turbine shall be systematically investigated for different downstream positions. As a second step, a downstream turbine is set up in the same location as the wake measurements were performed in order to measure the downstream turbine's power and thrust loads for different operating points of the upstream turbine. As the inter-turbine spacing is considered a main influence factor on downstream turbine power and loads, different streamwise turbine separation distances are investigated. The relative position of two wind turbines to each other varies with a changing wind direction. Thus, the effect of partial wake impingement on the power and yaw moments on a laterally offset downstream turbine shall be investigated. Partial wake situations are considered to be especially relevant for yaw angle control, as downstream turbine loads might be mitigated by upstream turbine yaw control.
Moreover, the wake characteristics are strongly dependent on the ambient turbulence level [5] and inflow shear [10]. Therefore, a further objective is to assess the influence of different inflow turbulence levels as well as a vertical shear on the effectiveness of wind farm control approaches. Special attention is given to the effect of these parameters on the mean and turbulent wake characteristics.
A review of publications on axial induction based control methods indicated a wide range of possible combined power, from slight power losses around 1% (Annoni et al., 2015) [4] to considerable increases of more than 7% (Gonzalez et al., 2015) [30]. The different modeling approaches might be accountable for the variations in results, motivating a further experimental study under controlled boundary conditions. Here, the focus shall be directed on a combined power and loads optimization. The influence of induction based wake control shall also be investigated for an array of three aligned model turbines. The objective of this is to investigate whether first or second turbine curtailment has any significant influence on a third turbine or if the problem can be reduced to an array of two turbines.
In the case wake deflection control through yaw, the potential for combined power increases seems to be very promising based on a literature review. However, a number of important questions yet remain open. The effects of inflow turbulence and shear on the yawed wake characteristics and its deflection therefore shall be investigated in more detail. A recent computational study by Vollmer et al. (2016) [78] showed the wakes' dependency on different atmospheric stabilities. However, the effects of inflow turbulence, shear and veer on the wake flow have not been investigated isolated from each other. Moreover, the

reasons for the asymmetries in the wake shape with respect to positive and negative upstream turbine yawing are not completely clear yet . Studies by Fleming et al. (2015) [20] or Schottler et al. (2016) [71] showed clear asymmetries in the combined power output, yet no coupling to the upstream turbine's wake flow has been performed. For this purpose, the wake deflection shall be investigated for both positive and negative yaw angles. Also, the influence of inflow turbulence and non-uniform shear on the wake symmetry shall be investigated.

Validation experiments for computational codes

The results of the wind tunnel experiments are not necessarily representative for full scale wind farms, as insurmountable scaling issues occur. Aside from an incorrect geometrical scaling, the Reynolds number is one to two magnitudes lower in wind tunnel model experiments than in full scale. Furthermore, solid wall blockage is an inevitable issue in wind tunnel experiments distorting the measured quantities. It is very difficult to generate realistic wind conditions, accurately reflecting a variable atmospheric boundary layer flow which full-scale wind turbines are exposed to. However, the inflow wind conditions and operational states of the wind turbines can be manipulated in a controlled manner, making it possible to draw direct conclusions to input parameter variations.
Wind tunnel data are moreover very valuable for the validation of computational simulation tools. Therefore, another objective of the thesis is to set up blind test experiments for the validation of CFD wake flow simulations. Following the footsteps of three previous blind test experiments by Krogstad and Eriksen (2013) [49], Pierella et al. [59] and Krogstad et al. [50], a fourth blind test shall explore the capability of different state of the art computational codes to predict the wake development and performance of a turbine array exposed to different inflow turbulence and shear. Outside the scope of this thesis, a fifth blind test is initiated comparing computational predictions of the complex wake flow behind one and two turbines operated in yaw.

Airfoil testing at low to moderate Reynolds numbers

As previously mentioned, the Reynolds number in model scale wind turbine experiments is one to two magnitudes lower than in full scale experiments. However, the rotors of the model turbines are designed based on the NREL S826 airfoil, which originally was intended for Reynolds numbers of at least one magnitude higher. Several modeling approaches, such as the blade element momentum (BEM) method, which is widely used for rotor performance and loads calculation or the actuator line (ACL) technique for wake modeling, are

based on airfoil polars at the operational Reynolds number range. This issue was already discussed in the first blind test workshop in 2011, whereupon measurement campaigns on a wing section of the airfoil were initiated at Denmark's Technical University (DTU) (Sarmast and Mikkelsen, 2013) [68] and Middle East Technical University (METU) (Ostovan et al., 2013) [58]. The two experimental datasets showed different characteristics at the transition to stall and very low Reynolds numbers. Consequently, it was decided to perform a third experiment on a wing section of the NREL S826 at NTNU's slow speed wind tunnel. The experimental dataset consisting of lift and drag polars as well as surface pressure distributions shall serve both as a reference experiment for aerodynamic modeling as well as input data for BEM and ACL models.

3 Thesis structure

The thesis is a collection of six papers, four of which share the thesis' main focus of wind turbine wake control methods. A graphical structure of the thesis and its papers is presented in Figure 3. Besides a classification of the single papers to a field of research, the experimental setup and the main parameter variations are sketched. In **PAPER 1** the effects of β- and λ-control on the wake flow and downstream turbine performance are compared. **PAPER 2** focuses on the comparison of the wake flow behind one and two turbines and investigates effects of tip speed ratio variations on the second and third row turbine. In **PAPER 3** the effects of inflow variations on the wake behind a yawed turbine are analyzed. **PAPER 4** focuses on the power and yaw-moments of two yaw-controlled turbines in different offset configurations. The last two papers' objective is to present two reference experiments for computational models. The experimental setup for the two reference experiments is however completely different. While **PAPER 5** compares computational predictions of the wake flow behind a model turbine, **PAPER 6** discusses modeling of the flow around an airfoil. The common ground is the low Reynolds number performance of the NREL S826 airfoil, on which the model turbine's rotor design is based. For a complete list of all papers, their authors and journals, see Section 7.

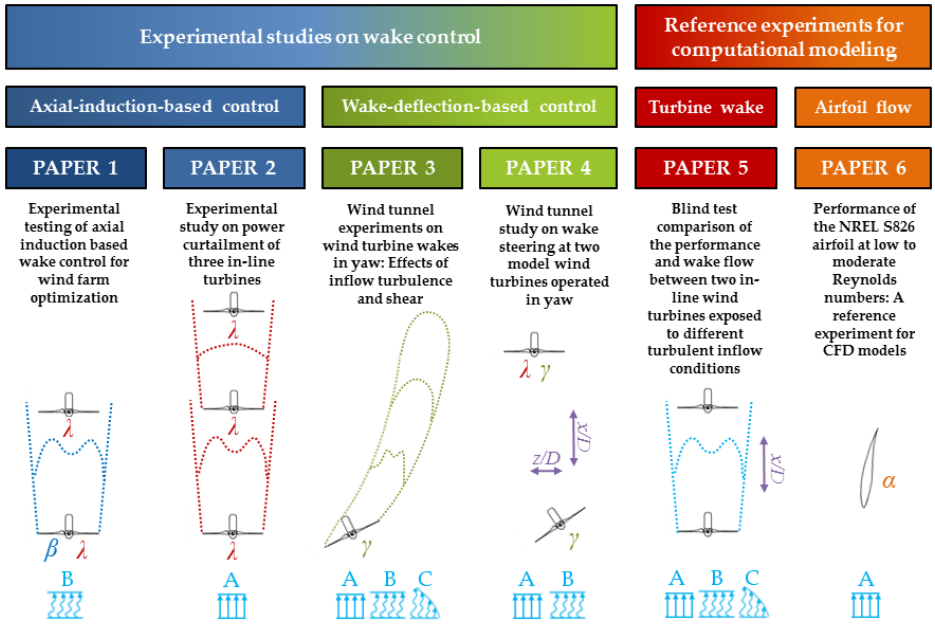

Fig. 3. Sketch of the setup of each paper, showing the main parameter variations. A, B and C denote three inflow conditions (see Section 4.4). β, λ, γ and α denote variations in blade pitch angle, tip speed ratio, turbine yaw angle and angle of attack, respectively. x/D and z/D denote a variation in streamwise and lateral separation distance between the turbines. Dotted lines indicate that wake measurements have been performed.

4 Methods

In this section some of the experimental techniques used in the scope of this thesis are shortly summarized. For a more detailed description of the methods used for a specific campaign, it is referred to the methods sections of the attached papers.

4.1 Wind tunnel and turbine models

All experimental data presented in this thesis was measured in the closed-loop low-speed wind tunnel at NTNU in Trondheim. The test section is 11.15 m long, 2.71 m wide and 1.81 m high. The inflow speed is controlled by a measurement of the differential pressure at an inlet contraction, and can be varied between $U_{inflow} = 0 - 30$ m/s. The suction type wind tunnel is driven by a 220 kW fan located downstream of the test section.
Three model wind turbines of the same blade geometry were mainly used for the research presented in this thesis (Figure 4). The wind turbine model referred to as *Turbine 1* (T1) has a rotor diameter of $D_{T1} = 0.944\,m$ while *Turbine 2* (T2) features a slightly smaller diameter of $D_{T2} = 0.894\,m$. A slightly different hub geometry of the turbine rigs causes the difference in rotor diameters; the blade geometry is however exactly the same. Turbines T1 and T2 were used for the measurement campaigns in **PAPER 1** and **PAPER 5**. For the test presented in **PAPER 2**, T1 was used as an upstream turbine, while two model turbines of the exactly same rotor and hub geometry by METU were used as downstream turbines. For the measurement campaigns in **PAPER 3** and **PAPER 4**, a new test rig was designed (Figure 4 (c)). In order to have a smaller influence of the nacelle and tower structures on the wake in yawed operation, the *Laterally Angled Rotating System 1* (LARS1) features a significantly slimmer tower and shorter nacelle than T1 or T2. All three turbines rotate counter-clockwise when observed from an upstream point of view. T1 and T2 are both driven by a 0.37 kW electric motor via a transition belt, which is

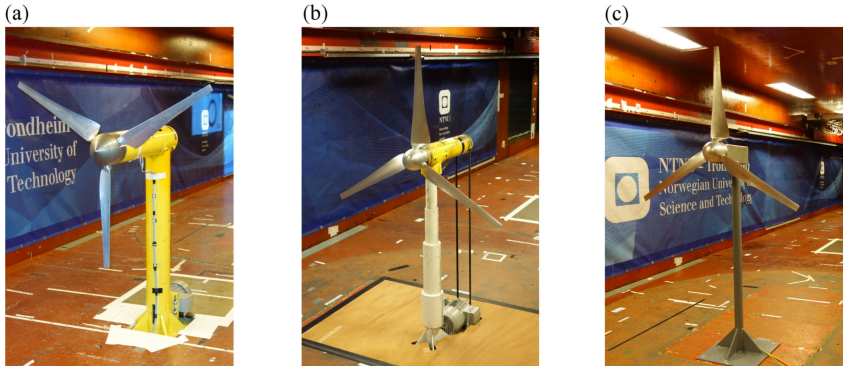

Fig. 4. Model wind turbines installed in NTNU's low-speed wind tunnel: **(a)** T1, **(b)** T2 and **(c)** LARS1

controlled by a Siemens frequency inverter. This enables the rotational speed to be varied from about 100 to 3000 rpm. LARS1 is directly driven by a Panasonic electric servo motor located inside the nacelle. For all turbines, the frequency-controlled motor ensures constant rotational speed, while the excessive power produced is burned off in an external load resistance. The rotors were designed by Krogstad and Lund (2012) [48] based on a NREL S826 airfoil, which is discussed in more detail in the following section. The blades are milled from aluminum, ensuring an accurate representation of the airfoil geometry. All three turbines have a design tip speed ratio (TSR) of $\lambda = 6$. Aside from the low-Reynolds operation another drawback is the considerable blockage of the model turbine of the wind tunnel. The rotor swept area of one turbine model blocks about 12.8 % of the wind tunnel's cross sectional area. The blockage's influence on turbine performance can be estimated with blockage correction models, e.g. by Ryi et al. (2015) [63]. A sensitivity study on the influence of blockage on wake characteristics behind the same rotor was performed through a LES investigation in domains of different sizes by Sarlak et al. (2016) [67]. The mean wake velocity was seen to be affected by blockage ratios higher than 10.0%, although the blockage did not significantly affect the mixing rate in the wake. Technical drawings of the model wind turbines *T1*, *T2* and *LARS1* are presented in Figures A.1, A.2 and A.3, respectively, in Appendix A.
Furthermore, experimental campaigns were conducted with turbine models designed at the ForWind center at the University of Oldenburg ($D_{ForWind} = 0.580\,m$) for paper **PAPER 9**, **PAPER 12** and **PAPER 13** as well as a downscaled version of the NTNU rotor ($D_{NTNU,small} = 0.450\,m$) used in **PAPER 14** and **PAPER 15**. Results of these campaigns are not directly included in this thesis.

4.2 NREL S826 blade geometry and airfoil model

The NREL S826 airfoil was created by Somers (2005) [73] at the National Renewable Energy Laboratory (NREL). The airfoil was designed for the blade tip of horizontal-axis wind turbines of a rotor diameter of $20-40m$, where it is supposed to operate at Reynolds number of $Re = 1.0 \times 10^6$. The design objectives were aiming for a high lift coefficient $C_L > 1.40$, low sensitivity to roughness and low profile drag [73]. Despite the original design for $Re \geq 1.0 \times 10^6$, the airfoil is used at Reynolds number about one magnitude lower in the model experiments ($Re_{tip} \approx 1.0 \times 10^5$). Figure 5 (b) shows a cross section of the airfoil at the blade tip, where it has a chord length of $C_{L,tip} = 0.026\,m$ at the blade tip. The normalized coordinates of the NREL S826 airfoil are documented in Table B.1 and sketched Figure B.1 in Appendix B. The blades' chord length and twist angle is defined in Table B.2 and depicted Figure B.2 in Appendix B.
In order to investigate the airfoil's characteristics at lower Reynolds numbers a non-twisted upscaled model of the airfoil has been built (Figure 5 (c)). The wing consists of three

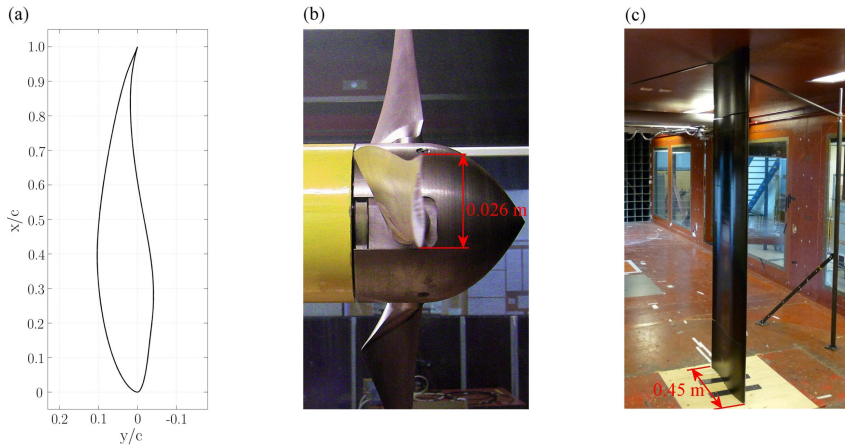

Fig. 5. NREL S826 airfoil: **(a)** airfoil coordinates definition, **(b)** airfoil in twisted blade geometry and **(c)** airfoil in upscaled 2D wing section.

sections, a main wing section in the center of the wind tunnel and two dummy sections close to the wind tunnel floor and roof. The dummies are not connected to the main wing section nor the force measurement and are designed to cancel out interactions with the floor and roof boundary layer of the wind tunnel. The single airfoil elements were CNC-milled from the polyurethane based board material *ebaboard 1200*, which were thereafter painted in gloss paint to feature a hydraulically smooth surface. At mid-span the wing is equipped with 32 pressure taps around the circumference to enable measurements of surface pressure distributions. The wing is mounted vertically in the wind tunnel and has a chord length of $C_{L,wing}$=0.45 m and a total height of h_{total}=1.78 m. For more details, it is referred to the experimental setup section in **PAPER 6**.

4.3 Measurement techniques

The test rigs of T1 and T2 are equipped with a HBM torque transducer of the type T20W-N/2-Nm, which is installed inside the nacelle and connected to the rotor shaft through flexible couplings. Moreover, the rotational speed is assessed via an optical photo cell also installed inside the nacelle. A multiplication of rotational speed and mechanical torque enables the calculation of the mechanical power on the rotor.

In order to also assess thrust forces and yaw moments on the model turbines these can be placed on a fully rotateable six-component force balance by Carl Schenck AG, which is located underneath the wind tunnel floor. The same force balance is applied for measurements of lift and drag characteristics of the S826 wing model. For this setup, the central main section of the wing is connected to the force balance through two iron rods.

For the measurement of the mean and turbulent wake flow behind the model turbines, the well established measurement techniques Hot-wire anemometry (HWA) and Laser-

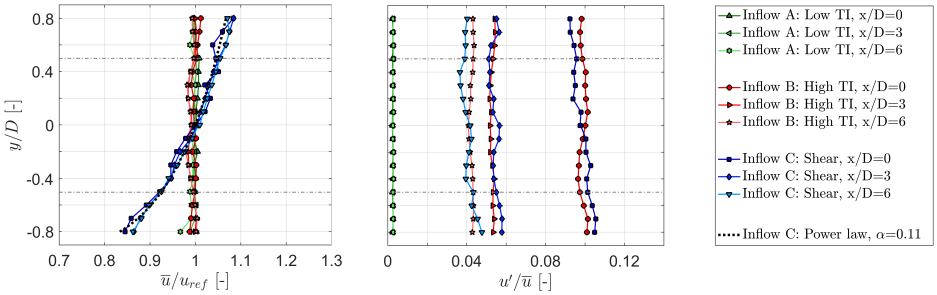

Fig. 6. Normalized mean velocity $\overline{u}/u_{ref}$ and turbulence intensity $u'/\overline{u}$ measured in the empty wind tunnel at the turbine position $x/D = 0$ and wake measurement positions $x/D = 3$ and $x/D = 6$. Inflow velocity was u_{ref}=10 m/s in all cases. The figure is adapted from **PAPER 3**.

Doppler anemometry (LDA) have been applied. A single hot-wire was used in constant temperature mode (CTA), sampling every measurement point for 45 s at 20 kHz. To avoid distortion by noise and low-frequency fluctuations the signals were filtered appropriately. The LDA system is a two-component Dantec FiberFlow system, which was used in Differential Doppler Mode. LDAs do not have a constant sampling rate, as they measure the Doppler-shift of the scattering by a randomly passing particle. For wake flow measurements 5×10^4 samples were recorded over a period of approximately 30s, resulting in an average sampling frequency of 1666Hz. The temperature in the wind tunnel is measured with a thermocouple. The assessment of the flow temperature is crucial for temperature corrections in hot-wire measurements and calculations of the air density ρ.

For measurements of surface pressure on the wing model an Electronically Scanned Pressure (ESP) transducer of the type DTC Initium is used. The single sensors of the pressure scanner are made of piezo-resistive silicon. A digital temperature compensation countervails temperature fluctuations in the wind tunnel. Pressure Measurements are sampled for 60 s with a sampling rate of 500 Hz.

4.4 Generation of turbulent inflow

The influence of different inflow conditions on the wake flow is investigated in **PAPER 3**, **PAPER 4** and **PAPER 5**. Three different inflows are tested in order to estimate the influence of inflow turbulence and shear. The normalized streamwise mean velocities and turbulent fluctuations measured at different positions in the empty wind tunnel are presented in Figure 6. Inflow A can be characterized as a typical laboratory flow, in which the turbine is exposed to the low turbulent, uniform, clean inflow of the wind tunnel (TI_A=0.23%). Inflow B is a grid-generated uniform inflow of higher turbulence intensity (TI_B=10.0%). The grid is placed two rotor diameters upstream of the turbine position. Further downstream, the turbulence decays to 5.5% at x/D=3 and 4.0% at x/D=6. The third inflow C is generated by another custom-made grid with non-uniformly spaced hor-

Table 1. Characteristics of the three different investigated inflow conditions

Inflow	TI [%]	spatial uniformity	power law coeff. α
A	0.23	uniform	0
B	10.0	uniform	0
C	10.0	non-uniform	0.11

izontal bars, which is described in detail in **PAPER 5**. A vertically sheared flow profile is observed to establish at all downstream positions. The profile can be approximated by the power law

$$\frac{u}{u_{ref}} = \left(\frac{y}{y_{ref}}\right)^{\alpha} \tag{13}$$

in which α describes the strength of the shear. For this flow, a shear coefficient of $\alpha = 0.11$ is seen to give a good approximation. Inflow C also has a turbulence intensity of TI_C=10.0% at the turbine position, making it a representative inflow for an onshore site at neutral atmospheric conditions [81]. The inflow velocity was set to $u_{ref} = 10.0\,m/s$ for the model turbine experiments in **PAPER 2**, **PAPER 3** and **PAPER 4**, while an inflow velocity of $u_{ref} = 11.5\,m/s$ was used in **PAPER 1** and **PAPER 5**.

4.5 Measurement uncertainties

The uncertainty in measurements of the power, thrust and mean velocity is calculated according to the procedure by Wheeler and Ganji (2004) [82]. Random errors are computed from repeated samples of a measurement and calculated based on a 95 % confidence interval. Moreover, systematic errors in the calibration and setup procedures are taken into account, wherein error estimates found by Pierella (2014) [60] and Eriksen (2016) [17] are taken as reference values. Herein, a systematic error of about ±1.0 % in the velocity calibration is seen to be the major contributor. The uncertainty in turbulent quantities is computed according to the method by Benedict and Gould (1996) [9]. The measurement uncertainties are included as errorbars in the blind test measurements in **PAPER 5**. For the purpose of a better comparability, errorbars have not been included in the plots of the other papers; however, representative error calculations have been performed and included in the text of a dedicated section. For the results shown in this summary section, error estimates basically follow the values given in **PAPER 4**. The total uncertainty in $C_{P,T1}$ at its design point is calculated to $e_{CP,T1}$=0.011 which corresponds to 1.9% of the total value. When varying the blade pitch angle to $\beta_{T1} = 2°$, the uncertainty in the power coefficient rises to $e_{CP,T1}$=0.023 corresponding to 5.0% of the total value. The main reason for the increased value is an additional uncertainty in the adjustment of the pitch angle. The uncertainty also rises with a variation of the turbine yaw angle. At a yaw angle of

$\gamma_{T1} = 30°$ a total uncertainty of $e_{CP,T1}$=0.017 (3.9%) is measured. The uncertainty in the thrust coefficient is observed to follow similar trends as in the power coefficient. At the design operating point an total error of $e_{CT,T1}$=0.013 (1.4%) is calculated. The uncertainty in normalized yaw moments $M^*_{y,T1}$ is assessed to $e_{My*,T1}$=0.0032, which corresponds to almost 15% of the absolute measurement value at $\gamma_{T1} = 30°$.

5 Summary of key results

In this section some of the key results of thesis are discussed. Results from purely experimental wind turbine wake and interaction studies are summarized in Section 5.1, while Section 5.2 reflects on key findings in the reference experiments for computational models. The figures presented in the single papers are not included in this section. For a more in-depth analysis of the single results it is referred to the papers, which are appended to this thesis.

5.1 Wake control for wind farm optimization

This section directly compares three wake control methods for a setup of two aligned turbines. The upstream turbine operating characteristics, mean wake velocities and downstream turbine power, thrust and yaw moments are analyzed. This is done for one inflow condition (uniform highly turbulent inflow B, $TI_B = 10.0\%$) only. For a direct comparison of all three wake control methods, several figures from **PAPER 1** and **PAPER 4** are combined. The results for a variation of inflow condition, lateral offset of a downstream turbine, or an array of three turbines, however, are discussed but not accentuated by any additional figures. For a deeper analysis of those results it is therefore referred to the single papers.

Upstream turbine power characteristics

At first, the measured operating characteristics of the upstream turbine are presented for variations in tip speed ratio λ_{T1}, blade pitch angle β_{T1} and yaw angle γ_{T1}. In Figure 7 the turbines operating characteristics are shown for one parameter being varied at a time. The model turbine's design operating point in all cases is $\lambda_{T1} = 6$, $\beta_{T1} = 0°$ and $\gamma_{T1} = 0°$. For a combined variation of tip speed ratio and pitch angle it is referred to **PAPER 1**, while a combined variation of tip speed ratio and yaw angle can be found in **PAPER 3**. At the turbines design point a maximum power coefficient of $C_{P,T1,opt} = 0.468$ is measured at a tip speed ratio of $\lambda_{T1} = 6.0$. For variations in tip speed ratio from $\lambda_{T1} = 4.0 - 8.0$ the power curve shows almost symmetrical characteristics around its maximum. When the blades are pitched towards feather, a decrease in power coefficient of $\Delta C_P = 0.027/1°$ is observed. Pitching the blades towards stall has been tested, but was not considered further for wake control studies. The power output of the upstream turbine dependency of its yaw misalignment is shown in Figure 7 (c). The power output is observed to be almost, but not perfectly symmetrical with respect to the yaw angle. The variation of the yaw angle up to $\gamma = \pm 40°$ may seem very high, as a full scale wind turbine probably would not be operated in these regions. In the first reported full scale field test of wake steering by Fleming et al. [22] the maximum yaw misalignment was set to $\gamma = 25°$ for

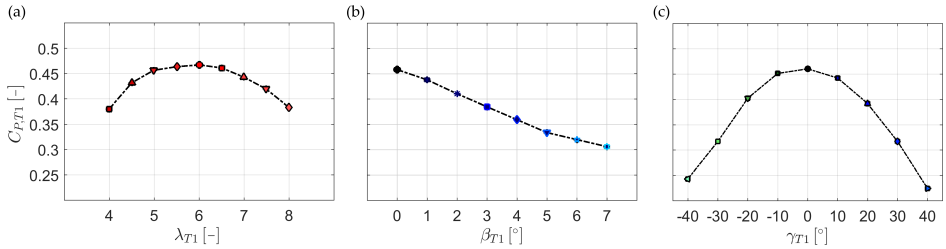

Fig. 7. Upstream turbine power coefficient $C_{P,T1}$ in dependence of **(a)** its tip speed ratio λ_{T1}, **(b)** blade pitch angle β_{T1} and **(c)** yaw angle γ_{T1}. The design operating point is $\lambda_{T1} = 6$, $\beta_{T1} = 0°$ and $\gamma_{T1} = 0°$.

limiting loads on the turbine. A variation of the tip speed ratio, pitch or yaw angle are seen to cause losses in upstream turbine power. However, the power lost on the turbine will be added to the wake flow and might be partially recovered by a downstream turbine. For a holistic optimization approach it is also important to take the thrust loads and yaw moments at the turbines into account. The characteristics of the upstream turbine's thrust coefficient and yaw moments are shown in Figures 12 and 13 together with those of an aligned downstream turbine.

Control-dependent wake flow

The concept of wake control has the primary purpose to add kinetic energy to the wake, which then can possibly be extracted by a downstream turbine. For this purpose wake measurements at different downstream positions x/D have been performed for different operating states of the upstream turbine. In Figure 8 the contours of the added mean velocity in the wake at $x/D = 3$ for an operation at a reduced tip speed ratio of $\lambda_{T1} = 4.5$, an increased pitch angle of $\beta_{T1} = 2°$ and a yaw angle of $\gamma_{T1} = 30°$ are compared. Only one of these parameters is varied at a time, while the other parameters are kept constant at the designed value.

For the case of reduced tip speed ratio in Figure 8 (a), it can be observed that kinetic energy is mostly added to the rotor swept area of a potential downstream turbine. However, a significant part of the added kinetic energy has diffused outside the rotor plane due to the expansion of the wake and cannot be recovered by a potential downstream turbine anymore. A similar distribution of added mean velocity is measured for a pitch angle of $\beta_{T1} = 2°$ as shown in Figure 8 (b). At the downstream distance of $x/D = 3$ a smaller amount of the added kinetic energy seems to have diffused into the freestream. The main difference in tip speed ratio and pitch angle control is the radial distribution of the added kinetic energy to the wake. When pitch angle control is applied, the induction is reduced at an equal rate over the entire blade span. Consequently, the mean velocity in the near wake increases almost evenly over the rotor swept area as observed for the

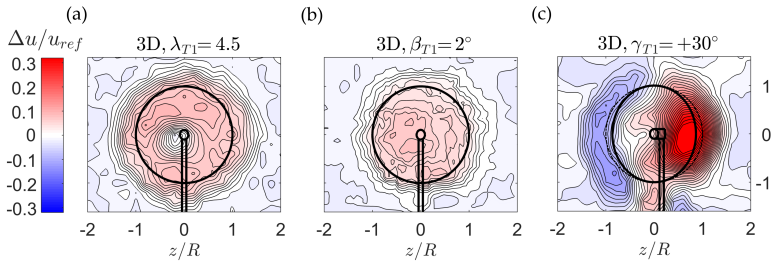

Fig. 8. Contours of normalized added mean velocity $\Delta u/u_{ref}$ in the wake x/D=3 at operatig points different than optimum (λ_{T1}=6.0, β_{T1}=0°, γ_{T1}=0°). **(a)** TSR controlled upstream turbine operated at $\lambda_{T1} = 4.5$, **(b)** Pitch controlled turbine operated at $\beta_{T1} = 2°$ and **(c)** Yaw controlled turbine operated at $\gamma_{T1} = 30°$.

wake profiles at $x/D = 3$ in Figure 9 (b). Adjusting the rotor's tip speed ratio away from its design point, the induction does not change constantly along the blade radius. The angle of attack is radially varied causing a non-constant induction on the flow. When the tip speed ratio is reduced to $\lambda_{T1} = 5$, for instance, smaller velocities are measured in the center of the near wake, while the wake's kinetic energy content increased in a circular region behind the outer blade elements (Figure 9 (a)). The opposite effect is observed for tip speed ratios higher than rated, in which case the velocity level in wake center is increased. A more detailed comparison of the two axial induction based control mechanisms is given in **PAPER 1**. With increasing downstream distance variations in the upstream turbine's induction have less effect on the wake flow. Small variations in tip speed ratio and pitch angle ($\beta_{T1} = 2°$) are seen to leave hardly any footprint in the wake profiles at $x/D = 6$ and especially $x/D = 9$ anymore. For higher downstream distances more kinetic energy is already diffused outside of the rotor swept area as indicated in the wake profiles in Figure 9 (b). These findings are consistent with LES computations on a full-scale turbine by Gebraad et al. (2015) [27], who also show an increased diffusion of the kinetic energy at higher downstream distances. This is assumed to be the main reason that both axial induction based turbine control methods are deemed to be more efficient for smaller turbine separation distances.

A completely different distribution of the added kinetic energy in the wake is obtained when the upstream turbine's yaw angle is changed as shown in Figure 8 (c). The wake is partially deflected away from an aligned virtual downstream rotor, resulting in a curled distribution of mean added kinetic energy. This method therefore offers great potential for steering the low kinetic energy fluid away from a downstream turbine and consequently increasing a wind farm's total power production. A detailed analysis of the symmetry, inflow effects and turbulence characteristics of the wake flow behind a positively and negatively yawed turbine is performed in **PAPER 3**. With increasing downstream distance a counter-rotating vortex pair is observed to create a kidney-shaped velocity deficit. Due to

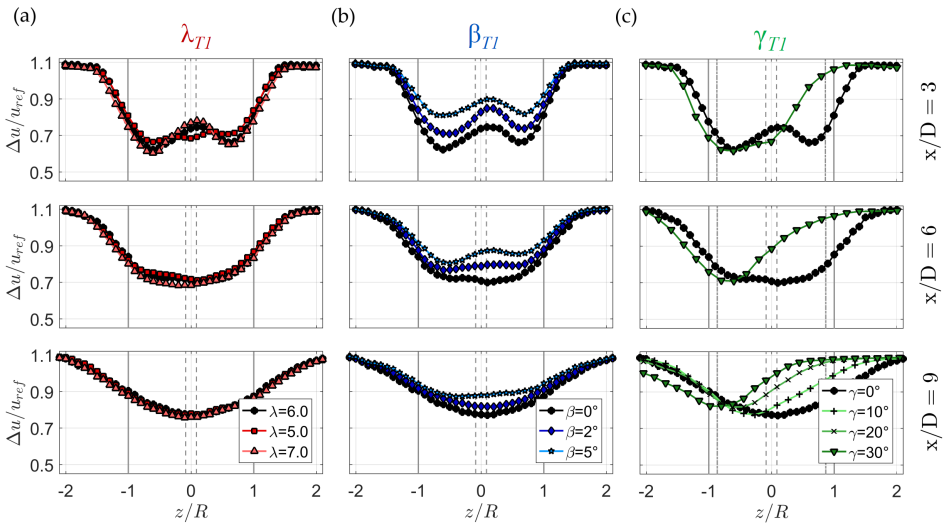

Fig. 9. Normalized mean velocity profile measured at hub height $y/D = 0$ in the wake $x/D = 3$, 6 and 9 behind the rotor. The upstream turbine **(a)** tip speed ratio λ_{T1}, **(b)** blade pitch angle β_{T1} and **(c)** yaw angle γ_{T1} is varied according to the legend. Line wakes for the yawed case are measured behind a smaller rotor of D=0.45m.

this complex three-dimensional shape, horizontal wake profiles at hub height as shown in Figure 9 (c) are not representative for the kinetic energy content in the wake. Nevertheless, the figure indicates a larger wake deflection with increasing downstream distance. As an increasingly large part of the low kinetic energy wake is deflected away from a potential downstream turbine, the effectiveness of yaw control for possible power gains might be higher for larger turbine separation distances. This is the opposite effect as for axial induction based wind farm control, which is considered to be most effective for small turbine separation distances. As shown for the downstream distance $x/D = 9$, larger upstream turbine yaw angles γ_{T1} cause a stronger lateral wake deflection.

The rotor generated turbulence profiles in the wake of a yawed wind turbine are shown in **PAPER 3**. It is observed that turbulence profiles peak as expected in regions of strong mean velocity gradients. However, the expansion of the turbulence footprints in the wake is observed to have a slightly wider expansion than the mean velocity profiles, which also should be taken into account in wind farm control models. An investigation by Schottler et al. in **PAPER 12** on the same measured wake dataset furthermore shows that an even wider wake should be defined when taking also locations of high flow intermittency into account. Heavy-tailed distributions of velocity increments are found in a ring surrounding the velocity footprint. This may be interpreted as instable flow state in this area, in which the flow is switching between wake and unaffected freestream.

An investigation of the effects of inflow turbulence and shear was also performed in **PAPER 3**. A moderate shear flow was observed not to have any significant influence on

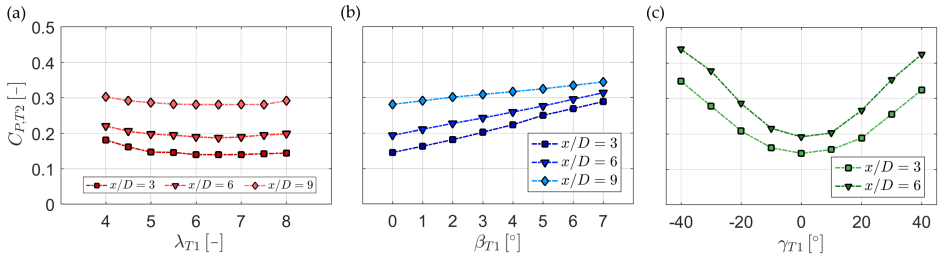

Fig. 10. Maximum downstream turbine power coefficient $C_{P,T1}$ in dependence of the upstream turbine's tip speed ratio λ_{T1}, blade pitch angle β_{T1} and yaw angle γ_{T1}. The downstream turbine is operated at $\beta_{T2} = 0°$ and $\gamma_{T2} = 0°$.

the wake characteristics. However, more measurements at stronger shear flows should be performed in order to assess the wake flow's sensitivity to this parameter. In contrast to that, a variation of the inflow turbulence is observed to have a more distinct influence on the wake's shape and deflection. Besides the obvious effects of a faster wake recovery and smoother mean velocity gradients with increased inflow turbulence, the curled wake shape is not as pronounced as for a low inflow turbulence level. Moreover, the wake behind a positively and negatively yawed turbine appear to feature a higher degree of symmetry than for low inflow turbulence. The interaction of the rotor wake with the tower wake is deemed to be weaker in this case.

Power output of an aligned downstream turbine

The power output of an aligned downstream wind turbine operated in the wake of a λ-, β- or γ-controlled upstream turbine is shown in Figure 10. Three different streamwise turbine spacings $x/D = [3, 6, 9]$ have been investigated for the axial induction based control techniques, only the two first spacings for yaw-based wake deflection control. The main reason for that is that a significant interaction of the deflected wake flow and the wind tunnel side walls would have occurred at a downstream distance of $x/D = 9$. At $x/D = 6$, however, the wake deflection was observed to be influenced by side wall blockage only to a very small extent, as shown in comparisons of wake measurements behind yawed turbines of different sizes (**PAPER 3**). As expected, the power of an aligned downstream turbine shows the opposite behaviour than the upstream turbine for all control mechanisms. In case the power of the upstream turbine reduces, it increases on the downstream turbine. As observed in Figures 10 (a) and (b) the λ- and β- control-dependent downstream turbine power curves have the highest slope for the smallest turbine spacing $x/D = 3$. That means that at this small separation distance, upstream turbine control has clear effect on the downstream turbine power output. In contrast to that, the downstream turbine power curves at $x/D = 9$ are significantly flatter, meaning that the effect of upstream turbine control is felt less at the downstream turbine.

The downstream turbine power's dependency on turbine spacing x/D is observed to be different for the case of upstream turbine yaw control as shown in Figure 10 (c). A higher slope of the downstream turbine power is measured for $x/D = 6$ than for $x/D = 3$. As previously shown, the wake is further deflected at higher downstream distances, making the control method more effective for larger streamwise turbine spacings. The downstream turbine power curves are also observed to be slightly asymmetric with respect to the upstream turbine yaw angle γ_{T1}. Higher downstream turbine power coefficients are measured for negative upstream turbine yaw angles. The previously discussed asymmetry in wake deflection is deemed to be the main reason for that observation. As shown in the wake deflection quantifications in **PAPER 3**, the wake deflection is larger for negative upstream turbine yaw angles than for positive angles in all inflow cases.

Combined power and loads

The crucial question with respect to all wind farm control approaches is whether the method is able to increase the overall power of the wind farm. For the presented test cases this question is limited to the investigated two-turbine array. There the question is reduced to whether the downstream turbine is able to recover or even surpass the power lost on the upstream turbine. For this purpose a normalized combined power is defined as the fraction of the combined power in off-design operation divided by the combined power in design operation as defined in Equation 14.

$$P^*_{T1+T2} = \frac{P_{T1}(\lambda_{T1},\, \beta_{T1},\, \gamma_{T1}) + P_{T2}(\lambda_{T1},\, \beta_{T1},\, \gamma_{T1})}{P_{T1,design} + P_{T2,design}} \tag{14}$$

Therein, $P_{T1,design}$ refers to the power extracted at $\lambda_{T1} = 6.0$, $\beta_{T1} = 0°$ and $\gamma_{T1}0°$ and $P_{T2,design}$ to the respective maximum power extracted of the downstream turbine for design operation of the upstream turbine. As shown in Figure 11 (a) a marginal combined power gain of about 0.5% is measured for $\lambda_{T1} = 5.5$ at the smallest turbine spacing of $x/D = 3$. This combined power gain has approximately the same magnitude as the measurement uncertainty and therefore is considered as insignificant. For higher turbine spacings, no combined power increase could be achieved. For slightly lower than designed tip speed ratios $\lambda_{T1} = 5.0 - 5.5$, the combined power is observed to be kept approximately constant. That means that the major part of the power losses on the upstream turbine could be recovered by the downstream turbine. For higher than design tip speed ratio, the combined power was seen to decrease.

Pitching the upstream turbine's blades did not results in any combined power gains as shown in Figure 11 (b). At the smallest tested pitch angle variation of $\beta_{T1} = 1°$, about 98.5% of the combined power in the designed case were produced of the two turbines. At even higher pitch angles more combined power is lost. As shown in Figures 12 (a) and

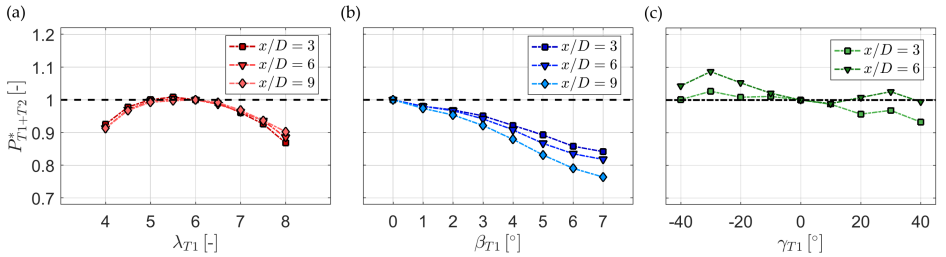

Fig. 11. Normalized combined power P^*_{T1+T2} in dependence of the upstream turbine's tip speed ratio λ_{T1}, blade pitch angle β_{T1} and yaw angle γ_{T1}. The downstream turbine is operated at $\beta_{T2} = 0°$, $\gamma_{T2} = 0°$ and a λ_{T2} at which maximum $C_{P,T2}$ is reached.

(b) the upstream turbine thrust is reduced at approximately the same value for a pitch angle reduction of 1° and a tip speed ratio reduction of −0.5 ($\Delta C_{T,T1,\Delta\beta=1°} = 0.062 \approx \Delta C_{T,T1,\Delta\lambda=-0.5} = 0.059$). The fact that the combined power in the tip speed controlled case is slightly higher, might have to do with the radial variation of the thrust along the length of a blade. While the kinetic energy was added at an approximately constant rate over the entire rotor swept area for the pitched case, kinetic energy was added in a ring at $r/R \approx 0.50 - 0.75$. This was previously shown in the wake profiles at $x/D = 3$ in Figures 9 (a) and (b). As the downstream wind turbine converts more energy on the outer blade elements of the rotor than the inner, tip speed ratio control is assumed to be the more effective method in this case. At larger downstream distances the choice of axial induction based method does not play an important role anymore.

Although, no significant power gains could be achieved for realistic turbine spacings $x/D \geq 6$ anymore, axial induction based control could possibly be used to mitigated loads on the upstream turbine. As shown in Figures 11 (a) and (b) the upstream turbine thrust coefficient decreases at a larger rate than the downstream turbine thrust rises for all investigated turbine separation distances. The upstream turbine thrust coefficient reduces at a rate of $\Delta C_{T,T1} = 0.118/1\lambda_{T1}$ while the thrust coefficient of the downstream turbine located at $x/D = 6$ increases only with $C_{T,T2,6D} = 0.017/1\lambda_{T1}$. This implies that a small variation in upstream turbine tip speed ratio or blade pitch angle, could be an effective method to mitigate upstream rotor loads while keeping the combined array power constant.

More significant gains in combined power could be achieved for upstream turbine yaw control. As shown in Figure 11 (c) the maximum combined power is obtained for an upstream turbine yaw angle of $\gamma_{T1} = \pm 30°$. The combined power profiles are moreover observed to be asymmetric with respect to the upstream turbine yaw angle. Higher power gains are generally obtained for negative upstream turbine yaw angles. As discussed above, the asymmetry in the mean velocity deficit in the wake was deemed to be the main reason for that finding. For the larger turbine spacing of $x/D = 6$ a relative power increase of 8% was assessed at an upstream turbine yaw angle of $\gamma_{T1} = -30°$. When the turbines were

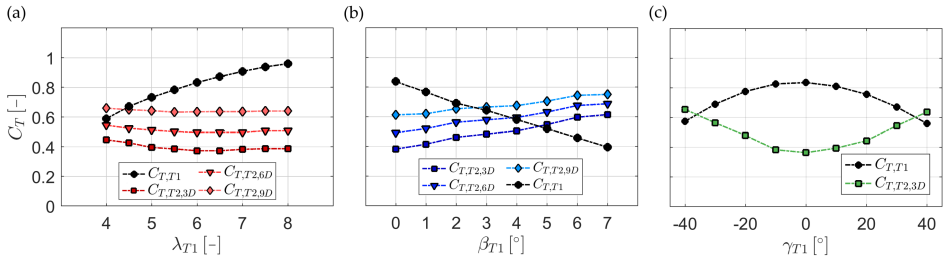

Fig. 12. Upstream turbine thrust coefficient $C_{T,T1}$ and downstream turbine thrust coefficient $C_{T,T2}$ in dependence of its tip speed ratio λ_{T1}, blade pitch angle β_{T1} and yaw angle γ_{T1}. The downstream turbine's positions are $x/D = 3$, 6 and 9.

separated $x/D = 3$, only 3.5% increase in combined power were measured at the same yaw angle. The thrust coefficients of the upstream and downstream turbine at $x/D = 3$ are shown in Figure 12 (c). As expected, the downstream turbine thrust shows the exact opposite trends compared to the upstream turbine thrust. The gradients in the yaw-angle-dependent thrust curves of both turbines seem to be very similar for this test case. Due to asymmetric loads in the yaw control test case, yaw moments on the upstream and downstream rotor were measured in addition to the power and thrust. The normalized yaw moments for the upstream turbine and an aligned downstream turbine located at $x/D = 3$ are presented in Figure 13. As indicated by the black line for $M^*_{y,T1}$, the obtained power gains for yaw angles $\gamma_{T1} \neq 0°$ were at the cost of increased yaw moments on the upstream rotor. High yaw moments are an indicator for unsteady flow conditions on the rotor blades during the course of one rotation. Therefore, increased loads on the blades and other structural components like rotor bearings are expected. The upstream turbine yaw moments were observed to grow linearly with increasing yaw angle; however, they were seen to be asymmetric with respect to the yaw angle as well. Moreover, yaw control also directly influences the yaw moments on a downstream rotor $M^*_{y,T2}$ as indicated by the green line in Figure 13. For aligned turbine positions, the downstream turbine yaw moments are observed to grow similarly as for the upstream turbine. For wind directions in which the turbines are aligned, upstream turbine yawing might therefore not be beneficial from a loads perspective.

Combined power of three aligned turbines

An array of two wind turbine models can be regarded as the smallest unit to study wake interaction effects. Power measurements on a row of aligned full-scale turbines by Barthelmie et al. (2010) [5] suggest that the single turbines' power production levels out after the second row. The largest change in turbine power output is confirmed to happen between the first and second row in LES studies by Churchfield et al. (2012) [12] and Andersen et al. (2017) [3]. Andersen et al., however, show a dependency of these characteristics on the

turbine spacing and turbulence intensity level in the inflow.

For a more detailed investigation of wake interactions in a larger unit of turbines, an experimental setup of three aligned model wind turbine was investigated in **PAPER 2**. Specifically, the effects of tip speed ratio control on the power output of a second and third row turbine were investigated. The small inter-turbine spacing of $x/D = 3$ and low background turbulence level of $TI_A = 0.23\%$ might not be representative for most full scale wind farms; however, this extreme case showed that tip speed ratio control on the front row turbine did not affect the power output of the third row turbine at all. For larger turbine spacings and a higher inflow turbulence level, the wake flow would have recovered even faster, mitigating the effects of upstream turbine control even more. The power outputs of the first three turbine rows measured in the experiment show good agreement with measurements from a full-scale wind farm of similar inter-turbine spacing as presented in Nilsson et al. (2015) [56]. Moreover, the experimental results in **PAPER 2** showed that controlling the tip speed ratio of the second row turbine hardly does not affect the power characteristics of a third row turbine. These findings support the hypothesis that the power of the third row turbine is rather independent of moderate induction based control of the first and second row. An analysis of the wake flow behind the first and second turbine discloses a considerably higher velocity deficit behind the second row. This observation explains a further power drop from the second to the third row turbine.

An attempt to control the three turbines to an optimized combined wind farm power resulted in insignificant power gains below 1%. This small gain was measured for a slightly lower than rated tip speed ratio of the front row turbine, which is a result previously found in the two turbine experiments of **PAPER 1** already. This supports the statement that a third turbine does not contribute any new dimensions to an axial induction based power optimization of a turbine row.

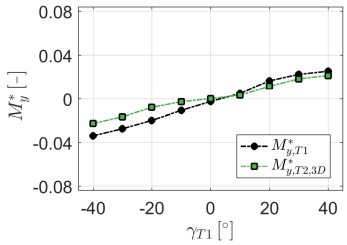

Fig. 13. Normalized yaw moment of the upstream turbine $M^*_{y,T1}$ and downstream turbine $M^*_{y,T2}$ positioned at $x/D = 3$ in dependence of the upstream turbine's yaw angle γ_{T1}.

Offset operation of the downstream turbine

A so far little investigated field of wake-interaction research is the offset operation of a downstream turbine. Depending on the site specific variations in wind direction, a partial overlap of a downstream rotor with the upstream turbine wake is inevitable for most setups and therefore considered to be a very relevant test case. In contrast to fully aligned turbines in complete wake overlap, the inflow field for a downstream turbine becomes highly asymmetrical when impinged by a partial wake. The blade forces on the downstream rotor are deemed to fluctuate during the course of one rotation in an asymmetric inflow. An experimental investigation of the downstream turbine loads in dependence of its position in the wake is performed by Schreiber et al. (2016) [72]. Therein, the turbine's position in a partial wake is estimated from azimuthal blade load variations. A model framework of two offset turbines and the potential for power and load optimization by upstream turbine yawing was recently presented by van Dijk et al. (2017) [76].

The effects of partial wake impingement on a downstream turbine were in studied in **PAPER 4** for this thesis. Besides power and thrust also yaw moments were measured on the upstream and downstream turbine. Wake steering by upstream turbine yaw misalignment demonstrated advantages for simultaneous load reduction and power gains on an offset downstream turbine. It is shown that upstream turbine yaw control is able to deflect the wake flow either on or away from the downstream rotor. For a wake deflection onto the rotor swept area, the downstream turbine experiences smaller yaw moments as its inflow conditions become more symmetrical. At the same time, however, also the downstream turbine's power production significantly reduces. In contrast to that, the wake can also be deflected away from the downstream turbine. If the lateral offset between the turbines is large enough, upstream turbine yawing might even be able to entirely deflect the wake away, maximizing the downstream turbine's power and canceling out yaw moments.

Another interesting result of the offset test case was found for intentional yawing of the downstream in a partial wake situation. As shown above in Figure 13 both a turbine operated in yawed condition as well as a non-yawed turbine operated in a partial wake experience yaw moments of about the same magnitude (for a turbine spacing of $x/D = 3$). The similar response of a turbine's yaw moment to yaw misalignment and a strongly sheared inflow suggested the concept of yaw moment mitigation by opposed yawing of a downstream turbine in a partial wake situation. The final test case in **PAPER 4** proved that yaw moments could be decreased for opposed yawing of the downstream turbine. Surprisingly, also the downstream turbine's power output was observed to increase for moderate downstream turbine yawing ($\gamma_{T2} = 5 - 10°$) in partial wake situations. In contrast to the aligned case, yaw control was shown to be advantageous for both load mitigation and power optimization at the same time in offset turbine setups.

5.2 Reference experiments for computational models

Wake flow simulation models

Model scale experiments are not necessarily representative for real effects in full scale wind farms, due to the previously mentioned scaling and blockage issues. However, a big advantage of wind tunnel experiments are the controlled boundary conditions, which allows for isolated parameter variations and repeatable experiments. For this reason, model scale wind turbine wake experiments can serve as a well defined reference experiment for wake simulations tools.

Efforts to simulate the wake flow with different prediction tools were made in our research group in the form of two Master thesis projects by Polster et al. (**PAPER 15**) and Göing et al. (**PAPER 16**. In Polster et al. (**PAPER 15**) six engineering wind turbine wake models were compared to wake measurements obtained in the wind tunnel. Moreover, the models' sensitivity to inflow turbulence and thrust variations (through pitch angle control) was tested. The classical wake model by Frandsen et al. (2006) [23] did not prove to predict the measured mean wake velocity profile sufficiently well. A better prediction was obtained by a recent model by Bastankah and Porte-Agél (2014) [7], although model the wake velocity level was generally overpredicted. Good mean velocity predictions were observed for a high inflow turbulence by a model by Ishihara et al. (2004) [39]. However, the model's sensitivity to variations in rotor thrust did not agree well with the measured data. In contrast to that, the classical Jensen PARK model [43] performed well with respect to thrust sensitivity. The best overall predictions at high background turbulence were given by the Jensen-Gaussian wake model, a further development of the PARK model, recently proposed by Gao et al. (2016) [24]. At very low background turbulence, however, the wake velocity predictions were observed to be far off. Reasonably good approximations of the wake development at low turbulence intensity were achieved by combining the Jensen-Gaussian wake model with a turbulence model proposed by Crespo and Hernández (1996) [15].

A high-fidelity Delayed Detached Eddy Simulation (DDES) of the wake flow behind the model wind turbine was performed by Göing et al. in **PAPER 16**. CFD simulations of this type require a significant amount of computational resources as they fully resolve the large eddies in the wake. The computational results of the DDES proved to accurately predict the wake flow behind the model wind turbine exposed to a sheared inflow. The mean streamwise and vertical velocity as well as turbulent kinetic energy distributions compared well at two tested downstream positions. In spite of the large requirements for computational power, the DDES technique proved to be an appropriate approach for the simulation of wind turbine wake interactions.

Wind tunnel measurements of the mean and turbulent wake were furthermore provided

as reference data for model predictions by external expert groups in CFD modeling. The tradition of NTNU's Blind test experiments initiated by Krogstad et al. (2013, 2014, 2015) [49, 59, 50] was continued in **PAPER 5** and **PAPER 13**. The fourth blind test (**PAPER 5**) experiment focused on the influence of inflow turbulence and shear on the wake flow and the interaction of two aligned turbines in different separation distances. Five external simulations were submitted, comprising a LES, a DDES and three RANS simulations. The performance of the upstream turbine was in general very well predicted by all simulations for all three inlet conditions, with an acceptable scatter of maximum $\pm 7\,\%$. However, the turbine's performance was documented from earlier blind tests. A larger variation was observed for the performance of the downstream turbine. The scatter in predictions was observed to increase for higher separation distances, from $\pm 15\,\%$ at $x/D = 2.77$ to $\pm 30\,\%$ at $x/D = 9.00$. Despite the large variations, the performance predictions had improved compared to previous blind test experiments, in which the downstream turbine power was scattered more than $\pm 100\,\%$ in [59] or $\pm 50\,\%$ in [50]. The most challenging task was however the prediction of inflow-dependent wake flow. Accurate predictions of the mean and turbulent velocities in the wake were consistently delivered by DDES and LES computations, which was confirmed by high statistical correlation scores of these simulations with the experimental data. As observed in previous blind tests, RANS simulations partly managed an acceptable prediction of the mean velocity profile, while the wake turbulence was in most cases far off the experimentally measured values. Fully resolved RANS models generally resulted in better predictions than RANS computations combined with actuator line or disc models. The characteristics of a slightly skewed wake behind a turbine exposed to non-uniform shear were well captured by most of the predictions. Outside the scope of the blind test workshop, an additional set of simulations of the blind test cases were amongst others performed by Ciri et al. (2017) [13]. The LES study compared an actuator line to a rotating actuator disc approach, resulting in more accurate predictions by the actuator line method. While the mean velocity profiles were generally well predicted a slight under prediction of the turbulent kinetic energy in the wake was observed.

Another fifth blind test workshop was held in May 2017, investigating the capability of computational models to predict the strongly three-dimensional and asymmetric wake flow behind yawed turbine configurations. Three test cases were designed investigating the wake flow behind a single yawed turbine, a two-turbine setup of which the first was operated in yaw as well as the yawed wake behind a new turbine geometry. Four external expert groups in CFD modeling contributed a dataset of full field wake predictions and turbine performance data. Three combined LES-ACL simulations were submitted, while a fourth contribution fully resolved the rotor geometry in a DDES simulation. The power coefficient of the yawed turbine was scattered within a range of $\pm 19\%$, which was slightly larger than in the previous blind test. The power coefficient of the downstream

turbine was varying in the range of ±49% from the experimentally measured value, indicating the difficult prediction of turbine performance in a partial wake situation. The best performance predictions were achieved by an actuator line approach, which used an experimentally measured dataset for the airfoil coefficients by Sarmast and Mikkelsen (2013) [68]. The higher accuracy of the measured force coefficients for larger than design angles of attack might have been of significant advantage for the prediction of a downstream turbine operated in a partial wake, which continuously experiences large variations in angle of attack during the course of one rotation. The mean streamwise and vertical velocities in the complex yawed wake flow field were generally very well predicted by all numerical simulations, confirming the mature development of LES/DES tools for wind turbine wake simulations. Smaller deviations could be attributed to inaccuracies in inflow modeling or a too coarse computational grid. One of the most positive results of the fifth blind tests were the very accurate predictions of the turbulent kinetic energy in the wake behind a single and two turbines. In contrast to all previous blind test, the locations and magnitude of turbulence peaks only showed very small deviations from the experimental results. In general, the results confirmed a continuous improvement in wake flow predictions from the first to the fifth blind test. Combined LES/actuator line methods as well as hybrid DES approaches emerged to be deliver the most accurate wake flow predictions. The fifth blind test moreover indicated that future developments trend towards codes performing accurate simulations at significantly less grid cells, increasing the computational efficiency for high-fidelity wake predictions and consequently making simulations of full wind farms possible.

Low-Reynolds airfoil flow simulations

Motivated by the low chord-based Reynolds number in the blind test experiments, another experiment focusing on the flow over an airfoil was established. A two-dimensional wing model of the NREL S826 airfoil was built (see Section 4.2) to measure lift, drag and mid-span surface pressure distributions. Besides a Master thesis project comprising the design and initial experiments by Aksnes (2015) [2], two computational simulations of the airfoil flow were performed by Sagmo et al. (2016) (**PAPER 8**) and Prytz et al. (2017) (**PAPER 10**).

In **PAPER 8** 2D and 3D steady state RANS simulations were performed at $Re = 1.0 \times 10^5$ using three different turbulence models. Both the Spalart-Allmaras and the Realizable $k-\epsilon$ turbulence model were observed to reproduced experimental results for lift well in a 2D setup. However, 2D simulations were observed to under predict drag significantly compared with 3D $k-\epsilon$ simulations. The three-dimensional simulations furthermore showed significant spanwise variations in surface pressure when stall kicks in and managed to

predict a single stall cell for large angles of attack. Similar three-dimensional effects resembling those of stall cells were also observed in DDES simulations by Prytz et al. in **PAPER 10**. Therein, the flow over the airfoil was simulated for Reynolds numbers varying from $Re = 5.0 \times 10^4$ to $Re = 1.0 \times 10^6$. Different RANS models were tested for the simulation part in the boundary layers, of which the Realizable $k - \epsilon$ resulted in the best match with the experimentally measured pressure distributions. Moreover, an excellent agreement with a previous LES computation of the airfoil flow by Sarlak (2014) [65] was achieved at significantly less computational cost.

After a repetition of the experimental measurements on the NREL S826 wing model, the experimental results were summarized in **PAPER 6**. As the lift and drag characteristics were observed to be affected by transitional effects in the form of laminar separation bubbles, additional computations applying the transitional $\gamma - Re_\theta$ model by Langtry-Menter were performed. The strongest transitional effects were observed for $Re < 0.7 \times 10^5$, leading to a collapse in the airfoils lift characteristics. At larger Reynolds numbers smaller laminar separation bubbles are observed on pressure and suction side, while their influence on lift an drag characteristics was decreasing with increasing Reynolds number. The $\gamma - Re_\theta$ model proved to be able to accurately predict the location and pressure levels of laminar separation bubbles for most cases in the linear lift range. When approaching stalled flow conditions, however, the $\gamma - Re_\theta$ as well as a fully turbulent Realizable $k - \epsilon$ underpredicted the measured lift coefficients, confirming the weakness of RANS models to accurately predict separated flow.

A comparison of the measured airfoil coefficients to earlier NREL S826 experiments performed at DTU [68] and METU [58] resulted in a good agreement in the linear lift region. At the onset of stall, however, significant differences were observed in the lift and drag characteristics. For instance, the experimental dataset recorded at NTNU at $Re = 1.0 \times 10^5$ showed a considerably higher maximum lift. A closer investigation suggested that these deviations in the stall region can be attributed to differences in the freestream turbulence level in the inflow to the wing model.

6 Conclusions

An experimental study investigating the wake-turbine interaction of three different wind farm control methods was presented. Additionally, model-scale reference experiments for computational wake and airfoil flow models were performed.

A comparison of the combined power output of an aligned two-turbine array demonstrated the effectiveness of yaw wake steering for the purpose of combined power gains. The combined power profiles were observed to be asymmetric with respect to the upstream turbine

yaw angle. A detailed analysis of the wake flow confirmed an asymmetric deflection of the mean kinetic energy distribution in the wake for different inflow conditions. However, the combined power gains were observed to be at the cost of increased yaw moments on a yawed upstream turbine as well as a downstream turbine operated in a partial wake. As raised levels of yaw moments indicate increased unsteady rotor loads, a careful analysis of structural loads on both turbines is suggested for future studies.

For offset positions of the downstream turbine, however, wake steering through intentional yaw misalignment of the upstream turbine was demonstrated to simultaneously increase combined power and mitigate yaw moments on the downstream turbine. For higher lateral offsets of approximately half a rotor diameter and a sufficiently high turbine spacing, the mean velocity deficit in the wake could be almost entirely deflected away from a downstream rotor. For situations in which partial wake impingement was inevitable, opposed yawing of a downstream rotor was demonstrated to mitigate loads and increase its power production at the same time. A more detailed analysis of downstream turbine rotor loads is however recommended to fully assess this strategy's potential for load mitigation on downstream rotors.

In tightly spaced wind farms, yaw control was observed to cause a partial wake inflow with strong velocity gradients for an aligned downstream turbine. In these situations, axial induction based wake control methods have been demonstrated to offer some advantages. Although no significant combined power gains through axial induction based control were measured, they were demonstrated to be able to effectively reduce upstream turbine thrust loads while the combined array power could be kept almost constant. A comparison of tip speed ratio and pitch angle control disclosed small local differences in the distribution of added kinetic energy in the wake flow. While pitch control was observed to add kinetic energy at a almost constant rate over the entire rotor swept area, a reduced tip speed caused a kinetic energy addition in a ring behind the outer blade elements. The possibilities to manipulate the near wake's kinetic energy distribution by these axial induction based control methods are however deemed to be highly dependent on the specific rotor design. In contrast to wake steering by yaw control, axial induction based methods become increasingly inefficient with increasing turbine spacing. For separation distances $x/D \geq 6$, small variations in upstream turbine pitch angle or tip speed ratio are observed to hardly have any influence on the mean wake flow or downstream turbine power. In an additional measurement campaign, coordinated tip speed ratio control was tested on a row of three aligned model wind turbines. The main result of this study was that moderate tip speed ratio control on the second row turbine almost did not affected the power characteristics of a third row turbine at all. As the power measured on the third row turbine was observed to be almost independent of moderate tip speed variations on the first and second row turbine, the statement that the most significant effects of small variations in turbine

induction happen between the first two turbines was confirmed.
The second part of this thesis described two reference experiments for computational flow solvers. The blind test experiments confirmed the capability of combined LES-Actuator line techniques and hybrid DES methods to perform exact predictions of the mean and turbulent wake flow. Challenging test cases featuring sheared inflow (blind test 4) or the interaction of a highly asymmetric yawed wake inflow with the wake of a non-yawed downstream turbine (blind test 5) were accurately predicted by these models. The blind tests furthermore indicated a competitive advantage for codes that are able to perform accurate wake predictions at a significantly reduced computational power.
Finally, a combined experimental and computational study on the flow around the model turbine's airfoil was performed at low to moderate Reynolds numbers. The experimental results showed good agreement with other experimental dataset in the linear lift region, while deviations at the onset of stall could be subscribed to different turbulence levels in the inflow. Transitional effects in the form of laminar separation bubbles could be accurately predicted by RANS solvers including transition modeling, while separated flow conditions in stall were still observed to be difficult to predict by all investigated RANS models.

7 Further work

The experiments presented in this work gave answers to some of the questions asked in the beginning of this project. While the data was evaluated and documented, however, hundreds of further questions arose. These issues concerned amongst other the validity of the tested inflow conditions, scaling effects and measurements of important parameters which could not be assessed with the existing setup. Further experimental research could investigate the sensitivity of the turbine loads and the wake flow on more realistic inflow conditions. Until now, only two turbulence levels and two shear coefficients have been investigated. A more elaborate adjustment of the turbulent length scales in the inflow could be performed. Unsteady inflow as present in real atmospheric conditions could for instance be reproduced by applying active grids. Another burning issue to be experimentally investigated would be the loads on aeroelastically scaled blades. Advanced blade structures and sensor technology would be needed for a detailed investigation of e.g. blade root bending moments. An experimental dataset of structural rotor loads of a turbine exposed to a matrix of different inflows would be extremely valuable for the validation of computational models. The investigated inflow conditions therein could be designed for a turbine exposed to different atmospheric stability classes, but also complex partial wake inflows to a downstream turbine.
The primary goal of future research in wake interactions is to develop fast and accurate

models that are able to predict and optimize power and loads in wind farms exposed to different inflows. High-fidelity computational wake models in LES/DES have reached a good level, but require too much computational resources to be fast enough for a controllable wind farm model. Research efforts for future research should therefore also be directed to simple and fast engineering models for inflow-turbine and wake-turbine interaction.

Appendix A: Model turbine geometry definition

Technical drawings of the model wind turbines *T1*, *T2* and *LARS1* are presented in Figures A.1, A.2 and A.3, respectively.

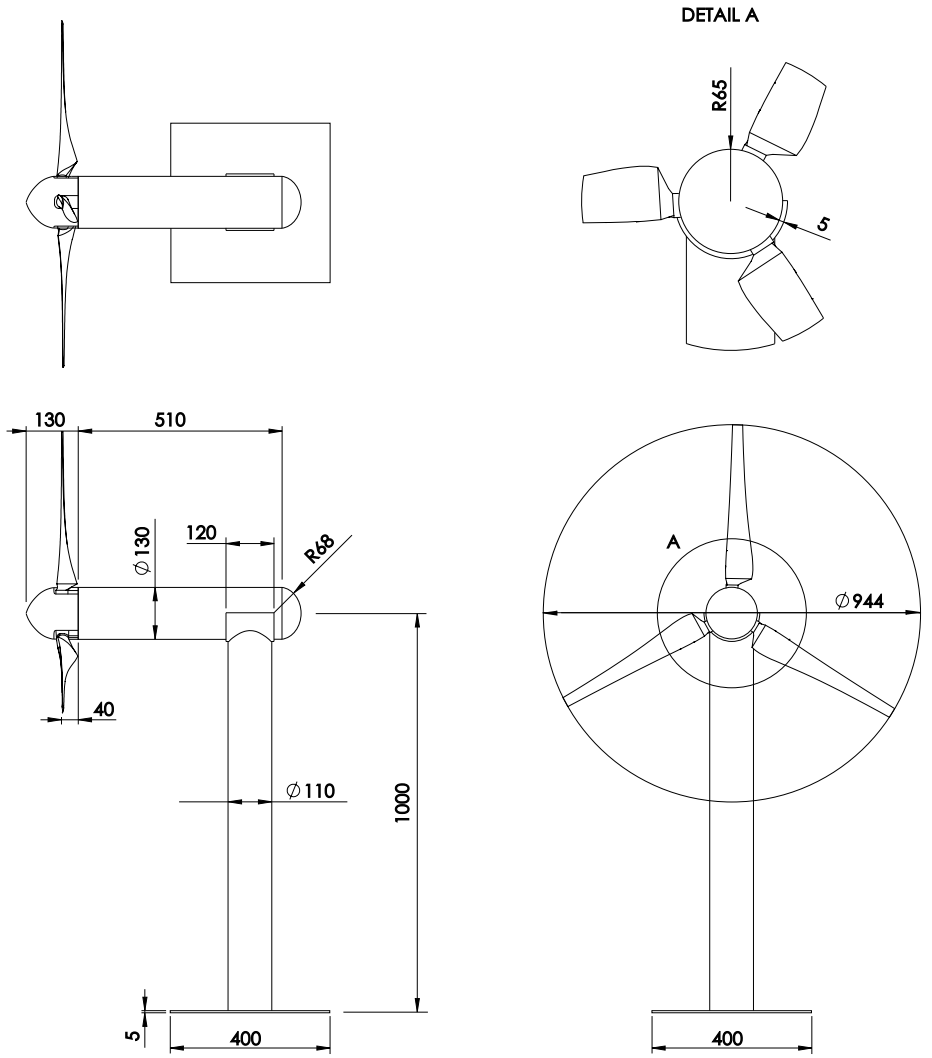

Fig. A.1. Geometry definition of model wind turbine *T1*.

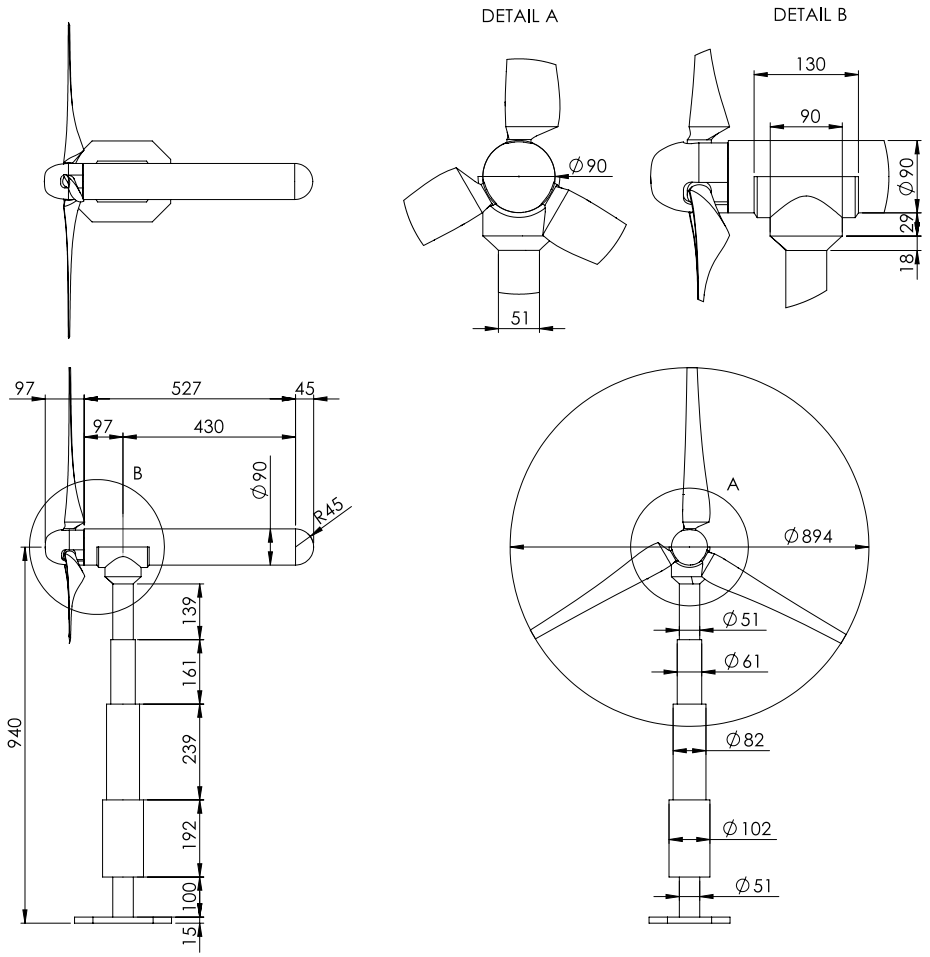

Fig. A.2. Geometry definition of model wind turbine *T2*.

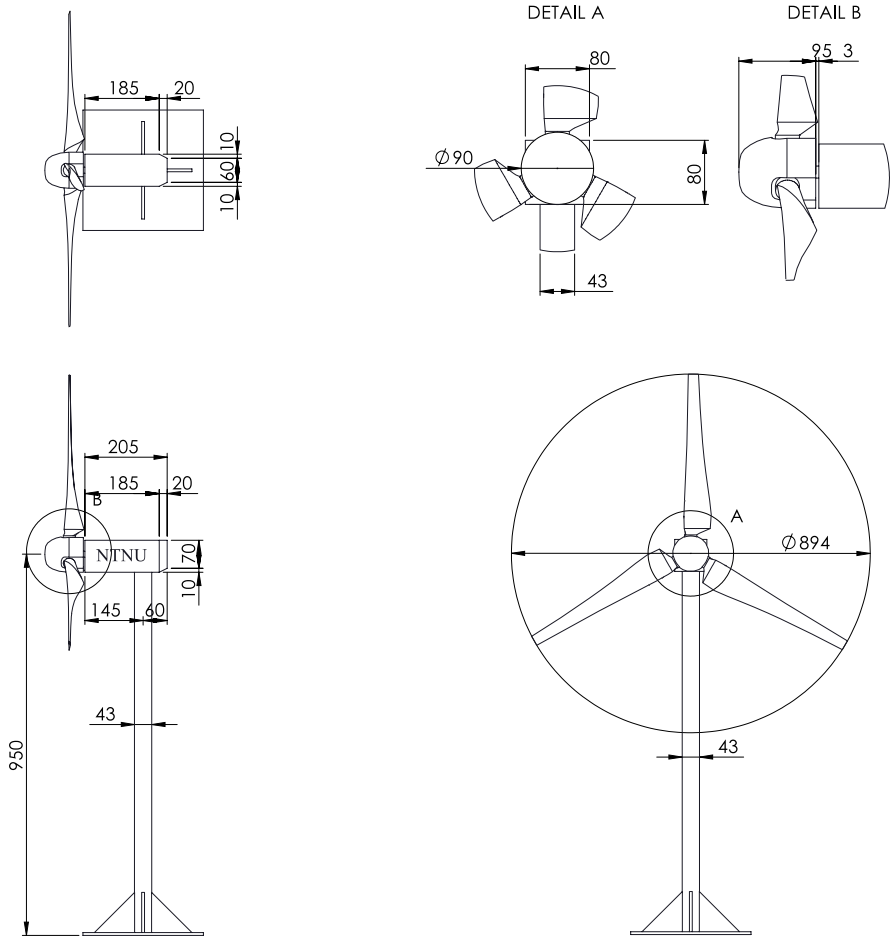

Fig. A.3. Geometry definition of model wind turbine *LARS1*.

Appendix B: Airfoil and rotor blade geometry definition

Table B.1 and Figure B.1 show the normalized coordinates of the NREL S826 airfoil.

Table B.1. Normalized NREL S826 airfoil coordinates.

Suction side		**Pressure side**	
x/c	y/c	x/c	y/c
0.00000	0.00000	0.00000	0.00000
0.00018	0.00159	0.00021	-0.00146
0.00255	0.00748	0.00093	-0.00274
0.00954	0.01638	0.00216	-0.00403
0.02088	0.02596	0.00367	-0.00525
0.03651	0.03580	0.01367	-0.01035
0.05636	0.04562	0.02920	-0.01518
0.08026	0.05519	0.04998	-0.01960
0.10801	0.06434	0.07580	-0.02362
0.13934	0.07288	0.10637	-0.02729
0.17395	0.08068	0.14133	-0.03091
0.21146	0.08758	0.17965	-0.03486
0.25149	0.09343	0.21987	-0.03855
0.29361	0.09807	0.26153	-0.04064
0.33736	0.10133	0.30497	-0.04051
0.38228	0.10294	0.35027	-0.03794
0.42820	0.10249	0.39779	-0.03280
0.47526	0.10005	0.44785	-0.02563
0.52324	0.09607	0.50032	-0.01720
0.57161	0.09094	0.55484	-0.00841
0.61980	0.08489	0.61055	-0.00015
0.66724	0.07816	0.66644	0.00699
0.71333	0.07095	0.72142	0.01254
0.75749	0.06341	0.77434	0.01621
0.79915	0.05572	0.82409	0.01784
0.83778	0.04798	0.86953	0.01741
0.87287	0.04029	0.90945	0.01498
0.90391	0.03262	0.94257	0.01113
0.93072	0.02479	0.96813	0.00689
0.95355	0.01695	0.98604	0.00324
0.97251	0.00982	0.99655	0.00084
0.98719	0.00431	1.00000	0.00000
0.99668	0.00103		
1.00000	0.00000		

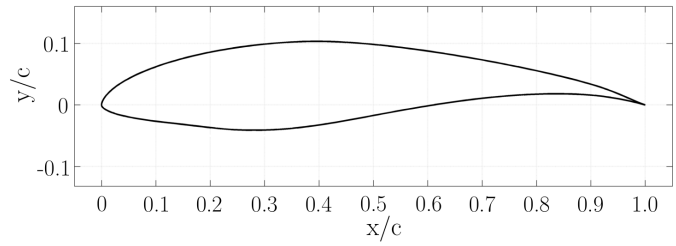

Fig. B.1. NREL S826 airfoil coordinates.

In Table B.2 and Figure B.2 the chord length and twist angle distribution of the NTNU blade are defined. Note that twist angles of $\varphi = 120.00°$ for the first three blade elements indicate circular sections at the blade root.

Table B.2. NTNU blade chord and twist distribution.

Blade element	**Radius** r **[m]**	**Chord** c **[m]**	**Twist angle** φ **[°]**
1	0.0075	0.013500	120.00
2	0.0225	0.013500	120.00
3	0.0490	0.013500	120.00
4	0.0550	0.049500	38.000
5	0.0675	0.081433	37.055
6	0.0825	0.080111	32.544
7	0.0975	0.077012	28.677
8	0.1125	0.073126	25.262
9	0.1275	0.069008	22.430
10	0.1425	0.064952	19.988
11	0.1575	0.061102	18.034
12	0.1725	0.057520	16.349
13	0.1875	0.054223	14.663
14	0.2025	0.051204	13.067
15	0.2175	0.048447	11.829
16	0.2325	0.045931	10.753
17	0.2475	0.043632	9.8177
18	0.2625	0.041529	8.8827
19	0.2775	0.039601	7.2527
21	0.3075	0.036201	6.5650
22	0.3225	0.034697	5.9187
23	0.3375	0.032017	4.7185
25	0.3675	0.030819	4.1316
26	0.3825	0.029704	3.5439
27	0.3975	0.028664	2.9433
28	0.4125	0.027691	2.2185
29	0.4275	0.026780	1.0970
30	0.4425	0.025926	-0.7167

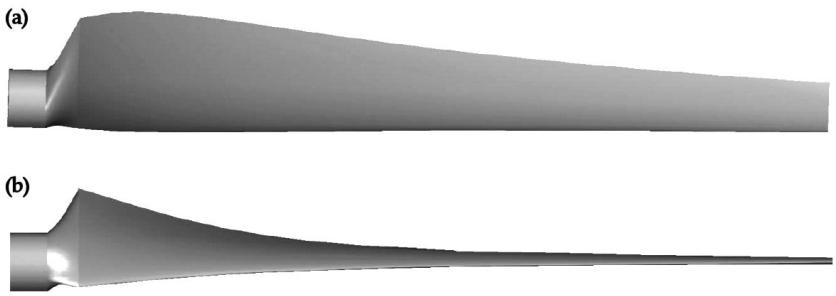

Fig. B.2. NTNU blade geometry: **(a)** suction side view and **(b)** leading edge view.

References

1. Adaramola, M. and P.-Å., K.: Experimental investigation of wake effects on wind turbine performance, Renewable Energy, 36, 2078–2086, doi: 10.1016/j.renene.2011.01.024, 2011.

2. Aksnes, N.Y.: Performance Characteristics of the NREL S826 Airfoil, Master thesis NTNU, 2015.

3. Andersen, S., Sørensen, J., and Mikkelsen, R.: Performance and Equivalent Loads of Wind Turbines in Large Wind Farms, Journal of Physics: Conference Series, 854, 012 001, doi:10.1088/1742-6596/854/1/012001, 2017.

4. Annoni, J., Gebraad, P.M.O., Scholbrock, A.K., Fleming, P. and van Wingerden, J.W.: Analysis of axial-induction-based wind plant control using an engineering and a high-order wind plant model, Wind Energy, 19, 1135–1150, doi: 10.1002/we.1891, 2015.

5. Barthelmie, R.J., Frandsen, S.T., Hansen, K., Schepers, J.G., Rados, K., Schlez, W., Neubert, A., Jensen, L.E., and Neckelmann, S.: Quantifying the Impact of Wind Turbine Wakes on Power Output at Offshore Wind Farms, Journal of Atmospheric and Oceanic Technology, 27(8), 1302–1317, doi: 10.1175/2010JTECHA1398.1, 2010.

6. Barthelmie, R.J. and Jensen, L.E.: Evaluation of wind farm efficiency and wind turbine wakes at the Nysted offshore wind farm, Wind Energy, 13, 573-586, doi: 10.1002/we.408, 2010.

7. Bastankhah, M. and Porté-Agel, F.: A new analytical model for wind-turbine wakes. Renewable Energy, 70, 116-123, doi:10.1016/j.renene.2014.01.002, 2014.

8. Bastankhah, M. and Porté-Agel, F.: Experimental and theoretical study of wind turbine wakes in yawed conditions, Journal of Fluid Mechanics, 806, 506–541, doi: 10.1017/jfm.2016.595, 2016.

9. Benedict, L. and Gould, R.: Towards better uncertainty estimates for turbulence statistics, Experiments in Fluids, 22, 129–136, doi: 10.1007/s003480050030, 1996.

10. Bromm, M., Vollmer, L. and Kühn, M.: Numerical investigation of wind turbine wake development in directionally sheared inflow, Wind Energy, doi: 10.1002/we.2010, 2016.

11. Campagnolo, F., Petrović, V., Bottasso, C. and Croce, A.: Wind Tunnel Testing of Wake Control Strategies, American Control Conference, doi: 10.1109/ACC.2016.7524965, 2016.

12. Churchfield, M., Lee, S., Moriarty, P., Martinez, L., Leonardi, S., Vijayakumar, G. and Brasseur, J.: A large-eddy simulation of wind-plant aerodynamics. Proceedings of the 50th AIAA Aerospace Sciences Meeting, Nashville, TN, USA, 912 January, 2012.

13. Ciri, U., Petrolo, G., Salvetti, M.V. and Leonardi, S.: Large-Eddy Simulations of Two In-Line Turbines in a Wind Tunnel with Different Inflow Conditions, Energies, 10(6), 821; doi: 10.3390/en10060821, 2017.

14. Corten, G.P. and Schaak, P.: Heat and Flux - Increase of Wind Farm Production by Reduction of the Axial Induction, EWEC 2003, 1619 June, Madrid, Spain, 2003.

15. A Crespo, A. and Hernández, J.: Turbulence characteristics in wind turbine wakes. Journal of wind engineering and industrial aerodynamics, 61, 71-85, doi: 10.1016/0167-6105(95)00033-X, 1996.

16. Damiani, R., Dana, S., Annoni, J., Fleming, P., Roadman, J., van Dam, J., and Dykes, K.: Assessment of Wind Turbine Component Loads Under Yaw-Offset Conditions, Wind Energy Science Discussions, doi: 10.5194/wes-2017-38, 2017.

17. Eriksen, P. E.: Rotor wake turbulence – An experimental study of a wind turbine wake, Doctoral thesis at NTNU 2017:34, isbn: 978-82-326-1408-0, 2016.

18. Eriksen, P. E. and Krogstad, P.-Å.: Development of coherent motion in the wake of a model wind turbine, Renewable Energy, 108, 449–460, doi: 10.1016/j.renene.2017.02.031, 2017.

19. Fleming, P.A., Gebraad, P.M.O., Lee, S., van Wingerden, J.W., Johnson, K., Churchfield, M., Michalakes, J., Spalart, P. and Moriarty, P.: Evaluating techniques for redirecting turbine wakes using SOWFA, Renewable Energy, 70, 211–218, doi: 10.1016/j.renene.2014.02.015, 2014.

20. Fleming, P.A., Gebraad, P.M.O., Lee, S., van Wingerden, J.-W., Johnson, K., Churchfield, M., Michalakes, J., Spalart, P., and Moriarty, P.: Simulation comparison of wake mitigation control strategies for a two-turbine case, Wind Energy, 18, 2135–2143, doi: 10.1002/we.1810, 2015.

21. Fleming, P.A., Ning, A., Gebraad, P.M.O. and Dykes, K.: Wind plant system engineering through optimization of layout and yaw control. Wind Energy, 19, 329–344, doi: 10.1002/we.1836, 2016.

22. Fleming, P.A., Annoni, J., Shah, J.J., Wang, L., Ananthan, S. Zhang, Z., Hutchings, K., Wang, P., Chen, W. and Chen, L.: Field test of wake steering at an offshore wind farm. Wind Energy Science, 2, 229-239, doi:10.5194/wes-2-229-2017, 2017.

23. Frandsen, S., Barthelmie, R., Pryor, S., Rathmann, O., Larsen, S., Højstrup, J. and Thøgersen, M.: Analytical modelling of wind speed deficit in large offshore wind farms. Wind Energy, 9, 39-53, doi: 10.1002/we.189, 2006.

24. Gao, X., Yang, H. and Lu, L.: Optimization of wind turbine layout position in a wind farm using a newly-developed two-dimensional wake model. Applied Energy, 174, doi: 10.1016/j.apenergy.2016.04.098, 192-200, 2016

25. Gaumond, M., Rethore, P.E., Bechmann, A., Ott, S., Larsen, G.C., Pena Diaz, A and Hansen, K.S. Benchmarking of wind turbine wake models in large offshore wind farms, Proceedings of the Science of Making Torque From Wind, url: www.eera-dtoc.eu/wp-content/uploads/files/Gaumond-et-al-Benchmarking-of-wind-turbine-wake-models-in-large-offshore-wind-farms5.pdf (accessed 12 Dec 2017), 2012.

26. Gebraad, P.M.O., Teeuwisse, F.W., van Wingerden, J.W., Fleming, P.A., Ruben, S.D., Marden, J.R. and Pao, L.Y.: A Data-Driven Model for Wind Plant Power Optimization by Yaw Control, American Control Conference, doi: 10.1109/ACC.2014.6859118, 2014.

27. Gebraad, P.M.O., Fleming, P.A., and van Wingerden, J.W.: Comparison of Actuation Methods for Wake Control in Wind Plants, American Control Conference, doi: 10.1109/ACC.2015.7170977, 2015.

28. Gebraad, P. M. O., Teeuwisse, F. W., van Wingerden, J. W., Fleming, P. A., Ruben, S. D., Marden, J. R., and Pao, L. Y.: Wind plant power optimization through yaw control using a parametric model for wake effects-a CFD simulation study, Wind Energy, 19, 95–114, doi: 10.1002/we.1822, 2016.

29. Global Wind Energy Council (GWEC), Press release, (25 April 2017), Strong Outlook for Wind Power, url: http://gwec.net/global-figures/graphs/ (last accessed 5.12.2017), 2017.

30. Gonzalez, J.S., Payan, M.B., Santos, J.R. and Rodriguez, A.G.G.: Maximizing the overall production of wind farms by setting the individual operating point of wind turbines, Renewable Energy, 80, 221–229, doi: 10.1016/j.renene.2015.02.009, 2015.

31. Grant, I., Parkin, P., and Wang, X.: Optical vortex tracking studies of a horizontal axis wind turbine in yaw using laser-sheet, flow visualisation, Experiments in Fluids, 23, 513–519, doi:10.1007/s003480050, 1997.

32. Grant, I. and Parkin, P.: A DPIV study of the trailing vortex elements from the blades of a horizontal axis wind turbine in yaw, Experiments in Fluids, 28, 368–376, doi:10.1007/s003480050, 2000.

33. Haans, W., Sant, T., van Kuik, G., and van Bussel, G.: Measurement of Tip Vortex Paths in the Wake of a HAWT Under Yawed Flow Conditions, Journal of Solar Energy Engineering, 127, 456–463, doi:10.1115/1.2037092, 2005.

34. Hansen, K.S., Barthelmie, R.J., Jensen, L.E. and Sommer, A.: The impact of turbulence intensity and atmospheric stability on power deficits due to wind turbine wakes at Horns Rev wind farm, Wind Energy, 15, 183–196, doi:10.1002/we.512, 2012.

35. Hansen, M.O.L.: Aerodynamics of Wind Turbines, Second Edition, Earthscan, isbn: 1849770409, 2013.

36. Horvat, T., Spudic, V. and Baotic, M.: Quasi-stationary optimal control for wind farm with closely spaced turbines, MIPRO International Convention, 829-834, 2012.

37. Howland, M.F., Bossuyt, J., Martinez-Tossas, L.A., Meyers, J. and Meneveau, C.: Wake Structure of Wind Turbines in Yaw under Uniform Inflow Conditions, AIP Journal of Renewable and Sustainable Energy, 8, 043301, doi: 10.1063/1.4955091, 2016.

38. International Energy Agency, World Energy Outlook, url: https://www.iea.org/weo2017/ (last accessed 5.12.2017), 2017.

39. Ishihara, T. Yamaguchi, A. and Fujino, Y.: Development of a new wake model based on a wind tunnel experiment. Technical report, Global Wind, Technical Report, url: windeng.t.u-tokyo.ac.jp/ishihara/posters/2004_gwp_poster.pdf (last accessed: 7.January 2018), 2004.

40. Jensen, N.O.: A note on wind generator interaction, Report RISØ-M-2411 isbn: 87-550-0971-9, url: orbit.dtu.dk/fedora/objects/orbit:88807/datastreams/file_3494b4b2-1dae-4442-941a-f2e628673f31/content (accessed on 12 Dec 2017), 1983.

41. Jiménez, Á., Crespo, A., and Migoya, E.: Application of a LES technique to characterize the wake deflection of a wind turbine in yaw, Wind Energy, 13, 559–572, doi:10.1002/we.380, 2010.

42. Johnson, K. and Fritsch, G.: Assessment of Extremum Seeking Control for Wind Farm Energy Production, Wind Engineering, 36(6), 701-716, doi: 10.1260/0309-524X.36.6.701, 2012.

43. Katic, I., Højstrup, J. and Jensen, N.O.: A simple model for cluster efficiency, European Wind Energy Association, Conference and Exhibition, 7-9 October 1986, Rome, Italy, 407-410, url: orbit.dtu.dk/fedora/objects/orbit:66401/datastreams/file_f7da8eb2-e49c-4dc9-9ee5-72846f40ef34/content (accessed on 12 Dec 2017), 1986.

44. Kim, H., Kim, K. and Paek, I.: Power Regulation of Upstream Wind Turbines for Power Increase in a Wind Farm. Int. J. Precis. Eng. Manuf., 17, 665–670, doi:10.1007/s12541-016-0081-1, 2016.

45. Knudsen, T., Bak, T. and Svenstrup, M.: Survey of wind farm controlpower and fatigue optimization, Wind Energy, 18, 1333–1351, doi:10.1002/we.1760, 2014.

46. Kragh, K. A. and Hansen, M. H.: Load alleviation of wind turbines by yaw misalignment, Wind Energy, 17, 971–982, doi:10.1002/we.1612, 2014.

47. Krogstad, P.Å., and Adaramola, M.S.: Performance and near wake measurements of a model horizontal axis wind turbine, Wind Energy, 15(5), 743–756, doi:10.1002/we.502, 2012.

48. Krogstad, P.Å and Lund, J.A.: An experimental and numerical study of the performance of a model turbine, Wind Energy, 15, 443–457, doi: 10.1002/we.482, 2012.

49. Krogstad, P.Å. and Eriksen, P.E.: "Blind test" calculations of the performance and wake development for a model wind turbine, Renew. Energ., 50, 325–333, doi:10.1016/j.renene.2012.06.044, 2013.

50. Krogstad, P.Å., Sætran, L., and Adaramola, M. S.: Blind Test 3 calculations of the performance and wake development behind two in-line and offset model wind turbines, J. Fluid. Struct., 52, 65–80, doi:10.1016/j.jfluidstructs.2014.10.002, 2015.

51. Larsen, G.C.: A simple wake calculation procedure. Technical report, Risø-M-2760, Technical University of Denmark, url: orbit.dtu.dk/files/55567186/ris_m_2760.pdf (last accessed: 7.January 2018), 1988.

52. Larsen, G.C.: A simple stationary semi-analytical wake model. Technical report, Risø-R-1713, Technical University of Denmark, url: http://orbit.dtu.dk/files/122941920/Simple_analytical_wake_model_final_10.pdf (last accessed: 7.January 2018), 2009.

53. Lee, J., Son, E., Hwang, B. and Lee, S.: Blade pitch angle control for aerodynamic performance optimization of a wind farm, Renewable Energy, 54, doi:10.1016/j.renene.2012.08.048124–130, 2013.

54. Marden, J.R., Ruben, S.D. and Pao, L.Y.: A Model-Free Approach to Wind Farm Control Using Game Theoretic Methods, IEEE Transactions on Control Systems Technology, 21(4), 1207-1214, doi:10.1109/TCST.2013.2257780, 2013.

55. Medici, D. and Alfredsson, P. H.: Measurements on a wind turbine wake: 3D effects and bluff body vortex shedding, Wind Energy, 9, 219–236, doi:10.1002/we.156, 2006.

56. Nilsson, K.; Ivanell, S.; Hansen, K.S.; Mikkelsen, R.; Sørensen, J.N.; Breton, S.-P. and Henningson, D.: Large-eddy simulations of the Lillgrund wind farm, Wind Energy, 18, 449–467, doi:10.1002/we.1707, 2015.

57. NRK, Press release, url: https://www.nrk.no/trondelag/bygger-gigantiske-vindparker-i-trondelag-1.12816583 (last accessed 5.12.2017), 2016.

58. Ostovan, Y., Amiri, H., and Uzol, O.: Aerodynamic Characterization of NREL S826 Airfoil at Low Reynolds Numbers, RUZGEM Conference on Wind Energy Science and Technology, METU Ankara Campus, Ankara, Turkey, 2013.

59. Pierella, F., Krogstad, P.Å., and Sætran, L.: Blind Test 2 calculations for two in-line model wind turbines where the downstream turbine operates at various rotational speeds, Renew. Energ., 70, 62–77, doi:10.1016/j.renene.2014.03.034, 2014.

60. Pierella, F.: Experimental Investigation of Wind Turbine Wakes and Their Interaction, Doctoral thesis at NTNU 2014:200, isbn: 978-82-326-0322-0, 2014.

61. Pierella, F. and Sætran, L.: Wind tunnel investigation on the effect of the turbine tower on wind turbines wake symmetry, Wind Energy, 20, 1753-1769, doi: 10.1002/we.2120, 2017.

62. Regjeringen, Press Release, url: https://www.regjeringen.no/en/topics/energy/renewable-energy/renewable-energy-production-in-norway/id2343462/ (last accessed 5.12.2017), 2016.

63. Ryi, J. Rhee, W. Hwang, U.C. and Choi, J.S.: Blockage effect correction for a scaled wind turbine rotor by using wind tunnel test data, Renewable Energy, 79, 227–235, doi: 10.1016/j.renene.2014.11.057, 2015.

64. Santhanagopalan, V., Rotea, M.A. and Iungo, G.V.: Performance optimization of a wind turbine column for different incoming wind turbulence. Renewable Energy, 116B, 232–243, doi:10.1016/j.renene.2017.05.046, 2017.

65. Sarlak, H.: Large Eddy Simulation of Turbulent Flows in Wind Energy, Ph.D. thesis, DTU Wind Energy, 2014.

66. Sarlak, H., Mikkelsen, R., Sarmast, S., and Sørensen, J. N.: Aerodynamic behaviour of NREL S826 airfoil at Re=100 000, J. Phys.: Conf. Series, 524, doi:/10.1088/1742-6596/524/1/012027, 2014.

67. Sarlak, H., Nishino, T., Martinez-Tossas, L.A., Meneveau, C. and Sørensen, J.N.: Assessment of blockage effects on the wake characteristics and power of wind turbines, Renewable Energy, 93, 340–352, doi: 10.1016/j.renene.2016.01.101, 2016.

68. Sarmast, S. and Mikkelsen, R.: The experimental results of the NREL S826 airfoil at low Reynolds numbers, Technical Report, url: www.urn:nbn:se:kth:diva-120583, 2013.

69. Schepers, J.G.: Engineering models in wind energy aerodynamics - Development implementation and analysis using dedicated aerodynamic measurements, PhD thesis TU Delft, isbn: 978-94-6191-507-8, url: repository.tudelft.nl/islandora/object/uuid:92123c07-cc12-4945-973f-103bd744ec87/datastream/OBJ/download (last accessed on 14 Feb 2017), 2012.

70. Schepers, J.G., Boorsma, K., and Munduate, X.: Final Results from Mexnext-I: Analysis of detailed aerodynamic measurements on a 4.5 m diameter rotor placed in the large German Dutch Wind Tunnel DNW, Journal of Physics: Conference Series, 555, 012 089, doi:10.1088/1742-6596/555/1/012089, 2014.

71. Schottler, J., Hölling, A., Peinke, J., and Hölling, M.: Wind tunnel tests on controllable model wind turbines in yaw, AIAA 34th Wind Energy Symposium, p. 1523, doi:10.2514/6.2016-1523, 2016.

72. Schreiber, J., Cacciola, S., Campagnolo, F., Petrovic, V., Mourembles, D., and Bottasso, C. L.: Wind shear estimation and wake detection by rotor loads - First wind tunnel verification, Journal of Physics: Conference Series, 753, 032 027, doi:10.1088/1742-6596/753/3/032027, 2016.

73. Somers, D. M.: The S825 and S826 Airfoils, Tech. Rep. SR-500-36344, NREL, url: wind.nrel.gov/airfoils/Documents/S825,S826-Design.pdf (last access 21 Feb 2017), 2005.

74. Statoil, Press release, URL: www.statoil.com/en/news/hywindscotland.html (last accessed 5.12.2017), 2017.

75. Steinbuch, M., de Boer, W.W., Bosgra, O.H., Peters, S.A. and Ploeg, J.: Optimal control of wind power plants, Journal of Wind Engineering and Industrial Aerodynamics, 27, 237–246, doi:10.1016/0167-6105(88)90039-6, 1988.

76. van Dijk, M., van Wingerden, J.-W., Ashuri, T., and Li, Y.: Wind farm multi-objective wake redirection for optimizing power production and loads, Energy, 121, 561–569, doi:10.1016/j.energy.2017.01.051:, 2017.

77. Vermeer, L.J., Sørensen, J.N. and Crespo, A.: Wind turbine wake aerodynamics, Progress in aerospace sciences, 39, 467–510, doi:10.1016/S0376-0421(03)00078-2, 2003.

78. Vollmer, L., Steinfeld, G., Heinemann, D., and Kühn, M.: Estimating the wake deflection downstream of a wind turbine in different atmospheric stabilities: an LES study, Wind Energy Science, 1, 129–141, doi:10.5194/wes-1-129-2016, 2016.

79. Wagenaar, J.W., Machielse, L.A.H. and Schepers, J.G.: Controlling Wind in ECNs Scaled Wind Farm, ECN report ECN-M-12-007 EWEA (Copenhagen), available at: www.ecn.nl/publications/PdfFetch.aspx?nr=ECN-M–12-007 (accessed on 7 February 2017), 2012.

80. Wang, J., Foley, S., Nanos, E. M., Yu, T., Campagnolo, F., Bottasso, C. L., Zanotti, A., and Croce, A.: Numerical and Experimental Study of Wake Redirection Techniques in a Boundary Layer Wind Tunnel, Journal of Physics: Conference Series, 854, 012 048, doi:10.1088/1742-6596/854/1/012048, 2017.

81. Wharton, S. and Lundquist, J. K.: Assessing atmospheric stability and its impacts on rotor-disk wind characteristics at an onshore wind farm, Wind Energy, 15, 525–546, doi: 10.1002/we.483, 2012.

82. Wheeler, A. J. and Ganji, A. R.: Introduction to engineering experimentation, Upper Saddle River, NJ, USA, Pearson/Prentice Hall, XI, third edition edn., 2004.

List of papers

In this section the scientific publications, which have been produced in the scope of this research project are listed and the authors' contributions specified. In total, seven journal papers were submitted, four of which as first author. Another seven papers were submitted to peer-reviewed conference proceedings. Three of those conference papers were written as first author. Six papers were selected to be included in this thesis as main publications, providing a representative summary of the investigated topics. The main publications are listed in Section 1, while additional publications are listed in Section 2.

1 Main publications

PAPER 1:

Jan Bartl and Lars Sætran. (2016)

Experimental testing of axial induction based control strategies for wake control and wind farm optimization.

Published in Journal of Physics, Conference Series, vol. 753(3):032035.

The authors' contribution: *Jan Bartl performed the experiments, evaluated the data and wrote the paper. The process was supervised and the manuscript reviewed by Lars Sætran.*

PAPER 2:

Jan Bartl, Yaşar Ostovan, Oguz Uzol and Lars Sætran. (2017).

Experimental study on power curtailment of three in-line turbines.

Published in Energy Procedia, vol. 137C, pp. 307-314.

The authors' contribution: *Jan Bartl and Yaşar Ostovan performed the experiments together. Jan Bartl evaluated the data and wrote the paper. The process was supervised and the manuscript reviewed by Oguz Uzol and Lars Sætran.*

PAPER 3:

Jan Bartl, Franz Mühle, Jannik Schottler, Lars Sætran, Joachim Peinke, Muyiwa Adaramola and Michael Hölling. (2018)

Wind tunnel experiments on wind turbine wakes in yaw: Effects of inflow turbulence and shear.

Accepted for publication in Wind Energy Science

The authors' contribution: *Jan Bartl, Franz Mühle and Jannik Schottler performed the experiments together. Jan Bartl evaluated the data and wrote the paper. The process was supervised and the manuscript reviewed by Michael Hölling, Joachim Peinke, Muyiwa Adaramola and Lars Sætran.*

PAPER 4:

Jan Bartl, Franz Mühle and Lars Sætran. (2018)

Wind tunnel study on power and loads optimization of two yaw-controlled model wind turbines.

In review in Wind Energy Science.

The authors' contribution: *Jan Bartl and Franz Mühle performed the experiments together. Jan Bartl evaluated the data and wrote the paper. The process was supervised and the manuscript reviewed by Lars Sætran.*

PAPER 5:

Jan Bartl and Lars Sætran. (2017)

Blind test comparison of the performance and wake flow between two in-line wind turbines exposed to different turbulent inflow conditions.

Published in Wind Energy Science, vol. 2, pp. 55-76.

The authors' contribution: *Jan Bartl performed the experiments, processed and evaluated the data and wrote the paper. The presented numerical data was submitted by external modelers as listed in the paper. The process was supervised and the manuscript revised by Lars Sætran.*

PAPER 6:

Jan Bartl, Kristian Sagmo, Tania Bracchi and Lars Sætran. (2018)

Performance of the NREL S826 airfoil at low to moderate Reynolds numbers: A reference experiment for CFD models.

In review in European Journal of Mechanics - B/Fluids.

The authors' contribution: *Jan Bartl performed the first set of experiments together with Nikolai Aksnes. Additional repetitions of the experiments were performed by Jan Bartl and Tania Bracchi. All the numerical simulations were performed by Kristian Sagmo. Jan Bartl and Kristian Sagmo wrote the paper together with a fifty-fifty share. The process was supervised and the manuscript revised by Tania Bracchi and Lars Sætran.*

2 Other publications

A number of papers have been co-authored inside and outside the scope of this PhD project. These publications are listed below, but not attached to this thesis.

PAPER 7:

Clio Ceccotti, Andrea Spiga, Jan Bartl and Lars Sætran. (2016)

Effect of upstream turbine tip speed variations on downstream turbine performance.

Published in Energy Procedia, vol. 94, pp. 478-486.

The authors' contribution: *Clio Ceccotti, Andrea Spiga, Szymon Luczynski, Piotr Wiklak and Jan Bartl performed the experiments together. Clio Ceccotti and Andrea Spiga evaluated the data and wrote the first draft of the paper. The paper was revised by Jan Bartl. The process was supervised and the manuscript reviewed by Lars Sætran.*

PAPER 8:

Kristian Sagmo, Jan Bartl and Lars Sætran. (2016)

Numerical simulations of the NREL S826 airfoil.

Published in Journal of Physics, Conference Series, vol. 753(8):082036.

The authors' contribution: *Kristian Sagmo performed the numerical simulations. Jan Bartl and Nikolai Aksnes performed the reference experiments together. Kristian Sagmo evaluated the data and wrote the paper. The process was supervised and the manuscript reviewed by Jan Bartl and Lars Sætran.*

PAPER 9:

Jannik Schottler, Franz Mühle, Jan Bartl, Muyiwa Adaramola, Lars Sætran, Joachim Peinke and Michael Hölling. (2017)

Comparative study on the wake deflection behind yawed wind turbine models.

Published in Journal of Physics, Conference Series, vol. 854(1):012032.

The authors' contribution: *Jannik Schottler, Franz Mühle and Jan Bartl performed the experiments together. Jannik Schottler, Franz Mühle and Jan Bartl evaluated the data and wrote the paper together. The process was supervised and the manuscript reviewed by Michael Hölling, Joachim Peinke, Muyiwa Adaramola and Lars Sætran.*

PAPER 10:

Erik Prytz, Øyvind Huuse, Bernhard Müller, Jan Bartl and Lars Sætran. (2017)

Numerical simulation of flow around the NREL S826 airfoil at moderate Reynolds number using delayed detached Eddy simulation (DDES).

Published in AIP Conference Proceedings 07/2017; vol. 1863(1):560086.

The authors' contribution: *Erik Prytz and Øyvind Huuse performed the simulations together. Jan Bartl and Nikolai Aksnes performed the reference experiments together. Erik Prytz and Øyvind Huuse evaluated the data and wrote the paper. The process was supervised and the manuscript reviewed by Berhard Müller and Lars Sætran.*

PAPER 11:

Julie Krøgenes, Lovisa Brandrud, Richard Hann, Jan Bartl, Tania Bracchi and Lars Sætran. (2017)

Aerodynamic Performance of the NREL S826 Airfoil in Icing Conditions.

In review in Wind Energy Science

The authors' contribution: *Julie Krøgenes, Lovisa Brandrud and Tania Bracchi performed the experiments together. Jan Bartl assisted in the experimental setup and data evaluation process. Richard Hann performed the numerical simulations. Julie Krøgenes and Lovisa Brandrud wrote the paper. The process was supervised and the manuscript reviewed by Richard Hann, Jan Bartl, Tania Bracchi and Lars Sætran.*

PAPER 12:

Jannik Schottler, Jan Bartl, Franz Mühle, Lars Sætran, Joachim Peinke and Michael Hölling. (2018)

Wind tunnel experiments on wind turbine wakes in yaw: Redefining wake-width.

In review in Wind Energy Science

The authors' contribution: *Jannik Schottler, Jan Bartl and Franz Mühle performed the experiments together. Jannik Schottler evaluated the data and wrote the paper. Jan Bartl and Franz Mühle reviwed the paper. The process was supervised and the manuscript reviewed by Michael Hölling, Joachim Peinke and Lars Sætran.*

PAPER 13:

Franz Mühle, Jannik Schottler, Jan Bartl, Romain Futrzynski, Steve Evans, Luca Bernini, Paolo Schito, Gabriel Usera, Martin Draper, Elektra Kleusberg, Dan Henningson, Michael Hölling, Joachim Peinke, Muyiwa Adaramola and Lars Sætran. (2018)

Blind test comparison of wake flow predictions behind yawed configurations of wind turbines.

Manuscript prepared for submission to Wind Energy Science

The authors' contribution: *Franz Mühle, Jan Bartl and Jannik Schottler performed the reference experiments together. Four groups submitted numerical simulations (Romain Futrzynski, Steve Evans), (Luca Bernini, Paolo Schito), (Gabriel Usera, Martin Draper), (Elektra Kleusberg, Dan Henningson). Franz Mühle evaluted the data and wrote the paper. Jan Bartl and Jannik Schottler reviewed the initial draft of the paper. The process was supervised and the manuscript reviewed by Michael Hölling, Joachim Peinke, Muyiwa Adaramola and Lars Sætran.*

PAPER 14:

Jan Bartl, Andreas Müller, Andrin Landolt, Franz Mühle, Mari Vatn, Luca Oggiano and Lars Sætran. (2018)

Validation of the real-time-response ProCap measurement system for full wake scans behind a yawed model-scale wind turbine.

In review in Journal of Physics: Conference Series, DeepWind 2018

The authors' contribution: *Jan Bartl, Andreas Müller and Andrin Landolt performed the ProCap experiments together. Franz Mühle and Mari Vatn performed the reference LDA experiments together. Jan Bartl evaluated the data and wrote the paper. The process was supervised and the manuscript reviewed by Andrin Landolt, Luca Oggiano and Lars Sætran.*

PAPER 15:

Felix Polster, Jan Bartl, Franz Mühle, Paul Uwe Thamsen and Lars Sætran. (2018)

Experimental validation of analytical wake and downstream turbine performance modeling.

In review in Journal of Physics: Conference Series, DeepWind 2018

The authors' contribution: *Felix Polster performed the simulations, evaluated all data and wrote the paper. The reference experiments were performed by Jan Bartl, Franz Mühle, Luis Garcia Salgado and Felix Polster. The process was supervised and the manuscript reviewed by Jan Bartl, Franz Mühle, Paul Uwe Thamsen and Lars Sætran.*

PAPER 16:

Jan Göing, Jan Bartl, Franz Mühle, Lars Sætran and Paul Uwe Thamsen. (2018)

A Detached Eddy Simulation: Proper Orthogonal Decomposition of the wake flow behind a model wind turbine.

In review in Journal of Physics: Conference Series, DeepWind 2018

The authors' contribution: *Jan Göing performed the simulations, evaluated all data and wrote the paper. The reference experiments were performed by Jan Bartl, Franz Mühle and Jannik Schottler. The process was supervised and the manuscript reviewed by Jan Bartl, Franz Mühle, Paul Uwe Thamsen and Lars Sætran.*

Part II

Papers

PAPER 1

Experimental testing of axial induction based wake control for wind farm optimization

Jan Bartl, Lars Sætran

Original version published by IOP Publishing in
Journal of Physics: Conference Series 753 (2016) 032035.
doi: 10.1088/1742-6596/753/3/032035

PAPER 1

Experimental testing of axial induction based wake control for wind farm optimization

Jan Bartl, Lars Sætran
Department of Energy and Process Engineering, Norwegian University of Science and Technology, Trondheim, 7491, Norway

Published in Journal of Physics: Conference Series 753 (2016) 032035

Submitted on 6 June 2016, published on 5 October 2016. Original version published by IOP Science.

Summary. In state-of-the-art wind farms each turbine is controlled individually aiming for optimum turbine power not considering wake effects on downstream turbines. Wind farm control concepts aim for optimizing the overall power output of the farm taking wake interactions between the individual turbines into account. This experimental wind tunnel study investigates axial induction based control concepts. It is examined how the total array efficiency of two in-line model turbines is affected when the upstream turbines tip speed ratio (λ-control) or blade pitch angle (β-control) is modified. The focus is particularly directed on how the wake flow behind the upstream rotor is affected when its axial induction is reduced in order to leave more kinetic energy in the wake to be recovered by a downstream turbine. It is shown that the radial distribution of kinetic energy in the wake area can be controlled by modifying the upstream turbines tip speed ratio. By pitching the upstream turbines blades, however, the available kinetic energy in the wake is increased at an equal rate over the entire blade span. Furthermore, the total array efficiency of the two turbine setup is mapped depending on the upstream turbines tip speed ratio and pitch angle. For a small turbine separation distance of $x/D = 3$ the downstream turbine is able to recover the major part of the power lost on the upstream turbine. However, no significant increase in the two-turbine array efficiency is achieved by altering the upstream turbines operation point away from its optimum.

Note: *In the original version of this paper the pitch angle was defined to be negative when the blades were pitched towards feathered position. This definition was not consistent with most other sources in literature. For this version of the paper the pitch angle definition was corrected to be positive in order to be consistent with the definition in the introductory section of this thesis.*

1 Introduction

Due to limited spacing in offshore wind farms, wake interactions between the single turbines cause significant power losses on the downstream turbines. For certain wind directions these power losses are estimated to account for up to 10-20% for large offshore wind farms [2] as the single turbines are controlled for the optimum individual operation condition. In order to reduce these effects and thus optimize the total power output of the farm, a holistic wind farm control approach is needed [14]. One promising control concept is to reduce the induction on the upstream rotors and thus increase the amount of kinetic power available in the wake that can be recovered by the downstream turbines. This can be done by altering the upstream turbines tip speed ratio through the turbines torque controller as well as varying the blade pitch angle. Steinbuch et al. (1988) [21] addressed the topic of wind farm control already in 1988. They underline the importance of controlling rotor loads through wind farm control methods. Furthermore, they indicate the potential of an increase in overall energy capture by downrating the upstream turbines. A theoretical optimization study of an array of eight aligned wind turbines is presented by Horvat et al. (2012) [10]. Applying a simple engineering wake model they calculate a total gain in wind farm efficiency of 2.85% when the power extraction of the first three turbines is reduced through pitching. Another study of adjusting the blade pitch angle for wind farm power optimization is presented by Lee et al. (2013) [18]. Applying an eddy viscosity model for representation of the wake while optimizing the upstream turbines pitch angles, they simulate a wind farm efficiency increase by 4.5% for a model of the Horns Rev wind farm layout. Johnson and Fritsch (2012) [13] apply an Extremum Seeking Control algorithm to optimize the power of simple wind farm consisting of three aligned turbines. For low atmospheric turbulence inflow conditions they find an increase in combined efficiency when reducing the induction on the first and second turbine. Their algorithm is using the engineering PARK wake model to simulate the aerodynamic interactions between the turbines. A different approach for the power optimization of three in-line turbines is presented by Marden et al. (2013). They utilize game theoretic methods for wind farm optimization and show its potential for an efficiency gain. Their model-free approach does not utilize a wake model and is based on some strongly simplified assumptions. González et al. (2015) [8] developed another algorithm for optimizing the wind farm efficiency by individual pitch angle and tip speed ratio control of each turbine. The turbine wake flow is for this case simulated by the PARK model. Considering wind directions that results in fully aligned

turbine rows, they model a total farm efficiency increase of 7.55%. A recent study by Annoni et al. (2016) [1] discusses the potential of induction-based wind farm control techniques. The higher-order wind plant model SOFWA based on Large Eddy Simulations (LES) is compared to a simpler engineering model, showing up discrepancies in the simple wake model. The simulations based on the engineering wake model predict a slight wind farm efficiency increase when pitching or downrating the upstream turbine, whereas the more advanced SOFWA simulations show that the energy lost on the upstream turbine cannot be fully recovered by the downstream turbine. Full-scale experiments on wind farm control are reported by Wagenaar et al. (2012) [22]. In a farm of 10 small wind turbines of a rotor diameter of D=7.6m spaced at 3.7D in one wind direction, the effect of yaw misalignment is studied. No significant overall farm efficiency increase is reported for this test case. In general, wind farm control methods based on wake deflection like yawing or individual pitch control have the big advantage that low kinetic energy fluid in the wake can be deflected away from the center of an aligned downstream rotor. Most of the studies investigating yaw control ([5], [12], [6], [7], [11]) report an effective deflection of the wake path around 0.6 rotor diameters, implicating an unsteady and a highly asymmetric blade load distribution for an aligned downstream turbine. Axial induction based wind farm control methods as discussed in this paper, are not able to deflect low kinetic energy fluid away from the downstream rotor. However, they have the advantage of being able to control the load distribution for the downstream turbine steadily over the entire rotor swept area of an aligned downstream turbine, implicating a more uniform load distribution for a downstream rotor.

2 Objectives

The objective of this experimental study is to show up the potential of axial-induction based control methods on the total wind farm efficiency. The focus is particularly directed on the mean wake flow affected by the upstream turbines operating condition. The distribution of kinetic energy in the wake is directly related to the power output of the downstream turbine. The total wind farm efficiency is mapped in dependency of the operation conditions of the upstream and downstream turbine for three representative turbine separation distances. A study of the wake behind the second turbine, and thus an indication for the available power of a third turbine is given by Bartl et al. (2012) [3]. Given the drawbacks of low Reynolds-numbers operation and wind tunnel blockage effects this study does not claim to represent a full-scale situation. Nevertheless, the study consists of a set of well-documented experimental data, which provides a defined test case for calibration and validation of CFD methods. A comparison of wake and performance data of CFD

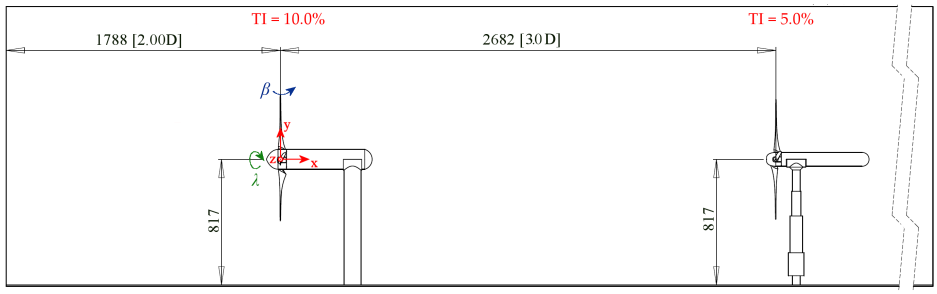

Fig. 1. Schematic of the experimental setup in the wind tunnel. The upstream rotor is set up at $x/D = 2$ from the turbulence grid. The downstream rotor is positioned $x/D = 3$ behind the upstream rotor.

predictions to experimental data from NTNUs wind tunnel is presented in the so-called Blind test experiments [15], [20], [17], [4].

3 Methods

In this experimental study the characteristics of the axial-induction-based control strategies are assessed for a setup of two in-line model wind turbines. The models have a rotor diameter of about D=0.90m and are installed in a closed wind tunnel test section of $2.7m \times 1.8m$ resulting in a solid blockage ratio of 13%. Figure 1 schematically shows the experimental setup, a detailed description of the turbine geometry can be e.g. found in Pierella et al., 2014 [20]. The turbine blades are based on the NREL S826 airfoil, which is shown to result in Reynolds-number-independent rotor performance for reference wind velocities above $u_{ref} = 11.5m/s$ [15]. The model turbines are equipped with a torque transducer and an optical photo cell making it possible calculating the mechanical power at the rotor shaft. Moreover, the turbines are mounted on a 6-component force balance allowing assessing the thrust force. The axial induction factor over the blade span is calculated by the means of Blade Element Momentum (BEM) method. 30 blade elements are chosen to get an approximation of the blade load distributions. Hotwire anemometry with a sampling frequency of f=20kHz is used to measure the mean and turbulent streamwise velocity in wake behind the upstream turbine. In order to simulate realistic atmospheric conditions a turbulence grid is set up at the test section inlet generating a background turbulence intensity of TI=10.0% at the first rotor plane, decaying to TI=5.0% at the position of the second rotor $x/D = 3$ rotor diameters downstream of the first rotor. The random error of the power, thrust and mean velocity measurements are calculated based on a 95% confidence interval. Systematic errors based on a uncertainty analysis of the calibration procedures are taken into account and thus a total error is calculated. Herein, the systematic error of ±1% from the velocity calibration is seen to be the major contributor to the total uncertainty in all presented quantities. The uncertainty in the upstream

turbine power coefficient at design conditions is calculated to be within ±3%, while it is lower than ±2% for the thrust coefficient. The total uncertainty in the mean velocities in the wake is calculated to be lower than ±1.5%.

4 Results

4.1 Tip speed ratio variation (λ-control)

In a first experimental setup the upstream turbine tip speed ratio is varied from its design point at λ_{T1}=6.0 and the influence on the performance of the downstream turbine assessed. The power coefficient $C_{P,T1}$ and the thrust coefficient $C_{T,T1}$ of the upstream turbine are shown in dependence of the tip speed ratio λ_{T1} in Figure 2 (a) and (b).

$$C_{P,T1} = \frac{P_{T1}}{0.5\,\rho\,A_{rot,T1}\,u_{ref}^3} \tag{1}$$

$$C_{T,T1} = \frac{F_{T,T1}}{0.5\,\rho\,A_{rot,T1}\,u_{ref}^2} \tag{2}$$

$$\lambda_{T1} = \frac{\omega\,R}{u_{ref}} \tag{3}$$

The upstream turbine power can be reduced by overspeeding the rotor to higher tip speed ratios, which on the other hand increases the total thrust and thus the total axial induction a_{ind} on the rotor.

$$a_{ind} = 0.5(1 - \sqrt{1 - C_T}) \tag{4}$$

The induction factor as calculated in from momentum conservation in equation (4) is a global parameter for the entire rotor. In reality, however, the axial induction factor is not distributed evenly over the rotor radius. This can, for instance, be shown by a simple Blade Element Momentum (BEM) calculation. In Figure 2 (c) the axial induction factor calculated by a BEM code is shown 30 blade elements over the blade root distance r/R for the five investigated tip speed ratios. It is shown that the axial induction is actually reduced in the inner part of the rotor up to about 0.4 times the blade span, and increased for the outer blade elements in case the rotor is overspeeded. This non-uniform change of the induction over the blade radius directly affects the wake flow behind the turbine. As

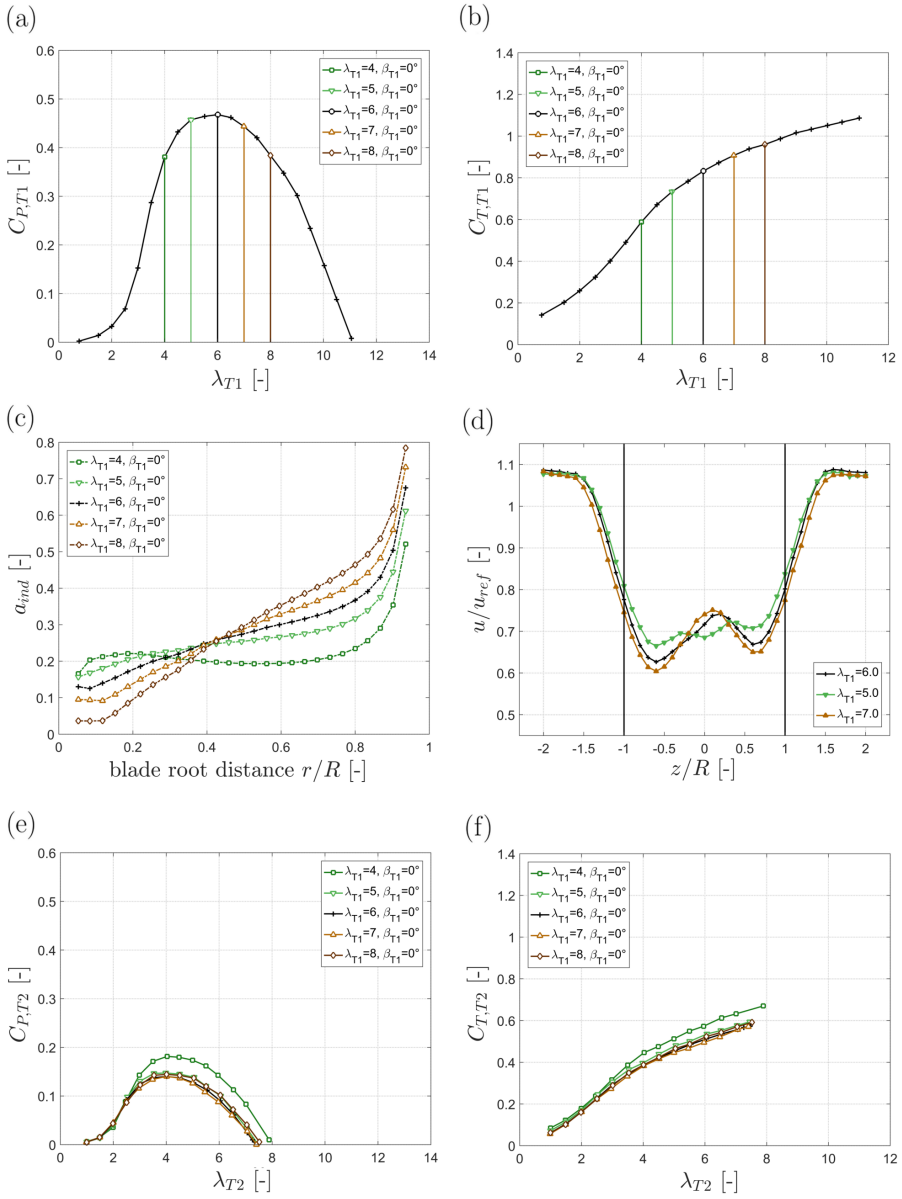

Fig. 2. Measured upstream turbine T1 power coefficient **(a)** and thrust coefficient **(b)**. Calculated axial induction factor over the upstream rotor blade span at different tip speed ratios **(c)**. Mean velocity measurements in a horizontal line at hub height, $x/D = 3$ behind the upstream rotor for three different tip speed ratios **(d)**. Measured downstream turbine T2 power coefficient **(e)** and thrust coefficient **(f)**

presented in Figure 2 (d) the mean velocity profile at hub height measured in a horizontal line at a downstream distance of $x/D = 3$ is showing two distinct minima which indicates that the measurement location in the near wake. For the case of overspeeding to λ_{T1}=7.0,

the velocity deficit near the blade tip is seen to increase, while more kinetic energy is left in the center of the wake. Thus, the total kinetic energy integrated over the rotor swept area stays rather constant compared to the to the design case at tip speed ratio λ_{T1}=6.0. Setting up another turbine at the exact same location at $x/D = 3$ makes it possible to measure the power coefficient $C_{P,T2}$ and thrust coefficient $C_{T,T2}$ of the downstream turbine as presented in Figure 2 (e) and (f).

$$C_{P,T2} = \frac{P_{T2}}{0.5\,\rho\,A_{rot,T2}\,u_{ref}^3} \tag{5}$$

$$C_{T,T2} = \frac{F_{T,T2}}{0.5\,\rho\,A_{rot,T2}\,u_{ref}^2} \tag{6}$$

Note that for better comparability the reference velocity u_{ref} for both model turbines is the velocity measured at the inlet contraction of the test section $x/D = 2$ upstream of the upstream turbine. It can be observed that the power and thrust coefficient for the downstream turbine is not significantly affected by overspeeding the upstream turbine. The downstream turbine experiences very similar total thrust and power indicated by matching performance curves. In case the upstream turbine is downrated, i.e. slowed down to lower tip speed ratios, both the power and thrust coefficients are reduced as indicated in Figure 2 (a) and (b). Although the total axial induction is also reduced, an increase of the induction factor is observed in the center of the rotor up to about r/R=0.3. The radial distribution of the induction factor is again modified, the opposite effect as for the case of overspeeding is observed. The induction increases in the center while it reduces towards the blade tips. The increase in axial induction consumes more energy in the center of the upstream rotor. As a consequence the mean velocity profile in the wake is observed to flatten out for λ_{T1}=5.0 (Figure 2 (d)). More kinetic energy is left in the tip region of the rotor, while the kinetic energy in the wake center is further reduced. In case of downrating the upstream rotor to λ_{T1}=5.0, only a slight increase of about 2% in the downstream turbine efficiency can be measured. When slowing down the upstream rotor to close-to-stalled-conditions at λ_{T1}=4.0, about 20% more power can be gained at the downstream rotor compared to the upstream case as shown in Figure 2 (e). This can, however, not account for the power losses at the upstream rotor. As a consequence the total wind farm efficiency is decreased as further discussed in section 4.3. Correspondingly, the downstream turbines thrust coefficient $C_{T,T2}$ is somewhat higher for when slowing down the upstream turbine to λ_{T1}=4.0, while it is almost not affected at all when slowing it down to λ_{T1}=5.0. The outer blade elements of the upstream rotor might be partly stalled λ_{T1}=4.0 already loving significantly more kinetic energy in the wake than at λ_{T1}=5.0.

4.2 Pitch angle variation (β-control)

In a second parameter variation the effect of an upstream turbine pitch angle variation on the performance characteristics of the downstream turbine is investigated. Therefore, the downstream turbines performance is measured when the upstream turbine is slightly pitched towards feathered position. A pitch angle range from β_{T1}=0° to β_{T1}=7° is investigated while the upstream rotor tip speed ratio is kept constant at λ_{T1}=6.0. In this study the pitch angle is defined to be positive when the blades are pitched towards feathered position. Thus, the angle of attack decreases with increasing pitch angle, which is in agreement with the definition given by Hau (2013) [9]. Figure 3 (a) and (b) display the power and thrust coefficients of the upstream turbine for different blade pitch angles. Pitching the rotor towards the feathered position, both the power and thrust coefficient decrease. It is observed that the run-away tip speed ratio is reached earlier when pitching the turbine towards feathered position. The general trends in C_P and C_T for a pitched turbine compare well to simulations on the NREL 5 MW reference turbine by Annoni et al. (2016) [1] as well as the data presented in Johnson and Fritsch (2012) [13] as well as Hau (2013) [9]. The pitch-dependent performance characteristics of the model turbine however differ for different rotor designs. A strong dependence on the specific blade design is observed. For the present design of the NTNU model turbines the optimum power point of the upstream turbine is shifted towards lower tip speed ratios at a rate of about $\lambda/\beta \approx 0.25/1°$ when the turbine is pitched out. This shift in optimum power point is indicated by the inclined brown line in Figure 3 (a) and (b).

A BEM calculation of the radial distribution of the axial induction factor for different pitch angles is presented in Figure 3 (c). It is observed that the induction factor is decreased uniformly over the entire blade radius when the turbine is pitched towards feathered position. This radially uniform reduction in induction is also visible in the mean wake profile measured at $x/D = 3$ downstream of the turbine. As shown in Figure 3 (d), significantly higher mean velocities are measured for the blade pitch angles β_{T1}=2° and β_{T1}=5° in the entire area behind the rotor. Due to the quite uniform reduction in induction the wake shape remains similar to the one of the design case at β_{T1}=0°. For both investigated pitch angles β_{T1}=2° and β_{T1}=5° the velocity profile features two distinct minima, while a local maximum is observed around z/R=0.2. The asymmetry in the wake profile can be ascribed to the influence of the turbine tower wake (Pierella et al., 2014 [20]). The velocity in the freestream ($z/R \approx \pm 1.5$) $x/D = 3$ behind the upstream turbine is measured to be slightly higher than the reference velocity u_{ref}. This local speed up in the freestream is due to the blockage effect by the wind tunnel walls. It is observed that the speed up due to blockage decreases when the upstream rotor is pitched and thus the induction is reduced. Furthermore, it can be observed that a small part of the added kinetic energy in the wake is diffused into the freestream flow at $z/R > 1$ and $z/R < -1$ already at $x/D = 3$ rotor

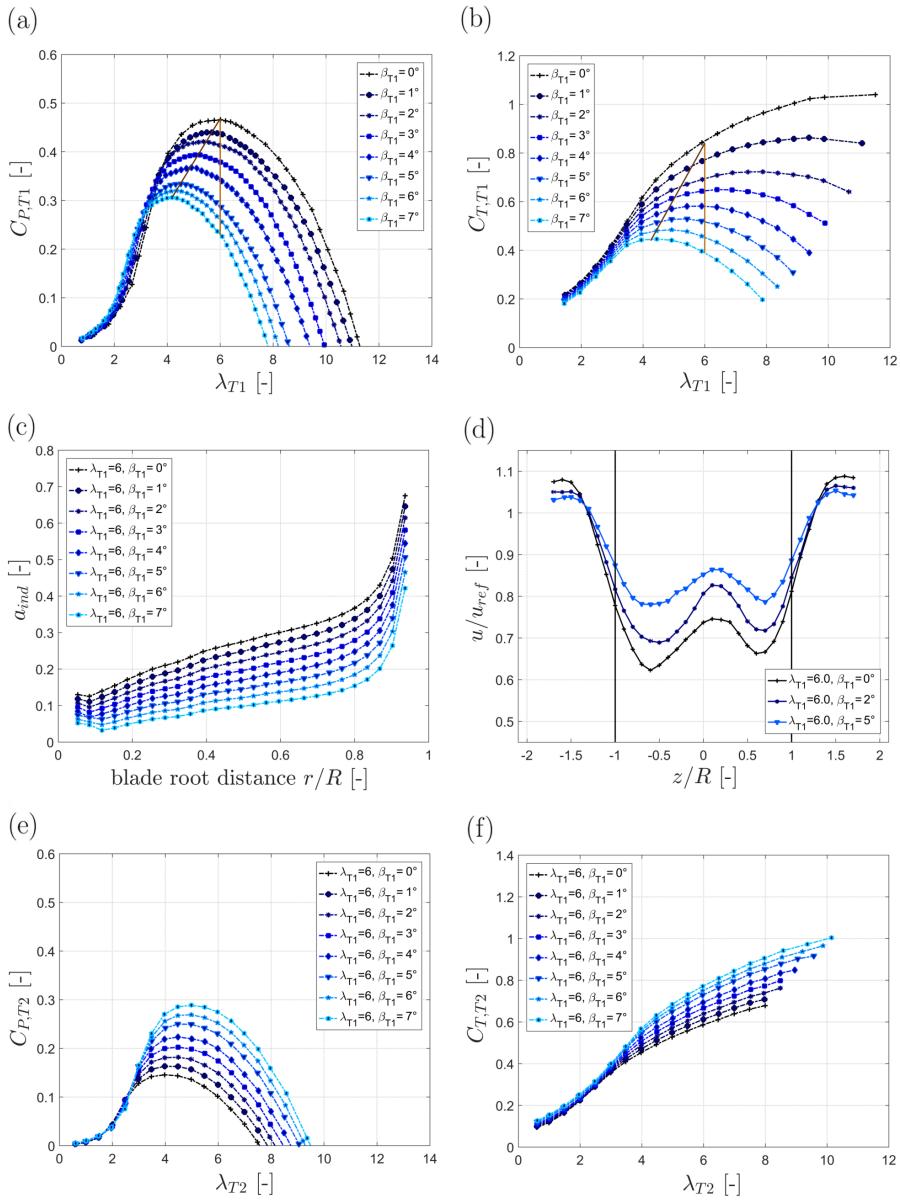

Fig. 3. Measured upstream turbine T1 power coefficient **(a)** and thrust coefficient **(b)** for different pitch angles. Calculated axial induction factor over the upstream rotor blade span for different pitch angles **(c)**. Mean velocity measurements in a horizontal line at hub height, $x/D = 3$ behind the upstream rotor for three different pitch angles **(d)**. Measured downstream turbine power coefficient $C_{P,T2}$ **(e)** and thrust coefficient $C_{T,T2}$ **(f)** for different upstream turbine pitch angles β_{T1}

diameters downstream. The power and thrust coefficients of a second turbine located at $x/D = 3$ downstream of the first rotor are presented in Figure 3 (e) and (f). In general, it is observed that more energy can be recovered by the downstream turbine when the up-

stream turbine is pitched towards the feathered position. In average, the power production of the downstream turbine increases at a rate of about $\Delta C_P/\Delta\beta_{T1} \approx 13\%/1°$. When pitching the upstream rotor blades β_{T1}=2° for instance, 26% more energy can be recovered at the downstream turbine compared to the reference case of β_{T1}=0°. The energy recovered by the downstream turbine does, however, not account for the energy missing on the upstream turbine as further discussed in section 4.3. The thrust coefficient of the downstream turbine $C_{T,T2}$ is trending accordingly. Up to a tip speed ratio of λ_{T2}=3.0, the upstream turbine pitch angle β_{T1} does not have any significant influence on the downstream turbine performance as itself operates in stalled conditions.

4.3 Wind farm efficiency

By altering the tip speed ratio of both turbines, a matrix of the array efficiency

$$E = \frac{P_{T1} + P_{T2}}{P_{T1,max} + P_{T2,max}} \tag{7}$$

of the two turbines is mapped for a separation distance of $x/D = 3$. The array efficiency is found to be rather constant over a tip speed ratio range from λ_{T1}=4.5 to λ_{T1}=6.5, varying in the range of ±1.0%, as shown in Figure 4 (a). Considering the measurement uncertainty no significant increase in wind farm efficiency can be found. That means that approximately the same amount of energy which is lost on the upstream rotor can be recovered for a low turbine separation distance of $x/D = 3$. In Figure 4 (b) a map of the combined wind farm efficiency is shown for a variation of the upstream turbines pitch angle. It is observed that the kinetic energy surplus in the wake behind a pitched upstream turbine is most efficiently recovered by the downstream turbine for very small upstream turbine pitch angles up to β_{T1}=1°. However, no increase in total wind farm efficiency is achieved for any of the investigated pitch angles.

These experimental findings contradict the calculated total efficiency improvements through axial induction based wind farm control as found by Horvat et al. (2012) [10], Lee et al. (2013) [18], Johnson and Fritsch (2012) [13], Marden et al. (2013) [19] or González et al. (2015) [8]. Most of these algorithms are, however, based on engineering wake models, which include a number of simplified assumptions. Annoni et al. (2016) [1] disclose some of the discrepancies of an engineering wake model by directly comparing it to a higher-order wake simulation based on LES computations. These higher-order simulations result in very similar trends as presented in this experimental study, although the turbine geometry and the boundary conditions are somewhat different. A possible explanation for the non-recovery of the added energy in the wake can be found by taking a closer look at the wake flow. Analyzing the wake flow (Figure 2 (d) and 3 (d)), it is observed that small parts of

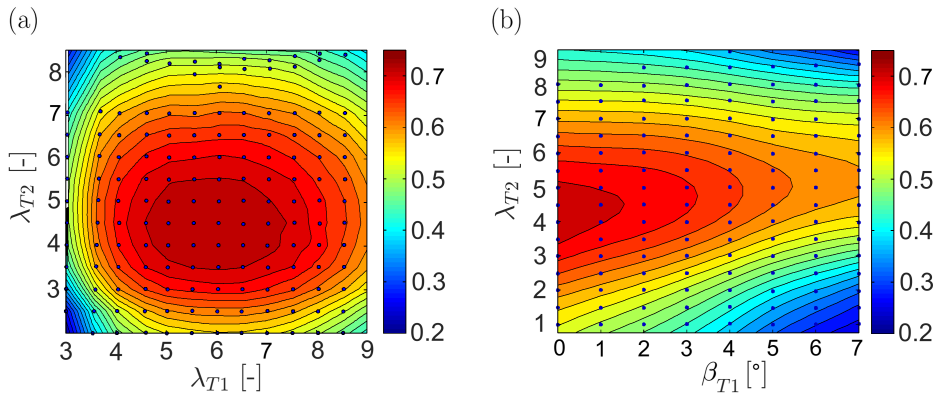

Fig. 4. Map of the combined farm efficiency $E = P_{T1} + P_{T2}/(P_{T1,max} + P_{T2,max})$ [-] of the two turbines setup at a separation distance of $x/D = 3$ in dependence of **(a)** upstream turbine tip speed ratio λ_{T1} at constant pitch angle β_{T1}=0° and **(b)** upstream turbine pitch angle β_{T1} at a constant tip speed ratio λ_{T1}=6.0.

the added kinetic energy in the wake diffuse into areas outside the downstream rotor swept area due to turbulent mixing. The added energy in the wake thus cannot be recovered by the downstream turbine anymore. For higher downstream distances the wake is supposed to re-energize, also meaning that even more added energy from the wake is diffused into the surrounding freestream flow. Consequently, controlling the upstream turbine is expected not to affect the wake flow and downstream turbine power to the same extent anymore for higher distances. From another point of view it can be stated that the combined power is not very susceptible to deviations from the optimum rotational speed and pitch angle. This finding implies that that axial induction based wind farm control could be beneficial for achieving a more even load distribution between two consecutive turbine rows. As the combined power is almost constant in region down to λ_{T1}=4.5 respectively β_{T1}=1°, induction based turbine control could be used to pass on loads to the next turbine row to the cost of only very small power losses.

5 Conclusions

It is shown that the radial distribution of kinetic energy in the wake area can be controlled by modifying the upstream turbines tip speed ratio. Controlling the tip speed ratio of the upstream turbine away from its design point is observed to modify the radial distribution of kinetic energy in the wake. The added kinetic energy in the wake is decreased in the centre region of the wake and increased in a circular region behind the outer blade elements when the upstream rotor is downrated. When downrating the upstream turbine in the range of $\lambda_{T1} = 4.5 - -6.0$, the major part of the kinetic energy can be recovered by the downstream turbine for low turbine separation distances up to $x/D = 3$. However, a significant overall

increase in power output of the two turbine array is not achieved. By pitching out the upstream turbines blades the available kinetic energy in the wake is increased at an equal rate over the entire blade span. The total array efficiency of the two turbine setup is observed to decrease when the upstream turbine is pitched towards the feathered position. Also for this wind farm control mechanism, no significant increase in the two-turbine array efficiency is measured. For both control mechanisms it is observed that some of the added kinetic energy in the wake is diffusing into the freestream and cannot be recovered by the downstream turbine anymore.

References

1. Annoni, J., Gebraad, P.M.O., Scholbrock, A.K., Fleming, P. and van Wingerden, J.W.: Analysis of axial-induction-based wind plant control using an engineering and a high-order wind plant model, Wind Energy, 19, 1135–1150, doi:10.1002/we.1891, 2016.

2. Barthelmie, R. J., Frandsen, S. T., Hansen, K., Schepers, J. G., Rados, K., Schlez, W., Neubert, A., Jensen, L.E., and Neckelmann, S.: Quantifying the Impact of Wind Turbine Wakes on Power Output at Offshore Wind Farms., Journal of Atmospheric and Oceanic Technology, 27(8), 1302–1317, doi:10.1175/2010JTECHA1398.1, 2010.

3. Bartl, J., Pierella, F., and Sætran, L.: Wake Measurements behind an Array of Two Model Wind Turbines, Energy Procedia, 24, 305–312, doi:10.1016/j.egypro.2012.06.113, 2012.

4. Bartl, J., and Sætran, L.: Blind test comparison of the performance and wake flow between two in-line wind turbines exposed to different turbulent inflow conditions, submitted to Wind Energy Science, 2016.

5. Bastankhah, M. and Port-Agel, F.: A wind-tunnel investigation of wind-turbine wakes in yawed conditions, Journal of Physics: Conference Series, 625, 012014, doi:10.1088/1742-6596/625/1/012014, 2015.

6. Fleming, P.A., Gebraad, P.M.O., Lee, S., van Wingerden, J.W., Johnson, K., Churchfield, M., Michalakes, J., Spalart, P. and Moriarty, P.: Evaluating techniques for redirecting turbine wakes using SOWFA, Renewable Energy, 70, 211–218, doi:10.1016/j.renene.2014.02.015, 2014.

7. Gebraad, P.M.O., Teeuwisse, F.W., van Wingerden, J.W., Fleming, P.A., Ruben, S.D., Marden, J.R. and Pao, L.Y.: A Data-Driven Model for Wind Plant Power Optimization by Yaw Control, American Control Conference, 2014

8. González, J.S., Payán, M.B., Santos, J.R. and Rodríguez, Á.G.G.: Maximizing the overall production of wind farms by setting the individual operating point of wind turbines, Renewable Energy, 80, 221–229, doi: 10.1016/j.renene.2015.02.009, 2015

9. Hau, E.: Wind Turbines Fundamentals, Technologies, Application, Economics, Third, translated edition, Springer, 2013

10. Horvat, T., Spudic, V. and Baotic, M.: Quasi-stationary optimal control for wind farm with closely spaced turbines, MIPRO International Convention, 829-834, 2012.

11. Howland, M.F., Bossuyt, J., Martinez-Tossas, L.A., Meyers, J. and Meneveau, C.: Wake Structure of Wind Turbines in Yaw under Uniform Inflow Conditions, AIP Journal of Renewable and Sustainable Energy, 8, 043301, doi: 10.1063/1.4955091, 2016

12. Jimenez, A., Crespo, A. and Migoya, E.: Application of a LES technique to characterize the wake deflection of a wind turbine in yaw, Wind Energy, 13, 559–572, doi:10.1002/we.380, 2010.

13. Johnson, K. and Fritsch, G.: Assessment of Extremum Seeking Control for Wind Farm Energy Production, Wind Engineering, 36(6), 701-716, doi: 10.1260/0309-524X.36.6.701, 2012.

14. Knudsen, T., Bak, T. and Svenstrup, M.: Survey of wind farm controlpower and fatigue optimization, Wind Energy, 18, 1333–1351, doi:10.1002/we.1760, 2014.

15. Krogstad, P. Å., and Adaramola, M. S.: Performance and near wake measurements of a model horizontal axis wind turbine, Wind Energy, 15(5), 743–756, doi:10.1002/we.502, 2012.

16. Krogstad, P. Å. and Eriksen, P. E.: "Blind test" calculations of the performance and wake development for a model wind turbine, Renew. Energ., 50, 325–333, doi:10.1016/j.renene.2012.06.044, 2013.

17. Krogstad, P. Å., Sætran, L., and Adaramola, M. S.: Blind Test 3 calculations of the performance and wake development behind two in-line and offset model wind turbines, J. Fluid. Struct., 52, 65–80, doi:10.1016/j.jfluidstructs.2014.10.002, 2015.

18. Lee, J., Son, E., Hwang, B. and Lee, S.: Blade pitch angle control for aerodynamic performance optimization of a wind farm, Renewable Energy, 54, doi:10.1016/j.renene.2012.08.048124–130, 2013.

19. Marden, J.R., Ruben, S.D. and Pao, L.Y.: A Model-Free Approach to Wind Farm Control Using Game Theoretic Methods, IEEE Transactions on Control Systems Technology, 21(4), 1207-1214, doi:10.1109/TCST.2013.2257780, 2013.

20. Pierella, F., Krogstad, P. Å., and Sætran, L.: Blind Test 2 calculations for two in-line model wind turbines where the downstream turbine operates at various rotational speeds, Renew. Energ., 70, 62–77, doi:10.1016/j.renene.2014.03.034, 2014.

21. Steinbuch, M., de Boer, W.W., Bosgra, O.H., Peters, S.A. and Ploeg, J.: Optimal control of wind power plants, Journal of Wind Engineering and Industrial Aerodynamics, 27, 237–246, doi:10.1016/0167-6105(88)90039-6, 1988.

22. Wagenaar, J.W., Machielse, L.A.H. and Schepers, J.G.: Controlling Wind in ECNs Scaled Wind Farm, ECN report ECN-M-12-007 EWEA (Copenhagen), available at: www.ecn.nl/publications/PdfFetch.aspx?nr=ECN-M–12-007 (accessed on 7 February 2016), 2012.

PAPER 2

Experimental study on power curtailment of three in-line turbines

Jan Bartl, Yasar Ostovan, Oguz Uzol, Lars Sætran

Original version published by Elsevier Ltd. in
Energy Procedia, vol. 137C, pp. 307-314.
doi: 10.1016/j.egypro.2017.10.355

PAPER 2

Experimental study on power curtailment of three in-line turbines

Jan Bartl[a], Yasar Ostovan[b], Oguz Uzol[b], Lars Sætran[a]

[a] Department of Energy and Process Engineering, Norwegian University of Science and Technology, 7491 Trondheim, Norway
[b] METU Center for Wind Energy, Department of Aerospace Engineering, Middle East Technical University, 06800 ankaya Ankara, Turkey

Energy Procedia, vol. 137C, pp. 307-314.

Submitted on 6 January 2017, revised on 17 March 2017, published on 14 December 2017
Original version published by Elsevier Ltd. Peer-reviewed under the responsibility of SINTEF Energi AS

Summary. A dataset of wind tunnel power and wake flow measurements on a setup of three aligned model wind turbines is presented. The power outputs of the three turbines are in good agreement with measurements from a full-scale wind farm of similar inter-turbine spacing. A comparison of the wake flow behind the first row and the second row shows a significantly higher mean velocity loss behind the second row justifying a further power drop from the second to the third row turbine. Curtailing the front row turbine to smaller than rated tip speed ratios resulted in insignificant total power gains below 1%. Curtailments of both the first and second row turbine indicate that the best combined array power results are achieved for slightly lower than rated tip speed ratios. Although power curtailment is observed to have a rather small potential for power optimization of a wind farm, it could be an effective method for load distribution at constant farm power.

1 Introduction

Depending on the inter-turbine spacing, wake interactions between individual turbines are estimated to cause power losses up to 10-20% in large offshore wind farms [2]. Therefore, holistic wind farm control approaches are proposed to optimize the farms capability of kinetic energy extraction from the wind [9]. Wind farm control methods can, in general, be classified as wake deflection methods like yaw control or axial induction based control methods like pitch or torque control of the upstream turbines. Even though the potential for power gains by wake deflection control is estimated to be larger [1], [4] axial induction based curtailment methods have the advantage of a more uniform load distribution over the downstream turbine rotor area. Depending on the turbine type, inter-turbine spacing, and the site-specific wind conditions, axial-induction based control is therefore considered an effective option for power and load control in tightly spaced wind farms. By reducing the induction of the upstream turbine through tip speed ratio or pitch control, more kinetic energy is left in the wake flow that can be used by the downstream turbines. A previous study by Bartl and Sætran (2016) [3] of induction based control on two in-line turbines indicates a higher potential for power gains for tip speed ratio control than for pitch control. An investigation by Hansen et al. (2012) [8] highlights that the level of atmospheric turbulence intensity significantly influences the wake recovery and thus the total power output of a wind farm. This is confirmed in a model scale study by Ceccotti et al. (2016) [5], in which a curtailment of the first row is shown to be effective for low background turbulence and small turbine separation distances ($\leq$ 3D) only. However, the potential power increase for a two turbine arrangement is observed to be within one percent. In full-scale wind farms measurements on aligned turbines show the biggest power drop between the first and second row [2], [8], [7]. The difference in power production from the second to the third row is considerably smaller, which leads to a more or less stable production for turbine rows located even further downstream. The additional energy extraction by rotors from the third row on seems to be balanced by the entrainment of high kinetic energy fluid from the surrounding freestream flow. Therefore, an investigation of two aligned turbines may not be conclusive for an entire wind farm as also the third turbine power output and further rows could be affected by a curtailment of the front row turbine. In a Large-Eddy-Simulation (LES) of the tightly spaced Lillgrund wind farm Nilsson et al. (2015) [10] investigate the potential for increasing the wind farm production by curtailment of the front row turbines. By pitching out the front row turbines, they could not observe a positive contribution to the overall wind farm power production. Another CFD study based on the actuator line technique by Mikkelsen et al. (2007) [11] on a row of three aligned turbines shows increased production of the second and third turbine for a pitched first row turbine. In this collaborative experiment between the Norwegian University of Science and Technology (NTNU) and Middle East Technical University (METU) Center

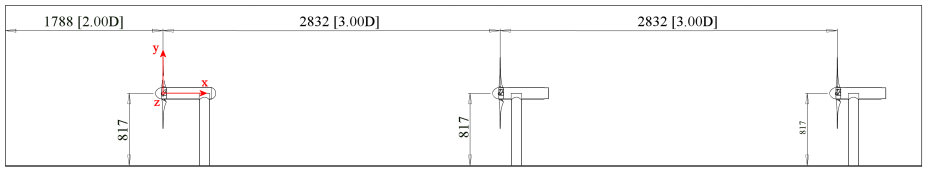

Fig. 1. Setup of the turbines in the wind tunnel and reference coordinate system.

for Wind Energy, measurements on three aligned model wind turbines of identical rotor geometry are carried out. It is investigated whether a curtailment of the first and second row can benefit the combined power output of a row of three aligned wind turbines.

2 Methods

2.1 Wind tunnel, model turbines and rotor geometry

The test section of the closed-loop wind tunnel at NTNU in Trondheim is 2.71m wide, 1.81m high and 11.15m long. Static pressure holes are installed at two defined circumferences at the inlet of the tunnel in order to control the inflow speed. The wind tunnel is driven by a 220kW fan, which is located behind the test section. The model wind farm consists of the first row turbine (T1) from NTNU and the second (T2) and third row turbine (T3) from METU. The turbines have the exactly same rotor and nacelle geometry. The three-bladed rotors have a diameter of D=0.944 m and turn in the counter-clockwise direction. The rotors are controlled by systems of electric motors and frequency inverters by Siemens (T1, NTNU) respectively Panasonic (T2 & T3, METU). The turbines rotational speed can be controlled up to about 3500 rpm, while the extensive power is consumed by external load resistances. The turbine blades are based on the NREL S826 airfoil and precision milled in aluminum. Three different sets of experimental performance data of the NREL S826 airfoil for low Reynolds numbers can be found in publications by Ostovan et al. (2013) [12], Sarmast and Mikkelsen (2013) [14] and Sagmo et al. (2016) [13], all of which can be used as input data for Blade Element Momentum (BEM) simulations.

2.2 Experimental setup

Figure 1 shows a side-view of the wind tunnel with the three model turbines installed. The first row turbine (T1) is mounted $2.00D$ from the tunnel inlet, while turbines T2 and T3 are set up with an inter-turbine spacing of $3.00D$. The turbine hub height is h_{hub}=$817mm$, which is slightly below the wind tunnel center. The figure also shows the reference coordinate system with its origin in the center of the first turbine rotor plane. The turbines are exposed to a uniform inflow of u_{ref}=$11.5m/s$. The turbulence intensity in the inflow is measured to be TI=0.23% at the first row turbine location. The design

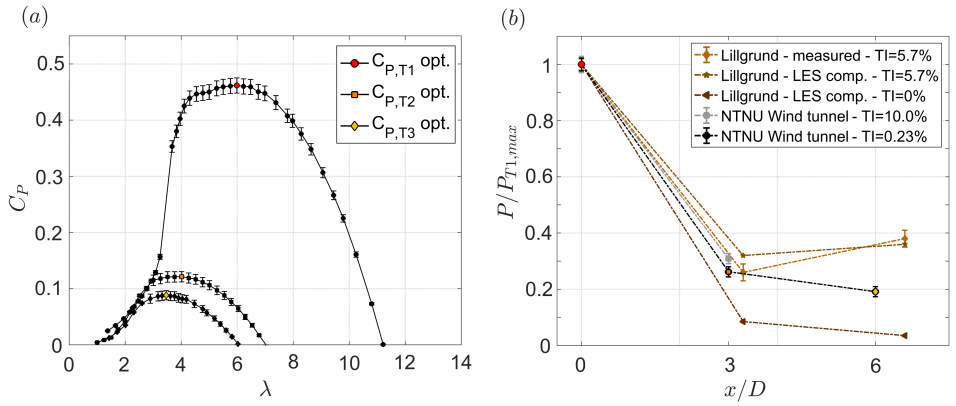

Fig. 2. (a) C_P-λ-curves of the three aligned turbines, their optimum points (red, orange, yellow); all referred to u_{ref}=11.5m/s. **(b)** Relative power of test cases compared to full-scale data from Lillgrund windfarm [10]

tip speed ratio of all three turbines is λ=6.0 which is giving an optimal axial induction factor of $a \approx$0.33 at r/R=0.8. In order to study the effect of variations in tip speed ratio of the first and second row turbines on the total array power, the first row turbine is set to discrete tip speed ratios λ_{T1}=[4.5, 5.0, 5.5, 6.0, 6.5]. Meanwhile, 15 tip speed ratios each in steps of $\Delta\lambda_{T2}$=$\Delta\lambda_{T3}$=0.20 around the optimum operation point are automatically scanned for the second and third turbine.

2.3 Measurement instrumentation and settings

All three turbines are equipped with in-nacelle torque transducers and optical cells for an acquisition of the rotational speed. Torque and rotational speed are averaged over 30s and the mechanical power on the rotor shaft calculated. The statistical uncertainty of the power coefficient of T1 at λ=6.0 is calculated to be lower than $\pm$3.0%. Wake flow measurements are carried out x/D=3 behind the first row turbine T1 without T2 and T3 being installed and x/D=3 behind T2, without T3 being installed. These locations are exactly the same locations of T2 respectively T3 and therefore represent the wake flow these turbines are exposed to. The velocity measurements are performed using a Laser Doppler Anemometer (LDA) by Dantec Dynamics. The statistical uncertainties of the mean velocities are calculated to be lower than $\pm$0.5% considering a 95% confidence interval.

3 Results

3.1 Power output of the turbine array

In a first test all three aligned turbines are individually controlled to their optimum power point. The three turbines have identical C_P-λ characteristics with a maximum power coefficient $C_{P,max}$=0.462 at rated tip speed ratio λ_{opt}=6.0 when exposed to the undisturbed freestream flow. When operated in the wake of one or more upstream turbines the power coefficients of the second and third row turbines are reduced to $C_{P,T2}$=0.121 and $C_{P,T3}$=0.088, respectively, as shown in Figure 2 (a). The C_P-λ characteristics are all referred to the reference inflow wind speed u_{ref}=11.5m/s upstream of T1 and the red, orange and yellow point the optimum power point when the turbines are individually controlled for optimum power output. Figure 2 (b) shows the relative power of the second and third row turbine relative to the optimum power output of the front row turbine. The measured powers show good agreement to a dataset of full scale measurements and LES simulations at Lillgrund wind farm, which was presented by Nilsson et al. (2015) [10]. The Lillgrund wind farm is a tightly spaced wind farm with an inter-turbine spacing of 4.3D in SW-NE direction respectively 3.3D in SE-NW direction, making it a convenient reference case for the presented model scale setup. For this comparison, only the outermost row furthest to NE with a separation distance of 3.3D is considered (row A, Nilsson et al., 2015). Only one side of this row is interacting with the wake flow from adjacent rows while the other side is exposed to the undisturbed freestream flow. The relative power of second turbine in this experiment with 0.23% inflow turbulence matches the measured value from Lillgrund with a background turbulence of 5.7% very well. Large Eddy Simulations (LES) by Nilsson et al. (2015) [10] with no background turbulence (TI=0%) resulted in significantly lower power outputs for the second turbine, which are considered to be unrealistically low. In order to reproduce more realistic atmospheric conditions, the power of the second turbine was also measured for a grid generated turbulence of TI=10.0%. This resulted in an 18% higher power output for the second turbine compared to the low turbulent inflow of TI=0.23%. This is consistent with findings by Churchfield et al. (2012) [6], who performed LES simulations on two aligned full-scale 5MW turbines in atmospheric boundary layers of different stability. They found 15-20% higher power production of the second row turbine for highly turbulent unstable conditions than for neutral conditions featuring lower background turbulence. The measured power output of the third row turbine, however, is significantly lower than the measured power from Lillgrund wind farm. In fact the power drops about 27% from the second to the third turbine, while it increases with about 46% in the measured full scale data. This noteworthy power increase is considered to stem from a strong re-energizing of the turbulent wake. As the background turbulence for the wind tunnel case is considerably lower, the wake does not re-energize as fast and the power

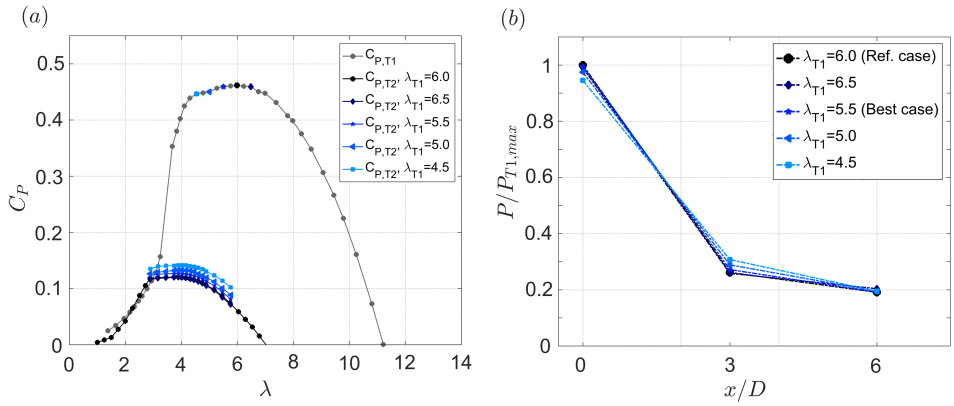

Fig. 3. (a) C_P-λ-curves of the second turbine T2 depending on different tip speed ratios of T1. **(b)** Relative power for T1, T2 and T3 for a curtailed first row turbine T1

Table 1. Total array power and operating points for five cases of first row turbine curtailment.

λ_{T1}	$\frac{P_{T1}}{P_{T1,max}}$	λ_{T2}	$\frac{P_{T2}}{P_{T1,max}}$	λ_{T3}	$\frac{P_{T3}}{P_{T1,max}}$	$\frac{P_{T1+T2+T3}}{P_{T1,max}}$	$\pm$ in %
6.0	1.0000	4.0	0.2620	3.5	0.1913	1.4533	$\pm$0%
5.5	0.9948	3.7	0.2721	3.5	0.1919	1.4588	+0.38%
5.0	0.9749	4.0	0.2892	3.5	0.1945	1.4587	+0.37%
4.5	0.9456	3.9	0.3075	3.3	0.2026	1.4558	+0.17%
6.5	0.9903	3.9	0.2607	3.3	0.2018	1.4527	−0.04%

of the third row is lower. A similar power drop from the second to the third turbine is observed in the LES computations by Nilsson et al. (2015) [10] for zero inlet turbulence.

3.2 Effects of power curtailment

According to momentum theory, a reduction of the front turbines induction benefits the total power production of a number of aligned turbines. The curtailment of a turbine can be done by blade pitching or a variation away from its optimum tip speed ratio. Bartl and Sætran (2016) [3] showed that curtailment through tip speed variation is the more promising option with respect to total power gains. For an operation at lower than rated tip speed ratios more kinetic energy is left in the center of the wake compared to the pitching case.

Front row turbine curtailment

At first, the effects of a curtailment of the first turbine are analyzed. Figure 3 (a) shows the C_P-λ characteristics of the second row turbine for four cases of first row turbine curtailment. In three cases T1 is slowed down, in one case slightly overspeeded. It is observed that the second turbine is able to recover about the same amount of energy

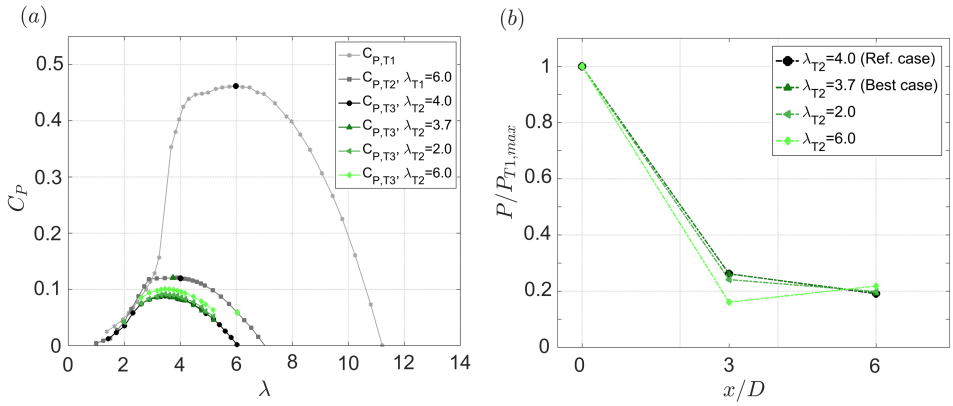

Fig. 4. (a) C_P-λ-curves of the third turbine T3 depending on different tip speed ratios of T2. **(b)** Relative power for T1, T2 and T3 for a curtailed second row turbine T2

Table 2. Total array power and operating points for five cases of second row turbine curtailment.

λ_{T1}	$\frac{P_{T1}}{P_{T1,max}}$	λ_{T2}	$\frac{P_{T2}}{P_{T1,max}}$	λ_{T3}	$\frac{P_{T3}}{P_{T1,max}}$	$\frac{P_{T1+T2+T3}}{P_{T1,max}}$	$\pm$ in %
6.0	1.0000	4.0	0.2620	3.5	0.1913	1.4533	$\pm$0%
6.0	1.0000	3.7	0.2616	3.5	0.1931	1.4547	+0.09%
6.0	1.0000	2.0	0.2414	3.5	0.1986	1.4399	−0.92%
6.0	1.0000	6.0	0.1609	3.5	0.2185	1.3793	−5.09%

that is lost through curtailment of the first turbine. The exact numerical values of the relative power measured are tabulated in Table 1. In Figure 3 (b) the relative power for all three turbine rows for cases when the front row turbine T1 is operated at off-design condition is presented. Turbines T2 and T3 are for these cases always controlled to their individual maximum power point. As indicated in the last two columns in Table 1, the combined power output of the three aligned turbines is observed to be very constant for these four cases of front row curtailment. Only very small gains in total power of less than one percent can be achieved. Although these power gains are insignificant considering a statistical measurement uncertainty of the same magnitude, the best gains are measured for tip speed ratios slightly lower than the rated TSR at λ_{T1}=6.0. Overspeeding to λ_{T1}=6.5 is observed to have a somewhat negative effect on the total power production. Remarkably, the power produced by the third row turbine T3 is observed to be very constant for all cases of front row turbine curtailment. In these test cases it seems that most of the kinetic energy lost at the front row turbine due to curtailment is recovered by the second row turbine. The third turbines production is rather unaffected, although the upstream turbine is extracting somewhat more energy from the flow.

Second row turbine curtailment

In another set of test cases the second row turbine T2 is curtailed while the first turbine T1 is constantly operated at its rated tip speed λ_{T1}=6.0. In Figure 4 (a) the C_P-λ characteristics of the third row turbine T3 are presented for four operating points λ_{T2}=[2.0, 3.7, 4.0, 6.0] of the second turbine. λ_{T2}=4.0 represents the reference case at which the second turbine is controlled to its maximum power point. Curtailing the second turbine to a slightly lower than optimum tip speed ratio of λ_{T2}=3.7 results in the best combined power production of these cases. A gain in total power production $P_{T1+T2+T3}$ of 0.09% as shown in Table 2, however, is even less significant than the gains achieved for the first turbine curtailment. The other two cases of λ_{T2}=2.0 and λ_{T2}=6.0 represent two cases of more distinct curtailment of the second row turbine T2. For λ_{T2}=2.0 the relative power of T2 is curtailed by about 2% of the relative power $P_{T2}/P_{T1,max}$, of which about 0.7% can be recovered by the third turbine T3. The losses in total array power are calculated to amount -0.92%, which is surprisingly little for this slowdown of half the rotational speed. For overspeeding the second turbine to λ_{T2}=6.0 about 10% less relative power $P_{T2}/P_{T1,max}$ is produced by T2. Accordingly, about 2.7% of relative power can be recovered by T3. The total power loss for this overspeeding case of -5.09% is significantly bigger than for the slowdown case. In order to understand the mechanisms behind the power production of the single turbine rows, the wake flow between the turbines has to be analyzed.

3.3 Wake flow analysis

A set of Laser-Doppler Anemometry (LDA) measurements at x/D=3 rotor diameters behind the first row as well as behind the second row turbine is performed in order to assess which inflow conditions each of the turbines in the array experiences. The wake flow is recorded in the exact same locations of the second respectively the third turbine without the second/third turbine being installed in the wind tunnel. The flow field is therefore considered representative for the inflow conditions, which the second/third turbine row experiences. In Figure 5 (a) and (b) the normalized mean velocity fields in the wake x/D=3 behind the first row turbine T1 and the second row turbine T2 are compared with the reference case (λ_{T1}=6.0, λ_{T2}=4.0). The wake behind the second row features a somewhat higher velocity deficit in the center of the wake than the wake behind the first row turbine, which is considered the main reason for a further drop in power from the second to the third turbine row. The wake behind T2 is more shaped like a bell compared to the steep velocity gradients around z/R=$\pm$1 and rather flat central area in the wake center for the wake behind T1.

Figure 6 (a) and (b) show the corresponding plots of normalized turbulent kinetic (TKE) energy in the wake. The peaks in TKE behind the second turbine are slightly

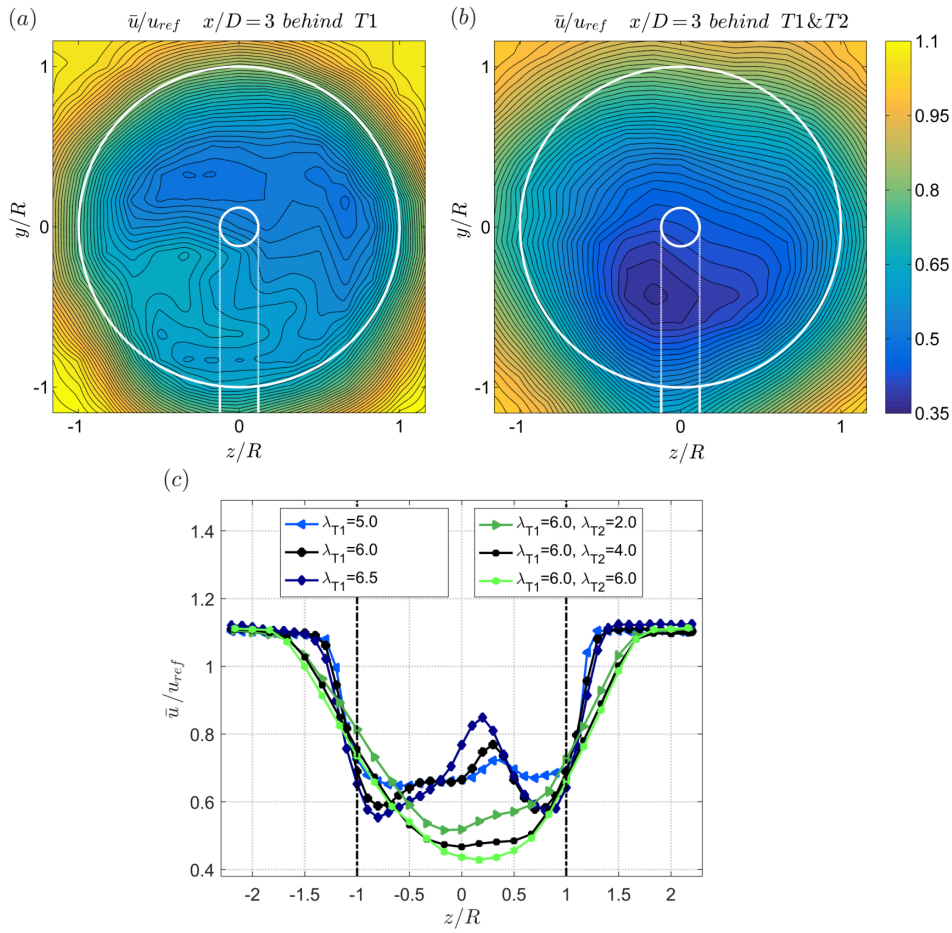

Fig. 5. Normalized mean velocity in the wake x/D=3 **(a)** behind T1 operated at λ_{T1}=6 (reference case); **(b)** behind T2 while T1 operated at λ_{T1}=6 and T2 operated at λ_{T2}=4 (reference case); **(c)** behind T1 operated at λ_{T1}=5, 6 and 7 (blue lines are the curtailed cases) respectively behind T2 while T1 operated at λ_{T1}=6 and T2 operated at λ_{T2}=2, 4 and 6 (green lines are the curtailed cases)

higher in the lower half of the wake, but generally feature the same magnitude as the wake behind the first turbine. The main difference is the more spread out TKE in the wake of T2, while the first turbine wake features very sharp distinct TKE peaks around in the blade tip region. The rotor generated turbulence of T1 is somewhat diffused at the T2 position and superimposed by the rotor generated turbulence of T2. Due to the more spread out turbulence distribution in the second turbine wake, the mixing and entrainment of higher kinetic energy freestream flow are increased resulting in a faster wake recovery (Hansen et al., 2012 [8]). In Figure 6 (c) normalized mean velocity profiles measured at hub height behind the curtailed first (blue lines) and second row turbine (green lines) are

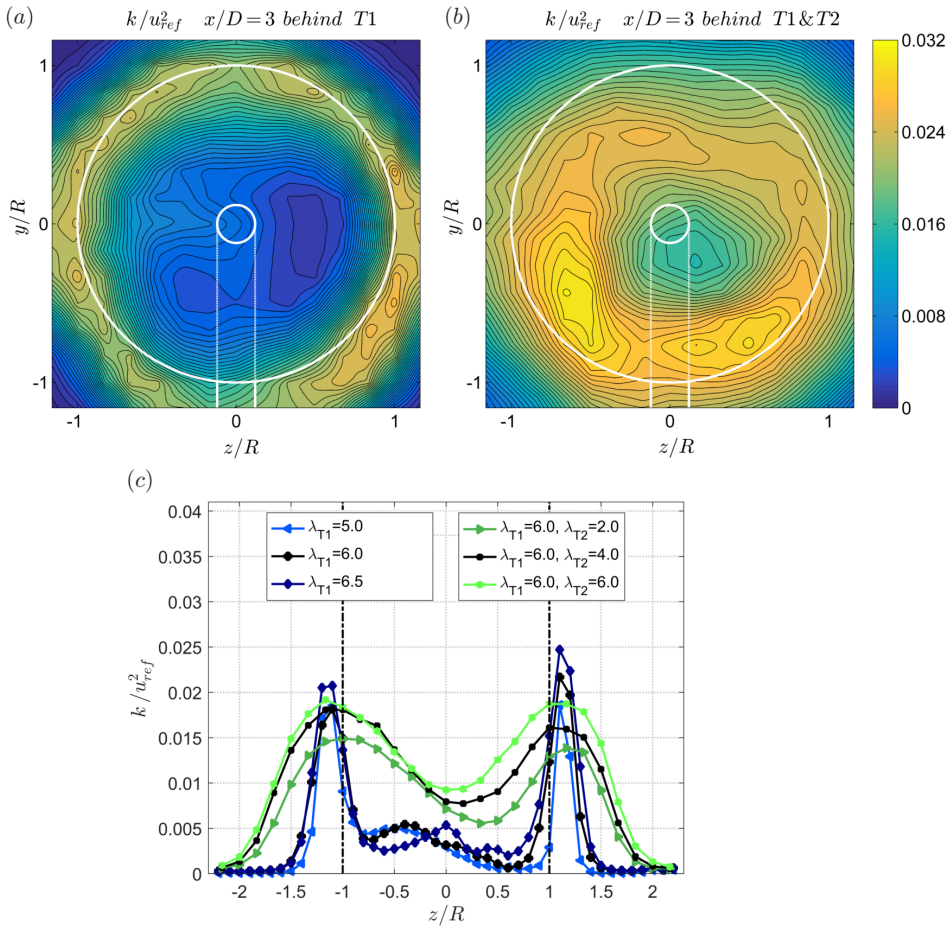

Fig. 6. Normalized turbulent kinetic energy in the wake x/D=3 **(a)** behind T1 operated at λ_{T1}=6 (reference case); **(b)** behind T2 while T1 operated at λ_{T1}=6 and T2 operated at λ_{T2}=4 (reference case); **(c)** behind T1 operated at λ_{T1}=5, 6 and 7 (blue lines are the curtailed cases) respectively behind T2 while T1 operated at λ_{T1}=6 and T2 operated at λ_{T2}=2, 4 and 6 (green lines are the curtailed cases)

compared to the velocity profiles of the reference case (black lines). When the first turbine is overspeeded to λ_{T1}=6.5 more energy is taken out of the flow in the regions close to the blade tip, while more energy is left in the flow in the center of the wake. The opposite effect is observed in the wake of the turbine curtailed to λ_{T1}=5.0. Less energy is extracted in the blade tip regions, and a much flatter wake profile is formed behind the rotor. The corresponding profiles of normalized turbulent kinetic energy are shown in Figure 6 (c). Herein, the TKE peaks in the shear layer are observed to be slightly reduced for smaller first turbine tip speed ratios.

The two cases of more distinct curtailment of the second turbine are shown in the green profiles in Figure 5 (c) and Figure 6 (c). Curtailment to a lower T2 tip speed ratio λ_{T2}=2.0 is observed to somewhat increase the kinetic energy left in the wake. This is not reflected in power measurements on the third row turbine, which is able to extract about the same amount of energy as for the reference case. An increase of the second turbine tip speed ratio to λ_{T2}=6.0 is observed to slightly reduce the mean velocity in the wake even further. This observation is in contradiction to a slightly higher power output for T3. The turbulence levels in the wake behind the second turbine are observed to be higher for higher tip speed ratios.

4 Conclusions

A comparison of the power outputs of the three first rows shows good agreement with measurements from a full-scale wind farm of similar inter-turbine spacing. As observed in most full-scale wind farms, the power drop from the first to the second row is a considerably bigger than the power drop from the second to the third row. A comparison of the wake flow behind the first row and second row shows a significantly higher mean velocity loss behind the second row justifying the further power drop from the second to the third row turbine. Furthermore, the time-averaged turbulent kinetic energy production behind the second turbine is spread out further into freestream and center of the wake than for the first turbine wake. The higher turbulence levels contribute to increased mixing and faster wake recovery behind the second turbine. Curtailing the front row turbine to smaller tip speed ratios only resulted in very small total power gains below 1%, which is insignificant considering a statistical measurement uncertainty of the same magnitude. Curtailments of both the first and second row turbine indicate that the best combined array power results are achieved for slightly lower than rated tip speed ratios. Although tip speed ratio curtailment seems to have a rather small potential for a wind farm power optimization, it could be an effective method to distribute loads between the turbine rows as an operation at a rather constant array power seems possible over a wide range of tip speed ratios.

References

1. Adaramola, M.S. and Krogstad, P.Å.: Experimental investigation of wake effects on wind turbine performance Renewable Energy, 36, 2078–2086, doi:j.renene.2011.01.024, 2011.

2. Barthelmie, R. J., Frandsen, S. T., Hansen, K., Schepers, J. G., Rados, K., Schlez, W., Neubert, A., Jensen, L.E., and Neckelmann, S.: Quantifying the Impact of Wind Turbine Wakes on Power Output at Offshore Wind Farms., Journal of Atmospheric and Oceanic Technology, 27(8), 1302–1317, doi:10.1175/2010JTECHA1398.1, 2010.

3. Bartl, J. and Sætran, L.: Experimental testing of axial induction based control strategies for wake control and wind farm optimization, J. Phys. Conf. Ser. B, Wind, wakes, turbulence and wind farms, 753:032035 doi:10.1088/1742-6596/753/3/032035, 2016.

4. Campagnolo, F., Petrovi, V., Schreiber, J., Nanos, E.M., Croce, A., Bottasso, C.L.: Wind tunnel testing of a closed-loop wake deflection controller for wind farm power maximization, Journal of Physics:Conference Series 753, 032006, doi:10.1088/1742-6596/753/3/032006, 2016.

5. Ceccotti, C., Spiga, A., Bartl, J., Sætran, L.: Effect of upstream turbine tip speed variations on downstream turbine performance, Energy Procedia, 94C, 478–486, doi:j.egypro.2016.09.218, 2016.

6. Churchfield, M.J., Lee, S., Michalakes, J., Moriarty, P.J.: A numerical study of the effects of atmospheric and wake turbulence on wind turbine dynamics, Journal of Turbulence, 13:N14, doi:10.1080/14685248.2012.668191, 2012.

7. Frandsen, S., Barthelmie, R., Pryor, S., Rathmann, O., Larsen, S., Højstrup, J., and Thøgersen, M.: Analytical modelling of wind speed deficit in large offshore wind farms, Wind Energy, 9, 39–53, doi:10.1002/we.189, 2006.

8. Hansen, K.S., Barthelmie, R.J., Jensen, L.E., Sommer, A.: The impact of turbulence intensity and atmospheric stability on power deficits due to wind turbine wakes at Horns Rev wind farm, Wind Energy, 15, 183-196, doi:10.1002/we.512, 2012.

9. Knudsen, T., Bak, T. and Svenstrup, M.: Survey of wind farm controlpower and fatigue optimization, Wind Energy, 18, 1333–1351, doi:10.1002/we.1760, 2014.

10. Nilsson, K., Ivanell, S., Hansen, K.S., Mikkelsen, R., Sørensen, J.N., Breton, S.-P., Henningson, D.: Large-eddy simulations of the Lillgrund wind farm, Wind Energy, 18, 449-467, doi:10.1002/we.1707, 2015.

11. Mikkelsen, R., Sørensen, J.N., Øye, S., Troldborg, N.: Analysis of power enhancement for a row of wind turbines using the actuator line technique, Journal of Physics:Conference Series, 75, 012044, doi:10.1088/1742-6596/75/1/012044/meta, 2007.

12. Ostovan, Y., Amiri, H., and Uzol, O.: Aerodynamic Characterization of NREL S826 Airfoil at Low Reynolds Numbers, RUZGEM Conference on Wind Energy Science and Technology, METU Ankara Campus, Ankara, Turkey, 2013.

13. Sagmo, K. F., Bartl, J., and Sætran, L.: Numerical simulations of the NREL S826 airfoil, J. Phys. Conf. Ser., 753:082036, doi:10.1088/1742-6596/753/8/082036, 2016.

14. Sarmast, S. and Mikkelsen, R.: The experimental results of the NREL S826 airfoil at low Reynolds numbers, Technical Report, available at: www.urn:nbn:se:kth:diva-120583 (last access: 7 February 2017), 2013.

PAPER 3

Wind tunnel experiments on wind turbine wakes in yaw: Effects of inflow turbulence and shear

Jan Bartl, Franz Mühle, Jannik Schottler, Lars Sætran, Joachim Peinke, Muyiwa Adaramola, Michael Hölling

Original version accepted for publication in
Wind Energy Science
doi: 10.5194/wes-2017-59

PAPER 3

Wind tunnel experiments on wind turbine wakes in yaw: Effects of inflow turbulence and shear

Jan Bartl[a], Franz Mühle[b], Jannik Schottler[c], Lars Sætran[a], Joachim Peinke[c,d], Muyiwa Adaramola[b], Michael Hölling[c]

[a] Department of Energy and Process Engineering, NTNU, Trondheim, Norway
[b] Faculty of Environmental Sciences, NMBU, Ås, Norway
[c] ForWind, Institute of Physics, University of Oldenburg, Germany
[d] Fraunhofer IWES, Oldenburg, Germany

Accepted for publication in Wind Energy Science (doi: 10.5194/wes-2017-59)

Summary. The wake characteristics behind a yawed model wind turbine exposed to different customized inflow conditions are investigated. Laser Doppler Anemometry is used to measure the wake flow in two planes at x/D=3 and x/D=6 while the turbine yaw angle is varied from $\gamma = [-30°, 0°, +30°]$. The objective is to assess the influence of grid-generated inflow turbulence and shear on the mean and turbulent flow components.

The wake flow is observed to be asymmetric with respect to negative and positive yaw angles. A counter-rotating vortex pair is detected creating a kidney-shaped velocity deficit for all inflow conditions. Exposing the rotor to non-uniform shear inflow changes the mean and turbulent wake characteristics only insignificantly. At low inflow turbulence the curled wake shape and wake center deflection are more pronounced than at high inflow turbulence. For a yawed turbine the rotor-generated turbulence profiles peak in regions of strong mean velocity gradients, while the levels of peak turbulence decrease at approximately the same rate as the rotor thrust.

1 Introduction

In the light of a steadily increasing worldwide use of wind energy, optimized control for wind farms has become a focus area of research. The reduced wind speeds in the wake leave significantly less energy for downstream turbines causing wind farm power losses up to 20% [2]. At the same time increased turbulence levels in the wake lead to higher fatigue loads on downstream rotors, which experience an increased probability for component failure [33]. In order to mitigate these unfavorable consequences of wake impingement, different wind farm control methods have been suggested for optimizing the total power output and minimizing loads on a wind farm's individual turbines [21, 14].

These methods include the reduction of the upstream turbine's axial-induction by varying its torque or blade pitch angle [1, 3] as well as wake redirection techniques, which intentionally apply a tilted thrust vector on the front row rotors. In Fleming et al. (2015) [11] different wake deflection mechanisms have been discussed with respect to higher wind farm power production and rotor loads. As individual pitch control has been shown to cause high structural loads and current turbine designs do not feature a degree of freedom in tilt direction, yaw actuation has been concluded to be a very promising technique.

For the development of wake deflection strategies by yaw misalignment, the characteristics of the mean and turbulent wake flow behind a yawed turbine have to be understood in detail. Besides the turbine's geometry and operational state, the wake flow is strongly dependent on the atmospheric conditions which represent the inflow state to the turbine. The stability of the atmospheric boundary layer can be described by height-dependent distributions of potential temperature, wind direction (veer), velocity distribution (shear) and turbulence intensity [34]. As it is rather impossible to simulate realistic atmospheric conditions in a wind tunnel environment, these parameters have to be investigated separately Therefore, the present study investigates the dependency of the wake flow behind yawed turbines for different customized inflow conditions. The wind tunnel study intends to shed light on the effects of non-uniform shear and inflow turbulence levels on the wake characteristics. Wind tunnel wake experiments have the advantage of being conducted in controlled laboratory environment. Thus, intentional variations of inflow conditions and turbine operating points can help to gain a deeper understanding of the effects on the wake flow. They furthermore can serve as validation data of numerical results and a base for the fine-tuning of engineering wake models.

An early set of experimental studies on the wake of a yawed turbine was reported by Grant et al. (1997) [17], in which they used optical methods in the wake behind a model turbine of D=0.90 m to track the tip vortices and calculate wake deflection and expansion. In a follow-up study, Grant and Parkin (2000) [16] presented phase-locked particle image velocimetry (PIV) measurements in the wake. The measured circulation in the wake showed clear asymmetries in the wake shape for positive and negative yaw angles. An asymmetric

wake was also reported by Haans et al. (2005) [18], who found non-symmetric tip vortex locations behind a yawed model turbine of D=1.20 m. Another yaw experiment was conducted by Medici and Alfredsson (2006) [24] on a small model turbine of D=0.12 m. They reported a clear cross-stream flow component deflecting the wake laterally. These experimental results were later used by Jiménez et al. (2010) [20] as verification data for a wake deflection model for yawed turbines. Based on large eddy simulations (LES) around a yawed actuator disc they developed a simple analytical model that is able to predict the wake skew angle and wake velocity deficit in the far wake. An engineering model for the axial induced velocity on a yawed turbine was developed by Schepers (1999) [26], which was based on inflow measurements in front of different yawed turbines.

An extensive study of flow and load characteristics on a yawed wind turbine rotor on a D=4.50 m rotor was presented by Schepers et al. (2014) [27]. In the so-called Mexnext project, a comparison of twenty different computations with detailed PIV and load measurements revealed modeling deficiencies while simultaneously shedding light on complex instationary flow at the rotor. The topic of utilizing yaw misalignment for improved wind farm control was thoroughly investigated by Fleming et al. (2015) [11] and Gebraad et al. (2016) [15]. They analyzed wake mitigation strategies by using both a parametric wake model and the advanced computational fluid dynamics (CFD) tool SOWFA. A recent follow-up study by Fleming et al. (2017) [13] focused on large-scale flow structures in the wake behind one and multiple aligned turbines and addresses a wake deflection behind a non-yawed downstream impinged by a partial wake of a yawed upstream turbine. In another LES investigation Vollmer et al. (2016) [34] studied the influence of three atmospheric stability classes on the wake characteristics behind a yawed turbine rotor. A strong dependency of the wake shape and deflection on the stability is found, showing significantly higher wake deflection for a stable atmosphere than for neutral or convective conditions. Another LES study on yaw misalignment was performed by Wang et al. (2017) [35], who highlighted the importance of including nacelle and tower structures in the computational model when comparing with experimental results.

Yaw angle dependent turbine performance and near-wake measurements were performed by Krogstad and Adaramola (2012) [22]. They found a power decrease proportional to $cos^3(\gamma)$ and showed that the near-wake deflection is dependent on the turbine's tip speed ratio. A combined experimental and computational wake study for a larger range of downstream distances was recently reported by Howland et al. (2016) [19]. The wake behind a yawed small drag disc of D=0.03 m was analyzed, describing the formation of a curled wake shape by a counter-rotating vortex pair. The influence of wake swirl, ground effect and turbulent diffusion on the formation mechanisms of this counter-rotating vortex pair was recently systematically investigated by Berdowski et al. (2018) [8] using a free-wake vortex filament method. An extensive contribution to the field of yawed turbine wakes was

recently made by Bastankhah and Porte-Agél (2016) [6]. In an experimental PIV study on a model turbine of D=0.15 m an asymmetric flow entrainment in the wake by both mean and turbulent momentum fluxes was shown. Moreover, an analytical model for the far wake of a yawed turbine was developed based on self-similar velocity and skew angle distributions.

An experimental study on the interaction of two model wind turbines was conducted by Schottler et al. (2016) [28] showing clear asymmetries of the downstream turbine power output with respect to the upstream turbine's positive or negative yaw angle. In a follow-up study the asymmetry was ascribed to a strong shear in the inflow, which caused an asymmetry in the opposite direction when the sheared inflow was vertically inverted [30]. These studies encouraged a more detailed investigation of the inflow-dependent wake flow behind a yawed turbine. As for the present study, we aim to close the gap between turbine interactions for yaw-controlled wind farms by presenting high-fidelity wake measurement data at controlled inflow conditions. The influence of turbulence and shear in the inflow on the wake's shape, deflection and symmetry with respect to yaw angle is quantified. This work is part of a joint experimental campaign by the NTNU Trondheim and ForWind in Oldenburg. While this paper examines the influence of varying inflow conditions on the wake of one model wind turbine, a second paper by Schottler et al. (2018) [29] compares the wake characteristics behind two different model wind turbines during exposed to one inflow only while also adding two-point statistics to the evaluation.

2 Experimental setup

2.1 Turbine model, inflow & operating conditions

Turbine model

The wind turbine model used for this study has a rotor diameter of D=0.90 m with a hub diameter of D_{hub}=0.090 m. The tower and nacelle structure of the turbine is a slimmer re-design of the turbines previously used in Bartl and Sætran (2017) [4]. The tower thickness and the nacelle length have been significantly reduced in size in order to minimize their impact on the wake flow behind the yawed rotor. Photographs of the turbine exposed to different inflow conditions are shown in Figure 1. The blades are milled in aluminum and based on an NREL S826 airfoil, which was originally designed at the National Renewable Energy Laboratory (NREL). The rotor turns in counter-clockwise direction when observed from an upstream point of view. The rotation is controlled via an electric servo motor of the type 400W Panasonic LIQI, which is located inside the nacelle. The frequency-controlled motor ensures a rotation at constant rotational speed, while the excessive power is burned off in an external resistor. The blade pitch angle was fixed to $\beta = 0°$ for the entire experiment.

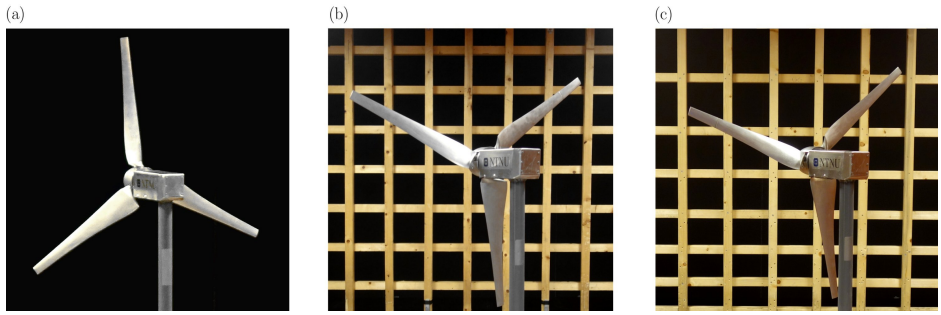

Fig. 1. Yawed model wind turbine exposed to different inflow conditions: **(a)** TI_A=0.23%, uniform **(b)** TI_B=10.0%, uniform **(c)** TI_C=10.0%, non-uniform shear.

Scaling and blockage

The experiments were performed at the low-speed wind tunnel at the Norwegian University of Science and Technology (NTNU) in Trondheim, Norway. The test section is 11.15 m long with an inlet cross-section of 2.71 m × 1.81 m (width × height). Compared to a full scale wind turbine, the model size is scaled down at a geometrical scaling ratio of approximately 1:100 resulting in a mismatch in Reynolds number in the model experiment. The turbine is operated at a Reynolds number of approximately $Re_{\text{tip}} \approx 10^5$ at the blade tip, which is more than one full order of magnitude lower than for full scale turbines. Re_{tip} is based on the chord length at the blade tip and the effective velocity during turbine operation. Furthermore, the rotor swept area of the turbine model blocks 12.8 % of the wind tunnel's cross sectional area. The wind tunnel height is approximately twice the rotor diameter while its width measures about three times the diameter. Consequently, there is about one full diameter of space for lateral wake deflection on each side behind the rotor. However, an influence of the wind tunnel walls on the wake expansion and deflection cannot be completely excluded.

Inflow conditions

The measurements are performed for three different stationary inflow conditions as listed in Table 1. As shown in Figure 1 inflows B and C are generated by static grids at the inlet. The streamwise mean velocities and turbulence intensity levels measured in the empty wind tunnel at the turbine position (x/D=0) and wake measurement locations (x/D=3 and x/D=6) are presented in Figure 2.

Inflow A can be characterized as a typical laboratory flow, in which the turbine is exposed to the uniform, low turbulence inflow of the wind tunnel (TI_A=0.23%). The low turbulence level in test case A is considered to be far below the intensities present in the

Table 1. Characteristics of the three different investigated inflow conditions.

Inflow	TI [%]	spatial uniformity	power law coeff. α
A	0.23	uniform	0
B	10.0	uniform	0
C	10.0	non-uniform	0.11

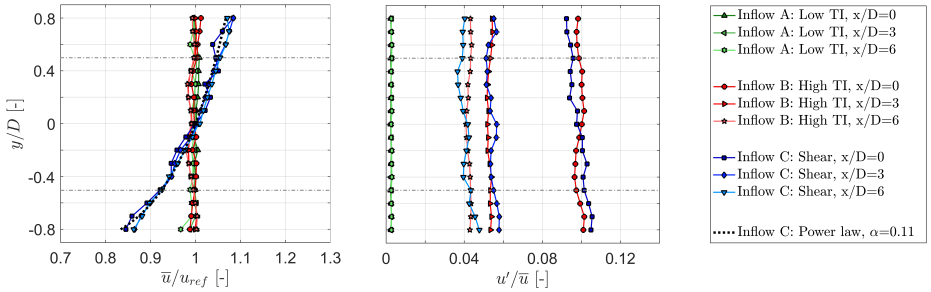

Fig. 2. Normalized mean velocity $\overline{u}/u_{ref}$ and turbulence intensity $u'/\overline{u}$ measured in the empty wind tunnel at the turbine position $x/D = 0$ and wake measurement positions $x/D = 3$ and $x/D = 6$.

real atmospheric boundary layer. Nevertheless, test case A is considered an extreme test case for the performance of computational prediction models. In order to generate a higher turbulence level for inflow B, a custom-made turbulence grid with evenly spaced horizontal and vertical bars is placed at the test section inlet x/D=-2 upstream of the turbine. At the turbine position (x/D=0) a mean streamwise turbulence level of TI_B=10.0% is measured, which decays to 5.5% at x/D=3. Test case B represents turbulence conditions that are comparable to those of a neutral atmospheric boundary layer, although the inevitable decay of the grid-generated turbulence in the experiment is not representative for real conditions. Over the rotor swept area, inflow A is measured to be uniform within ±0.8% in y- and z-direction for all downstream distances. For inflow B, wakes of the single grid bars are still observed at x/D=0, causing a spatial mean velocity variation within ±2.5%, while already at x/D=3 the grid-generated turbulent flow is uniform within ±1.0%.
The non-uniform shear inflow C is created by a grid with non-uniformly spaced horizontal bars, which is described in more detail in Bartl and Sætran (2017) [4]. The vertical flow profile establishes for all streamwise positions and can be approximated by the power law

$$\frac{u}{u_{ref}} = \left(\frac{y}{y_{ref}}\right)^{\alpha} \tag{1}$$

in which α describes the strength of the shear profiles gradient du/dy. The grid generated shear flow is approximated by a shear coefficient of $\alpha = 0.11$. Combined with a turbulence intensity of TI_C=10.0%, inflow C resembles conditions measured at an onshore site

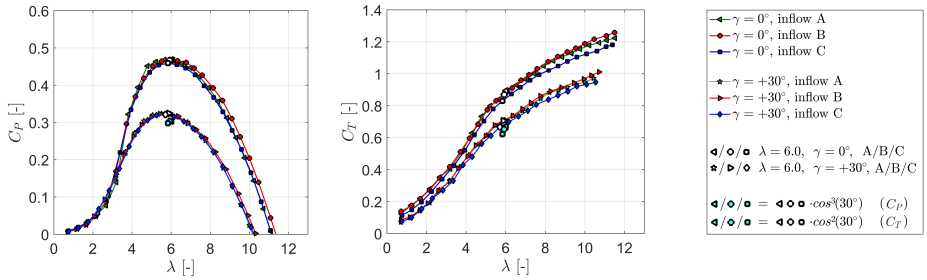

Fig. 3. Operating conditions of the model wind turbine: **(a)** power coefficient C_P and **(b)** thrust coefficient C_T for different turbine yaw angels and inflow conditions. The white points indicate the operational conditions, at which wake measurements are performed. Cyan colored points indicate a theoretical power and thrust reduction by yawing of $C_{P,\gamma=0} \cdot cos^3(30°)$ respectively $C_{T,\gamma=0} \cdot cos^2(30°)$.

for a neutral atmospheric boundary layer [36]. In the z-direction, inflow C is measured to be spatially uniform within ±1.0% over the rotor-swept area. The v-component of the flow is observed to be slightly negative for inflow C ranging from v/u_{ref}=[-0.005 -0.080] for all measurement positions. The influence of the negative v-component in the inflow is deemed insignificant for the streamwise velocity u/u_{ref} in the wake. For the analysis of three-dimensional flow effects in the wake the v-component from the inflow is subtracted. All presented mean velocity profiles and turbulence levels are measured in the empty wind tunnel at the reference velocity of $u_{ref} = 10.0m/s$.

Operating conditions

Figure 3 shows the turbine's measured power and thrust curves for different inflow conditions and yaw angles γ=0° and γ=+30°. In general, power and thrust measurements show very similar behavior for all three inflow conditions as shown in Table 2. Minor differences in the performance curves occur in the transition from stall around λ=3 as previously discussed in Bartl and Sætran (2017) [4].

Performance curves measured for γ=-30° match well with those of γ=+30°, but are not plotted for clarity. For this study, the turbine tip speed ratio is kept constant at its design point at $\lambda_{opt} = 6.0$ for all yaw angles and inflow conditions. For the investigated yaw angles $\gamma = \pm 30°$ the power reduces about 30% compared to the maximum power of the non-yawed turbine. An approximation of this reduction can be obtained with sufficient accuracy by multiplying the maximum power of the non-yawed turbine by $cos^3(30°)$. An adequate estimate of the thrust coefficient of the yawed rotor can be obtained assuming a reduction by $cos^2(30°)$ on the thrust of the non-yawed rotor. This corresponds well to previous measurements by Krogstad and Adaramola (2012) [22].

Table 2. Turbine performance (C_P and C_T) at the optimal operating point ($\lambda = 6.0$) for different yaw angles and inflow conditions.

	Inflow A		Inflow B		Inflow C	
γ [°]	C_P [−]	C_T [−]	C_P [−]	C_T [−]	C_P [−]	C_T [−]
0	0.468	0.893	0.467	0.870	0.459	0.830
+30	0.322	0.707	0.324	0.706	0.321	0.667
-30	0.328	0.711	0.331	0.713	0.327	0.679

2.2 Measurement techniques

Power and force measurements

In order to assess the rotor power characteristics, the rotor was installed at another test rig equipped with an HBM torque transducer of the type T20W-N/2-Nm. Flexible couplings connect the torque transducer to the rotor shaft. An optical photo cell is installed on the shaft enabling to measure the rotor rotational speed. The friction in the ball bearing between the rotor and torque sensor is measured without the rotor and thereafter subtracted from the total mechanical power. For the wake measurements the rotor is then installed on a smaller nacelle, which interacts less with the flow. The rotational speed is controlled via a servo motor, ensuring the same power characteristics. For measurements of rotor thrust the model turbine is installed on a six-component force balance produced by Carl Schenck AG.

Flow measurements

The wake flow was measured with a two-component Dantec FiberFlow Laser Doppler Anemometer (LDA) system used in Differential Doppler Mode. The laser was set up to record the streamwise flow component u as well as the vertical flow component v. In order to obtain results for the lateral flow component w, the laser was turned in $u - w$ direction for one wake measurement. The reference coordinate system and measurement grid is shown in Figure 4. 5×10^4 samples are taken for each measurement point over a period of approximately $30s$, resulting in an average sampling frequency of $1666Hz$. A grid consisting of 357 points is scanned for one full wake contour. For that purpose the LDA system is traversed from -1.0D to +1.0D in z-direction and from -0.8D to +0.8D in y-direction. The distance between two measurement points is 0.1D. For further analysis, these values are interpolated to a finer grid of $401 \times 321 \approx 129000$ grid points. The natural neighbor interpolation method is used, which gives a smoother interpolation of the value distribution according to Sukumar (1997) [32].

2.3 Measurement uncertainties

The uncertainty of the measured mean velocity is assessed for every sample following the procedure described in Wheeler and Ganji (2004) [37]. The LDA manufacturer Dan-

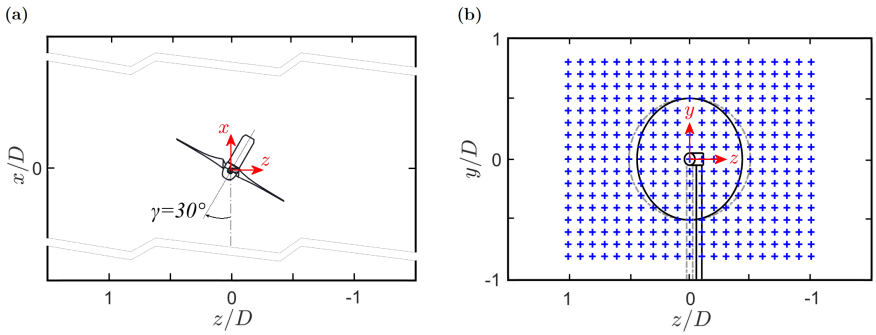

Fig. 4. Reference coordinate system in the wind tunnel: **(a)** top view of yawed turbine setup and **(b)** grid for wake measurements.

tec Dynamics specifies the uncertainty on measured velocity by 0.04%. Random errors are computed from repeated measurements of various representative measurement points based on a 95 % confidence interval. In the freestream flow as well as in the wake center the calculated uncertainties are below 1%, while increased uncertainties of up to 4% are calculated in the shear layers. Small inaccuracies in the adjustment of the traversing system are deemed to be the main contributor. The uncertainty in turbulent kinetic energy is computed according to the method proposed by Benedict and Gould (1996) [7]. Corresponding to the mean velocity the highest uncertainties up to 5% are found in the shear layer between wake and free stream flow.

3 Methods

3.1 Wake shape parametrization

In order to compare the shape of the mean wake for different inflows, the velocity contours are parametrized. The wake contours are therefore sliced into horizontal profiles for each of the 321 interpolated vertical positions. 201 of these 321 velocity profiles are located behind the rotor swept area from y/D=-0.5 to y/D=0.5. These profiles are fitted with an eighth order polynomial to smoothen out local unsteadinesses. Then, an algorithm is applied to locate the z-position of the minimum fitted velocity for each profile. When plotting the z-positions of all these minima versus their y-position, an arc shaped curve is obtained. The curves allow for a direct wake shape comparison depending on inflow condition and yaw angle.

3.2 Wake deflection assessment

As intentional yaw misalignment could possibly be utilized for optimized wind farm control, an exact quantification of the inflow-dependent wake deflection is an important input

parameter. However, several methods to quantify the wake deflection have been used in the past, showing a large method-dependent variation in the deflection. Some of these methods are discussed in Section 5. In the present study an available power approach is used, which is deemed to give a solid assessment of the wake deflection. In order to assess the deflection of the wake, the potential power of an imaginary downstream turbine for various lateral offset positions is calculated. The z-position, at which the available power P^* is minimum, is then defined as the position of wake center deflection $\delta(z/D)$. In this study the available power P^* is calculated for 50 different locations ranging from $-0.5 \leq \mathrm{z/D} \leq 0.5$. The details of the method including an illustration are described in Schottler et al. (2017b) [30].

4 Results

4.1 Mean wake flow

At first the mean wake flows for all three yaw angles $\gamma = [-30, 0, +30]^\circ$, both downstream distances x/D=[3, 6] and all three inflow conditions [A, B, C] are analyzed. Full cross-sectional wake measurements are presented in Figure 5. At the top, the wake flow for inflow A (TI_A=0.23%) is presented. The velocity deficit in the wake is observed to reduce significantly when the turbine is yawed. As the rotor thrust is reduced, a smaller amount of streamwise momentum is lost in x-direction. For a yawed rotor, a cross-stream momentum in z-component is induced. Due to this lateral force component, the wake flow is deflected sideways. This is clearly observed at x/D=3, where the wake is seen to be deflected. Comparing the wake contours at γ=-30° and γ=+30°, an asymmetry in the mean velocity distribution is obvious. The asymmetry between positive and negative wake deflection is even more pronounced at x/D=6, where the wakes are seen to form a kidney shape. Both wake deflection and location of maximum velocity deficit are not symmetric, which is analyzed in more detail in the following sections.

Effects of inflow turbulence

In the center of Figure 5 the mean velocity results of test case B, in which the inflow turbulence level is increased to TI_B=10.0%, are shown. Due to a faster wake recovery the velocity deficits are observed to be smaller for all yaw angles. Increased turbulent mixing smoothened out the gradients between wake and freestream flow compared to test case A. The general wake shape and its lateral deflection for $\gamma = \pm 30^\circ$ is seen to be similar as for the low turbulence inflow. A curled kidney-shaped velocity deficit is also observed at x/D=6 for test case B; however, the curl is not as pronounced as in test case A. Increased mixing might have smoothened the strong gradients in cross-flow direction in this case. The wake behind a positively and negatively yawed turbine appears to feature a higher

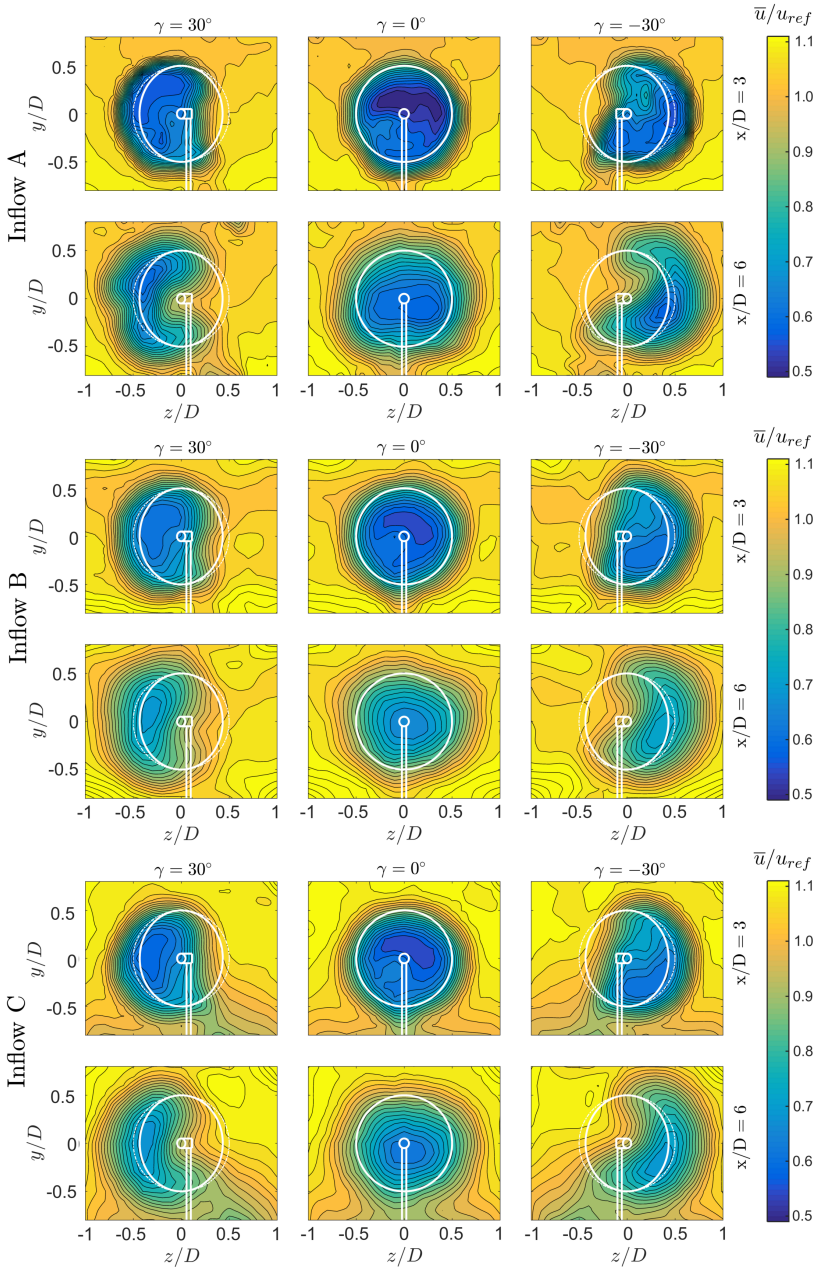

Fig. 5. Normalized mean velocity components $\overline{u}/u_{ref}$ for all measured yaw angles $\gamma = [-30, 0, +30]°$, downstream distances x/D=[3, 6] and inflow conditions [A, B, C].

degree of symmetry than in test case A. Yet an asymmetry of the minimum wake velocity is still obvious for the increased background turbulence level in test case B.

Effects of inflow shear

The wake results for a turbine exposed to inflow shear are shown at the bottom of Figure 5. The turbulence level TI_C=10.0% is the same as in test case B, but shear is present in the inflow. Despite the sheared inflow the wake shapes for all three yaw angles and both downstream distances are observed to be very similar to those of test case B. The normalized velocity levels as well as the inner structure of the wake are almost identical. In the freestream region outside the wake the shear is clearly visible, especially the lower half. Compared to test case B, the wake of the tower is detectable in test case C. The tower wake recovery seems to be slower as the freestream fluid near the tunnel floor contains less kinetic energy in test case C.

Curled wake shape

At x/D=6 a kidney-shaped velocity deficit is observed, showing a higher local velocities behind the rotor center (Figure 5). In other words, the maximum wake deflection is found at hub height. The curled kidney shape of the wake can be explained by the formation of a counter-rotating vortex pair, which was previously discussed by Howland et al. (2016) [19] as well as Bastankhah and Porte-Agél (2016) [6]. Bastankhah and Porte-Agél also presented a comprehensive explanation by the means of the differential form of the continuity equation. An illustration of the counter-rotating vortex pair at x/D=6 is presented in Figure 6, where the velocity vector $\overrightarrow{u_{yz}}$ as well as the mean streamwise vorticity $\overline{\omega_x}$ are calculated from all three velocity components. The velocity vector in the yz-plane is defined as $\overrightarrow{u_{yz}} = (v, w)$, while the streamwise time-averaged vorticity is defined as $\overline{\omega_x} = \partial v/\partial z - \partial w/\partial y$. As shown in terms of $\overrightarrow{u_{yz}}$ the two vortex centers are formed approximately at the lower and upper boundary of the rotor swept area. The clockwise rotating vortex meets the counter-clockwise rotating vortex in the center behind the wake, leading to strong lateral velocities deflecting the wake sideways.

The locations of high rotation are furthermore visualized by increased levels of vorticity $\overline{\omega_x}$ around the vortex centers. The phenomenon of a counter-rotating vortex pair is not limited to rotating wind turbines. Howland et al. (2016) [19] detected the similar large-scale vortices behind a non-rotating drag disc. Counter-rotating vortex pairs have previously been investigated for jet flows exposed to a cross-flow e.g. by Cortelezzi and Karagozian (2001) [9], a phenomenon which can be interpreted is the inverse to the wake flow behind a skewed rotor. In both phenomena the free shear flow, i.e. a wake or a jet, is superimposed with a strong lateral cross-flow, leading to the formation of a counter-rotating vortex pair at higher downstream distances.

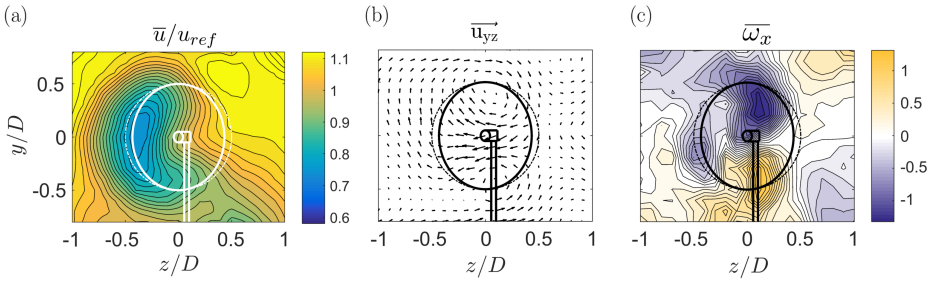

Fig. 6. (a) Streamwise mean velocity $\overline{u}/u_{ref}$, **(b)** velocity vector $\mathbf{u_{yz}}$ in the yz-plane and **(c)** streamwise mean vorticity $\overline{\omega_x}$ at $\gamma = 30°$ and $x/D = 6$ at inflow C.

Tower wake deflection

On the bottom of the wake contour plots in Figure 5, the wake of the turbine tower is indicated. The tower wake is observed to be deflected in the opposite direction than the rotor wake when the turbine is yawed. The deflection of the tower wake in the opposite direction is believed to have two reasons. Firstly, the turbine tower has a slight offset from z/D=0 as the center of yaw-rotation was set to the rotor midpoint and not the tower. Secondly, the tower wake experiences an additional deflection in opposite direction due to an adversely directed cross-flow component outside near the wind tunnel floor (Figure 6 (b)). This cross-flow balances the counter-rotating vortex pair above and possibly deflects the tower wake further to the side.

Wake curl symmetry

In order to compare the three-dimensional wake shapes behind a positively versus negatively yawed turbine more quantitatively, the curled shapes of the velocity deficit area are parametrized to a two-dimensional line. For this purpose, the minimum values in streamwise velocity $\overline{u}/u_{ref}$ are extracted from the fitted wake contours for each vertical position ranging from y/D=[-0.5, ..., 0.5]. The detailed method is described in Section 3.1. This results in the z_{min} lines as presented in Figure 7, which indicate the inflow-dependent wake curl. In addition to that, the position of the minimum velocity $(z/y)_{min}$ in both y- and z-direction is extracted and depicted in the plot by different symbols. The z_{min} lines for all inflow conditions are observed to be slightly tilted in clockwise direction for both downstream distances x/D=3 and x/D=6. The counter-clockwise rotating turbine induces an initial clockwise rotation to the wake flow. Superimposing the clockwise wake rotation with the counter-rotating vortex pair thus results in a slightly tilted curled wake shape. As previously mentioned the wake curl is seen to be more asymmetric for the low background turbulence test case A. A significant bulge is visible for γ=-30° in the upper

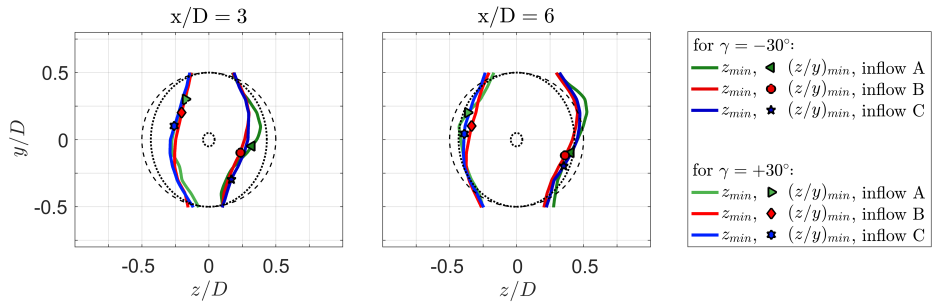

Fig. 7. Minimum values in streamwise velocity $\overline{u}/u_{ref}$. Curl shapes and minimum positions are presented at x/D=3 (left) and x/D=6 (right) for the three different inflow conditions.

half of the wake for both downstream positions. For inflow conditions B and C the curl parametrization lines are almost coinciding, confirming the insignificant influence of the moderately sheared inflow on the wake shape. Analyzing the locations of minimum velocities $(z/y)_{min}$ in the wake contours, a deviation from the horizontal centerline y/D=0 for both positive and negative yaw angles is obvious. For γ=-30° the minimum velocities $(z/y)_{min}$ are deflected to the lower half of the wake, while an upward deflection happens for positive yaw angles γ=+30°. In agreement with [6], the wake rotation is assumed to turn the velocity minimum in clockwise direction initially. The deflection from the wake centerline is observed to be larger for x/D=3 than for x/D=6, where mixing processes already have smoothened the gradients. In the case of sheared inflow of test case C, the locations of minimum wake velocity $(z/y)_{min}$ are found to be lower than for test cases A and B.

Overall wake deflection

The three-dimensional Available power method is used to quantify the overall deflection of the kinetic energy contained in the wake. As explained in Section 3.2 the minimum available power in a circular area in the wake is located, which is reducing the full wake flow field to a single parameter representing the overall wake deflection. A comparison of the minimum available power in the wakes behind a positively versus negatively yawed turbine enables a comparison of symmetry in the deflection of the energy contained in the wake with respect to the yaw angle. Additionally, a two-dimensional Gaussian fit method for the wake center detection at the turbine's hub-height is used to demonstrate systematic differences in the deflection quantification methods. In order to judge possible blockage effects, another rotor of a smaller diameter ($D_{Rot,small}$=0.45 m, $\sigma_{Blockage,small} = \frac{A_{Rot,small}}{A_{Tunnel}}$=3.3%) was used in addition to the 0.90 m ($\sigma_{Blockage,large}$=12.8%) rotor. The details of the experimental setup featuring the smaller 0.45 m rotor are described in Bartl et al. [**?**]. Further, the results are compared with two different wake models by Jimenez et al. [41] (JCM) and Bastankhah and Porte-Agél [8] (BPA). The recommended default model-parameters

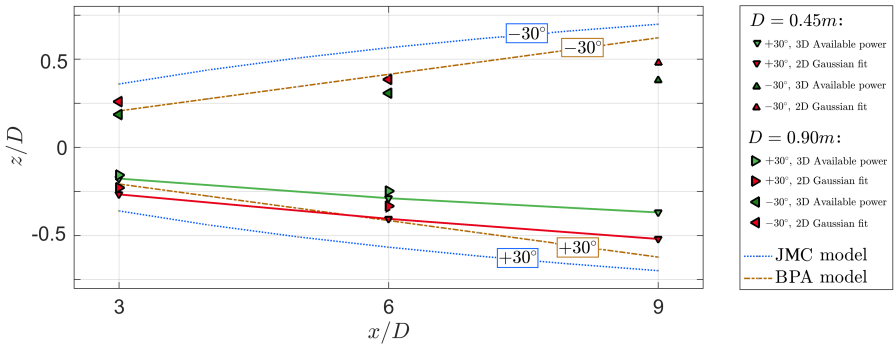

Fig. 8. Calculated wake deflection $\delta(z/D)$ for the NTNU rotor ($D = 0.90m$), a downscaled NTNU rotor ($D = 0.45m$) as well as Jiménez et al.'s and Bastankhah and Porte-Agél's wake deflection model. The inflow turbulence level is $TI_A = 0.23\%$.

were used in the implementation of both wake deflection models. For the JCM-model the linear wake expansion factor $\beta = 0.125$, while $k_y = 0.022$, $k_z = 0.022$, $\alpha* = 2.32$ and $\beta* = 0.154$ were used in the case of the BPA-model. The comparison of the wake deflections are shown in Figure 8. At x/D=3 the wake deflection for γ=+30° of the smaller rotor and the original rotor match very well. At x/D=6 a small deviation in the wake deflection after the rotors of different sizes and blockage is calculated. It can be assumed that blockage by the wind tunnel walls influences the wake deflection; however, the difference in deflection between the different rotors is observed to be rather small. Comparing the measured deflection with the prediction models discloses larger deviations. The deflection predicted by the JCM-model is generally observed to be larger than the one predicted by the BPA-model. The calculated wake deflection by the available power method at x/D=3 is still well predicted by the BPA-model, while more significant deviations are observed at x/D=6. Obviously larger differences in wake deflection are predicted by the JCM-model, both at x/D=3 and x/D=6. A number of reasons are possible to cause the significant deviations between measured and modeled deflection results. Besides the discussed wind tunnel blockage, a major source of uncertainty in this comparison arises from the method used to calculate the wake deflection. Quantifying the wake deflection by he minimum of a fitted Gaussian on the hub height velocity profiles results in a better match with the BPA-model at x/D=6 as shown by the red curve in Figure 8. However, using the hub height profile only for the wake center deflection does not take the total mean kinetic energy content in the wake into account. Due to the complex three dimensional shape of the velocity deficit, a reduction of the wake deflection to one single value has been shown to be difficult. A number of different methods have been proposed, resulting in many different deflection quantifications [78]. Further, the wake deflection $\delta(z/D)$ for all three inflow conditions is compared. These results are shown in Figure 9 and compared to the BPA-model. In contrast to the JCM-model, the inflow turbulence intensity is an

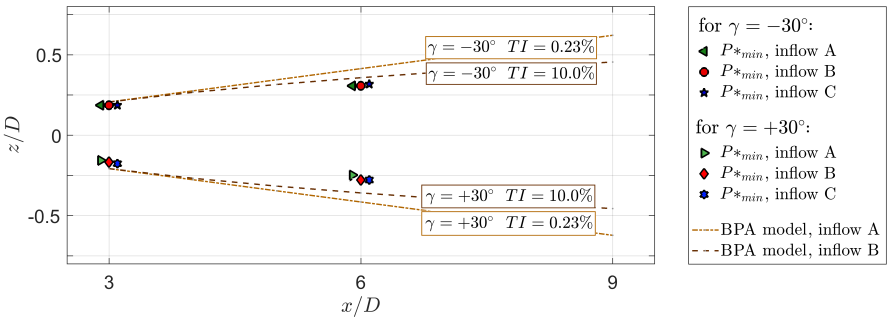

Fig. 9. Calculated wake deflection $\delta(z/D)$ at x/D=3 and x/D=6 for three different inflow conditions A, B and C compared to TI-dependent deflection predictions by Bastankhah and Porte-Agél's wake deflection model. Note that a small offset in x/D of the measured values was chosen for better visibility.

Table 3. Lateral deflection $\delta(z/D)$ [−] and wake skew angle ξ [°] calculated with the available power method.

		Inflow A		Inflow B		Inflow C	
γ [°]	x/D [−]	$\delta(z/D)$	ξ [°]	$\delta(z/D)$	ξ [°]	$\delta(z/D)$	ξ [°]
0	3	0.015	0.29	0.005	0.10	0.015	0.29
+30	3	-0.157	-2.99	-0.167	-3.18	-0.177	-3.38
-30	3	0.187	3.57	0.187	3.57	0.187	3.57
0	6	0.026	0.24	0.036	0.34	0.036	0.34
+30	6	-0.248	-2.36	-0.278	-2.65	-0.278	-2.65
-30	6	0.308	2.94	0.308	2.94	0.318	3.03

input variable in the BPA-model. It can be observed that the BPA-model predicts a higher wake deflection for a smaller inflow turbulence level. Bastankhah and Porte-Agél (2016) [6] argue that smaller inflow turbulence reduces the flow entrainment in the far wake and thus increases the wake deflection. The calculated lateral deflection values $\delta(z/D)$ and the associated wake skew angle ξ are furthermore listed in Table 3.

In general, a very similar wake deflection is observed for all three inflow conditions at both downstream distances. A systematic asymmetry in the wake deflection represented by the minimum available power behind a turbine yawed γ=-30° and γ=+30° is observed. The wake shows a higher deflection for negative yaw angles in all inflow cases. Also the wake behind the non-yawed turbine is seen to be slightly deflected in positive z-direction, which is assumed to stem from the interaction of the rotating wake with the turbine tower. As discussed by Pierella and Sætran (2017) [25] who performed experiments on the same rotor with a larger tower, the tower-wake-interaction leads to an uneven momentum entrainment in the wake. For a non-yawed setup, they observed both a lateral and vertical displacement of the wake vortex center, induced by an interaction with the tower wake.

It can therefore be assumed that also the interaction of the counter-rotating vortex pair with the tower wake slightly displaced wake vortex in the yawed cases might be influence by an interaction with the tower wake, which is the only source of asymmetry in an otherwise perfectly symmetrical setup. Increasing the turbulence level from TI_A=0.23% to TI_B=10.00% is found to only have a small influence on the wake deflection. In fact, no difference is detected for γ=-30°. For γ=+30°, however, a slightly smaller wake deflection is calculated for the lower inflow turbulence. This can also be interpreted as a higher degree of asymmetry for low background turbulence. Adding shear to the inflow is not observed to change the wake deflection significantly. This confirms the above-mentioned similarity in wake shapes measured for test cases B and C.

4.2 Rotor-generated turbulence

For the measurements presented in the this study the kinetic energy is considered to be fully dominated by turbulent motions from $x/D \geq$3 for inflow A, as Eriksen and Krogstad (2017) [10] recently showed that the production of rotor-generated turbulent kinetic energy is finished at x/D=3 for measurements on the same rotor and inflow condition. For inflow conditions B and C, the transition to fully turbulent motions is expected to take place at even smaller downstream distances.

Effects of yawing on turbulent kinetic energy locations

At the top of Figure 10 the TKE levels in the wake are presented for test case A (TI_A=0.23%). As observed in earlier studies [4, 18] a ring of high turbulence levels is formed behind the tips of the rotor blades for a non-yawed turbine. In this region the tip vortices decayed into turbulent motions. With increasing downstream distance the sharp peaks decrease in magnitude and blur out to their surrounding. For a yawed turbine, the ring of peak turbulence is laterally deflected and deformed accordingly. For x/D=3 the peaks are clearly separated by an area of low turbulence in the center of the deflected wake. For x/D=6, this area is observed to be significantly smaller. The peaks are still distinct, but it is expected that they start merging into one peak for higher downstream distances. The strongest TKE levels are observed for locations of the highest gradient in mean streamwise velocity. Thus, the TKE-ring's extension is observed to be slightly larger than the contours of the mean streamwise velocity, emphasizing the need to take the parameter TKE into account in wind farm site planning or yaw control studies.

Effects of inflow turbulence and shear

The TKE contours for increased inflow turbulence of test case B are shown in the center of Figure 10 as well as the red lines in Figure 11. At x/D=3, slightly smaller TKE peaks and higher centerline turbulence are measured for test case B than for test case A. The

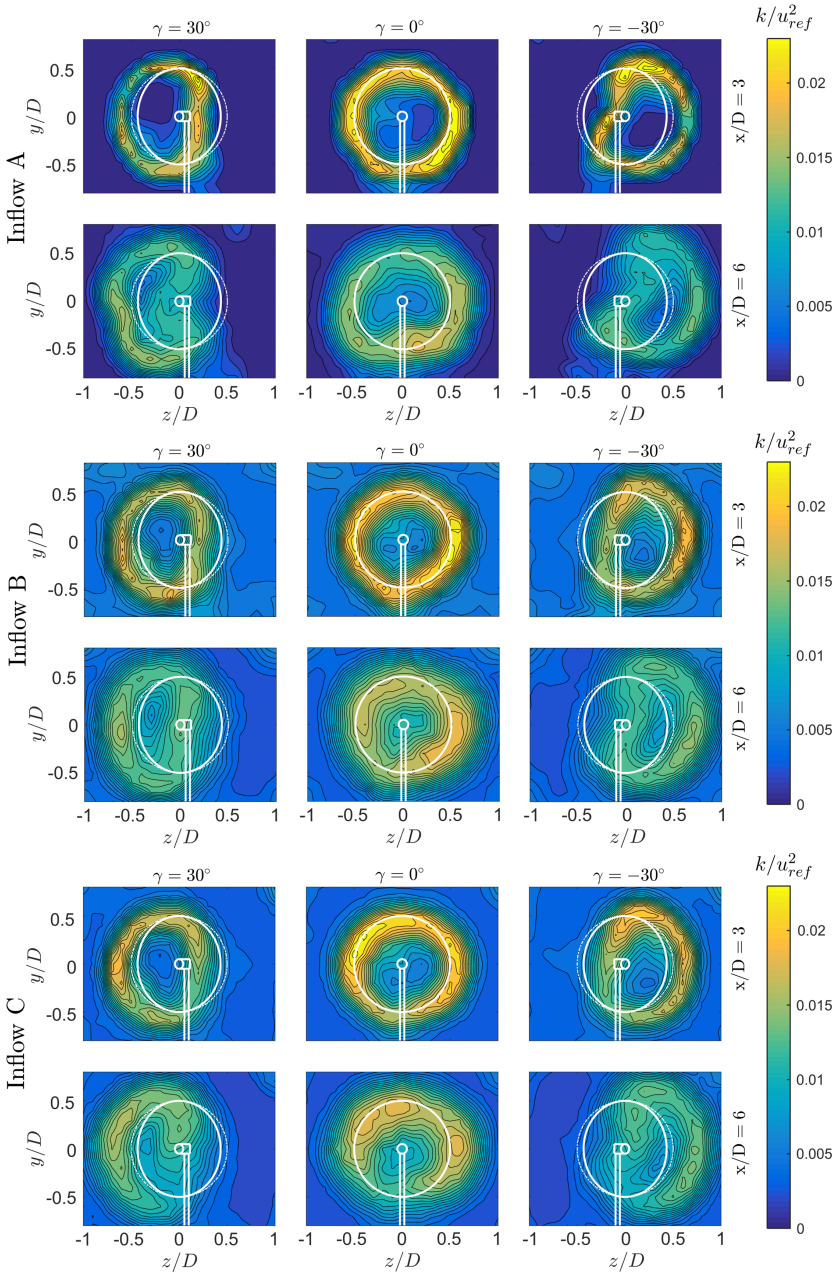

Fig. 10. Turbulent kinetic energy k/u_{ref}^2 for all measured yaw angles $\gamma = [-30, 0, +30]°$, downstream distances x/D=[3, 6] and inflow conditions [A, B, C].

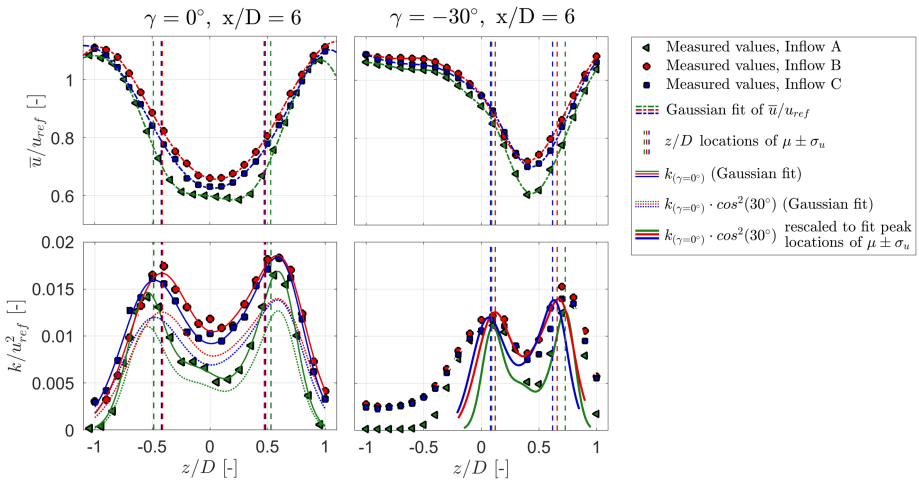

Fig. 11. Normalized mean velocity and turbulent kinetic energy k/u_{ref}^2 profiles at hub height $y = 0$ and x/D=6. The yaw angles are set to $\gamma = 0°$ and $\gamma = -30°$. Vertical dashed lines give the borders of standard deviations of fitted velocity profiles $\mu \pm \sigma_u$. Dotted lines indicate TKE profiles at $\gamma = 0°$ multiplied by $cos^2(\gamma = -30°)$. Full lines have the same magnitude as the dotted lines, but are linearly scaled in z to fit the peak locations of $\mu \pm \sigma_u$.

higher TKE levels in the freestream lead to an increased mixing, which is reducing the TKE peaks in the tip region. At x/D=6 the TKE peaks are observed to be at about the same level for both inflow conditions. For the yawed cases also the turbulence level in the wake center has evened out between inflow cases A and B. The TKE levels for the sheared inflow in test case C are observed to be very similar to those of test case B for all investigated yaw angles. These findings suggest that the presence of a moderate shear flow in a highly turbulent boundary layer does not influence the production of rotor-generated turbulent kinetic energy significantly.

Effects of yawing on turbulent kinetic energy levels

The levels of peak turbulence are observed to decrease considerably when the rotor is yawed. For a direct case-to-case comparison, TKE-profiles at hub height y=0 at x/D=6 are presented for $\gamma = 0°$ and $\gamma = -30°$ in Figure 11.

For a yawed turbine, the rotor thrust reduces with approximately $cos^2(\gamma)$ as previously shown in Figure 3. Multiplying also the TKE levels generated by the non-yawed rotor with $cos^2(\gamma)$ is observed to result in a decent first order approximation of the turbulence levels behind the yawed rotor. The reduced TKE levels for $\gamma = -30°$ are indicated by the dotted lines in Figure 11. In order to also find the lateral deflection of the turbulence peaks for yawed rotors, another first order approximation of their location proposed by Schottler et al. (2017a) [29] is applied. In this approach the expected value and standard deviation of the fitted velocity profile behind a yawed rotor is calculated. Adding the standard de-

viation to the expected value $\mu \pm \sigma_u$ gives a rough estimate of the corresponding TKE peak locations, as shown by the vertical dashed lines in Figure 11. Thus, it is possible to rescale the TKE peak locations and levels by knowing TKE and mean velocity for the now-yawed case. This might be a useful addition for modeling the rotor-generated turbulence in yawed wakes. For a complete assessment of mean velocity and turbulent kinetic energy in a yawed wind turbine wake, the model for streamwise velocity profiles by Bastankhah and Porte-Agél (2016) [6] could be extended by the proposed relations for the rotor generated turbulence.

5 Discussion

The present wind tunnel investigation showed detailed flow measurements in the wake of a yawed model turbine for different inflow conditions. A number of modeling techniques and turbine sizes were used in previous yaw wake studies in the literature, resulting in a significant variation in wake shapes and their deflection. However, a number of general flow effects in the wake behind a yawed turbine seem to be reproducible

Our results indicated minor asymmetries in the wake flow behind positively and negatively yawed turbines. The interference of the modified flow field around the tower and wake rotation is deemed to be the source for this asymmetry. This explanation is consistent with findings by Grant and Parkin (2000) [16], who reported clear asymmetries in the tip vortex shedding and circulation in the wake for positive and negative yaw angles. Our experimental measurements showed a kidney shaped mean velocity deficit at x/D=6 for all inflow conditions. These results agree well with recently discussed experimental results by Howland et al. (2016) [19]. Although the wake shape was not specifically discussed, a curled wake shape was already indicated in the results presented by Medici and Alfredsson (2006) [24]. The results presented by Bastankhah and Porte-Agél (2016) [6] offer a good comparison as wakes were measured at a number of yaw angles and downstream distances. The wake shape and velocity deficit at $\gamma = \pm 30°$ and x/D=6 match qualitatively well with our results, when an opposite sense of turbine rotation is taken into account. A direct comparison of the wakes at x/D=3 and x/D=6 of the here presented results of test case B with an equivalent setup for a slightly smaller model turbine of different rotor geometry was performed by Schottler et al. (2018) [29] and Schottler et al. (2017b) [31] and. These results show a more distinct curl in the wake already at x/D=3 while velocity deficit and wake deflection are generally found to be very similar for both model turbines. Our study moreover indicates that the wake shape and deflection is affected by inflow turbulence. This confirms the implementation of the inflow turbulence as an input parameter in the recently developed wake model by Bastankhah and Porte-Agél (2016) [6]. The influ-

ence of the inflow turbulence seems to be slightly overpredicted by their model, although a more thorough analysis for different yaw angles and downstream distances on a smaller, unblocked rotor are needed for a solid assessment of the model's sensitivity to inflow turbulence. Furthermore, the comparison of the model-predicted deflection and experimentally obtained results is not straightforward. Due to the various different calculation methods used the assessment of the wake center deflection is found to be equivocal. Gaussian fitting to locate the minimum wake velocity was amongst others used by Jiménez et al. (2010) [20] as well as Fleming et al. (2014) [12], while Luo et al. (2015) [23] and Howland et al. (2016) [19] calculated the center of mass of the three-dimensional velocity contour. A comparison of different wake deflection methods was presented by Vollmer et al. (2016) [34], showing the significant method-related variation in deflection quantification.
Another focus of the present study was to assess whether the wake's properties are significantly influenced by sheared inflow. Shear is present in most atmospheric boundary layer flows and highly dependent on stability and the terrain's complexity and roughness. The strength of the investigated shear in test case C is rather moderate and considered typical for a neutral atmospheric boundary layer Wharton and Lundquist (2011) [36]. As the study investigated only two different shear flows (α_B=0.0 and α_C=0.11), solid statements about the wake flow's sensitivity to this parameter cannot be made. The results do however indicate a rather insignificant effect of such a moderate shear on the wake flow. Possibly, a considerably stronger shear at lower inflow turbulence would have resulted in more distinguishable wake characteristics. In contrast to a recent full-scale LES study by Vollmer et al. (2016) [34], our results seem to shown a rather small dependency of the wake characteristics on the inflow conditions. However, Vollmer et al. (2016) [34] varied four different inflow parameters (turbulence intensity, potential temperature wind shear and veer) simultaneously, which made direct conclusions on the sensitivity to a single inflow parameter difficult. In conclusion, our results do not contradict with their findings as the inflow conditions in both setups were modeled very differently.

6 Conclusions

An experimental study on the inflow-dependent wake characteristics of a yawed model wind turbine was realized. In accordance with previous studies, it is confirmed that intentional turbine yaw misalignment is an effective method to laterally deflect the velocity deficit in the wake and thus offers a large potential for power optimization in wind farms. For the equally important optimization of downstream turbine fatigue loads, a careful planning of wind farm layout and control strategy should thus also take the strength and expansion of rotor-generated turbulence footprints into account. We show that the rotor-

generated turbulence distributions are deflected in the same degree as the mean velocity profiles, but feature a slightly wider expansion. Further analysis demonstrated that an increasing yaw angle reduces the levels of the peak turbulence, which is decreasing at a similar rate as the rotor thrust.

The study moreover recommends a consideration of the inflow turbulence level as an important parameter for deflection models implemented in wind farm controllers, as it is affecting the yaw-angle dependent symmetry in shape and deflection. The degree of asymmetry was observed to be higher for lower inflow turbulence. The recently proposed wake deflection model by Bastankhah and Porte-Agél (2016) [6] proved to deliver good approximations of inflow-turbulence-dependent wake deflection. However, more wake measurements at different yaw angles and various downstream distances should be performed to fully assess the model's sensitivity to inflow turbulence. As the influence of a gentle inflow-shear on the wake characteristics was found to be insignificant, an inclusion of this parameter in wake models is thus not considered to be essential at this stage. The experimental results revealed very similar velocity deficit and rotor-generated turbulence distributions to those measured for an uniform inflow.

Acknowledgments

The authors would like to acknowledge the IPID4all travel support granted by the German Academic Exchange Service (DAAD).

References

1. Annoni, J., Gebraad, P., Scholbrock, A., Fleming, P., and van Wingerden, J.-W.: Analysis of axial-induction-based wind plant control using an engineering and a high-order wind plant model, Wind Energy, 19, 113–1150, doi: 10.1002/we.1891, 2016.

2. Barthelmie, R. J., Pryor, S. C., Frandsen, S. T., Hansen, K. S., Schepers, J. G., Rados, K., Schlez, W., Neubert, a., Jensen, L. E., and Neckelmann, S.: Quantifying the impact of wind turbine wakes on power output at offshore wind farms, Journal of Atmospheric and Oceanic Technology, 27, 1302–1317, doi: 10.1175/2010JTECHA1398.1, 2010.

3. Bartl, J. and Sætran, L.: Experimental testing of axial induction based control strategies for wake control and wind farm optimization, Journal of Physics: Conference Series, 753, 032 035, doi: 10.1088/1742-6596/753/3/032035, 2016.

4. Bartl, J. and Sætran, L.: Blind test comparison of the performance and wake flow between two in-line wind turbines exposed to different turbulent inflow conditions, Wind Energy Science, 2, 55–76, doi: 10.5194/wes-2-55-2017, 2017.

5. Bartl, J., Müller, A., Landolt, A., Mühle, F., Vatn, M., Oggiano, L., and Sætran, L.: Validation of the real-time-response ProCap measurement system for full field flow measurements in a

model-scale wind turbine wake, Manuscript submitted to Journal of Physics: Conference Series, DeepWind 2018 Conference, 2018.

6. Bastankhah, M. and Porté-Agel, F.: Experimental and theoretical study of wind turbine wakes in yawed conditions, Journal of Fluid Mechanics, 806, 506–541, doi: 10.1017/jfm.2016.595, 2016.

7. Benedict, L. and Gould, R.: Towards better uncertainty estimates for turbulence statistics, Experiments in Fluids, 22, 129–136, doi: 10.1007/s003480050030, 1996.

8. Berdowski, T., Ferreira, C., van Zuijlen, A., and van Bussel, G.: Three-Dimensional Free-Wake Vortex Simulations of an Actuator Disc in Yaw, AIAA SciTech Forum, Wind Energy Synopsium 2018, doi: 10.2514/6.2018-0513, 2018.

9. Cortelezzi, L. and Karagozian, A.: On the formation of the counter-rotating vortex pair in transverse jets, Journal of Fluid Mechanics, 446, 347–373, doi: 10.1017/S0022112001005894, 2001.

10. Eriksen, P.E. and Krogstad, P.-Å.: Development of coherent motion in the wake of a model wind turbine, Renewable Energy, 108, 449–460, doi: 10.1016/j.renene.2017.02.031, 2017.

11. Fleming, P., Gebraad, P.M.O., Lee, S., van Wingerden, J.-W., Johnson, K., Churchfield, M., Michalakes, J., Spalart, P., and Moriarty, P.: Simulation comparison of wake mitigation control strategies for a two-turbine case, Wind Energy, 18, 2135–2143, doi: 10.1002/we.1810, 2015.

12. Fleming, P., Gebraad, P.M.O., Lee, S., van Wingerden, J.-W., Johnson, K., Churchfield, M., Michalakes, J., Spalart, P., and Moriarty, P.: Evaluating techniques for redirecting turbine wakes using SOWFA, Renewable Energy, 70, 211–218, doi: 10.1016/j.renene.2014.02.015, 2014.

13. Fleming, P., Annoni, J., Churchfield, M., Martinez, L., Gruchalla, K., Lawson, M., and Moriarty, P.: From wake steering to flow control, In review in Wind Energ. Sci. Disc., doi: 10.5194/wes-2017-52, 2017.

14. Gebraad, P. M. O., Fleming, P. A., and van Wingerden, J. W.: Comparison of Actuation Methods for Wake Control in Wind Plants, American Control Conference, doi: 10.1109/ACC.2015.7170977, 2015.

15. Gebraad, P. M. O., Teeuwisse, F. W., van Wingerden, J. W., Fleming, P. A., Ruben, S. D., Marden, J. R., and Pao, L. Y.: Wind plant power optimization through yaw control using a parametric model for wake effects-a CFD simulation study, Wind Energy, 19, 95–114, doi: 10.1002/we.1822, 2016.

16. Grant, I. and Parkin, P.: A DPIV study of the trailing vortex elements from the blades of a horizontal axis wind turbine in yaw, Experiments in Fluids, 28, 368–376, doi: 10.1007/s003480050, 2000.

17. Grant, I., Parkin, P., and Wang, X.: Optical vortex tracking studies of a horizontal axis wind turbine in yaw using laser-sheet, flow visualisation, Experiments in Fluids, 23, 513–519, doi: 10.1007/s003480050, 1997.

18. Haans, W., Sant, T., van Kuik, G., and van Bussel, G.: Measurement of Tip Vortex Paths in the Wake of a HAWT Under Yawed Flow Conditions, Journal of Solar Energy Engineering, 127, 456–463, doi: 10.1115/1.2037092, 2005.

19. Howland, M. F., Bossuyt, J., and Mart, L. A.: Wake Structure of Wind Turbines in Yaw under Uniform Inflow Conditions, Journal of Renewable and Sustainable Energy, 8, 043 301, doi: 10.1063/1.4955091, 2016.

20. Jiménez, Á., Crespo, A., and Migoya, E.: Application of a LES technique to characterize the wake deflection of a wind turbine in yaw, Wind Energy, 13, 559–572, doi: 10.1002/we.380, 2010.

21. Knudsen, T., Bak, T., and Svenstrup, M.: Survey of wind farm controlpower and fatigue optimization, Wind Energy, 18, 1333–1351, doi: 10.1002/we.1760, 2014.

22. Krogstad, P.-Å. and Adaramola, M. S.: Performance and near wake measurements of a model horizontal axis wind turbine, Wind Energy, 15, 743–756, doi: 10.1002/we.502, 2012.

23. Luo, L., Srivastava, N., and Ramaprabhu, P.: A Study of Intensified Wake Deflection by Multiple Yawed Turbines based on Large Eddy Simulations, AIAA SciTech Forum, (AIAA 2015-0220), doi: 10.2514/6.2015-0220, 2015.

24. Medici, D. and Alfredsson, P. H.: Measurements on a wind turbine wake: 3D effects and bluff body vortex shedding, Wind Energy, 9, 219–236, doi: 10.1002/we.156, 2006.

25. Pierella, F. and Sætran, L.: Wind tunnel investigation on the effect of the turbine tower on wind turbines wake symmetry, Wind Energy, 20, 1753-1769, doi: 10.1002/we.2120, 2017.

26. Schepers, J. G.: An Engineering Model For Yawed Conditions, Developed On Basis Of Wind Tunnel Measurements, American Institute of Aeronautics and Astronautics, 99-0039, 164–174, doi: 10.2514/6.1999-39, 1999.

27. Schepers, J. G., K. Boorsma, K., and Munduate, X.: Final Results from Mexnext-I: Analysis of detailed aerodynamic measurements on a 4.5 m diameter rotor placed in the large German Dutch Wind Tunnel DNW, Journal of Physics: Conference Series, 555, 012 089, doi: 10.1088/1742-6596/555/1/012089, 2014.

28. Schottler, J., Hölling, A., Peinke, J., and Hölling, M.: Wind tunnel tests on controllable model wind turbines in yaw, AIAA 34th Wind Energy Symposium, p. 1523, doi: 10.2514/6.2016-1523, 2016.

29. Schottler, J., Bartl, J., Mühle, F., Sætran, L., Peinke, J., and Hölling, M.: Wind tunnel experiments on wind turbine wakes in yaw: Redefining the wake width, Wind Energy Science Discussions, doi: 10.5194/wes-2017-58, 2018.

30. Schottler, J., Hölling, A., Peinke, J., and Hölling, M.: Brief communication: On the influence of vertical wind shear on the combined power output of two model wind turbines in yaw, Wind Energy Science, 2, 439–442, doi: 10.5194/wes-2-439-2017, 2017b.

31. Schottler, J., Mühle, F., Bartl, J., Peinke, J., Adaramola, M. S., Sætran, L., and Hölling, M.: Comparative study on the wake deflection behind yawed wind turbine models, Journal of Physics: Conference Series, 854, 012032, doi: 10.1088/1742-6596/854/1/012032, 2017c.

32. Sukumar, N.: A Note on Natural Neighbor Interpolation and the Natural Element Method (NEM), Theoretical and Applied Mechanics, Northwestern University, IL 60208, (last access: 25 February 2017), 1997.

33. Thomsen, K. and Sørensen, P.: Fatigue loads for wind turbines operating in wakes, Journal of Wind Engineering and Industrial Aerodynamics, 80, 121–136, doi: 10.1016/S0167-6105(98)00194-9, 1999.

34. Vollmer, L., Steinfeld, G., Heinemann, D., and Kühn, M.: Estimating the wake deflection downstream of a wind turbine in different atmospheric stabilities: an LES study, Wind Energy Science, 1, 129–141, doi: 10.5194/wes-1-129-2016, 2016.

35. Wang, J., Foley, S., Nanos, E. M., Yu, T., Campagnolo, F., Bottasso, C. L., Zanotti, A., and Croce, A.: Numerical and Experimental Study of Wake Redirection Techniques in a Boundary Layer Wind Tunnel, Journal of Physics: Conference Series, 854, 012 048, doi: 10.1088/1742-6596/854/1/012048, 2017.

36. Wharton, S. and Lundquist, J. K.: Assessing atmospheric stability and its impacts on rotor-disk wind characteristics at an onshore wind farm, Wind Energy, 15, 525–546, doi: 10.1002/we.483, 2012.

37. Wheeler, A. J. and Ganji, A. R.: Introduction to engineering experimentation, Upper Saddle River, NJ, USA, Pearson/Prentice Hall, XI, third edition edn., 2004.

PAPER 4

Wind tunnel study on power and loads optimization of two yaw-controlled model wind turbines

Jan Bartl, Franz Mühle, Lars Sætran

Original version in review in
Wind Energy Science
doi: 10.5194/wes-2018-24

PAPER 4

Wind tunnel study on power and loads optimization of two yaw-controlled model wind turbines

Jan Bartl[a], Franz Mühle[b], Lars Sætran[a]

[a] Department of Energy and Process Engineering, NTNU, Trondheim, Norway
[b] Faculty of Environmental Sciences, NMBU, Ås, Norway

In review in Wind Energy Science (doi: 10.5194/wes-2018-24)

Summary. In this experimental wind tunnel study the effects of intentional yaw misalignment on the power production and loads of a downstream turbine are investigated for full and partial wake overlap situations. Power, thrust force and yaw moment are measured on both the upstream and downstream turbine. The influence of inflow turbulence level and streamwise turbine separation distance are analyzed for full wake overlap situations. For partial wake overlap, the concept of downstream turbine yawing for yaw moment mitigation is examined for different lateral offset positions.

Results indicate that upstream turbine yaw misalignment is able to increase the combined power production of the two turbines for both partial and full wake overlap setups. For aligned turbine setups the combined power is increased between 3.5% and 11% depending on the inflow turbulence level and turbine separation distance. The increase in combined power is at the expense of increased yaw moments on both upstream and downstream turbine. For partial wake overlap situations, yaw moments on the downstream turbine can be mitigated through upstream turbine yawing, while simultaneously increasing the combined power production. A final test case demonstrates the concept of opposed downstream turbine yawing in partial wake situations, which is shown to reduce its yaw moments and increasing its power production by up to 5%.

1 Introduction

In wind farms the individual wind turbines interact aerodynamically through their wakes. Besides significant power losses, rotors exposed to upstream turbines' wakes experience higher unsteady loading (Kim et al., 2015) [16]. The reduced power and increased rotor loads are dependent on the downstream turbine's lateral and streamwise location in the wake, the upstream turbine's control settings and the characteristics of the incoming wind. The inflow characteristics are governed by the atmospheric stability, in which the turbulence level as well as the degree of shear and veer are important parameters. In combination with the wind farm layout, the site dependent wind statistic, such as wind speed and direction distributions, define the occurrence for downstream turbines to be fully or partially exposed to the upstream turbine's wake.

In order to mitigate power losses and wake induced loads on downstream turbines, different upstream turbine control strategies have recently been suggested (Knudsen et al. 2014 [17]; Gebraad et al., 2015 [12]). These include methods to reduce the axial-induction of an upstream turbine and thus also mean and turbulent gradients in the wake (Annoni et al., 2016 [3]; Bartl and Sætran, 2016 [4]) as well as wake redirection techniques (Fleming et al., 2015 [11]). The most discussed wake deflection mechanisms include individual pitch angle control, tilt angle variation and yaw angle actuation. In a computational fluid dynamics (CFD) study Fleming et al. (2015) [11] compare these techniques with regards to power gains and blade out-of-plane bending loads on a two turbine setup. Individual pitch control was observed to cause high structural loads. Most current turbine designs do not feature tilt mechanisms, while yaw actuation is concluded to be a promising technique due to its simple implementability. As all modern wind turbines are equipped with yaw actuators, intentional yaw misalignment can be used to laterally deflect the wake flow and potentially increase the wind farm power output.

A number of recent research focused on the wake characteristics behind a yawed wind turbine. In a combined experimental and computational study Howland et al. (2016) [14] measured the wake of yawed small drag disc and conducted a Large-Eddy-Simulation (LES) behind an actuator disc/line modeled rotor. They discussed different quantifications for wake deflection and characterized the formation of a curled wake shape due to a counter-rotating vortex pair. A similar wake shape was found in a LES study by Vollmer et al. (2016) [27], who found a significant variation of wake shape and deflection depending on the atmospheric stability. The yawed wake characteristics' dependency on inflow turbulence and shear were investigated in an experimental study by Bartl et al. (2017) [6]. The inflow turbulence level was observed to influence the shape and deflection of the wake, in contrast to a moderate shear in the inflow. Schottler et al. (2017) [23] highlight the importance of considering non-Gaussian distributions of velocity increments in wind farm control and layout optimizations. A ring of strongly intermittent flow is shown to

surround the mean velocity deficit locations, suggesting a much wider wake expansion as based on the mean velocity. An extensive theoretical and experimental study on yaw wakes was performed by Bastankhah and Porté-Agel (2016) [7]. They presented a theoretical description for the formation of the counter-rotating vortex pair in the wake and developed a sophisticated analytical model for the far wake of a yawed turbine. Including inflow turbulence as an additional input parameter makes Bastankhah and Porté-Agel's model a favorable alternative to the wake deflection model by Jimenez et al. (2010) [15].
Moreover, various research investigated the potential of overall wind farm power gains through intentional yaw misalignment. An experimental study by Adaramola and Krogstad (2011) [1] on two aligned model wind turbines ($x/D = 3$) demonstrated an increase in combined efficiency with increasing upstream turbine yaw angle. For a yaw angle of 30°, they measured an increase of 12% in combined power compared to the reference case at 0°. For the same separation distance Schottler et al. (2016) [22] measured a combined power increase of about 4% for an upstream turbine yaw angle of −18°. Their experimental study on two aligned model turbines furthermore pointed out clear asymmetries of the downstream turbine power output with regards to the upstream turbine yaw angle. Another experimental study on three model wind turbines was presented by Campagnolo et al. (2016) [8], who measured a combined power increase of 21% for an lateral offset of $\Delta z/D = 0.45$ between the turbines. Comprehensive studies on yaw misalignment for optimized full wind farm control haven been presented by Fleming et al. (2014) [10] and Gebraad et al. (2016) [13]. They analyzed wake mitigation strategies by using both the advanced LES code SOWFA as well as a parametric wake model. A dedicated full-scale study by McKay et al. (2013) [19] investigated the connection of yaw alignment and power output of a downstream turbine operated in the wake of an upstream turbine. They found an independent yaw alignment for the purpose of individual power increase of downstream turbines operated in partial wake situations.
Most of these studies focus on the possibilities for power optimization through yaw control; however, the discussion of increased structural loads is often left open. Yet, yaw misalignment of an undisturbed turbine was observed to create increased unsteady loading on the yawed rotor. In a simulation by Kragh and Hansen (2014) [18] these loads are quantified for different inflow conditions. It is furthermore shown that load variations due to wind shear can potentially be alleviated by yaw misalignment. Load characteristics on a yawed model turbine rotor were compared to various computational approaches by Schepers et al. (2014) [21]. The so-called Mexnext project revealed modeling deficiencies while shedding light on complex unsteady flow phenomena during yaw. In a recent paper by Damiani et al. (2017) [9] damage equivalent loads and extreme loads under yaw misalignment are measured and predicted for a fully instrumented wind turbine. They observed rather complex, inflow-dependent load distributions for yaw angle offsets. In a computational setup

of ten aligned, non-yawed wind turbines Andersen et al. (2017) [2] recently investigated the influence of inflow velocity, turbulence intensity and streamwise turbine spacing on the yaw moments and other equivalent loads on downstream turbines operated in the wake. The study shows up unexpected load peaks for every second or third downstream turbine in below-rated operating conditions. A way to utilize measured rotor loads such as yaw moments to estimate rotor yaw misalignment, inflow shear or partial wake rotor operation is investigated by Schreiber et al. (2016) [25]. Using a computational framework of a wake model, BEM model for power and loads and a gradient-based optimizer van Dijk et al. (2017) [26] investigated the effects of yaw misalignment on power production and loads in full and partial wake overlap situations. They found that upstream turbine yaw-misalignment is able to increase the total power production of their modeled wind farm, while reducing the loads in partial wake overlap situations.
The objective of the present study is to analyze potentials of yaw control for the often contradicting goals of combined power gains and load mitigation. Balancing the benefits of power gains and costs of increased rotor loads is of utmost importance for the design of cost-effective wind farm control strategies. For this purpose the parameters turbine separation distance x/D, lateral turbine offset $\Delta z/D$ and turbine yaw settings γ_{T1} and γ_{T2} are systematically varied in this wind tunnel experiment. Special focus is given to the concept of downstream turbine yawing in partial wake situations for the purpose of load reduction and combined power gains. Together with the inflow-dependent wake flow measurements on the same experimental setup presented in Bartl et al. (2017) [6], this study completes the link between detailed wake flow characteristics and power, yaw moments and thrust forces on a turbine operated in the wake.

2 Experimental setup

2.1 Wind turbine models

Two wind turbine models of the exactly same rotor geometry were used for this study. The rotor was designed based on the NREL S826 aifoil and has a total diameter of $D = 0.894\,m$. The tower and nacelle structure of the upstream turbine (T1) is slightly slimmer than that of the downstream turbine (T2), in order to minimize the effect on the wake flow behind the yawed upstream turbine. The maximum power point of both turbines is reached at a tip speed ratio of $\lambda_{T1} = \lambda_{T2} = 6.0$ in undisturbed inflow. In this experiment T2 is controlled to its optimum power point, which strongly varies for different positions and upstream turbine operational parameters. The exact geometry and detailed performance curves of T1 are described in Bartl et al. (2017) [6], while T2's characteristics can be found in Bartl and Sætran (2017) [5]. In contrast to most other turbines, the investigated model turbines rotate counter-clockwise. Positive yaw is defined as indicated in Figure 2.

The experiments were performed in the closed-loop wind tunnel at the Norwegian University of Science and Technology (NTNU) in Trondheim, Norway. The tunnel's cross-section measures 2.71 m in width, 1.81 m in height and 11.15 m in length. The turbine models are operated at a blade tip Reynolds numbers of approximately $Re_{\text{tip}} \approx 10^5$.
Moreover, about 12.8% of the wind tunnel's cross sectional area are blocked by the turbines' rotor swept area. The wind tunnel width measures about three times the turbine's rotor diameter, which leaves sufficient space for lateral wake deflection and offset positions for T2. However, a speed-up of the flow in free-stream areas around the rotors is observed due to blockage effects as described in Bartl et al. (2017) [6].

2.2 Inflow conditions

The influence of different inflow turbulence levels is investigated in this study. For this purpose the turbines are exposed to an inflow of very low turbulence intensity $TI_A = 0.23\%$ (Inflow A) as well as high turbulence intensity $TI_B = 10.0\%$ (Inflow B). Inflow B is generated by a static grid at the wind tunnel inlet. The grid-generated turbulence decays with increasing downstream distance to about $TI_B = 5.5\%$ at $x/D = 3$ and to $TI_B = 4.0\%$ at $x/D = 6$. The profiles of streamwise mean velocity and turbulence intensity measured in the empty wind tunnel for different downstream positions are presented by Bartl et al. (2017) [6]. Inflow A is assessed to be uniform within $\pm 0.8\%$ over the rotor swept area. A velocity variation of $\pm 2.5\%$ is measured at $x/D = 0$ for Inflow B, as the footprint of the grid's single bars are still detectable At $x/D = 3$, however, the grid-generated turbulent flow is seen to be uniform within $\pm 1.0\%$. Both test cases were performed at the constant reference velocity of $u_{ref} = 10.0 m/s$.

2.3 Measurement techniques

The mechanical power on both rotors was measured in separate steps with a HBM torque transducer of the type T20W-N/2-Nm, which is installed in the nacelle of the downstream turbine T2. The transducer is connected to the rotor shaft through flexible couplings. An optical photo cell inside the nacelle makes the rotor's rotational speed assessable On the test rig of T1 the rotational speed is controlled via a servo motor, ensuring the same power and load characteristics as for T2.
For the purpose of thrust force and yaw moment measurements the model turbines are separately installed on a six-component force balance by Carl Schenck AG. By constantly recording signals obtained from the three horizontal force cells, the yaw moments referred to the rotor center can be calculated. For the assessment of the rotor thrust, the drag force

Table 1. Overview of test cases.

Test case		Inflow TI	Yaw angle γ_{T1}	Streamwise sep. x/D	Lateral offset $\Delta z/D$	Yaw angle γ_{T2}
1 (a)	Aligned turbines	0.23%	[-40°,..., +40°]	3 & 6	0	0°
1 (b)	Aligned turbines	10.0%	[-40°,..., +40°]	3 & 6	0	0°
2 (a)	Offset turbines	10.0%	0°	3	[-0.5,...+0.5]	0°
2 (b)	Offset turbines	10.0%	+30°	3	[-0.5,...+0.5]	0°
3 (a)	Downstream turbine yaw	10.0%	0°	3	[-0.5,...+0.5]	[-30°,...,+30°]
3 (b)	Downstream turbine yaw	10.0%	+30°	3	[-0.5,...+0.5]	[-30°,...,+30°]

on tower and nacelle is measured isolated and then subtracted from the total thrust. No such correction is applied for the assessment of the yaw moments.

2.4 Statistical measurement uncertainties

The statistical measurement uncertainties for power coefficients, thrust coefficient and normalized yaw moments have been calculated following the procedure described by Wheeler and Ganji (2004) [28]. Random errors are computed from repeated measurements of various representative measurement points based on a 95 % confidence interval. Furthermore, the match of power and thrust values of the baseline cases (e.g. $\gamma_{T1} = 0°$, $x/D = 3$, $\Delta z/D = 0$) with previous results e.g. by Bartl and Sætran (2017) [5] has been checked for consistency.

For the purpose of clarity, errorbars are not shown in the resulting graphs in Section 3. Instead, a short overview of uncertainties for the different measures is given here. The total uncertainty in T1's power coefficient is 0.011 (1.9%) for non-yawed operation, rising up to about 0.017 (3.9%) for a yaw angle of $\gamma_{T1} = 30°$. The uncertainty in T1's thrust coefficient is assessed to be very similar, varying from 0.013 (1.4%) to 0.018 (3.1%) for yaw angles 0° and ±40°, respectively. The uncertainty in normalized yaw moments M_y^* is 0.0032, which corresponds to almost 15% of the absolute measurement value at $\gamma_{T1} = 30°$. Due to very small absolute values of the yaw moments, the relative uncertainty is rather high. In the case of T2, the uncertainties are presented representatively for the aligned test case, in which the upstream turbine is operated at $\gamma_{T1} = 30°$ and T2 located at $x/D = 3$ and operated at $\gamma_{T2} = 0°$. The total uncertainties in power and thrust coefficient are 0.006 (2.5% of the absolute C_P-value) respectively 0.007 (0.9% of the absolute C_T-value). The normalized yaw moment of the downstream turbine for this case is amounts 0.0019 (about 8% of the absolute value).

2.5 Test case definition

Three main test cases are investigated in this study. In a first test case the two model turbines are installed in an aligned arrangement in the wind tunnel, i.e. T2 is immersed in

the full wake of T1 (for $\gamma_{T1} = 0°$). The upstream turbine's yaw angle is then systematically varied at nine different values $\gamma_{T1} = [-40°, -30°, -20°, -10°, 0°, +10°, +20°, +30°, +40°]$. Moreover, the streamwise separation distance between the turbines is varied from x/D=3 to x/D=6. Finally, the inflow turbulence intensity is varied from $TI_A = 0.23\%$ (Inflow A) to $TI_B = 10.0\%$ (Inflow B).

In a second test case, the effect of the lateral offset position $\Delta z/D$ of the downstream turbine T2 in the wake of an upstream turbine T1 is investigated. That means that T2 is in most cases exposed to partial wake situations. For this purpose, the lateral offset is set to seven different positions ranging from $\Delta z/D = [-0.50, -0.33, -0.16, 0, +0.16, +0.33, +0.50]$. This is done for two upstream turbine yaw angles $\gamma_{T1} = 0°$ and $\gamma_{T1} = +30°$. The turbine separation distance is kept constant at $x/D = 3$ and only the highly turbulent inflow condition (Inflow B) is investigated.

In a third and final test case the downstream turbine yaw angle γ_{T2} is varied as an additional parameter while it is operated at different lateral offset positions $\Delta z/D$. This concept intends to demonstrate the possibility for yaw moment mitigation in partial wake situations by opposed yawing of the downstream turbine. In this test case T2 is therefore operated at 13 different yaw angles ranging from $\gamma_{T2} = [-30°, ..., +30°]$. An overview of all investigated test cases is presented in Table 1.

For all test cases the power coefficient C_P, thrust coefficient C_T and normalized yaw moment M_y^* are assessed on T1 and T2. The power coefficient is the measured mechanical power normalized with the kinetic power of the wind in a streamtube of the same diameter:

$$C_P = \frac{P}{1/8\,\rho\,\pi\,D^2\,U_{ref}^3}. \tag{1}$$

The thrust coefficient is defined as the thrust force normal to the rotor plane normalized with the momentum of the wind in a streamtube:

$$C_T = \frac{F_T}{1/8\,\rho\,\pi\,D^2\,U_{ref}^2}. \tag{2}$$

The yaw moment M_y is normalized in a similar way as the thrust force with an additional rotor diameter D to account for the normalization of the yaw moment's lever:

$$M_y^* = \frac{M_y}{1/8\,\rho\,\pi\,D^3\,U_{ref}^2}. \tag{3}$$

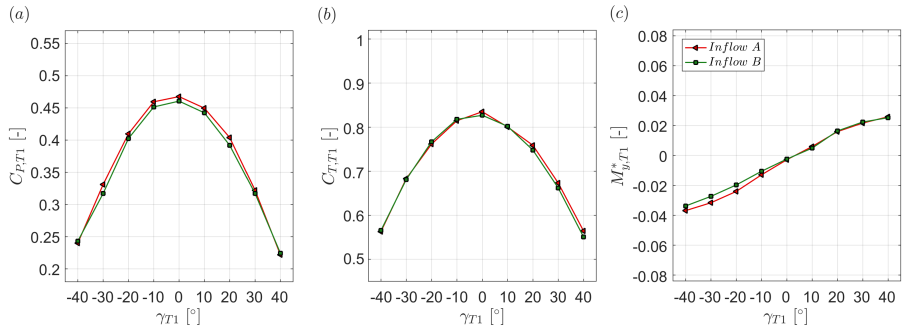

Fig. 1. (a) Power coefficient $C_{P,T1}$ **(b)** thrust coefficient $C_{T,T1}$ and **(c)** normalized yaw moment $M^*_{y,T1}$ of the undisturbed upstream turbine T1 for different inflow conditions. The turbine is operated at $\lambda_{opt,T1} = 6.0$ for all yaw angles.

3 Results

3.1 Operating characteristics of T1

At first the yaw-angle dependent operating characteristics of the upstream wind turbine are presented for two inflow conditions in Figure 1. The model turbine is operated at a tip speed ratio of $\lambda_{T1} = 6.0$ for all yaw angles. The downstream turbine shows the exactly same operating characteristics when operated in undisturbed inflow. For measurements showing the power and thrust coefficient depending on the tip speed ratio λ_{T1} it is referred to Bartl et al. (2017) [6].

At $\gamma_{T1} = 0$ the upstream turbine reaches a power coefficient of about $C_{P,T1} = 0.460$ for both inflow conditions. It is observed that an increase in inflow turbulence results in the same performance characteristics. As discussed in Bartl et al. (2017) [6], the decrease in power coefficient can be approximated $C_{P,\gamma_{T1}=0} \cdot cos^3(\gamma_{T1})$ when the turbine yaw angle is varied. The thrust coefficient's reduction through yawing is observed to match well with $C_{T,\gamma_{T1}=0} \cdot cos^2(\gamma_{T1})$. The normalized yaw moment shows an almost linear behavior around the origin. However, minor asymmetries between positive and corresponding negative yaw angles are observed. These asymmetries are slightly stronger for inflow A ($TI_A = 0.23\%$).

3.2 Test case 1: Aligned turbines

In the first test case both rotors are installed in the center of the wind tunnel at $(y, z) = (0, 0)$ aligned with the main inflow direction. The downstream turbine position is varied from $x/D = 3$ to $x/D = 6$, while the upstream turbine yaw angle is systematically changed in steps of $\Delta\gamma_{T1} = 10°$ from $\gamma_{T1} = [-40°, ..., +40°]$. Figure 2 shows two example cases, in which the downstream turbine is operated in the upstream turbine's wake for $\gamma_{T1} = 0°$ and $\gamma_{T1} = 30°$. The sketched wake flow contours in the xz-plane at hub height are Laser Doppler Anemometry (LDA) measurements of an example case and

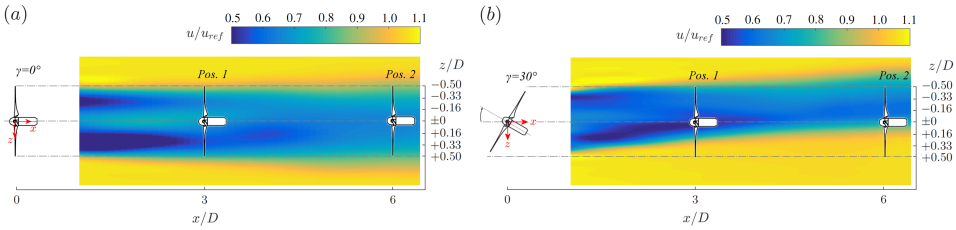

Fig. 2. Topview of the aligned downstream turbine operated in the wake of an upstream turbine at the two different positions $x/D = 3$ and $x/D = 6$. The wake flow is indicated by measured example cases for **(a)** $\gamma_{T1} = 0°$ and **(b)** $\gamma_{T1} = 30°$.

are only included for illustrative purposes. An exact quantification of the wake can be obtained from cross-sectional measurements in the yz-plane as presented in Bartl et al. (2017) [6]. The results for the downstream turbine $C_{P,T2}$, $C_{T,T2}$ and $M^*_{y,T2}$ at inflow B in dependency of its tip speed ratio λ_{T2} are shown in Figure 3. The downstream turbine's power is observed to increase with an increasing absolute value of the upstream turbine yaw angle. As the wake is laterally deflected, the downstream turbine is partly exposed to higher flow velocities in the freestream. The power recovery of the downstream turbine is observed to be asymmetric with respect to the upstream turbine yaw angle. Higher downstream turbine power coefficients are measured for negative upstream turbine yaw angles. Obviously, the optimum downstream turbine T2's operating point shifts to higher tip speed ratios λ_{T2} the more kinetic energy is available in the wake. A corresponding asymmetry between positive and negative upstream turbine yaw angles is also observed in T2's thrust coefficient, showing higher values for negative upstream turbine yaw angles. The yaw moments experienced by the downstream turbine are observed to grow with increasing upstream turbine yaw angle. As expected, downstream turbine yaw moments are positive for positive upstream turbine yaw angles and vice versa. For low tip speed ratios, i.e. during stall the yaw moments are seen to be small and below 0.01. As soon as the flow is attached the absolute value of the yaw moments is observed to strongly rise. Again, an asymmetry between negative and positive upstream turbine yaw angles is observed. The asymmetric wake deflection is considered to be the main reason for the asymmetric distribution of T2's yaw moments.

The effect of a variation in inflow turbulence level ($TI_A = 0.23\%$ versus $TI_B = 10.0\%$) on the downstream turbine's $C_{P,T2}$, $C_{T,T2}$ and $M^*_{y,T2}$ is shown in Figure 4. The results are presented for varying upstream turbine yaw angle γ_{T1}. The downstream turbine T2 is operated at a λ_{T2}, for which $C_{P,T2}$ was maximum for the specific conditions. Note that for $x/D = 6$ neither thrust nor yaw moments were measured.

The downstream turbine's power coefficient $C_{P,T2}$ is in general observed to be higher for a higher inflow turbulence (Inflow B). The wake flow recovers at a higher rate leaving more kinetic energy for the downstream turbine to extract. The difference in T2's power extrac-

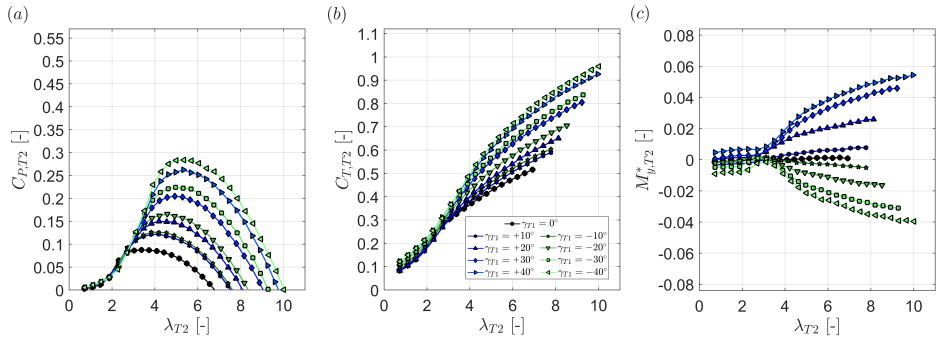

Fig. 3. Downstream turbine **(a)** power coefficient, **(b)** thrust coefficient and **(c)** normalized yaw moment as a function of its tip speed ratio λ_{T2} for different upstream turbine yaw angles γ_{T1}. The downstream turbine T2 is located at $x/D = 3$. The turbines are exposed to inflow B.

tion between the two inflow turbulence levels is observed to be highest at small upstream turbine yaw angles γ_{T1}. At high yaw angles $\gamma_{T1} \geq 30°$, however, the power coefficient $C_{P,T2}$ is very similar for the two different inflow turbulence levels. For these high yaw angles the wake's mean velocity deficit has the largest lateral deflection, exposing about half of T2's rotor swept area to the freestream. The kinetic energy content in the freestream is about the same for both inflows, which brings T2's power levels closer together. Moreover, the downstream turbine's power output at low inflow turbulence (inflow A) is observed to be more asymmetric with respect to γ_{T1} than at high inflow turbulence (B). Especially for $x/D = 6$, the downstream turbine power $C_{P,T2}$ is strongly asymmetric for inflow A. For extreme yaw angles $\gamma_{T1} = \pm 40°$, T2's power coefficient reaches levels of $C_{P,T2} = 0.45 - 0.46$, which is about the same magnitude of $C_{P,T1}$ at $\gamma_{T1} = 0°$. Although a considerable part of the downstream turbine rotor is impinged by T1's wake, blockage-increase freestream velocity levels of $\overline{u}/u_{ref} = 1.10$ lift the downstream turbine's power to these levels.

Similar trends are observed for the downstream turbine thrust coefficient $C_{P,T2}$ (Figure 4 (b)), where higher thrust forces are measured for the higher turbulence level in Inflow B. Inflow A implicates a higher asymmetry in $C_{T,T2}$ with respect to γ_{T1}. As previously discussed, the downstream turbine yaw moments $M^*_{y,T2}$ are observed to increase with larger upstream turbine yaw angles γ_{T1}. For both inflow cases, the yaw moments' absolute values are seen to be higher for positive γ_{T1} than for negative γ_{T1}. Larger yaw moments are measured for Inflow A than for Inflow B, which possibly stems from stronger mean velocity gradients in the wake flow in Inflow A. The yaw moments $M^*_{y,T2}$ on the downstream turbine located at $x/D = 3$ have approximately the same magnitude as the yaw moments measured on the upstream turbine $M^*_{y,T1}$. Consequently, an intentional upstream turbine yaw misalignment implicates significant yaw moments on the upstream turbine it self as well as an aligned downstream turbine.

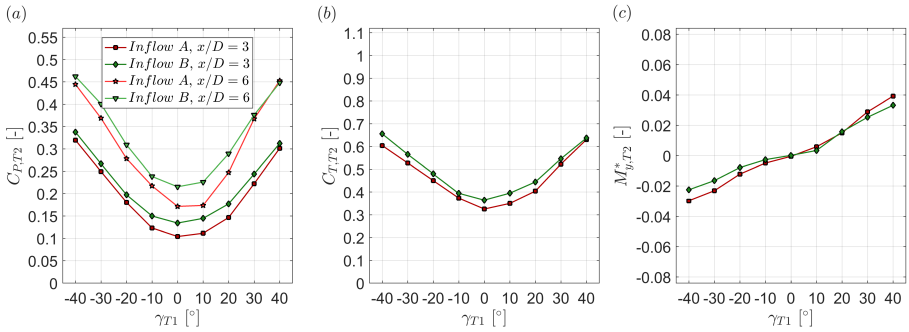

Fig. 4. Downstream turbine **(a)** power coefficient, **(b)** thrust coefficient and **(c)** normalized yaw moment as a function of the upstream turbine's yaw angle γ_{T1}. The downstream turbine T2 is located at $x/D = 3$ and $x/D = 6$ respectively. The turbines are exposed to inflows A and B.

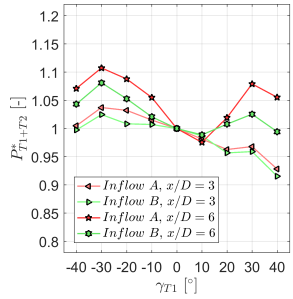

Fig. 5. Combined relative power P^*_{T1+T2} of two turbines for different upstream turbine yaw angles γ_{T1}. The downstream turbine T2 is located at $x/D = 3$ and $x/D = 6$ respectively. The turbines are exposed to inflows A and B.

A main goal of this study is to find out if upstream turbine yawing can positively affect the total power output. As observed in Figure 1 yawing the upstream turbine reduces its power output, while Figure 4 shows that the downstream turbine's power increases simultaneously. In order to quantify if the gain in T2 power can make up for the losses in T1, we define the combined relative power output of the two turbine array

$$P^*_{T1+T2} = \frac{P_{T1}(\gamma_{T1}) + P_{T2}(\gamma_{T1})}{P_{T1,\gamma_{T1}=0} + P_{T2,\gamma_{T1}=0}}. \tag{4}$$

The results for the combined relative power are presented in Figure 5 for both inflow conditions and two turbine separation distances. In all of these four setups an increase in combined power between 3.5% and 11% was measured for upstream turbine yawing. For a both turbine spacings, the maximum combined efficiencies were measured for $\gamma_{T1} = -30°$. The combination of a larger wake deflection and a progressed wake recovery at higher separation distances are seen to shift the optimum of the energy balance between T1 and T2 to higher yaw angles γ_{T1}. Moreover, the combined relative power is seen to be asymmetric with higher values for negative yaw angles γ_{T1}. Both, upstream turbine power $C_{P,T1}$ and

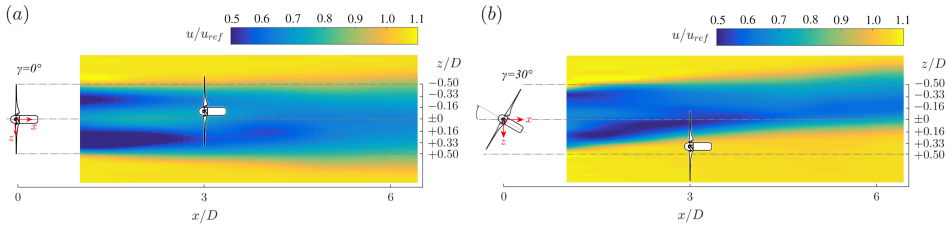

Fig. 6. Topview of two lateral offset positions (**(a)** $\Delta z/D = -0.16$ and **(b)** $\Delta z/D = +0.33$) of the downstream turbine while operated in the wake of an upstream turbine at $x/D = 3$. The upstream turbine is operated at **(a)** $\gamma_{T1} = 0°$ and **(b)** $\gamma_{T1} = 30°$.

downstream turbine power $C_{P,T2}$ have seen not to be perfectly symmetrical, the larger portion can however be subscribed to the power extraction of downstream turbine exposed to asymmetric wake flow fields for positive and negative yaw angles. Furthermore, the relative power gains are observed to be significantly larger for lower inflow turbulence levels (Inflow A). Relative power gains of about 11% were measured for Inflow A, while only 8% were obtained for Inflow B at the same yaw angle of $\gamma_{T1} = -30°$.

3.3 Test case 2: Offset turbines

The power and loads of the downstream turbine T2 are dependent on many different parameters, such as the inflow conditions, the operating point of the upstream turbine T1, its relative streamwise and lateral position with respect to T1 as well as its operating point. In a second test case we therefore investigate the downstream turbine's performance in lateral offset. That means that T2 experiences partial wake situations. The turbine separation distance is in this test case fixed to $x/D = 3$, while different offset positions $\Delta z/D = [-0.50, -0.33, -0.16, \pm 0, +0.16, +0.33, +0.50]$ are investigated. This is done for Inflow B ($TI_B = 10.0\%$) only, while upstream turbine yaw angles of $\gamma_{T1} = 0°$ and $\gamma_{T1} = +30°$ are investigated. In Figure 6 two example positions of the downstream turbine are sketched, illustrating two different wake impingement situations.

Figure 7 shows the downstream turbine's $C_{P,T2}$, $C_{T,T2}$ and $M^*_{y,T2}$ while operated in the wake of the upstream turbine at $\gamma_{T1} = 0°$ in dependency of its tip speed ratio λ_{T2} and lateral offset position $\Delta z/D$. As expected, the power coefficient is seen to increase with increasing lateral offset $\Delta z/D$ as the downstream turbine is partly exposed to a flow of higher kinetic energy. T2's power coefficient is observed not to be entirely symmetric with respect to its lateral position in the wake. Slightly higher power coefficients are measured for negative offset positions. The reason for this is deemed to be a not perfectly axis-symmetric velocity deficit at $x/D = 3$ as indicated in Figure 6 (a) and Bartl et al. (2017) [6]. As observed earlier, T2's optimum operating point shifts to higher tip speed ratios λ_{T2} with increasing kinetic energy being available in the wake.

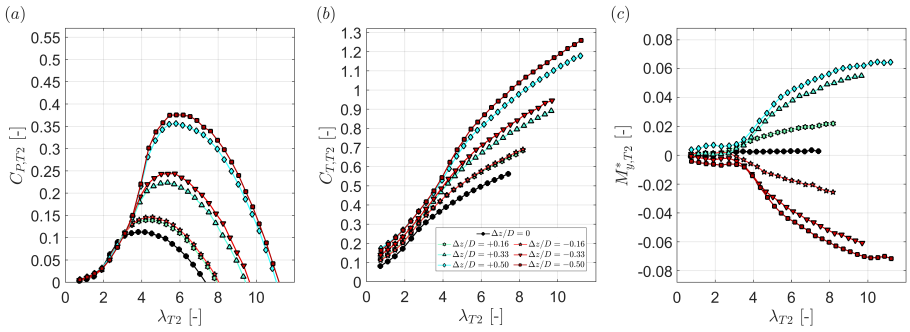

Fig. 7. Downstream turbine **(a)** power coefficient, **(b)** thrust coefficient and **(c)** normalized yaw moment as a function of its tip speed ratio λ_{T2} for different lateral offset positions $\Delta z/D$. The upstream turbine yaw angle is kept constant at $\gamma_{T1} = 0°$. The downstream turbine T2 is located at $x/D = 3$. The turbines are exposed to inflow B.

Similar trends are observed for the downstream turbine thrust coefficient $C_{T,T2}$, which was measured to be slightly higher for negative offset positions. The yaw moments experienced by the downstream turbine are seen to increase for larger lateral offsets as the rotor is impinged by stronger mean velocity gradients. The largest increases are detected for a change from $\Delta z/D = \pm 0$ to ± 0.16 and from ± 0.16 to ± 0.33, while a position change from ± 0.33 to ± 0.50 only causes a small increase in yaw moment. The curves are generally observed to be almost symmetric with respect to the offset position, but also show slightly higher absolute values for negative offset positions.

The effect of a variation in upstream turbine yaw angle from $\gamma_{T1} = 0°$ to $\gamma_{T1} = 30°$ on the downstream turbine's characteristics in different lateral offset positions is presented in Figure 8. For the shown results the downstream turbine T2 is operated at a its optimum λ_{T2}, which differs for each offset position.

The red curves summarize the results for $\gamma_{T1} = 0°$ already shown in Figure 7 for their optimum operating point, while the blue curves represent a setup, in which T1 is operated at $\gamma_{T1} = 30°$ (see Figure 6). For this upstream turbine yaw angle, the wake center is shifted to $\Delta z/D = -0.167$ (Bartl et al., 2017 [6]) and correspondingly the blue curves minima in $C_{P,T2}$ and $C_{T,T2}$ are shifted to $\Delta z/D = -0.16$ (Figure 8 (a) and (b)). The yaw moment $M^*_{y,T2}$ as depicted in Figure 8 (c) is observed to be around zero for this offset position, as the rotor is approximately impinged by a full wake. For an offset position around $\Delta z/D = +0.16$ to $\Delta z/D = +0.33$ the yaw moments reach a maximum level, as roughly half the rotor swept area is impinged by the low velocity region of the wake, while the other have is impinged by the high velocity freestream flow. At a lateral offset of $\Delta z/D = +0.50$ the yaw moments on T2 are observed to decrease again. A large part of the rotor is exposed to the freestream flow; however, the wake is not yet entirely deflected away from T2. For this offset position the power and thrust coefficient are seen to reach very high levels as the rotor is exposed to a large portion of high kinetic energy freestream

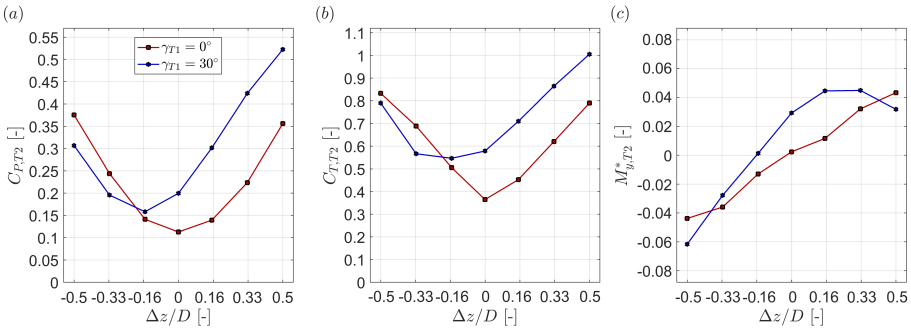

Fig. 8. Downstream turbine **(a)** power coefficient, **(b)** thrust coefficient and **(c)** normalized yaw moment as a function of its lateral offset position $\Delta z/D$. The upstream turbine yaw angle is kept constant at $\gamma_{T1} = 0°$. The downstream turbine T2 is located at $x/D = 3$. The turbines are exposed to inflow B.

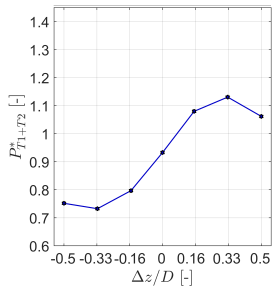

Fig. 9. Combined relative power P^*_{T1+T2} of the two-turbine-array for different lateral offset positions $\Delta z/D$. The combined power is calculated for a change of upstream turbine yaw angle from $\gamma_{T1} = 0°$ to $+30°$ for each position. The downstream turbine T2 is located at $x/D = 3$. The turbines are exposed to inflow B.

flow. A power coefficient of $C_{P,T2} > 0.50$ can be explained by increased freestream velocity levels of $\overline{u}/u_{ref} = 1.10$ (Bartl et al, (2017) caused by wind tunnel blockage. The power and thrust coefficient still are referred to u_{ref} measured $x/D = -2$ upstream of T1.

The combined relative power output of the two-turbine array is in this case calculated for a change of upstream turbine yaw angle from $\gamma_{T1} = 0°$ to $+30°$. It has to be kept in mind, that the upstream turbine power is constant, independent of the downstream turbine position. The combined power for each offset position is calculated as

$$P^*_{T1+T2} = \frac{P_{T1,\gamma_{T1}=30} + P_{T2,\gamma_{T1}=30}(z/D)}{P_{T1,\gamma_{T1}=0} + P_{T2,\gamma_{T1}=0}(z/D)}. \tag{5}$$

Figure 9 shows the resultant combined relative power output. For an offset position of $\Delta z/D = +0.33$ a maximum combined power increase of 13% is measured, as a major part is deflected away from the downstream rotor. Surprisingly, the relative power gains measured for an offset $\Delta z/D = +0.50$ are measured to be smaller, amounting about

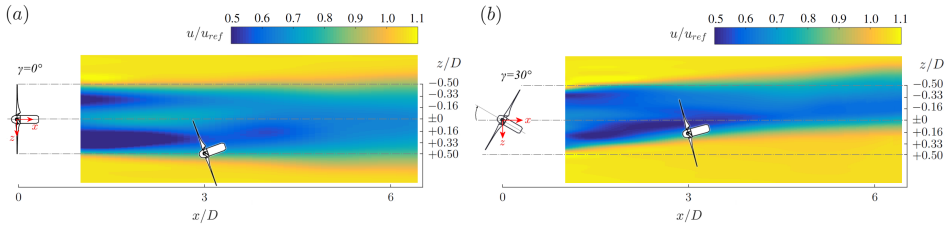

Fig. 10. (a) Topview of the downstream turbine T2 operated at a lateral offset position $\Delta z/D = +0.50$ and a yaw angle of $\gamma_{T2} = -20°$ in the wake of an upstream turbine T1 operated at $\gamma_{T1} = 0°$. **(b)** Topview of the downstream turbine T2 operated at a lateral offset position ($\Delta z/D = +0.16$) and a yaw angle of $\gamma_{T2} = -15°$ in the wake of an upstream turbine T1 operated at $\gamma_{T1} = 30°$.

6%. This can be explained by significantly larger $C_{P,T2}$-values in the non-yawed case for $\Delta z/D = +0.50$ than for $\Delta z/D = +0.33$, allowing smaller relative gains. For zero lateral offset, about 5% in combined power are lost when yawing T1 to $\gamma_{T1} = +30°$ as previously observed in Figure 5. In the case of the downstream turbine being located at negative offset positions $\Delta z/D$, the wake is deflected directly on T2's rotor, significantly reducing its power output and consequently also the combined power.

In conclusion, is has been demonstrated that intentional upstream turbine yaw control is favorable in lateral offset situations when considering both, the power output and yaw moments on a downstream turbine. Depending on the downstream turbine's streamwise and lateral position, the wake can be partly or even fully deflected away from its rotor swept area.

3.4 Test case 3: Downstream turbine yawing

The third and final test case investigates whether a variation in downstream turbine yaw angle γ_{T2} contributes to a yaw-load mitigation and power optimization. As previously seen, both partial wake impingement and turbine yaw misalignment are possible sources for increased yaw moments. An intentional yaw misalignment opposed to the partial wake impingement is therefore considered to cancel out yaw loading on the turbine. For this purpose, the downstream turbine yaw angle is systematically varied from γ_{T2}=$[-30°, ..., +30°]$ in steps of 5° for all seven lateral offset positions and upstream turbine yaw angles γ_{T1}=$[0°, +30°]$. A sketch of two downstream turbine yaw angles at two offset positions is presented in Figure 10.

The resulting $C_{P,T2}$, $C_{T,T2}$ and $M^*_{y,T2}$ of the downstream turbine in dependency of its yaw angle γ_{T2} and lateral offset position $\Delta z/D$ for a constant upstream turbine yaw angle of $\gamma_{T1} = 0°$ are shown in Figure 11. The points for $\gamma_{T2} = 0°$ correspond to the previously shown red lines in Figure 8. In case the downstream turbine rotor is fully impinged by the upstream turbine's wake, i.e. $\Delta z/D = 0$, a variation of its yaw angle γ_{T2} reduces its power output and increases uneven yaw moments. During a lateral offset however, the

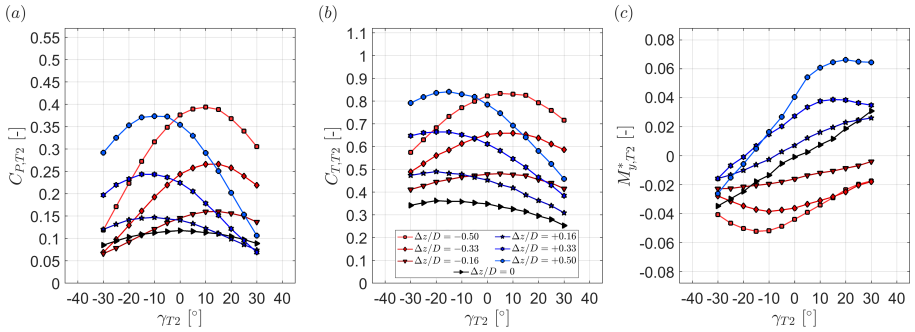

Fig. 11. Downstream turbine **(a)** power coefficient, **(b)** thrust coefficient and **(c)** normalized yaw moment as a function of its yaw angle γ_{T2} for different lateral offset positions $\Delta z/D$. The upstream turbine yaw angle is kept constant at $\gamma_{T1} = 0°$. The downstream turbine T2 is located at $x/D = 3$. The turbines are exposed to inflow B.

maximum power output and minimum yaw moments are found for yaw angles $\gamma_{T2} \neq 0°$. At a lateral offset position of $\Delta z/D = +0.16$, for instance, the maximum $C_{P,T2}$ is assessed for $\gamma_{T2} = -10°$. Simultaneously, the yaw moment is measured to be around zero at this yaw angle. The downstream turbine is exposed to a strong shear flow in the partial wake situation, mitigating yaw moments by actively yawing opposed to that shear. The simultaneous power increase for the oppositely yawed downstream rotor is a positive side effect, although the exact reasons for the power increase are not entirely clear at this stage. Higher power outputs and decreased yaw moments are also measured for moderate yaw angles around $\gamma_{T2} = -10°$ at larger lateral offsets of $\Delta z/D = +0.33$ and $\Delta z/D = +0.50$. The slope of the power curves in Figure 11 (a) and yaw moment curves in Figure 11 (c) are observed to be even steeper for larger lateral offsets. The power gains when yawing the turbine from $\gamma_{T2} = 0°$ to $\gamma_{T2} = -10°$ are larger for higher lateral offsets. At the same time, the relative yaw moment reduction is larger, implying that opposed downstream yawing is deemed to be even more effective for higher lateral offsets.
For negative lateral offset positions, obviously the opposite trends are observed, i.e. maximum power and smallest absolute yaw moments are measured for positive downstream turbine yaw angles γ_{T2}. The power output and yaw moment distribution is however not completely symmetrical with respect to yaw angle γ_{T2} and offset position $\Delta z/D$.

The concept of downstream turbine yawing in partial wake impingement situations is moreover investigated for an upstream turbine yaw angle of $\gamma_{T1} = +30°$. The wake flow features a significantly higher asymmetry in this case. The results for $C_{P,T2}$, $C_{T,T2}$ and $M^*_{y,T2}$ are shown in Figure 12. As previously observed, an offset of $\Delta z/D = -0.16$ approximately corresponds to an impingement of the full wake. Thus, the power coefficient has an almost symmetric distribution with respect to downstream turbine yaw angle γ_{T2}. The yaw moments are observed to be rather low for this offset position and around zero

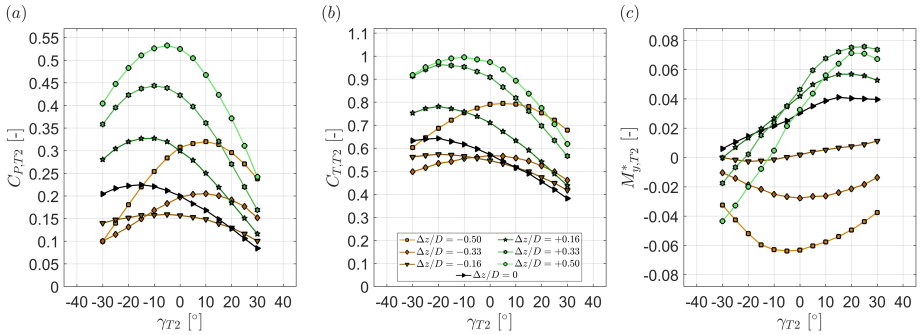

Fig. 12. Downstream turbine **(a)** power coefficient, **(b)** thrust coefficient and **(c)** normalized yaw moment as a function of its yaw angle γ_{T2} for different lateral offset position $\Delta z/D$. The upstream turbine yaw angle is kept constant at $\gamma_{T1} = 30°$. The downstream turbine T2 is located at $x/D = 3$. The turbines are exposed to inflow B.

for $\gamma_{T2} = 0$. For partial wake impingement situations at $\Delta z/D \geq 0$, negative downstream turbine yaw angles are again seen to reduce the yaw moments acting on the rotor. The gradients in yaw moment reduction per degree of yaw angle are observed to be steeper for larger lateral offsets. The maximum power coefficients are again measured for moderate downstream turbine yaw angles around $\gamma_{T2} \pm 10°$.

Power gains by downstream turbine yawing are assessed by a relative combined power of the two-turbine array

$$P^*_{T1+T2} = \frac{P_{T1} + P_{T2}(\gamma_{T2}, z/D)}{P_{T1,\gamma_{T1}=0,z/D=0} + P_{T2,\gamma_{T1}=0,\gamma_{T2}=0,z/D=0}}. \tag{6}$$

As a reference the power measured for the non-yawed upstream turbine, a non-yawed downstream turbine in an aligned setup ($\Delta z/D = 0$) is used. The results are shown in Figure 13. For an upstream turbine yaw angle of $\gamma_{T1} = 0°$ (Figure 13 (a)) combined power gains of approximately 3% are measured for a moderate downstream turbine yaw angles ($\gamma_{T2} \pm 10 - \pm 15°$). The combined power characteristics are observed to be quite symmetrical with respect to downstream turbine offset and its yaw angle. Slightly higher relative power gains are obtained for the case of an upstream turbine yaw angle of $\gamma_{T1} = +30°$ (Figure 13 (b)). A maximum power gain of about 5% is measured for offset positions $\Delta z/D = 0$ and +0.16 and a downstream turbine yaw angle between $\gamma_{T1} = -10°$ and $-15°$.

In conclusion, this third test case demonstrates that moderate downstream turbine yawing can be an effective method to mitigate yaw moments acting on the rotor in partial wake situations, while simultaneously obtaining slight power gains.

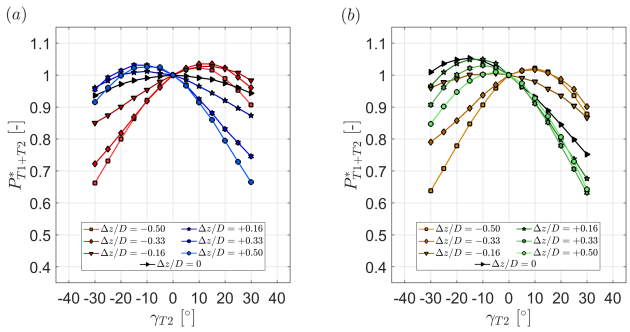

Fig. 13. Combined relative power P^*_{T1+T2} of two turbines as a function of the downstream turbine yaw angle γ_{T2} for different lateral offset positions $\Delta z/D$. The upstream turbine yaw angle is kept constant at **(a)** $\gamma_{T1} = 0°$ and **(b)** $\gamma_{T1} = 30°$ respectively. The downstream turbine T2 is located at $x/D = 3$. The turbines are exposed to inflow B.

4 Discussion

When assessing the operational characteristics of the upstream turbine in dependency of its yaw angle, some asymmetries were apparent. While the power and thrust curves only showed slight deviations for positive and the corresponding negative yaw angle, higher asymmetries were found for the yaw moment. Although it is not entirely clear where these stem from, the only reasonable source for an asymmetric load distribution in an uniform inflow is the rotor's interaction with the turbine tower. In the course of a revolution, the blades of a yawed turbine experience unsteady flow conditions, i.e. fluctuations in angle of attack and relative velocity. When superimposing an additional low-velocity zone, tower shadow or shear for example, the yaw-symmetry is disturbed. Asymmetric load distributions for turbines exposed to sheared inflow were recently reported by Damiani et al. (2017) [9]. They showed that vertical wind shear causes asymmetric distributions of angle of attack and relative flow velocity in the course of a blade revolution. They link these to rotor loads and conclude further consequences on wake characteristics and wind farm control strategies.

Moreover, our study emphasized even stronger asymmetries in loads and power on an aligned downstream turbine. The combined power output of a two turbine setup consequently also featured an asymmetric distribution, which has been previously observed in an computational study Gebraad et al. (2016) [13] and a similar experimental setup by Schottler et al. (2016) [22]. In a recent follow-up study, Schottler et al. (2017a) [24] attributed the asymmetry to a strong shear in the inflow to the two-turbine setup. As the inflow in the present study was measured to be spatially uniform, inflow shear is not a reason for the observed asymmetries. The major contributor to an asymmetric combined power distribution was seen to be the downstream turbine power. The yaw angle dependency of downstream turbine power is in direct relation to an asymmetric wake deflection

observed on the same setup by in Bartl et al. (2017) [6]. Therein, the wake deflection is slightly larger for negative yaw angles than for the corresponding positive yaw angles, a trend which is seen to directly affect the downstream turbine power, thrust and yaw moment distribution.

The present results further demonstrate a significant influence of the inflow turbulence level on the effectiveness of wake steering by yaw. The relative power gains were observed to be significantly larger for lower inflow turbulence levels (11% versus 8%). The reason might to a small degree be differences in wake deflection Bartl et al. (2017) [6], but can mostly be subscribed to lower average kinetic energy levels in wakes for turbines exposed to low inflow turbulence. When deflecting a kinetic energy sink away from the downstream rotor, the relative gains in combined power are higher. Alongside with combined power increases, the results demonstrated a linear increase in the upstream turbine's yaw moments with its yaw angle. For wake steering behind an upstream turbine, partial wake impingement situations arise for an aligned downstream turbine, resulting in increased yaw moments also on the downstream turbine.

In a real wind farm exposed to varying wind directions, however, partial wake situations, in which the downstream turbine is laterally offset are just as important as the aligned case. For a lateral offset of half a rotor diameter, for instance, it is demonstrated, that upstream turbine yaw control is able to steer most of the wake flow away from an offset downstream turbine. Consequently, both the combined power increases and yaw moments on the downstream turbine are significantly mitigated. This finding experimentally confirms results of a similar test case recently computed with a model-framework by van Dijk et al. (2017) [26]. For an offset of $\Delta z/D = +0.33$, we measured a maximum power increase of about 13% for when yawing the upstream turbine from $\gamma_{T1} = 0°$ to $+30°$. Although not directly comparable, this result is estimated to be at the same order of magnitude as power gains experimentally obtained by Campagnolo et al. (2016) [8], who measured a combined power increase of 21% for a setup of three model turbines with an lateral offset of $\Delta z/D = +0.45$. Furthermore, our results indicated a not perfectly symmetrical distribution of the downstream turbine power and thrust coefficients with respect to its positive or negative offset position, as slightly higher power coefficients were obtained for negative offset positions. The reason for this is deemed to be an asymmetric velocity deficit in the non-yawed wake as indicated in Pierella and Sætran (2017) [20] and Bartl et al. (2017) [6].

In a final test case, we introduced the concept of downstream turbine yawing in partial wake overlap situations for the purpose of load mitigation. The concept suggests that yawing a downstream turbine opposed to a strong horizontally sheared flow is able to mitigate rotor's yaw moments while simultaneously increasing the rotor's power output. The horizontally sheared flow is in this case the transition zone between the low- velocity wake flow to the high-velocity freestream flow. A mitigation of yaw moments by yawing the rotor op-

posed to the shear is intuitively imaginable, while the simultaneous power increase might be surprising. Similar effects have, however, been reported in full-scale data evaluation by McKay et al. (2013) [19], who found an offset in the downstream turbine's yaw alignment for the purpose of optimized power output when operated in a partial wake of an upstream turbine. The downstream turbine yaw angle was observed to adjust itself opposed to the velocity gradient in the partial wake impinging the downstream rotor. These findings are in total agreement with the optimal downstream turbine yaw angle measured in our wind tunnel experiment. The potential of load reductions of a single turbine by yawing has been previously discussed by Kragh and Hansen (2014) [18], in situations where the rotor was exposed to vertically sheared inflows. In the present test case, however, the partial wake impingement on the rotor represents a situation of a strongly horizontally sheared flow. Whether the shear in the incoming wind field is horizontal or vertical obviously makes a big difference, but mitigation of loads and maximization of power might be possible with yaw adjustments in both cases.

The power output and yaw moment distribution was however not completely symmetrical with respect to yaw angle γ_{T2} and offset position $\Delta z/D$. Besides the slightly asymmetric streamwise wake flow, also the interaction of the downstream turbine with respect to the wake rotation of the upstream turbine might cause this asymmetry. A characterization of the wake rotation and asymmetric freestream flow entrainment in the wake behind the same rotor is given by Pierella and Sætran (2017) [20]. As a yawed operation of a downstream rotor in a partial wake of an upstream turbine is highly complex, a combination of a number of different factors are assumed to influence wake-rotor interaction, making a clear conclusion difficult at this stage.

5 Conclusions

A wind tunnel experiment studying the effects of intentional yaw misalignment on the power production and yaw moments of a downstream turbine was presented. Both, full wake impingement and partial wake overlap situations were investigated. For partial wake overlap the concept of downstream turbine yawing for yaw moment mitigation was investigated for different lateral offset positions.

It is demonstrated that upstream turbine yaw misalignment is able to increase the combined power production of the two turbines for both partial and full wake overlap setups. For aligned turbines the combined array power was increased up to 11% for a separation distance of $x/D = 6$ and low inflow turbulence levels ($TI_A = 0.23\%$). At a higher inflow turbulence of $TI_B = 10.0\%$, however, the relative power increase was assessed to be only 8%. For smaller turbine separation distances, combined power gains were assessed to be even smaller. The distribution of combined power gains in dependency of the upstream

turbine yaw angle was observed to be rather asymmetrical. The formation of not entirely symmetric velocity deficit shapes in the wake was deemed to be the main reason for that finding.

The obtained power gains were assessed to be at the cost of increased yaw moments on the upstream rotor. The yaw moments on the upstream rotor are observed to increase roughly linearly with increasing yaw angle, but are not entirely symmetrical distributed. Upstream turbine yaw control is moreover seen to directly influence the yaw moments on a downstream rotor. For aligned turbine positions, the downstream turbine yaw moments are observed to increase to similar magnitudes as for the upstream turbine. These results highlight the importance of also taking loads into account when optimizing layout and control of a wind farm.

Further, we demonstrate advantages of upstream turbine yaw control for load reduction and power increases on an offset downstream turbine. For situations, in which the downstream turbine is impinged by a partial wake, upstream turbine yaw control can redirect the wake either on or away from the downstream rotor. In case the wake is directed onto the downstream turbine's rotor swept area, its yaw moments and power production reduce. If the lateral offset between the turbines is large enough, the wake can be deflected entirely away from the downstream turbine, maximizing its power and canceling out yaw moments.

Moreover, a final test case proved the concept of yaw control for yaw moment mitigation on a downstream turbine operated in a partial wake overlap situation. While yaw moments are observed to decrease when yawing the rotor opposed to the shear layer in the incoming wake flow, also the turbine's power output is seen to increase. These results illustrate the importance for combined power and load optimization on all turbines in a wind farm.

References

1. Adaramola, M. and Krogstad, P.-Å., K.: Experimental investigation of wake effects on wind turbine performance, Renewable Energy, 36, 2078–2086, doi:10.1016/j.renene.2011.01.024, 2011.

2. Andersen, S., Sørensen, J., and Mikkelsen, R.: Performance and Equivalent Loads of Wind Turbines in Large Wind Farms, Journal of Physics: Conference Series, 854, 012 001, doi:10.1088/1742-6596/854/1/012001, 2017.

3. Annoni, J., Gebraad, P., Scholbrock, A., Fleming, P., and van Wingerden, J.: Analysis of axial-induction-based wind plant control using an engineering and a high-order wind plant model, Wind Energy, 19, 1135–1150, doi:10.1002/we.1891, 2016.

4. Bartl, J. and Sætran, L.: Experimental testing of axial induction based control strategies for wake control and wind farm optimization, Journal of Physics: Conference Series, 753, 032 035, doi:10.1088/1742-6596/753/3/032035, 2016.

5. Bartl, J. and Sætran, L.: Blind test comparison of the performance and wake flow between two in-line wind turbines exposed to different turbulent inflow conditions, Wind Energy Science, 2, 55–76, doi:10.5194/wes-2-55-2017, 2017.

6. Bartl, J., Mühle, F., Schottler, J., Hölling, M., Peinke, J., Adaramola, M., and Sætran, L.: Wind tunnel experiments on wind turbine wakes in yaw: Influence of inflow turbulence and shear, In review in Wind Energy Sci. Discuss., doi:10.5194/wes-2017-59, 2018.

7. Bastankhah, M. and Porté-Agel, F.: Experimental and theoretical study of wind turbine wakes in yawed conditions, Journal of Fluid Mechanics, 806, 506–541, doi:10.1017/jfm.2016.595, 2016.

8. Campagnolo, F., Petrović, V., Bottasso, C., and Croce, A.: Wind Tunnel Testing of Wake Control Strategies, American Control Conference, doi:10.1109/ACC.2016.7524965, 2016.

9. Damiani, R., Dana, S., Annoni, J., Fleming, P., Roadman, J., van Dam, J., and Dykes, K.: Assessment of Wind Turbine Component Loads Under Yaw-Offset Conditions, Wind Energy Science Discussions, doi:10.5194/wes-2017-38, 2017.

10. Fleming, P., Gebraad, P., Lee, S., van Wingerden, J.-W., Johnson, K., Churchfield, M., Michalakes, J., Spalart, P., and Moriarty, P.: Evaluating techniques for redirecting turbine wakes using SOWFA, Renewable Energy, 70, 211–218, doi:10.1016/j.renene.2014.02.015, 2014.

11. Fleming, P., Gebraad, P. M., Lee, S., van Wingerden, J.-W., Johnson, K., Churchfield, M., Michalakes, J., Spalart, P., and Moriarty, P.: Simulation comparison of wake mitigation control strategies for a two-turbine case, Wind Energy, 18, 2135–2143, doi:10.1002/we.1810, 2015.

12. Gebraad, P. M. O., Fleming, P. A., and Wingerden, J. W. v.: Comparison of Actuation Methods for Wake Control in Wind Plants, American Control Conference, doi:10.1109/ACC.2015.7170977, 2015.

13. Gebraad, P. M. O., Teeuwisse, F. W., van Wingerden, J. W., Fleming, P. A., Ruben, S. D., Marden, J. R., and Pao, L. Y.: Wind plant power optimization through yaw control using a parametric model for wake effects-a CFD simulation study, Wind Energy, 19, 95–114, doi:10.1002/we.1822, 2016.

14. Howland, M., Bossuyt, J., Martinez-Tossas, L., Meyers, J., and Meneveau, C.: Wake Structure of Wind Turbines in Yaw under Uniform Inflow Conditions, Journal of Renewable and Sustainable Energy, 8, 043 301, doi:10.1063/1.4955091, 2016.

15. Jiménez, Á., Crespo, A., and Migoya, E.: Application of a LES technique to characterize the wake deflection of a wind turbine in yaw, Wind Energy, 13, 559–572, doi:10.1002/we.380, 2010.

16. Kim, S.-H., Shin, H.-K., Joo, Y.-C. and Kim, K.-H.: A study of the wake effects on the wind characteristics and fatigue loads for the turbines in a wind farm, Renewable Energy, 74, 536–543, doi: 10.1016/j.renene.2014.08.054, 2015.

17. Knudsen, T., Bak, T., and Svenstrup, M.: Survey of wind farm controlpower and fatigue optimization, Wind Energy, 18, 1333–1351, doi:10.1002/we.1760, 2014.

18. Kragh, K. A. and Hansen, M. H.: Load alleviation of wind turbines by yaw misalignment, Wind Energy, 17, 971–982, doi:10.1002/we.1612, 2014.

19. McKay, P., Carriveau, R., and Ting, D. S-K.: Wake impacts on downstream wind turbine performance and yaw alignment, Wind Energy, 16, 221–234, doi:10.1002/we.554, 2013.

20. Pierella, F. and Sætran, L.: Wind tunnel investigation on the effect of the turbine tower on wind turbines wake symmetry, Wind Energy, 20, 1753–1769, doi:10.1002/we.2120, 2017.

21. Schepers, J. G., K. Boorsma, K., and Munduate, X.: Final Results from Mexnext-I: Analysis of detailed aerodynamic measurements on a 4.5 m diameter rotor placed in the large German Dutch Wind Tunnel DNW, Journal of Physics: Conference Series, 555, 012 089, doi:10.1088/1742-6596/555/1/012089, 2014.

22. Schottler, J., Hölling, A., Peinke, J., and Hölling, M.: Wind tunnel tests on controllable model wind turbines in yaw, AIAA 34th Wind Energy Symposium, 2016-1523, doi:10.2514/6.2016-1523, 2016.

23. Schottler, J., Bartl, J., Mühle, F., Sætran, L., Peinke, J., and Hölling, M.: Experiments on wind turbine wakes in yaw: Redefining the wake width, Submitted to Wind Energy Science, 2017.

24. Schottler, J., Hölling, A., Peinke, J., and Hölling, M.: Brief communication: On the influence of vertical wind shear on the combined power output of two model wind turbines in yaw, Wind Energy Science, 2, 439–442, doi:10.5194/wes-2-439-2017, 2017a.

25. Schreiber, J., Cacciola, S., Campagnolo, F., Petrovic, V., Mourembles, D., and Bottasso, C. L.: Wind shear estimation and wake detection by rotor loads - First wind tunnel verification, Journal of Physics: Conference Series, 753, 032 027, doi:10.1088/1742-6596/753/3/032027, 2016.

26. van Dijk, M., van Wingerden, J.-W., Ashuri, T., and Li, Y.: Wind farm multi-objective wake redirection for optimizing power production and loads, Energy, 121, 561–569, doi:10.1016/j.energy.2017.01.051:, 2017.

27. Vollmer, L., Steinfeld, G., Heinemann, D., and Kühn, M.: Estimating the wake deflection downstream of a wind turbine in different atmospheric stabilities: an LES study, Wind Energy Science, 1, 129–141, doi:10.5194/wes-1-129-2016, 2016.

28. Wheeler, A. J. and Ganji, A. R.: Introduction to engineering experimentation, Upper Saddle River, NJ, USA, Pearson/Prentice Hall, XI, third edition edn., 2004.

PAPER 5

Blind test comparison of the performance and wake flow between two in-line wind turbines exposed to different turbulent inflow conditions

Jan Bartl, Lars Sætran

Original version published by Copernicus Publications in
Wind Energy Science, vol. 2, pp. 55-76.
doi: 10.5194/wes-2-55-2017

PAPER 5

Blind test comparison of the performance and wake flow between two in-line wind turbines exposed to different turbulent inflow conditions

Jan Bartl, Lars Sætran

Department of Energy and Process Engineering, Norwegian University of Science and Technology, Trondheim, 7491, Norway

Published in Wind Energy Science, vol. 2, pp. 55-76.

Received on 23 August 2016, public discussion started on 5 September 2016, revised version received on 3 December 2016, accepted for publication on 16 January 2017, published on 9 February 2017

Original version published by Copernicus. Peer-reviewed under the responsibility of EAWE.
Edited by: J. Peinke Reviewed by: three anonymous referees

Summary. This is a summary of the results of the fourth blind test workshop that was held in Trondheim in October 2015. Herein, computational predictions on the performance of two in-line model wind turbines as well as the mean and turbulent wake flow are compared to experimental data measured at the wind tunnel of the Norwegian University of Science and Technology (NTNU). A detailed description of the model geometry, the wind tunnel boundary conditions and the test case specifications was published before the workshop. Expert groups within computational fluid dynamics (CFD) were invited to submit predictions on wind turbine performance and wake flow

without knowing the experimental results at the outset. The focus of this blind test comparison is to examine the model turbines' performance and wake development with nine rotor diameters downstream at three different turbulent inflow conditions. Aside from a spatially uniform inflow field of very low-turbulence intensity (TI = 0.23 %) and high-turbulence intensity (TI = 10.0 %), the turbines are exposed to a grid-generated highly turbulent shear flow (TI = 10.1 %).
Five different research groups contributed their predictions using a variety of simulation models, ranging from fully resolved Reynolds-averaged Navier–Stokes (RANS) models to large eddy simulations (LESs). For the three inlet conditions, the power and the thrust force of the upstream turbine is predicted fairly well by most models, while the predictions of the downstream turbine's performance show a significantly higher scatter. Comparing the mean velocity profiles in the wake, most models approximate the mean velocity deficit level sufficiently well. However, larger variations between the models for higher downstream positions are observed. Prediction of the turbulence kinetic energy in the wake is observed to be very challenging. Both the LES model and the ID-DES (improved delayed detached eddy simulation) model, however, consistently manage to provide fairly accurate predictions of the wake turbulence.

1 Introduction

Given the constraints of transmission and installation costs, the available area for offshore wind farm installations is fairly limited. Under these circumstances wake interactions play an important role when evaluating the energy production since the energy captured by an upstream wind turbine leaves significantly less energy in the wake for the downstream turbine. For certain wind directions these power losses are estimated to be up to 10–20 % for large offshore wind farms (Barthelmie et al., 2009) [4]. Furthermore, the rotor-generated turbulence in the wake is a source of augmented material fatigue on the downstream rotor.

In order to be able to come up with holistic control approaches for optimizing a wind farm, well-performing prediction tools for the wake flow behind a wind turbine rotor for all kinds of atmospheric conditions are needed. Therefore, the development of simple wake models already began in the early 1980s. Analytical wake models by Jensen (1983) [16], Ainslie (1988) [2], Crespo et al. (1988) [**?**], Frandsen et al. (2006) [13] and Larsen et al. (2008) [21] are based on a number of simplifications and are calibrated with empirical parameters. Most of the state-of-the-art software used for industrial wind farm planning is still based on these engineering wake models. However, they are not able to reconstruct the wake characteristics in a sufficient degree of detail (Sanderse et al., 2011) [31].

With an increase in computational power, advanced computational fluid dynamics (CFD) models based on more fundamental physics arose. These CFD models are computationally more expensive but are able to resolve the flow structures in much larger detail. In general, two types of CFD approaches are state of the art in wake modeling: Reynolds-averaged Navier–Stokes (RANS) equations that average the turbulent fluctuations and the computationally more expensive large eddy simulations (LESs), which solve for large

eddies only. Hybrid models like detached eddy simulations (DESs) combine the advantages of calculating unsteady flow effects from LES as well as resolving small scales in the boundary layers like RANS does. Another challenge is the modeling of the interaction of the wind turbine rotor with the flow: the rotor geometry can either be fully resolved or simplified as a two-dimensional force field. The latter option is usually more efficient with respect to computational time. In RANS models it is possible to fully resolve the rotor geometry and thus model complex three-dimensional flow. In LES models, however, a full resolution of the rotor geometry is difficult because the smaller scales that determine the forces at the interaction surface are not resolved. Thus, the rotor is often modeled as a two-dimensional force field, which requires detailed knowledge of the lift and drag forces that act under certain inflow conditions.

Even though the wake behind full-scale wind turbines was recently measured (Kocer et al., 2011 [17]; Kumer et al., 2015 [18]; Trujillo et al., 2016 [40]), the unsteady inflow conditions in full-scale experiments make it very difficult to use those data to verify wake prediction models. Therefore, wind tunnel experiments on model turbines under controlled boundary conditions are an appropriate method for verifying simulation tools.

Despite the drawbacks of low Reynolds numbers and possible wall blockage effects in model experiments, a number of well-defined comparison tests have been conducted. One of the first model-scale experiments was the investigation by Talmon (1985) [39]. The wake was measured on a small rotor with a diameter of $D = 0.36\,\mathrm{m}$ in order to serve as a reference experiment for calculations. In addition to uniform inflow, the wake development was studied in a simulated atmospheric boundary layer. Another seminal investigation was conducted by Medici and Alfredsson (2006) [24]. With three-dimensional wake flow measurements on a $D = 0.18\,\mathrm{m}$ model turbine down to $x/D = 9$, they shed light on phenomena like wake rotation, wake deflection in yawed operation and bluff body vortex shedding frequencies from the rotor.

At the Norwegian University of Science and Technology (NTNU) two model turbines of the rotor diameter $D = 0.90\,\mathrm{m}$ were extensively investigated. Adaramola and Krogstad (2011) [1] analyzed the effect of modifying tip speed ratio, blade pitch angle and yaw angle on a downstream turbine. Eriksen (2016) [12] investigated the three-dimensional rotor-generated turbulence in the wake of one model turbine in detail. Bartl et al. (2012) [6] examined the wake behind two model turbines, while special attention to asymmetries and wake rotation was given by Schümann et al. (2013) [36]. A recent study by Bartl and Sætran (2016) [5] investigated the interrelation of wake flow and the performance of a downstream turbine for axial-induction-based wind farm control methods.

The largest rotor investigated for wake comparison studies was the MEXICO rotor, with a diameter of 4.5 m (Schepers et al., 2010) [34], in which the rotor performance as well as the wake flow were examined in detail. A second campaign investigating even more

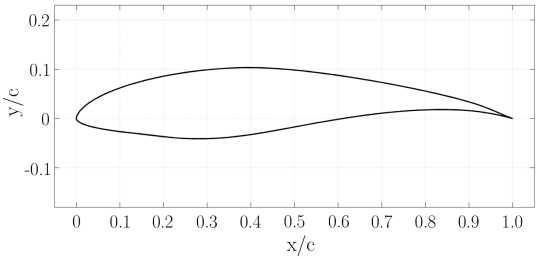

Fig. 1. NREL S826 airfoil geometry.

effects, including span-wise pressure distributions, yaw misalignment and unsteady effects, was realized at a large German–Dutch Wind Tunnel (DNW). A benchmark comparison of the comprehensive set of measurement data with numerical calculations is found in Schepers et al. (2014) [35].

In 2011 the first blind test workshop on turbine performance and wake development behind one model turbine was organized. The geometry of the model turbine and wind tunnel environment was made available to the public, and dedicated research groups were invited to predict the model turbine's performance and the wake development up to $x/D = 5.0$ rotor diameters downstream. A total of 11 sets of predictions were submitted and reported by Krogstad and Eriksen (2013) [19]. This first blind test experiment showed a significant scatter in the performance predictions, with a variation of several magnitudes in predictions of turbulent quantities in the wake between the different contributions. Therefore, it was decided to perform another blind test workshop in 2012, increasing the test complexity by adding a second turbine aligned with the upstream turbine. The participants were asked to predict the performance of both turbines as well as the wake behind the downstream turbine. Nine different submissions were received, showing clear variations in the quality of the predictions between the different modeling methods (Pierella et al., 2014) [27]. For a third blind test workshop held in 2013, the complexity was increased slightly again. The two model wind turbines were positioned with a span-wise offset of half a rotor diameter. The results reported by Krogstad et al. (2015) [20] showed that a LES simulation method proved to simulate this complex flow case fairly well. For the present fourth blind test workshop held in Trondheim in October 2015, the focus was directed on the effect of different turbulent inflow conditions on the performance of an aligned two-turbine setup. Test cases of low turbulent uniform inflow, highly turbulent inflow as well as nonuniform highly turbulent shear are investigated. The wake flow behind the upstream turbine is analyzed, which defines the inflow conditions to the downstream turbine. Five different groups contributed CFD simulations ranging from RANS to LES to DES computations. Although a general improvement in the results is observed over the years, this report shows the strengths and drawbacks of the different modeling methods

and underlines the persistent importance of validation of CFD codes with well-defined experimental datasets.

2 Methods

2.1 Test case description

Wind tunnel

The experimental data of this study are measured in the closed-loop wind tunnel at NTNU in Trondheim. The rectangular test section of the wind tunnel is 2.71 m broad, 1.81 m high and 11.15 m long. The wind tunnel roof is adjusted for a zero pressure gradient, generating a constant velocity in the entire test section. The wind tunnel inlet speed is controlled by an inlet contraction, which is equipped with static pressure holes at the circumferences at two defined cross sections. The wind tunnel is driven by a 220 kW fan located downstream of the test section, able to generate maximum wind speeds of up to $U_{max} = 30\,\mathrm{m\,s^{-1}}$.

Model turbines, rotor and airfoil characteristics

The model wind turbines have a three-bladed rotor with diameters of $D_{T1} = 0.944\,\mathrm{m}$ and $D_{T2} = 0.894\,\mathrm{m}$. The small difference in rotor diameter stems from a slightly different hub geometry of the rigs. Apart from that the blade geometry is exactly the same. Both turbines rotate counter-clockwise when observed from an upstream point of view. The rotors are both driven by a 0.37 kW AC Siemens electric motor and controlled by a Siemens Micromaster 440 frequency inverter. The motor rotational speed can be varied from about 100 to 3000 rpm, while the generated power is burned off by an external load resistance.

The turbine blades were designed using the NREL S826 airfoil from the root to the tip. The airfoil, as shown in Fig. 1, was designed at the National Renewable Energy Laboratory (NREL) and a detailed description of the airfoil's characteristics is given by Somers (2005) [**?**]. Herein, the geometry is specified and the performance characteristics are estimated. Lift and drag coefficients are presented for a range of operating Reynolds numbers ($Re_{C,tip,FS} = 10^6$) for a full-scale turbine, which are 1 order of magnitude higher than the Reynolds numbers prevailing in this model experiment ($Re_{C,tip,model} = 10^5$). In order to be able to also characterize the airfoil's performance at model-scale Reynolds numbers, a number of two-dimensional experiments on airfoil performance have been conducted. Sarmast and Mikkelsen (2013) [32] performed an experiment on a two-dimensional S826 wing section of the chord length $c_L = 0.10\,\mathrm{m}$ at DTU in Denmark. They observed hysteretic behavior for $Re_C < 10^5$, which is assumed to be the cause for Reynolds-dependent behavior of the inner blade elements of the upstream turbine under design conditions. Another experimental set of S826 airfoil data was presented by Ostovan et al. (2013) [26]

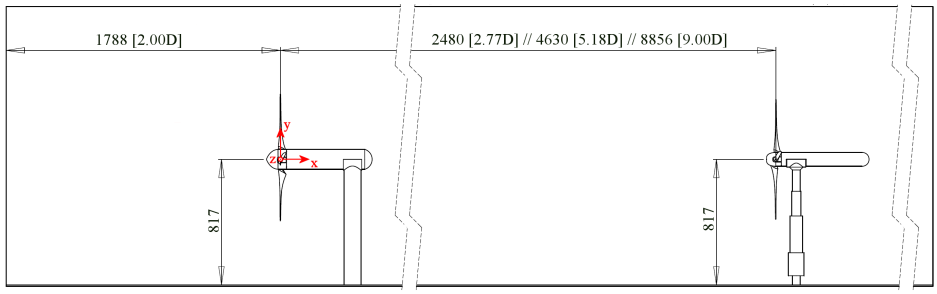

Fig. 2. Setup of the model wind turbines in the wind tunnel and reference coordinate system.

from Middle East Technical University (METU) in Turkey. They investigated lift and drag coefficients from $Re_C = 7.15 \times 10^4$ to $Re_C = 1.45 \times 10^5$ on a two-dimensional wing with a chord length of $c_L = 0.20\,\text{m}$. No hysteretic effects for low Reynolds numbers were found in this experiment. A third experimental set of airfoil characteristics from $Re_C = 7.00 \times 10^4$ to $Re_C = 6.00 \times 10^5$ was measured by Aksnes (2015) on a wing section of $c_L = 0.45\,\text{m}$ at NTNU, Norway. No Reynolds-dependent behavior was found at low Reynolds numbers in this experiment either. The measured lift and drag coefficients of these three experiments are in good agreement in the linear lift region, while in the pre-stall and stall regions, significant differences between the three datasets are present. For $Re_C = 10^5$ DTU's measurements predict stall already at $\alpha \approx 8°$, while in METU's and NTNU's experiments, stall presents later around $\alpha \approx 11°$. Furthermore, somewhat higher lift values are measured in NTNU's dataset in the pre-stall region compared to the other datasets. Numerical simulations by Sagmo et al. (2016) [30] as well as Prytz et al. (2017) [28] point out strong three-dimensional flow effects caused by stall cells in the pre-stall and stall regions. This could be a possible cause for varying experimental results in this region.

Both rotors are designed for an optimum tip speed ratio of $\lambda_{T1} = \lambda_{T2} = 6.0$. The blades are milled from aluminium and the blade tips are cut straight. More details about the blade geometry, such as detailed chord and twist data, are found in an invitational document by Sætran and Bartl (2015) [29]. In this blind test experiment the model turbines are positioned at the wind tunnel center line. The upstream turbine T1's rotor plane is located at $2.00\,D$ from the test section inlet, which is verified to be far enough away to not affect the reference velocity measurement at the inlet contraction. The downstream turbine T2 is positioned at 2.77 and $5.18\,D$, $9.00\,D$ downstream of the upstream turbine rotor. The hub height of both turbines is adjusted to $h_{hub} = 0.817\,\text{m}$. In Fig. 2 a side cut of the wind tunnel is shown, indicating a reference coordinate system and the wind turbine positions.

Fig. 3. Test case A: low-turbulence uniform inflow **(a)**; test case B: high-turbulence uniform inflow **(b)**; test case C: high-turbulence shear inflow **(c)**.

Inflow conditions

For this blind test experiment three different turbulent inflow conditions are investigated. This is supposed to shed light on the effects of various turbulence levels, as well as shear in the atmosphere, on the performance of a wind turbine and its wake. As it is almost impossible to create realistic conditions that resemble atmospheric stability classes in a wind tunnel environment, simplified cases of turbulent inflow are created.

The first inflow condition investigated is a uniform inflow of very low turbulence and is described from here on as test case A. As shown in Fig. 3 (a), there is no grid installed at the inlet of the test section, resulting in a clean and uniform flow. Hot-wire measurements at the upstream turbine position give a turbulence intensity level of $\mathrm{TI} = 0.23\,\%$ on an integral turbulent length scale of $L_{uu} = 0.045\,\mathrm{m}$. Over the rotor swept area, the mean velocity in the empty tunnel is found to be uniform to within $\pm 0.6\,\%$. The boundary layer thickness at wind tunnel walls was measured to be $y_{BL} = 0.200\,\mathrm{m}$ at the upstream turbine position.

In order to investigate the effects of turbulence on wind turbine performance and wake development, the measurements of test case B are performed using a large-scale turbulence grid at the inlet to the test section (Fig. 3 (b)). The biplanar grid has a solidity of 35 % and is built from wooden bars with a $47\,\mathrm{mm} \times 47\,\mathrm{mm}$ cross section. The grid mesh size is $M = 0.240\,\mathrm{m}$, which generates a turbulence intensity of $\mathrm{TI} = 10.0\,\%$ at the position of the upstream turbine. The integral length scale here is assessed from an autocorrelation of a hot-wire time series and is calculated to be $L_{uu} = 0.065\,\mathrm{m}$ at this position. The grid produces considerable span-wise variations in the flow, but as soon as the flow reaches the position of the upstream turbine T1, the mean velocity is measured to be uniform to within $\pm 1.5\,\%$ over the rotor area. The turbulence intensity is also assessed to be constant to within $\pm 1.0\,\%$. In this grid-generated turbulent flow, the turbulent kinetic energy decays with increasing distance from the grid. As the flow reaches the first position of the downstream turbine T2, $2.77\,D$ downstream of T1, the turbulence intensity in the empty tunnel decays to $\mathrm{TI} = 4.8\,\%$, while the integral length scale increases

to $L_{uu} = 0.100\,\mathrm{m}$. In a third test case C, the effect of shear flow combined with high turbulence is investigated. For this purpose a large-scale shear-flow-generating turbulence grid is installed at the inlet of the test section, as shown in Fig. 3 (c). The horizontal mesh width is constant at $M_h = 0.240\,\mathrm{m}$, while the vertical mesh heights vary between $M_{v,min} = 0.016\,\mathrm{m}$ near the floor and $M_{v,max} = 0.300\,\mathrm{m}$ underneath the roof. The grid is biplanar and has a solidity of 38 %. As for the evenly spaced turbulence grid, it is again built from wooden bars with a 47 mm × 47 mm cross section. At the position of the upstream turbine T1, a turbulence intensity of 10.1 % is measured at hub height. The turbulent length scale is estimated to be $L_{uu} = 0.097\,\mathrm{m}$ for this case. The kinetic energy in the flow decays with the distance from the grid. The turbulence intensity decays to TI = 5.2 % 2.77 D further downstream, while the length scale increases to $L_{uu} = 0.167\,\mathrm{m}$. At 5.18 D downstream of T1, the turbulence intensity decays to TI = 4.1 %, while at 9.00 D only TI = 3.7 % remains.

Because wind shear and turbulence are generated only at the grid position at the tunnel inlet, their development throughout the tunnel is measured for all turbine positions. Wind shear can be described by the power law in Eq. (1), which expresses the wind speed U as a function of height y, provided that the wind speed at an arbitrary reference height y_{ref} is known:

$$\frac{U}{U_{ref}} = \left(\frac{y}{y_{ref}}\right)^{\propto}. \tag{1}$$

The power law coefficient α describes the strength of shear in the wind profile. A wind profile based on a shear coefficient of about $\alpha = 0.11$ is chosen for this experiment, resembling the shear at typical stable atmospheric conditions (Hsu et al., 1994) [15], although the grid-generated turbulence in the wind tunnel is much higher than in a stable boundary layer. The mean and turbulent flow profiles at all relevant positions are shown in Fig. 4.

During the present experiments, the reference wind speed was kept constant at $U_{ref} = 11.5\,\mathrm{m\,s^{-1}}$, which is tested to give a Reynolds-number-independent turbine performance for all inflow conditions. Since the downstream turbine T2 experiences significantly lower average wind speeds when operating in the turbulent wake, Reynolds-number-independent performance characteristics are measured down to an inflow velocity of $U_{inflow} = 6.0\,\mathrm{m\,s^{-1}}$ at TI = 5.0 % background turbulence. For test case C, in which the velocity increases with height, the reference velocity of $U_{ref} = 11.5\,\mathrm{m\,s^{-1}}$ is set at the turbine hub height $h_{hub} = 0.817\,\mathrm{m}$. This reference height is chosen for simplicity reasons, although the rotor-equivalent wind speed (Wagner et al., 2014 [42]) that represents the center of kinetic power in the shear inflow is found to be slightly below the turbine hub height (Maal, 2014 [23]).

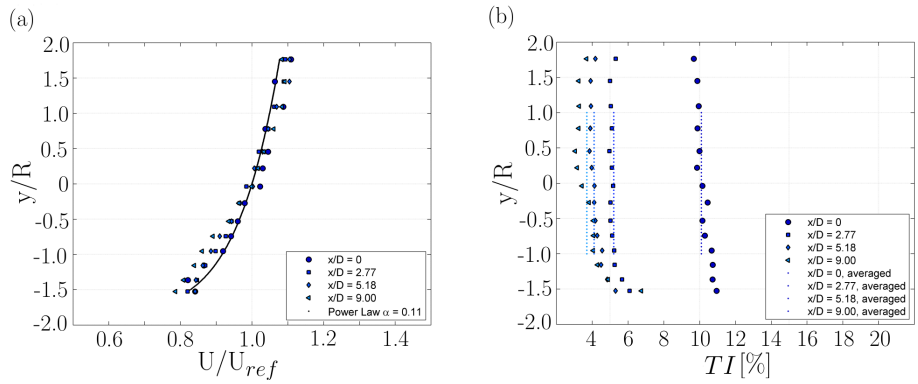

Fig. 4. Measured and rotor-averaged values of normalized mean velocity U/U_{ref} **(a)** and turbulence intensity TI [%] **(b)** at the position of T1 ($x/D = 0$) and the positions of T2 ($x/D = 0$, 2.77, 5.18, 9.00) in the empty tunnel for test case C (shear flow grid).

2.2 Experimental methods

Power and thrust measurements

Both model turbines are equipped with a HBM torque transducer of the type T20W-N/2-Nm, which is connected to the rotor shaft through flexible couplings. In addition, an optical photo cell is installed on the shaft, giving a defined peak signal for every full rotation of the rotor. After subtracting the measured friction in the ball bearing between the rotor and torque sensor, the mechanical power in the rotor shaft can be calculated. The power in both turbines is measured and controlled simultaneously to ensure a stable operation of both turbines. The thrust force is measured by a six-component force balance produced by Carl Schenck AG. The drag force on the tower and nacelle structure is first measured without the rotor being present. Thus, it is possible to assess the rotor thrust by subtracting the tower–nacelle drag from the total drag.

Wake flow measurements

The mean and turbulent velocities in the wake behind the upstream turbine T1 are measured by a single hot-wire anemometer (HWA) in constant temperature mode (CTA). Each measurement point is sampled for 45 s at 20 kHz, resulting in a total of 9.0×10^5 samples. The signals are amplified and filtered appropriately to avoid distortion by noise, for example. All the wake measurements are repeated using a two-component laser Doppler anemometry (LDA) system from Dantec Dynamics for verification. A time series of 5.0×10^4 samples is sampled for a varying period of about 30 s. The reference velocity U_{ref} used for normalization of the mean and turbulent wake velocity, as well as the non-dimensional power and thrust coefficients, is measured at the inlet contraction of the wind

tunnel. The pressure difference around the circumferences of two defined cross sections is logged simultaneously for every measuring point. The air density ρ in the experiment is calculated from the measured air temperature and atmospheric pressure in the test section for every measurement point.

Statistical measurement uncertainties

The statistical uncertainty of every sample of the power, thrust and mean velocity measurements is calculated following the procedure proposed by Wheeler and Ganji (2004) [43]. Random errors are computed from the standard deviations of the various measured signals on a 95 % confidence interval. Also taking systematic errors from the calibration procedures into account by following the procedure of Eriksen (2016) [12], a total error is calculated. Herein, the systematic error of about $\pm 1.0\,\%$ from the velocity calibration is seen to be the major contributor to the total uncertainty. The uncertainty in the turbulent quantities in the wake flow is calculated according to the approach of Benedict and Gould (1996) [7]. The uncertainty in the upstream turbine power coefficient at design conditions is calculated to be within $\pm 3.0\,\%$, while it is lower than $\pm 2.0\,\%$ for the thrust coefficient. It is observed that the uncertainty of the mean velocity is somewhat larger in the free stream outside the wake. At higher velocities the sensitivity of the hot-wire probe is smaller, which produces higher uncertainties. The measured values of the turbulent kinetic energy are observed to feature the highest uncertainty in the shear layer between wake and free stream flow.

2.3 Computational methods

The computational methods applied by the five different contributors are described in the following subsections. Furthermore, an overview of the different simulation methods and parameters is presented in Table 1.

Uppsala University and DTU (UU–DTU)

S. Sarmast, R. Mikkelsen and S. Ivanell from Uppsala University, Campus Gotland, Sweden, and Technical University of Denmark (DTU), Campus Lyngby, Denmark, contributed with a dataset simulated by LES methods combined with an ACL approach. The DTU in-house code EllipSys3D, which is based on a multi-block finite volume approach, was used to solve the Navier–Stokes computations. The convective terms are herein discretized by a combination of third-order and a fourth-order schemes. The resolution of the time domain is defined small enough, that a blade tip moves less than a half cell size per time step. The flow field around the wind turbine rotor was simulated using the actuator line

Table 1. Overview of simulation methods and parameters. Abbreviations for rotor models: actuator line (ACL), blade element momentum (BEM), fully resolved rotor (FRR). Abbreviations for flow models: improved delayed detached eddy simulation (IDDES), large eddy simulation (LES), Reynolds-averaged Navier–Stokes simulation (RANS).

	Simulation software	Rotor model	Airfoil data	Flow or turbulence model	Mesh properties	Number of cells or nodes	Tunnel blockage
UU-DTU	▶ EllipSys3D	ACL	Exp. DTU	LES	Cartesian	2.9×10^7 cells	Yes
Vrije (flow)	■ OpenFOAM	FRR	–	RANS k-ω	Hexahedral	3.5×10^7 cells	Yes
Vrije (forces)	■ Matlab	BEM	XFoil	–	–	–	–
LUT (ACL)	◆ ANSYS CFX	ACL	XFoil	RANS k-ω SST	Arbitrary	3.7×10^6 nodes	Yes
LUT (FRR)	◆ ANSYS CFX	FRR	–	RANS k-ω SST	Structured	4.2×10^4 nodes	Yes
CD-adapco	★ Star-CCM+	FRR	–	IDDES Sp.-Al.	Hexah./Polyh.	2.5×10^7 cells	Yes
CMR	◀ Music	BEM	XFoil	RANS k-ε	Structured	5.0×10^5 nodes	Yes

technique developed by Sørensen and Shen (2002) [38]. Herein, the Navier–Stokes equations are solved with body forces distributed along rotating lines representing the blades of the wind turbine. The lift and drag coefficients are taken from the previously mentioned self-generated dataset for the NREL S826 airfoil by Sarmast and Mikkelsen (2013) [32]. For each of the 43 blade points the forces are interpolated for the local Reynolds numbers in a range of 40 000 to 120 000. Additionally, a force line is introduced to account for the drag force generated by the tower. The wake flow field is calculated by solving the Navier–Stokes equations using LES with an integrated sub-grid-scale (SGS) viscosity model.

A regular Cartesian grid, which is divided into 875 blocks, makes out the computational domain. With 32 points in each block and 43 points representing each blade, a total of 28.6 million mesh points are used to simulate the various test cases. This resolution was tested to give a grid-independent simulation result.

The inlet turbulence is modeled by implanting synthetically resolved turbulent fluctuations 1.5 D upstream of the position of the upstream rotor T1. These fluctuations from a pre-generated turbulence field are superimposed to the mean velocities through momentum sources, yielding isotropic homogeneous turbulence. The mean and turbulent profiles of the different test cases are tested to give a good match with the corresponding wind tunnel values. In addition, the effect of shear flow combined with high turbulence is investigated. The shear profile is implemented to match the profile given in the invitational document by Sætran and Bartl (2015) [29]. A more detailed description of the method can be found in Sarmast et al. (2014) [33].

Vrije University Brussels (Vrije)

N. Stergiannis from Vrije University and Von Karman Institute (VKI) in Brussels, Belgium, performed Reynolds-averaged Navier–Stokes (RANS) simulations using the open-source software package OpenFOAM in combination with a multiple rotating frame (MRF) approach. Therein, the full rotor geometry is resolved in its own frame of reference and

the flow is calculated around the "frozen rotor". The subdomain is connected to the stationary frame of reference by an arbitrary mesh interface (AMI). A grid independency test was executed investigating different cell sizes, giving an independent result with a total number of 3.5×10^7 cells. Slip conditions are used at the wind tunnel walls, which was deemed to save computational effort and still takes into account the blockage effect generated by the walls. The rotor and the nacelle are completely resolved, but the turbine towers are not simulated in the final computations. The boundary layers on the blades and nacelle are resolved down to $y^+ \approx 30$. The standard k-ω turbulence model as implemented in OpenFOAM v.2.4 is applied for the presented simulations. The mean and turbulent inlet velocities were matched with the experimental values provided in the invitational document. Because the blade forces could not be directly extracted from the fully resolved rotor simulations, a blade element momentum (BEM) code based on the method by Ning (2014) [22] was used to calculate the power and thrust characteristics of the model wind turbines. The lift and drag coefficients are computed with the open-source software XFoil (Drela, 2013 [11]) for the NREL S826 airfoil at all prevailing Reynolds numbers. The reference velocity for the downstream turbine is calculated as the average velocity over a line of one radius $x/D = 1$ upstream of the downstream rotor. Only test cases A and B are modeled.

Łódź University of Technology (LUT)

M. Lipian, M. Karczewski and P. Wiklak from the Institute of Turbomachinery at Łódź University of Technology, Poland, contributed two datasets computed by the commercial CFD software ANSYS CFX. All simulations were performed to find a steady state solution of the RANS equations using the k-ω SST model for turbulence closure.

For test cases A, B and C they fully resolved the rotor geometry. Thus, the solver resolves the actual flow around the rotor and no additional assumptions needed to be made. These simulations will be denoted as fully resolved rotor model LUT (FRR) from now on. Two rotating subdomains are established around the rotors, while the main wind tunnel domain is stationary. A structural mesh is created with the software ICEM CFD to discretize the domains. The wind tunnel is discretized by a total number of 3.0×10^4 plus two refined subdomains around the rotors of 6.0×10^3 nodes each. A grid independence test was executed for the rotor subdomain to prove grid-independent convergence.

For the test cases B_1, B_2 and B_3 a different approach was chosen. The rotors are represented by a custom-made actuator line model, which will be denoted as LUT (ACL). Herein, the blades are modeled as parallel epipedons, representing a subdomain in which the RANS equations are modified. The flow is modified by an addition of force components, which are calculated from tabulated lift and drag data dependent on the local chord and angle of attack. The lift and drag data are taken from the invitational document and

Table 2. Overview of turbine operating conditions downstream turbine positions as well as wake measurement positions for the five different test cases.

Test case	Inflow	Inlet turbulence at position of T1	Tip speed ratio λ_{T1}	Position x/D of downstream turbine T2	Tip speed ratio λ_{T2}	Wake measurement position at x/D
A	uniform	0.23 %	6.0	5.18	4.5	2.77
B1	uniform	10.0 %	6.0	2.77	4.5	–
B2	uniform	10.0 %	6.0	5.18	4.5	–
B3	uniform	10.0 %	6.0	9.00	4.5	2.77/5.18/8.50
C	shear	10.1 %	6.0	5.18	4.5	2.77

were originally created with XFoil. Furthermore, the ACL model includes a Prandtl tip-loss correction. For these test cases an unstructured mesh is used in the wind tunnel main domain and parallel epipedon around the blades, discretized by a total number of 1.7×10^6 nodes in the main domain plus 2 times 1.0×10^6 nodes in the subdomains around the rotors. Because the test cases B and B_2 are identical, a direct comparison between the performance and wake results of the FRR and ACL simulations is possible.

CD-adapco (CD-adapco)

S. Evans and J. Ryan from CD-adapco, London, United Kingdom, contributed a full dataset of predictions simulated by improved delayed detached eddy simulations (IDDES). The IDDES Spalart–Allmaras turbulence model is used for turbulence closure in the boundary layers. Both the meshing and the actual simulation are carried out with their commercial software package STAR-CCM+, which is a finite-volume solver using cells of arbitrary shape. Aside from the turbine rotors, the exact geometry of the turbine nacelles, towers and wind tunnel walls is modeled. The computational domain is divided into three subdomains. In the main wind tunnel domain, a hexahedral dominant grid is applied, which is further refined around the turbines and in the wake region. In the disc-shaped regions around the rotors, an isotropic polyhedral mesh of even finer resolution is utilized. The boundary layers around the blade surfaces are resolved down to $y^+ < 2$. The rotating disk domains around the turbine rotors are connected to the main domain via an arbitrary sliding interface. For the entire computational domain, around 2.5×10^7 grid cells are applied.

The inlet conditions are modeled with the synthetic eddy method, generating an inflow field of defined turbulence intensity and length scales that correspond to the values given in the invitational document. For test case C, a shear flow is defined by a power law at the wind tunnel inlet. Explicit transient modeling is used to simulate the wind turbine interactions, while the turbine rotations are modeled as a rigid body motion. A transient second-order model with a time step of $\mathrm{d}t = 1.0 \times 10^{-4}$s is used. Advanced limiter options for minimum limiting and higher-order spatial schemes are used in a segregated solver. The transient calculation is run for 1 s in test cases A, B_1, B_2 and C and 2.5 s in test

case B_3 due to the higher separation distance. The required values are thereafter averaged for a time period of 0.5 s.

More information about the use of Star-CMM+ in rotating flows can be found in Mendonça et al. (2012) [25], for example.

CMR Instrumentation (CMR)

A. Hallanger and I. Ø. Sand from CMR Instrumentation in Bergen, Norway, provided a dataset based on RANS simulations combined with a BEM approach. For the calculation of the mean and turbulent flow quantities, their in-house CFD code called Music was used. The RANS equations are solved with a standard k-ε model with Launder–Spalding coefficients. Furthermore, a sub-grid turbulence model is applied to represent the rotor-generated turbulence. Therein, it is assumed that the production rate of turbulent kinetic energy and its rate of dissipation are integrated over the wake of the wind turbine and distributed over the near field. Convective and diffusive fluxes are approximated with the second-order Van Leer (1974) [41] and central difference schemes. The turbulent intensity and length scales at the inlet are specified according to the experimental values given in the invitational document for the three different test cases. For test case C, a power law profile is used.

The rotors are included as sub-models in the CFD code. They are represented by their reaction forces on the flow field. The blade forces are simulated by a BEM code, including wake rotation. The blades are divided into 30 blade elements in radial direction. The BEM code includes the Prandtl tip-loss correction as well as Glauert's empirical model for highly loaded rotors. The lift and drag coefficients were calculated from the software XFoil (Drela, 2013 [11]) depending on angle of attack, Reynolds number and relative turbulence intensity. Therein, the transition amplification numbers (N_{crit}) represent the turbulence intensity levels present at the different positions in the wind tunnel. Three-dimensional corrections for two-dimensional force coefficients according to the BEM method by Ning (2014) [22] were applied. These forces were used as source terms for axial and rotational momentum conservation. The turbine hubs and towers were modeled as flow resistances in the same control volume as the rotors. Turbine hubs were represented by a drag coefficient of $C_{D,hub} = 0.6$, while the tower drag was approximated by $C_{D,tower} = 1.2$.

Wind tunnel walls were modeled by wall functions. The entire wind tunnel environment including the two rotors was resolved in a total of 5×10^5 structured grid nodes. Steady state simulations of the blade forces were performed with an angular increment of 15°, resulting in a total of 24 azimuthal positions of the turbine rotors. This was deemed to be sufficient to include the effects of shear flow on the first turbine. A detailed description of the computational methods applied is given in Hallanger and Sand (2013) [14].

2.4 Required output

In total, five different test cases are provided for simulation in this blind test experiment. An overview of the turbine operating conditions and position as well as the measurement station of the wake measurements is shown in Table 2.

Wind turbine performance

For all five test cases the power coefficients $C_{P,T1}$ and $C_{P,T2}$ (Eq. 2) as well as the thrust coefficients $C_{T,T1}$ and $C_{T,T2}$ (Eq. 3) of both turbines are compared:

$$C_{P,T1/T2} = \frac{8\,P_{T1/T2}}{\rho\,\pi\,D_{T1/T2}^2\,U_{ref}^3}, \tag{2}$$

$$C_{T,T1/T2} = \frac{8\,F_{T1/T2}}{\rho\,\pi\,D_{T1/T2}^2\,U_{ref}^2}. \tag{3}$$

Herein, $P_{T1/T2}$ denotes the mechanical power of the turbine shaft, $F_{T1/T2}$ the thrust force in the stream-wise direction on the rotor and ρ the air density. The upstream turbine T1 is operated at a tip speed ratio of $\lambda_{T1} = \omega \times D_{T1}/2 \times U_{ref} = 6.0$, whereas the downstream turbine T2 is run at $\lambda_{T2} = \omega \times D_{T2}/2 \times U_{ref} = 4.5$. Note that the same reference velocity U_{ref} defined at the test section inlet is used for both turbines. The optimal tip speed ratio for the downstream turbine T2 is also $\lambda_{T2} = \lambda_{T1} = 6.0$ when the turbine is unobstructed. Since T2 operates in the wake, the velocity that was actually experienced was considerably lower, also reducing the optimal rotational speed and thus the tip speed ratio λ_{T2}. The optimal tip speed ratio at which the maximum power P_{T2} is achieved in fact varies between $\lambda_{T2} = 4.0$ and 5.0 depending on the turbine separation distance x/D and inlet turbulence level TI_{Inlet}. For better comparability, a fixed tip speed ratio of $\lambda_{T2} = 4.5$ was chosen.

Mean and turbulent wake flow

Furthermore, the horizontal profiles of the mean and turbulent flows are compared at the predefined wake measurement positions (Table 2). The upstream turbine is still operated at $\lambda_{T1} = 6.0$ for all five test cases. The profiles of the normalized mean velocity U^* (Eq. 4) and the normalized turbulent kinetic energy k^* (Eq. 5) are calculated at the turbine hub height $h_{hub} = 0.817\,\mathrm{m}$:

$$U^* = U/U_{ref}, \tag{4}$$

$$k^* = k/U_{ref}^2. \tag{5}$$

In a Cartesian coordinate system the turbulent kinetic energy k is defined as

$$k = \frac{1}{2}(u_x'^2 + u_y'^2 + u_z'^2). \tag{6}$$

According to Bruun (1995), the HWA measures an effective cooling velocity U_{eff} that can be described by the Jørgensen equation (Eq. 7).

$$U_{eff}^2 = U_x^2 + k\,U_y^2 + h\,U_z^2 \tag{7}$$

Depending on the magnitude of the flow velocity, the coefficients k and h typically have values around 1.05 and 0.2 (Bruun, 1995) [8], which means that U_{eff} can be approximated by the velocity perpendicular to the wire. For flows with $U_x \gg U_y$, the effective cooling velocity has the same magnitude as the stream-wise component U_x, which is in this case a reasonable assumption for wake measurements at downstream positions starting at $x/D = 2.77$.

Therefore, the isotropic normal stress approximation (Eq. 8) is used to determine the turbulent kinetic energy in each measurement point:

$$k = \frac{3}{2}u_x'^2. \tag{8}$$

This approximation is most certainly not appropriate for the zones with high anisotropy, but Krogstad et al. (2015) [20] showed that the isotropic normal stress approximation is a well-fitting approximation in the turbine wake. They measured all three components of the stress tensor with a cross-wire probe for one wake profile at $x/D = 1$. Furthermore, they demonstrated a very good agreement of the isotropic approximation and the component-wise calculation of k.

For the LDA measurements the stream-wise and cross-wise flow components U_x and U_z are measured. Since the stress tensors u_x' and u_z' from these measurements are seen to be very isotropic, the turbulent kinetic energy k is also in this case approximated by the stream-wise stress u_x' only (Eq. 8).

The computed values of mean velocity as well as turbulent kinetic energy from HWA and LDA measurements compare very well. In regions of increased rotation, as in the wake center, the HWA consistently predicts slightly lower mean velocity values. Here, the influence of binormal cooling velocity U_y is more pronounced, though not really significant.

2.5 Comparative methods

Direct comparison of turbine performances

The predictions of the power coefficients $C_{P,T1}$ and $C_{P,T2}$ as well as the thrust coefficients $C_{T,T1}$ and $C_{T,T2}$ at the pre-defined operating points are directly compared to the experimentally measured values in graphs and tables. The deviations from the measured reference value are discussed on a percentage basis in the text.

Statistical performance measures for wake prediction

The predictions of the mean and turbulent wake flow U^* and k^* are compared in graphs to the measured profiles from the HWA and LDA experiments. In order to provide a more general comparison of the predictions with the experimental results, statistical performance measures are computed as proposed by Chang and Hanna (2004) [9]. These measures include the fractional bias (FB), the normalized mean square error (NMSE), the geometric mean bias (MG), the geometric variance (VG) and the correlation coefficient (R). For this purpose, the predictions are compared to the experimental measurements using HWA in the exact same locations as the 41 measurement points along a horizontal line at a hub height from $z/R = -2.0$ to $z/R = 2.0$. Thus, the following statistical performance measures are calculated and compared in tables for each test case:

$$FB = \frac{\overline{x_m} - \overline{x_p}}{0.5(\overline{x_m} + \overline{x_p})}, \tag{9}$$

$$NMSE = \frac{\overline{(x_m - x_p)^2}}{\overline{x_m} \times \overline{x_p}}, \tag{10}$$

$$MG = \exp\left(\overline{\ln x_m} - \overline{\ln x_p}\right), \tag{11}$$

$$VG = \exp\left[\overline{(\ln x_m - \ln x_p)^2}\right], \tag{12}$$

$$R = \frac{\overline{(x_m - \overline{x_m}) \times (x_p - \overline{x_p})}}{\sigma_{x_m} \times \sigma_{x_p}}. \tag{13}$$

Herein, x_m are the measured values and x_p the values predicted by the models. In this case the compared values x are the normalized mean velocity $U^* = u/U_{ref}$ and normalized turbulent kinetic energy $k^* = k/U_{ref}^2$. The overbar $\overline{x}$ means that an average over all the data points from $z/R = -2$ to $z/R = 2$ is taken, and σ_x refers to the standard deviation of the dataset from $z/R = -2$ to $z/R = 2$.

A perfect model prediction would result in a FB and NMSE of zero and MG, VG and R of 1. It has to be stated that these statistical performance measures can by no means give a comprehensive evaluation of the performance of a model, but only provide a general correlation of all data points.

FB and MG are measures of the systematic error, while FB is measured on a linear scale and MG is based on a logarithmic scale. Note that it still might be possible to get a perfect correlation using FB and MG even though the single points are far off at the specific measurement locations. Conversely, NMSE and VG represent the scatter in the correlation of measured and predicted data and include both systematic and random errors (Chang and Hanna, 2004 [9]). Finally, the widely used correlation coefficient R indicates the linear correlation between the measured and predicted values. In this study it is the only measure that directly compares the predicted and measured values at a specific location. Since R is insensitive to addition or multiplication of constants, it is often not recommended as a stand-alone value for the evaluation of a model (Chang and Hanna, 2004 [9]). For the comparison in this blind test experiment, however, the correlation coefficient R is deemed a robust method. The addition or multiplication of the predicted values is in most cases not relevant in the prevailing test cases. All predictions start from the same predefined boundary conditions, meaning that there is not a big offset in most data.

3 Results

The comparisons of the predictions and experimental results are analyzed for the different inflow conditions. In Sect. 3.1, power, thrust and wake predictions for test case A (low-turbulence inflow) are presented. Thereafter, all the test cases for high-turbulence inflow conditions for all three separation distances (test cases B_1, B_2. B_3) are analyzed in Sect. 3.2. Finally, the results of test case C, featuring a highly turbulent shear flow, are compared in Sect. 3.3.

Experimental results for power and thrust are indicated by filled black circles for the upstream turbine and empty circles for the downstream turbine. The measurements of the wake profiles using HWA are marked with filled black circles, while flow measurements using LDA are indicated by filled grey circles. The different contributions of numerical simulations are assigned one consistent symbol and color for power, thrust and wake flow predictions.

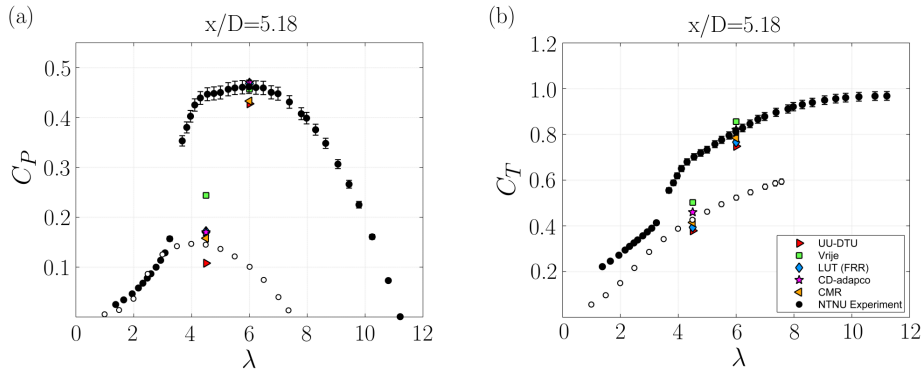

Fig. 5. Power coefficient C_P **(a)** and thrust coefficient C_T **(b)** for T1 (filled circles) and T2 (empty circles) compared for test case A. The downstream turbine T2 is positioned at $x/D = 5.18$ downstream of T1, and the upstream turbine T1 is operated at $\lambda_{T1} = 6.0$. The reference velocity is $U_{ref} = 11.5\,\mathrm{m\,s^{-1}}$.

3.1 Test case A: low-turbulence uniform inflow

Power and thrust predictions

The power and thrust predictions for test case A (low-turbulence inflow, TI = 0.23 %) from the five contributions are compared to the experimental results in Fig. 5. The respective numerical values are listed in Table 3. The experimentally measured power coefficient of the upstream turbine has its maximum $C_{P,max} = 0.462$ at $\lambda = 6.0$ and its runaway tip speed ratio at $\lambda = 11.1$. At a turbine tip speed ratio of about $\lambda = 3.5$, a rapid transition of $C_{P,T1}$ into stall is observed. The predictions of the power coefficient of the upstream turbine T1 at its design operating point $\lambda_{T1} = 6.0$ show a scatter of about $\pm 7\,\%$ compared to the measured $C_{P,T1}$. This points out significant differences in the modeling methods. While CMR generated a Reynolds-dependent dataset for lift- and drag coefficients using the airfoil design and analysis code XFoil (Drela, 2013) [11] as an input for their BEM model, UU-DTU used an experimentally generated lift and drag dataset produced by Sarmast and Mikkelsen (2013) [32] as an input for their ACL model. Another aspect is how the predictions modeled the influence of solid wall blockage on the C_P values. Because the flow cannot expand freely around the turbine, the induction is reduced, resulting in higher power production of the turbine than that in an unblocked flow. All five contributions took the wind tunnel boundaries into account, resulting in fairly good approximations of the upstream turbine's C_P at design conditions.

The scatter in C_P for the downstream turbine T2 is considerably larger than for T1. T2 is operated around its design point at $\lambda_{T2} = 4.5$ (referring to U_{ref} measured upstream of T1) in the wake at a separation distance of $x/D_{T2} = 5.18$ from the upstream turbine T1. The power is underestimated by up to 25 % and overpredicted by no more than

Table 3. Numerical values of power coefficient C_P and thrust coefficient C_T for test case A. The downstream turbine T2 is positioned at 5.18 D downstream of T1. T1 is operated at $\lambda_{T1} = 6.0$ and T2 is operated at $\lambda_{T1} = 4.5$, referring to the far upstream reference velocity $U_{ref} = 11.5\,\mathrm{m\,s^{-1}}$.

		Upstream turbine T1		Downstream turbine T2	
		$C_{P,T1}$	$C_{T,T1}$	$C_{P,T2}$	$C_{T,T2}$
UU-DTU	▶	0.428	0.748	0.108	0.379
Vrije	▫	0.457	0.856	0.244	0.502
LUT (FRR)	◆	0.468	0.766	0.171	0.394
CD-adapco	★	0.470	0.820	0.170	0.460
CMR	◀	0.433	0.785	0.158	0.415
Experiment	●○	0.462	0.811	0.145	0.427

30 %. However, some predictions such as CMR, LUT and CD-adapco manage to match the experimental result reasonably well, overestimating the downstream turbine power by only 9–17 %. This is a rather small deviation given the large scatter of more than 100 % observed in previous blind test experiments (Pierella et al., 2014 [27]; Krogstad et al., 2015 [20]).

The predictions of the thrust coefficient for turbines T1 and T2 give a similar picture, as shown in Fig. 5 (b). Even though the upstream turbine thrust is slightly underpredicted by most simulations, the scatter is significantly smaller than in earlier blind tests. The C_T predictions for the downstream turbine show approximately the same scatter as the upstream turbine. The BEM predictions by CMR matched the experimental results very closely for both turbines.

Wake predictions

For the low inlet turbulence test case A, predictions of the wake flow at $x/D_{T2} = 2.77$ behind the upstream turbine are compared. Horizontal profiles of the normalized mean velocity U^* and the normalized turbulent kinetic energy k^* are compared at hub height, as shown in Fig. 6 (a) and (b). As already observed in a very similar test case in blind test 1 (Krogstad and Eriksen, 2013 [19]), the mean velocity profile at $x/D = 2.77$ features two distinct minima located behind the blade tips of the rotor (Fig. 6 (a)). The evident asymmetry in the wake center is caused by the advection of the tower wake into the swirling rotor wake as shown in rotor wake experiments by Schümann et al. (2013) [36]. The wake shape and levels of velocity deficit are very well predicted by CD-adapco and UU-DTU, reflected in well-matching statistical performance measures, as presented in the left part of Table 4. Aside from small error values of FB_{U^*} and NMSE_{U^*}, the correlation coefficient scores of $R_{U^*,CD-adapco} = 0.960$ and $R_{U^*,UU-DTU} = 0.927$ score significantly better than the other predictions. CD-adapco's IDDES simulations furthermore manage to capture the shape of the wake profile very well, including the asymmetries caused by the tower wake

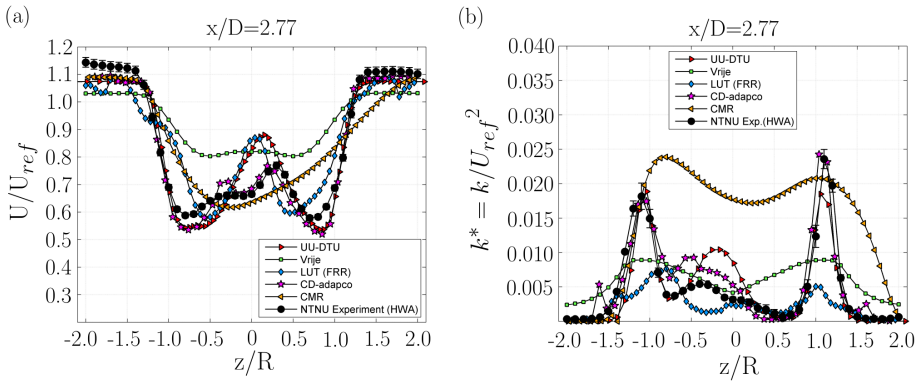

Fig. 6. Normalized mean velocity U/U_{ref} **(a)** and normalized turbulent kinetic energy k/U_{ref} **(b)** in the wake $x/D = 2.77$ behind T1 measured for test case A. The upstream turbine T1 is operated at $\lambda_{T1} = 6.0$. The reference velocity is $U_{ref} = 11.5\,\mathrm{m\,s^{-1}}$.

in the center of the profile. Another good prediction of the two minima and correct wake deficit levels is given by the fully resolved rotor simulations by LUT. However, the vertical wake extension as modeled by LUT is too small for this low-turbulence inflow test case, reflected in a somewhat lower correlation coefficient of $R_{U^*,LUT} = 0.877$. CMR's RANS simulations based on a k-ε turbulence model predict a Gaussian wake shape with only one minimum already at $x/D = 2.77$ downstream of the rotor, suggesting a much more homogenous flow, as measured in the experiments. A slightly poorer correlation coefficient of $R_{U^*,LUT} = 0.877$ is therefore calculated. Integrating over CMR's mean wake profile, however, gives a fair estimate of the kinetic energy contained in the wake flow, which is seen in error values $\mathrm{FB}_{U^*,CMR}$ and $\mathrm{NMSE}_{U^*,CMR}$ that are approximately zero, as well as $\mathrm{MG}_{U^*,CMR}$ and $\mathrm{VG}_{U^*,CMR}$, which are close to the perfect model value 1. The reason for that is that these measures do not specifically take the measurement location into account, but are calculated based on different averages over the entire wake. Vrije's method does not resolve the details in the mean velocity profile because the turbine tower was not included in the simulation. The velocity deficit in the wake is significantly underestimated; in average it amounts to only about 50 % of the experimentally measured values. Still, a fairly good correlation coefficient of $R_{U^*,Vrije} = 0.895$ is computed. This unexpectedly high value might be due to the fact that the correlation coefficient is insensitive to addition and multiplication of constants, as discussed by Chang and Hanna (2004) [9]. This is confirmed by significantly higher deviations of Vrije's prediction in FB_{U^*}, NMSE_{U^*}, MG_{U^*} and VG_{U^*} from the perfect model than the other models.

The normalized turbulent kinetic energy profiles are compared in Fig. 6 (b). The experimental profile shows two distinct peaks in the shear layer generated by the tip vortices around $z/R = \pm 1$. A third, substantially smaller peak slightly left of the wake center is as-

Table 4. Statistical performance measures FB, NMSE, MG, VG and R of the normalized mean velocity U^* and normalized turbulent kinetic energy k^* predictions of the five different models for test case A. The wake flow is predicted at stream-wise measurement position $x/D = 2.77$ downstream of T1.

		FB_{U^*}	$NMSE_{U^*}$	MG_{U^*}	VG_{U^*}	R_{U^*}	FB_{k^*}	$NMSE_{k^*}$	MG_{k^*}	VG_{k^*}	R_{k^*}
UU-DTU	▶	0.031	0.001	1.032	1.010	0.927	−0.047	0.002	1.797	6.828	0.870
Vrije	■	−0.081	0.007	0.897	1.041	0.895	−0.218	0.048	0.411	6.038	0.669
LUT (FRR)	◆	−0.009	0.000	0.980	1.017	0.877	0.675	0.515	1.522	1.879	0.547
CD-adapco	★	0.042	0.002	1.047	1.006	0.960	−0.206	0.043	0.918	2.528	0.938
CMR	◀	0.000	0.000	0.988	1.016	0.886	−1.019	1.404	0.338	89.922	0.378

cribed to the turbulence generated by the tower and nacelle structures. It can be observed that the turbulent kinetic energy in the shear layer is very well predicted by UU-DTU's LES as well as CD-adapco's IDDES model, which both match the turbulence peaks generated by the tip vortices perfectly. The statistical performance measures of the turbulence predictions of all models, as presented in the right part of Table 4, show a similar picture as previously observed in the mean velocity predictions. CD-adapco predicts the turbulence profile very well, resulting in a high correlation coefficient of $R_{k^*,CD-adapco} = 0.938$. The slightly lower correlation of UU-DTU's profile ($R_{k^*,UU-DTU} = 0.870$) is mainly due to an overprediction of the turbulence generated by the tower in the center of the wake. LUT's RANS simulation based on the k-ω SST turbulence model shows the three distinct peaks but underpredicts the turbulence levels significantly. This is underlined by considerably higher error values of $FB_{k^*,LUT} = 0.675$ and $NMSE_{k^*,LUT} = 0.515$ than in the other simulations. Vrije's simulations based on a k-ω turbulence model indicate the two peaks in the shear layer; however, these predictions also give far too low of TKE values in the shear layer. In the unaffected free stream flow, however, Vrije's model predicts a significantly too-high TKE, although the free stream turbulence should be predefined as an input value. Therefore, a slightly poorer correlation coefficient of $R_{k^*,Vrije} = 0.669$ is calculated, while the geometrical variance of the turbulence profile with $VG_{k^*,Vrije} = 6.038$ is rather high. CMR's simulation shows two TKE peaks in the shear layer of the same magnitude as in the experimental dataset. However, the turbulence prediction in the wake center and in the free stream are obviously too high, similar to the aforementioned model. The k-ε model seems to not be able to resolve strong spatial gradients in the distribution of turbulent kinetic energy. Aside from a significantly lower correlation coefficient $R_{k^*,CMR} = 0.378$ than in the other predictions, the geometrical variance $VG_{k^*,CMR} = 89.922$ is almost 1 order of magnitude higher than in the other predictions.

Table 5. Numerical values of power coefficient C_P and thrust coefficient C_T for test cases B_1, B_2 and B_3. The downstream turbine T2 is positioned at $2.77\,D$ (B_1), $5.18\,D$ (B_2) and $9.00\,D$ (B_3) downstream of T1. T1 is operated at $\lambda_{T1} = 6.0$ and T2 is operated at $\lambda_{T1} = 4.5$, referring to the reference velocity $U_{ref} = 11.5\,\mathrm{m\,s^{-1}}$.

		Upstream turbine T1		Downstream turbine T2 at $2.77\,D$ (B_1)		Downstream turbine T2 at $5.18\,D$ (B_2)		Downstream turbine T2 at $9.00\,D$ (B_3)	
		$C_{P,T1}$	$C_{T,T1}$	$C_{P,T2}$	$C_{T,T2}$	$C_{P,T2}$	$C_{T,T2}$	$C_{P,T2}$	$C_{T,T2}$
UU-DTU	▶	0.447	0.758	0.115	0.383	0.152	0.423	0.192	0.462
Vrije	■	0.453	0.853	0.115	0.336	0.149	0.415	0.166	0.486
LUT (ACL)	◆	0.453	0.788	0.157	0.449	0.228	0.518	0.339	0.605
LUT (FRR)	◆	0.456	0.756	–	–	0.194	0.419	–	–
CD-adapco	★	0.470	0.830	0.130	0.410	0.170	0.440	0.230	0.480
CMR	◀	0.436	0.785	0.145	0.411	0.218	0.490	0.294	0.576
Experiment	●○	0.468	0.833	0.137	0.423	0.188	0.500	0.270	0.569

3.2 Test case B: high-turbulence uniform inflow

Power and thrust predictions

A second set of power and thrust predictions is compared for inflow conditions of higher turbulence. A turbulence grid installed at the wind tunnel inlet generates a uniform wind field with a turbulence intensity of $\mathrm{TI} = 10.0\,\%$ at the location of the first turbine rotor. For this high background turbulence level, the turbine power and thrust are compared for three turbine separation distances $x/D =$ 2.77, 5.18 and 9.00 (test cases B_1, B_2 and B_3). The power and thrust predictions for test case B are compared in Fig. 7 (a)–(f). A comparison of the respective numerical values is presented in Table 5.

Comparing the upstream turbine power curve for high background turbulence (test cases B_2, Fig. 7 (c)) to the upstream turbine power curve of low background turbulence (test case A, Fig. 5 (a)) a very similar curve shape is observed. At increased background turbulence, the maximum power coefficient is measured at the same level as for low background turbulence. Furthermore, the runaway tip speed ratio at $\lambda = 11.4$, at which the rotor no longer produces energy, is very similar for both inlet turbulence levels. The most noticeable difference is the transition to stall at a tip speed ratio of about $\lambda = 3.5$ and lower. For higher background turbulence, the transition into stall is much smoother compared to low inlet turbulence.

The predictions of $C_{P,T1}$ at its design operating point $\lambda_{T1} = 6.0$ are again very accurate, scattering only about $\pm 7\,\%$ around the experimental value. The predictions of the thrust coefficient $C_{T,T1}$ also match very well. As previously observed in test case A, the $C_{T,T1}$ is slightly under predicted, up to $-9\,\%$ at the most in this case. Comparing the performance results of the downstream turbine, the best predictions are made for the lowest turbine separation distance $x/D = 2.77$ (test case B_1, Fig. 7 (a)). The experimentally measured power coefficient $C_{P,T2}$ is well matched, with a total deviation of about $\pm 15\,\%$. The downstream turbine thrust coefficient $C_{T,T2}$ is predicted within $\pm 10\,\%$ by all the

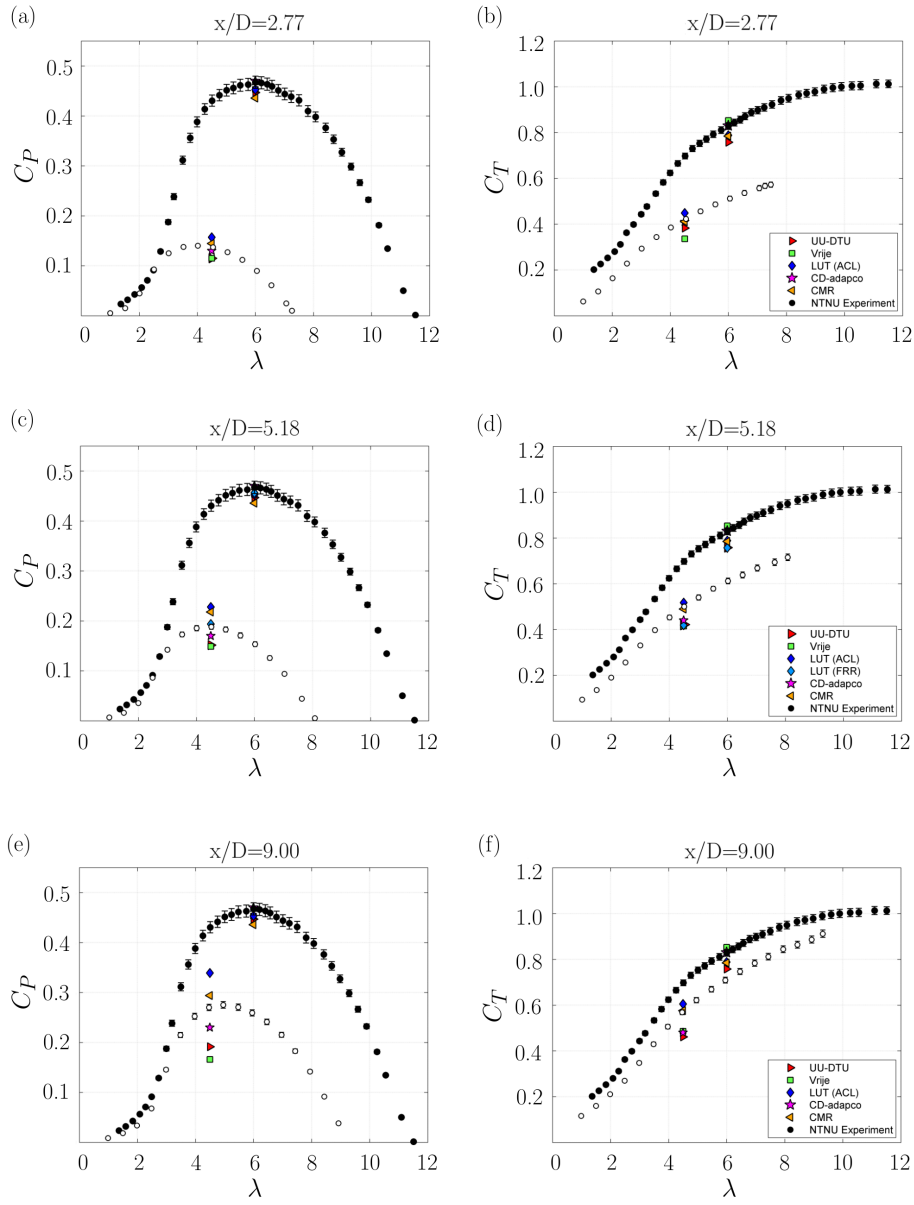

Fig. 7. Power coefficient C_P **(a, c, e)** and thrust coefficient C_T **(b, d, f)** for T1 (filled symbols) and T2 (empty circles) compared for test cases B_1, B_2 and B_3. The downstream turbine T2 is positioned at $x/D = 2.77$ **(a, b)**, 5.18 **(c, d)** and 9.00 **(e, f)** downstream of T1. The upstream turbine T1 is operated at $\lambda_{T1} = 6.0$. The reference velocity is $U_{ref} = 11.5\,\mathrm{m\,s^{-1}}$.

modellers in test case B_1. The predictions by CMR and CD-adapco most closely match the experimental results.

Increasing the turbine separation distance to $x/D = 5.18$ in test case B_2, the scatter in the results becomes significantly larger (Fig. 7 (c)). The scatter in the downstream turbine power coefficient $C_{P,T2}$ increases to about $\pm 20\,\%$ in both directions. The FRR model by LUT results in a very good prediction of the downstream turbine power coefficient, while their ACL model overpredicts the power significantly. This can be directly related to different wake flow predicted by the two models. The wake flow acts as inflow for the downstream turbine (compare Fig. 8 (a) further down). Conversely, UU-DTU's Ellipsys3D calculation underpredicts the downstream turbine performance significantly, even though the wake characteristics are predicted very accurately. Vrije also underpredicts the downstream turbine power significantly. This is rather surprising since the wake deficit at $x/D = 5.18$ is slightly underpredicted as well, and more power should be left in the flow for the downstream turbine. The scatter in the thrust calculations, as presented in Fig. 7 (d), is in general smaller than for the power predictions for all models, with most simulations underpredicting the experimental value. The thrust coefficient is less sensitive to a correct prediction of the incoming velocity field than the power coefficient. The thrust coefficient is indirectly proportional to the incoming velocity squared ($\sim U_{ref}^2$), while the power coefficient is even more sensible to an incorrect prediction of the incoming velocity field ($\sim U_{ref}^3$). Surprisingly, LUT's FRR model gives the smallest value for the downstream turbine thrust coefficient, although the power and wake predictions for this downstream distance match the experimental results very well.

With a further increase in turbine separation distance to $x/D = 9.00$ (test case B_3), the experimentally measured downstream turbine power coefficient recovers to $C_{P,T2} = 0.270$. The variation in the simulations, as shown in Fig. 7 (e), is seen to be even bigger for this downstream distance, reaching a scatter of more than 30 %. The same trend as already seen for smaller separation distances is observed: UU-DTU's and Vrije's simulations clearly underpredict the power coefficient, while LUT's ACL model considerably overestimates the downstream turbine power . The thrust predictions show similar tendencies to the power predictions but are seen to match the experimentally measured value better (Fig. 7 (f)).

Wake predictions

For the high background turbulence test case B, the participants were asked to predict the mean and turbulent wake characteristics at three downstream distances $x/D_{T2} = 2.77$, 5.18 and 8.50. Note that the horizontal wake profiles were extracted from test case B_3, in which the downstream turbine T2 was installed at $x/D_{T2} = 9.00$ and operated at $\lambda_{T2} = 4.5$. The wake flow as measured at $x/D_{T2} = 8.50$ therefore experienced the induction of the downstream turbine, which was located only $x/D_{T2} = 0.50$ further downstream. The

Table 6. Statistical performance measures FB, NMSE, MG, VG and R of the normalized mean velocity U^* and normalized turbulent kinetic energy k^* predictions of the five different models for test case B3. The wake flow is predicted at stream-wise measurement positions $x/D = 2.77$, 5.18 and 8.50 downstream of T1.

		FB_{U^*}	$NMSE_{U^*}$	MG_{U^*}	VG_{U^*}	R_{U^*}	FB_{k^*}	$NMSE_{k^*}$	MG_{k^*}	VG_{k^*}	R_{k^*}
$x/D = 2.77$	UU-DTU	0.027	0.001	1.025	1.002	0.968	−0.329	0.111	0.671	1.219	0.911
	Vrije	0.003	0.000	1.005	1.002	0.959	0.222	0.050	1.239	1.847	−0.008
	LUT (ACL)	−0.013	0.000	0.981	1.013	0.845	0.055	0.003	1.048	1.243	0.468
	LUT (FRR)	−0.009	0.000	0.988	1.003	0.949	0.525	0.296	1.771	1.539	0.720
	CD-adapco	0.048	0.002	1.060	1.006	0.970	−0.007	0.000	1.035	1.057	0.912
	CMR	−0.014	0.000	0.982	1.007	0.913	−0.771	0.698	0.404	2.720	0.417
$x/D = 5.18$	UU-DTU	0.021	0.000	1.017	1.002	0.964	−0.203	0.041	0.794	1.124	0.850
	Vrije	0.020	0.000	1.024	1.003	0.957	0.047	0.002	0.988	1.361	0.371
	LUT (ACL)	−0.035	0.001	0.954	1.012	0.929	0.423	0.188	1.459	1.405	0.273
	CD-adapco	0.054	0.003	1.065	1.007	0.971	−0.128	0.017	0.942	1.059	0.934
	CMR	−0.030	0.001	0.963	1.005	0.937	−0.598	0.393	0.483	1.980	0.705
$x/D = 8.50$	UU-DTU	0.028	0.001	1.029	1.001	0.970	−0.059	0.004	0.964	1.052	0.812
	Vrije	0.062	0.004	1.078	1.014	0.958	−0.159	0.026	0.830	1.112	0.656
	LUT (ACL)	0.018	0.000	1.015	1.001	0.936	0.706	0.569	2.095	1.828	0.594
	CD-adapco	0.116	0.013	1.143	1.032	0.962	0.166	0.028	1.259	1.130	0.811
	CMR	−0.040	0.002	0.957	1.004	0.955	−0.465	0.228	0.596	1.410	0.804

horizontal wake profiles of the normalized mean velocity U/U_{ref} and normalized turbulent kinetic energy $k^* = k/U_{ref}^2$ are compared in Fig. 8 (a)–(f).

The wake characteristics of the flow $x/D_{T2} = 2.77$ downstream of T1 are presented in Fig. 8 (a) and (b). For this case, LUT simulated the wake flow with two different models, the simpler ACL model and the computationally more expensive FRR model. At this downstream distance the mean wake profiles are characterized by two distinct minima. The experimental results clearly show that a Gaussian wake shape has not yet developed. A very accurate prediction of the mean wake shape is given by UU-DTU's simulation, but the CD-adapco model and the FRR model by LTU also capture the shape very well. LTU's ACL model, however, only predicts one distinct minimum in the mean wake profile. Only one minimum is also predicted by CMR, while the mean velocity profile is rather skewed. Vrije's simulations match the experimental measurements significantly better for a higher background turbulence level than for the lower turbulence level of test case A, predicting both the level and wake shape fairly well.

The fact that all predictions approximated the level of mean velocity deficit fairly well is also reflected in the statistical performance measures as presented in Table 6 (upper left section). FB_{U^*} and $NMSE_{U^*}$ are close to zero, while MG_{U^*} and VG_{U^*} show only very small deviations from the perfect correlation value 1 for all predictions. The highest correlation coefficient R_{U^*} is reached by CD-adapco with 0.970, closely followed by UU-DTU, Vrije and the FRR model by LUT. The correlation coefficient of CMR's prediction is a few percent lower, while LUT's ACL model that only predicts one minimum scores lowest.

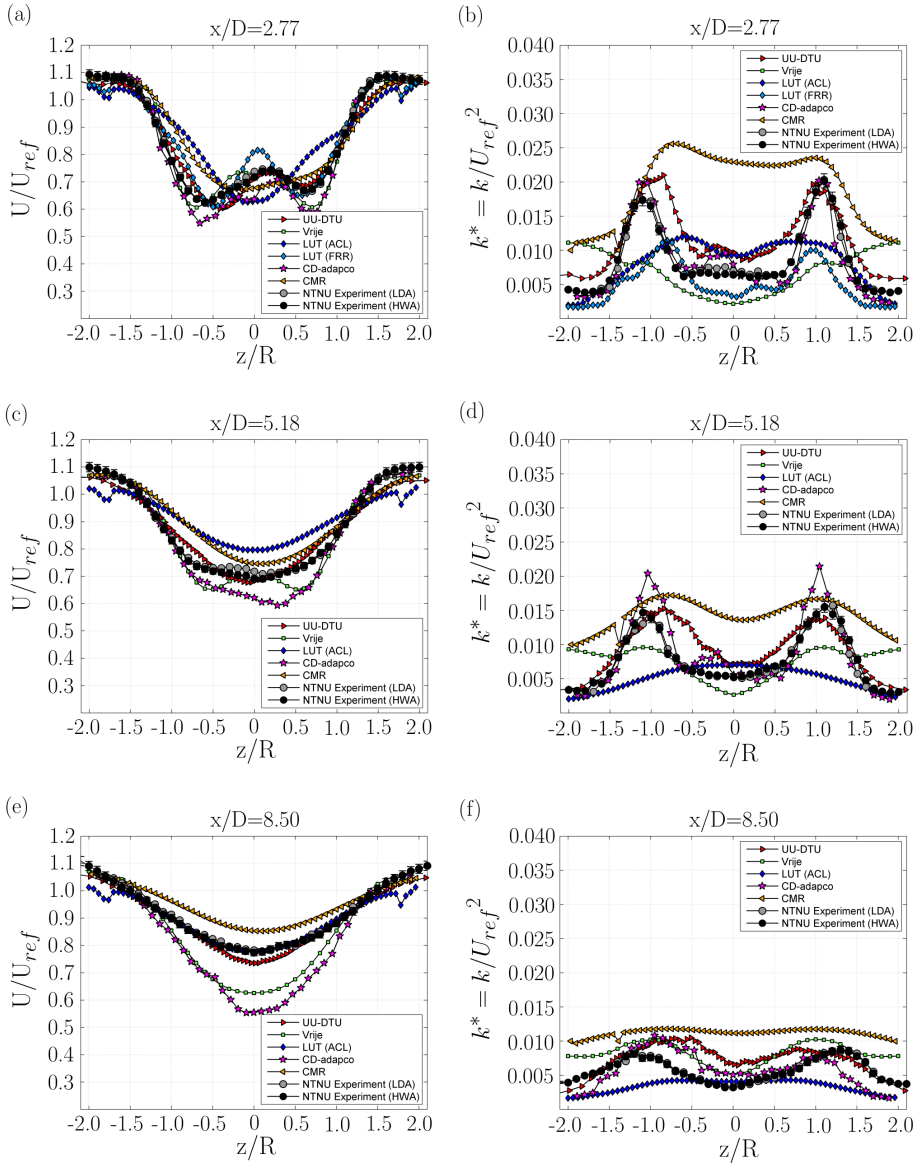

Fig. 8. Normalized mean velocity U/U_{ref} **(a, c, e)** and normalized turbulent kinetic energy k/U_{ref}^2 **(b, d, f)** in the wake $x/D = 2.77$ **(a, b)**, 5.18 **(c, d)** and 8.50 **(e, f)** behind T1 for test case setup B_3. The upstream turbine T1 is operated at $\lambda_{T1} = 6.0$. The reference velocity is $U_{ref} = 11.5\,\mathrm{m\,s^{-1}}$.

Very good predictions of the distribution of the turbulent kinetic energy are presented by CD-adapco as well as UU-DTU. Both simulations predict the magnitude and location of the two peaks around $z/R = \pm 1$ as well as the region of lower turbulence in the center of the wake very accurately. This is also reflected in the high values of the correlation coefficient $R_{k^*,CD-adapco} = 0.912$ and $R_{k^*,UU-DTU} = 0.911$ as shown in the upper left section of Table 6. LUT's FRR simulation manages to reproduce the general shape of the turbulence profile, but the levels are about 50 % below the measured turbulence values, resulting in a significantly lower correlation coefficient $R_{k^*,LUT(FRR)} = 0.720$. Similar levels are observed for LUT's ACL simulation, which additionally smears out the turbulence to the center of the wake, giving a correlation coefficient of $R_{k^*,LUT(ACL)} = 0.468$. It has been discussed that the tip-loss correction model included in the ACL model could have contributed to killing the turbulent peaks. Vrije's model based on a standard k-ω turbulence model underpredicts the peaks in the shear layer significantly; they are observed to be lower than the turbulence levels in the free stream flow, which are overpredicted by more than 1 order of magnitude. A very low and negative correlation coefficient of $R_{k^*,Vrije} = -0.008$ confirms this observation. The negative sign stems from a mainly negative correlation, meaning that turbulence levels are predicted to decrease from the free stream to the shear layer, while they actually increase in the experimentally measured profile. CMR's simulations predict too-high turbulence levels at the peaks, but surprisingly also in the wake center and in the unaffected free stream flow. A rather low correlation of $R_{k^*,CMR} = 0.417$ with the experimental data is achieved, while the normalized mean squared error $\mathrm{NMSE}_{k^*,CMR} = 0.698$ is significantly higher than for the other predictions. A possible reason for that blurry turbulence distribution could be the k-ε turbulence model used.

Moving downstream to $x/D_{T2} = 5.18$, a more Gaussian mean velocity profile with only one distinct minimum develops, as shown in Fig. **??** (c). The general shape of the mean velocity profile is in this case well predicted by almost all the simulations; only Vrije's simulation indicates a near-wake shape with two minima, but it still results in fairly good statistical performance measures, as presented in the middle left section of Table 6. Again, UU-DTU's model gives a very good match with the experimentally measured profiles, which is also reflected in very low FB_{U^*} and NMSE_{U^*} values. MG_{U^*} and VG_{U^*} approach the perfect value 1 very closely and a very high correlation coefficient of $R_{U^*,UU-DTU} = 0.964$ is calculated. CMR's model computes a slightly asymmetric mean wake profile, somewhat underpredicting the velocity deficit, but still performing well overall, as indicated in the correlation coefficient of $R_{U^*,CMR} = 0.937$. LUT modeled the $5.18\,D$ wake using their simpler ACL model, which considerably underpredicts the mean velocity deficit. The statistical performance measures are therefore slightly poorer than for the other predictions for this case, as shown in Table 6. CD-adapco's IDDES simulation overpredicts the mean wake velocity deficit to some extent, but still reaches the highest

correlation coefficient $R_{U^*,CD-adapco} = 0.971$. This might be due to the almost perfect correlation of the flow in the free stream and shear layer, although the mean velocities in the wake center are predicted somewhat lower than measured in the experiment.

The turbulence profiles for $x/D_{T2} = 5.18$ as presented in Fig. 8 (d) show a similar picture as seen earlier for $x/D_{T2} = 2.77$. The best predictions are made by CD-adapco's IDDES computation and UU-DTU's LES simulation, with both predictions resulting in very low error indicators FB_{k^*} and NMSE_{k^*}. A very high correlation coefficient $R_{k^*,CD-adapco} = 0.934$ to the experimental dataset is achieved by CD-adapco's prediction, although the turbulence peaks in the tip vortex region at $z/R = \pm 1.0$ are somewhat overpredicted. The magnitude of the peaks in the shear layer is almost perfectly predicted by UU-DTU's computation. However, compared to the experimental dataset, the peaks are too broad, which overpredicts the TKE in the wake center. This is reflected in a fairly good but somewhat lower correlation coefficient of $R_{k^*,UU-DTU} = 0.850$. Too-smooth turbulence profiles are predicted by CMR as well as LUT's ACL model, clearly overpredicting ($\mathrm{MG}_{k^*,CMR} = 0.483$) or underpredicting ($\mathrm{MG}_{k^*,LUT} = 1.495$) the mean turbulence levels. Vrije's turbulence prediction is very similar to the profile measured at $x/D = 2.77$ and again results in a rather low correlation coefficient of $R_{k^*,Vrije} = 0.371$.

A challenging test case is shown for the wake measured at downstream position $x/D_{T2} = 8.50$, only half a rotor diameter upstream of the rotor of T2 (Fig. 8 (e) and (f)). A smooth Gaussian mean velocity profile developed, while velocity deficit further decreased. Again, UU-DTU predicted the mean wake well, scoring the highest in the correlation coefficient $R_{U^*,UU-DTU} = 0.970$, as shown in the lower left section of Table 6. Although the mean profile predicted from LUT's ACL model matches the experimental values very well for this case, it is very similar to the profile that was already predicted for $5.18\,D$, where it clearly underpredicted the velocity deficit. Very low error values of $\mathrm{FB}_{U^*,LUT}$ and $\mathrm{NMSE}_{U^*,LUT}$ are computed, while $\mathrm{MG}_{U^*,LUT}$ and $\mathrm{VG}_{U^*,LUT}$ are close to 1. The correlation coefficient $R_{U^*,LUT} = 0.936$ is fairly good, but scores slightly lower than the other predictions. This might be due to obvious discontinuities of the mean velocity profile at $z/R = \pm 1.7$. CD-adapco's simulation strongly overpredicts the mean velocity deficit in the wake at this downstream distance. Surprisingly, the mean velocity deficit even grows noticeably in comparison to the mean wake profile predicted at $5.18\,D$. As shown in the numbers in the lower left section of Table 6, this obvious deviation is also resembled in significantly higher deviations of the mean geometrical bias MG_{U^*} and geometrical variance VG_{U^*} compared with the corresponding values of the other predictions. Vrije's simulation also overpredicts the mean velocity deficit for this case. Correspondingly, MG_{U^*} and VG_{U^*} give the second highest deviation from the experimentally measured profile. Remarkably, the averaged velocity deficit at $8.50\,D$ did not recover very much from the one predicted at $5.18\,D$. As already observed for smaller downstream distances, CMR also predicts a

slightly too low velocity deficit for 8.50 D. Almost all statistical performance measures for CMR, however, are significantly better at this further wake distance than at the closer measurement stations. Analyzing the turbulence profile as shown in Fig. 8 (f), the tip vortex peaks decay to about 50 % of the magnitude measured at 5.18 D. Both CD-adapco's IDDES simulation and UU-DTU's LES simulation give a fairly good approximation of the turbulence profile, as reflected in the highest correlation coefficients $R_{k^*,CD-adapco} = 0.811$ and $R_{k^*,UU-DTU} = 0.812$. Because the decay of the turbulence in the wake center is slightly underpredicted by both simulations, these values do not score as high as for the near-wake measurement stations. CMR overpredicts the turbulence levels at 8.50 D, smearing out the turbulence profile to an almost constant line. The acceptably good correlation coefficient $R_{k^*,CMR} = 0.804$ gives a wrong impression in this case because R is insensitive to addition, as introductory stated in Sect. 2.5.2, and the profile is basically shifted upwards. The high deviations from 1.00 in $\mathrm{MG}_{k^*,CMR}$ and $\mathrm{VG}_{k^*,CMR}$, however, indicate the significant mismatch. Conversely, LUT's ACL model underpredicts the turbulence considerably. Higher deviations in $\mathrm{MG}_{k^*,LUT}$ and $\mathrm{VG}_{k^*,LUT}$ are observed compared to for the other predictions. The turbulence levels predicted by Vrije's k-ω model at 8.50 D are observed to be very similar to those already predicted at lower separation distances. This indicates that the turbulent decay rate is not well captured for this case. Compared the lower separation distances, the predicted TKE profile matches better with the measured profile, resulting in acceptable statistical performance measures (e.g., $R_{k^*,Vrije} = 0.656$).

3.3 Test case C: high-turbulence nonuniform shear flow

Power and thrust predictions

For the last test case the complexity of the inflow conditions is increased. The inflow to the test section is no longer spatially uniform. Another custom-made grid with vertically increasing distance between the horizontal bars is placed at the test section inlet, generating a shear flow that can be approximated by the power law exponent $\alpha = 0.11$. The background turbulence of this grid is measured to be $\mathrm{TI} = 10.1\,\%$ over the rotor area at the location of the first turbine rotor. This makes the effects of shear flow well comparable to test case B since basically the same background turbulence level is predominating. For test case C the turbine power and thrust are compared only for one turbine separation distance, $x/D_{T2} = 5.18$. The power and thrust predictions for the shear flow test case are presented in Fig. 9, while the exact numerical values are shown in Table 7. Comparing the upstream turbine power curve of test case C (Fig. 9 (a)) to the upstream turbine power curve of uniform inflow test case B (Fig. 7 (c)), a very similar curve shape is observed. Taking a closer look, however, a slightly lower maximum power coefficient is measured in case C and a marginally earlier run-away point is found at $\lambda = 11.2$. This is assumed to

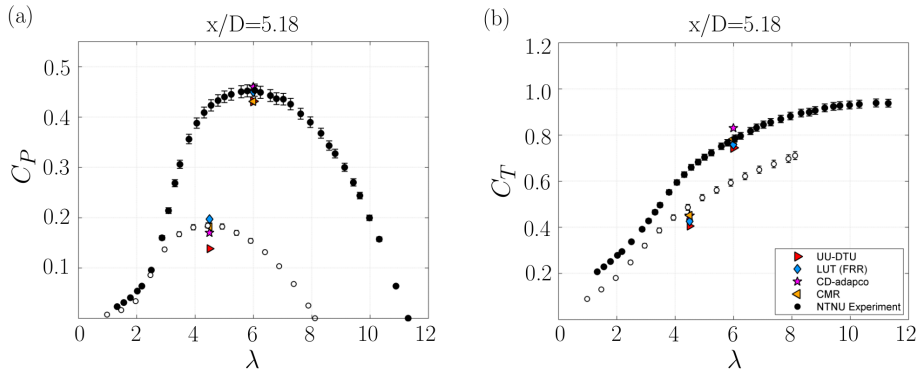

Fig. 9. Power coefficient C_P **(a)** and thrust coefficient C_T **(b)** for T1 (filled symbols) and T2 (empty circles) compared for test case C. The downstream turbine T2 is positioned at $x/D = 5.18$ downstream of T1, and the upstream turbine T1 is operated at $\lambda_{T1} = 6.0$. The reference velocity $U_{ref} = 11.5\,\mathrm{m\,s^{-1}}$ is the velocity experienced by T1 at hub height.

Table 7. Numerical values of power coefficient C_P and thrust coefficient C_T for test case C. The downstream turbine T2 is positioned at $5.18\,D$ downstream of T1. T1 is operated at $\lambda_{T1} = 6.0$ and T2 is operated at $\lambda_{T1} = 4.5$, referring to the reference velocity $U_{ref} = 11.5\,\mathrm{m\,s^{-1}}$ measured at hub height.

	Upstream turbine T1		Downstream turbine T2	
	$C_{P,T1}$	$C_{T,T1}$	$C_{P,T2}$	$C_{T,T2}$
UU-DTU ▶	0.432	0.745	0.139	0.405
LUT (FRR) ◆	0.451	0.758	0.197	0.426
CD-adapco ★	0.460	0.830	0.170	0.450
CMR ◀	0.431	0.782	0.182	0.452
Experiment ●○	0.453	0.785	0.184	0.486

stem from the fact that the reference velocity U_{ref} for this test case is defined at the center of the rotor at hub height. Due to the vertically nonlinear gradient in velocity distribution (see Fig. 4), the rotor equivalent wind speed (Wagner et al., 2014 [42]) is found to be slightly higher than U_{ref} measured at hub height. Therefore, the C_P and C_T calculations that are a priori defined to refer to the hub height reference wind speed $U_{ref} = 11.5\,\mathrm{m\,s^{-1}}$ are slightly lower for test case C than for test case B. The rotor-swept area is exposed to the same kinetic energy in cases B and C. The wind speed at the predefined reference height in test case C, however, does represent the rotor-averaged wind speed (for a more detailed investigation the reader is referred to Wagner et al., 2014).

The predictions of $C_{P,T1}$ at the turbine design operating point $\lambda_{T1} = 6.0$ are again very precise, showing a scatter of less than $\pm 5\,\%$ from the measured value. All the contributions predict a little lower $C_{P,T1}$ value than in test case B, confirming the tendency measured in the experiment. All the predictions of the thrust coefficient $C_{T,T1}$ also give a very good match with the experiment. In this case the spread is about $\pm 5\,\%$, which is just slightly outside the measurement uncertainty. Analyzing the performance results of the

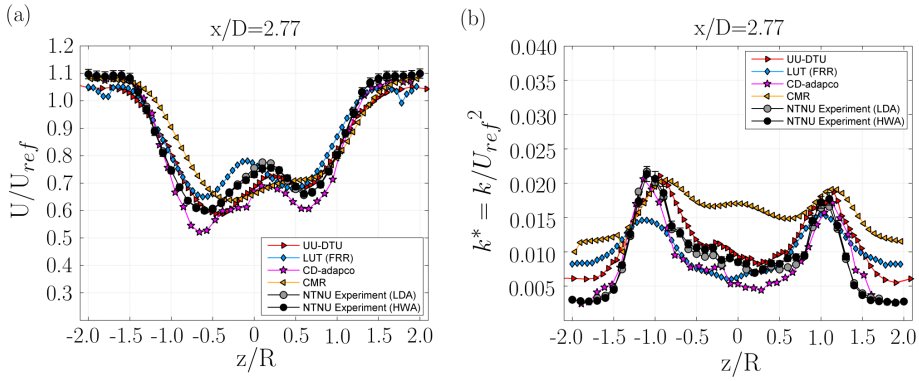

Fig. 10. Normalized mean velocity U/U_{ref} **(a)** and normalized turbulent kinetic energy k/U_{ref} **(b)** in the wake $x/D = 2.77$ behind T1 measured for test case C. The upstream turbine T1 is operated at λ_{T1} =6.0. The reference velocity $U_{ref} = 11.5\,\mathrm{m\,s^{-1}}$ is the velocity experienced by T1 at hub height.

Table 8. Statistical performance measures FB, NMSE, MG, VG and R of the normalized mean velocity U^* and normalized turbulent kinetic energy k^* predictions of the four different models for test case C. The wake flow is predicted at stream-wise measurement position $x/D = 2.77$ downstream of T1.

		FB_{U^*}	$NMSE_{U^*}$	MG_{U^*}	VG_{U^*}	R_{U^*}	FB_{k^*}	$NMSE_{k^*}$	MG_{k^*}	VG_{k^*}	R_{k^*}
UU-DTU	▶	0.042	0.002	1.038	1.003	0.965	−0.246	0.061	0.684	1.353	0.866
LUT (FRR)	◆	−0.005	0.000	0.986	1.004	0.952	−0.081	0.007	0.788	1.475	0.666
CD-adapco	★	0.061	0.004	1.072	1.007	0.972	0.068	0.005	1.041	1.170	0.795
CMR	◀	−0.002	0.000	0.993	1.009	0.898	−0.517	0.286	0.493	2.161	0.742

downstream turbine at $x/D_{T2} = 5.18$, the predictions are very good. The scatter in $C_{P,T2}$ is within ±7 %, except from UU-DTU's prediction, which is about 24 % lower than the experimental value. This seems to be a systematic deviation because significantly low values have been observed in test cases B already. The predictions of the thrust coefficient are very close to each other; however, they are up to 16 % lower than the measured value at $\lambda_{T2} = 4.5$. A general tendency to underpredict the thrust is again seen for all test cases (A, B, C), but the predictions are significantly closer compared to previous blind test comparisons.

Wake predictions

One single wake profile behind the upstream turbine is compared for test case C, in which the turbine is exposed to highly turbulent shear flow at the test section inlet. The mean and turbulent wake characteristics at $x/D_{T2} = 2.77$ behind the upstream turbine are compared in Fig. 10.

The mean velocity profile (Fig. 10(a)) has a very similar shape to the wake behind the same turbine exposed to uniform inflow of the same turbulence intensity (Fig. 8 (a)). The

mean velocity profile for shear inflow is also characterized by two distinct minima and a smooth transition from the wake to the free stream. Taking a closer look, the wake in case C is slightly skewed compared to the one measured in test case B. Especially the minimum velocity peak at $z/R \approx -0.7$ is somewhat lower compared to in test case B. It is assumed that low kinetic energy fluid that encounters the lower half of the rotor is transported into the measurement plane by the rotation in the wake. Turbulent mixing processes have most likely already evened out this effect at $x/D = 2.77$, yet a small difference is detectable.

Four different predictions are compared since Vrije did not simulate test case C. As observed for the earlier test cases, UU-DTU's LES simulation predicts the mean wake shape very accurately. The levels of the two minima are matched very closely, which is also reflected in a high correlation coefficient of $R_{U^*,UU-DTU} = 0.965$, as presented in Table 8. LUT's fully resolved rotor simulation gives a good agreement as well ($R_{U^*,LUT} = 0.952$); however, the skew in the wake is not as distinct as in the measured profile. CD-adapco predicts the skewed shape of the wake very well, as indicated in the highest correlation coefficient $R_{U^*,CD-adapco} = 0.972$ for this test case; however, the kinetic energy deficit is again slightly too high in the blade tip regions, which is reflected by slightly higher deviations in the fractional bias FB_{U^*} and geometrical mean bias MG_{U^*}. As previously observed for test case B, the two mean velocity minima are combined into one in CMR's simulations. Nevertheless, the simulations predict skew in the mean wake profile when compared to CMR's mean wake prediction for test case B. The correlation coefficient $R_{U^*,CMR} = 0.898$ is therefore slightly lower than for the other predictions, but it indicates good performance overall.

Analyzing the turbulent kinetic energy profiles for test case C (Fig. 10 (b)), obvious similarities to those of test case B (Fig.8 (b)) are observed. UU-DTU's simulations match the experimental results very accurately in the center and the tip region, whereas the turbulence level in the free stream is slightly too high. A similar correlation coefficient $R_{k^*,UU-DTU} = 0.866$ as for test case B is computed. LUT's FRR simulations underpredict one peak significantly, while the turbulence level in the free stream is significantly higher than in the measurements. This is also reflected in a poorer correlation with the experimental data since a correlation coefficient of $R_{k^*,LUT} = 0.666$ is achieved. The TKE predictions by CD-adapco are a very close match to the experimental values for this case. The turbulence peaks in the shear layer as well as the free stream level match the measured profiles very well, while the levels in the wake center are insignificantly underpredicted. The resulting correlation coefficient $R_{k^*,CD-adapco} = 0.795$ is almost the same magnitude as $R_{k^*,UU-DTU}$. Similar observations as in test case B are made for the turbulence predictions of CMR. Although the shear layer peaks are on the same level as the experimental values, the levels of turbulence in the wake center and the free stream flow are significantly

overpredicted. This observation is confirmed by significantly poorer MG_{k^*} and VG_{k^*} than for the other predictions, as shown in the right section of Table 8.

4 Discussion and conclusions

Five different research groups predicted the performance and wake flow between two in-line model wind turbines with a number of different simulation methods. The methods cover different approaches, ranging from commercial software to in-house developed codes. The effects of three different inflow conditions, low-turbulence uniform inflow (test case A), high-turbulence uniform inflow (test case B) and high-turbulence nonuniform shear inflow (test case C) are investigated.

The performance of the upstream turbine ($C_{P,T1}$, $C_{T,T1}$) was commonly well predicted by all predictions for all three inlet conditions, with an acceptable scatter of ± 5 to $\pm 7\,\%$ depending on the test case. However, the upstream turbine's performance was well-known from earlier blind tests. The scatter in the performance data of the downstream turbine at design conditions is generally observed to be larger. For $x/D = 5.18$ separation distance, the $C_{P,T2}$ predictions varied within $\pm 20\,\%$. By decreasing the separation distance to $x/D = 2.77$, the deviations from the measured results were reduced to $\pm 15\,\%$, while an increase in separation distance to $9.00\,D$ resulted in an even bigger scatter of $\pm 30\,\%$ in all the predictions. The scatter in the downstream turbine thrust coefficient is commonly seen to be smaller than in the power coefficient, while a tendency to underpredict the measured thrust value is observed. Nevertheless, a significant improvement in the predictions downstream of the turbine's performance is observed compared to earlier blind test experiments, in which the scatter was more than $\pm 100\,\%$ (Pierella et al., 2014 [27]) or $\pm 50\,\%$ (Krogstad et al., 2015 [20]).

Comparing wake profiles behind the upstream turbine, it can be concluded that both CD-adapco's IDDES computations and UU-DTU's LES simulation consistently deliver very accurate predictions of the experimentally measured mean and turbulent characteristics for all inflow conditions and separation distances. CD-adapco and UU-DTU clearly score highest in the statistical correlation coefficients for all the test cases. It seems that CD-adapco's IDDES simulations have a marginally better resolution of flow details, as reflected in very accurate predictions of the shape of the mean velocity and turbulence intensity profiles. This could be due to a better resolution of the small scales in the boundary layers of the rotor, hub and tower geometry, in which the IDDES technique takes advantage of a finer grid resolution in a RANS model. The very precise predictions of the wake shape are also confirmed in a marginally higher score of the correlation coefficients R_{U^*} and R_{k^*}, which describe correlation of the profile shape well but are insensitive to an offset or multiplication of the data points. Conversely, UU-DTU's simulations predicted

the levels of mean velocity deficit slightly better. CD-adapco's mean velocity results have the tendency to predict a marginally too-high velocity deficit, which is reflected in somewhat higher values of the mean geometrical bias MG_{U^*} and geometrical variance VG_{U^*} compared to UU-DTU's generally very precise prediction of the mean velocity levels.

The mean wake profiles are well predicted by the fully resolved k-ω SST simulations from LUT, whereas the rotor-generated turbulence in the wake is clearly underpredicted. Simulations by the same group based on an ACL approach are observed not to resolve the flow structures in sufficient detail, which is indicated by somewhat more poorly averaged correlation coefficients R_{U^*} and R_{k^*} for the ACL than for the FRR approach.

CMR's wake predictions based on the k-ε turbulence model mostly manage to approximate the levels of mean velocity deficit reasonably well; however, the details are often lost due to an overprediction of turbulent diffusion. This is also the case for the k-ω simulations by Vrije, in which acceptable approximations of the mean velocity deficit for high background turbulence inflows are predicted, while the predicted turbulence distributions are observed to be too smooth. The challenges of the more complex nonuniform shear flow were resolved fairly well by most of the simulations since most of them were able to predict a slightly skewed wake.

The discussion in the workshop disclosed that the quality of the wake predictions is dependent not only on the turbulence model, but rather a complex combination of user-dependent factors. These could be different methods of meshing, choice of turbulence parameters or force coefficients for rotor modeling, for example. Nevertheless, this blind test also confirms that it is possible to make very accurate performance and wake flow predictions given that the model and input parameters are chosen correctly.

Acknowledgments

The authors would like to thank NOWITECH for supporting the costs of the workshop.

References

1. Adaramola, M. S. and Krogstad, P. Å.: Experimental investigation of wake effects on wind turbine performance, Renew. Energ., 36, 2078–2086, doi:10.1016/j.renene.2011.01.024, 2011.

2. Ainslie, J. F.: Calculating the flowfield in the wake of wind turbines, J. Wind Eng. Ind. Aerod., 27, 213–224, doi:10.1016/0167-6105(88)90037-2, 1988.

3. Aksnes, N. Y.: Performance Characteristics of the NREL S826 Airfoil – An assessment of Re-independency and effect of inflow turbulence, Master's thesis NTNU, 2015.

4. Barthelmie, R. J., Hansen, K., Frandsen, S. T., Rathmann, O., Schepers, J. G., Schlez, W., Phillips, J., Rados, K., Zervos, A., Politis, E. S., and Chaviaropoulos, P. K.: Modelling and measuring flow and wind turbine wakes in large wind farms offshore, Wind Energy, 12, 431–444, doi:10.1002/we.348, 2009.

5. Bartl, J. and Sætran, L.: Experimental testing of axial induction based control strategies for wake control and wind farm optimization, J. Phys. Conf. Ser. B, Wind, wakes, turbulence and wind farms, 753:032035 doi:10.1088/1742-6596/753/3/032035, 2016.

6. Bartl, J., Pierella, F., and Sætran, L.: Wake Measurements behind an Array of Two Model Wind Turbines, Energy Procedia, 24, 305–312, doi:10.1016/j.egypro.2012.06.113, 2012.

7. Benedict, L. and Gould, R.: Towards better uncertainty estimates for turbulence statistics, Exp. Fluids, 22, 129–136, doi:10.1007/s003480050030, 1996.

8. Bruun, H. H.: Hot-wire anemometry, Principle and signal analysis, Oxford Science Publications, Oxford, UK, ISBN: 9780198563426, 1995.

9. Chang, J. and Hanna, S.: Air quality model performance evaluation, Meteorol. Atmos. Phys., 87, 167–196, doi:10.1007/s00703-003-0070-7, 2004.

10. Crespo, A., Hernandez, J., Fraga, E., and Andreu, C.: Experimental validation of the UPM computer code to calculate wind turbine wakes and comparison with other models, J. Wind Eng. Ind. Aerod., 27, 77-88, doi:10.1016/0167-6105(88)90025-6, 1988.

11. Drela, M.: Xfoil 6.99, available at: http://web.mit.edu/drela/Public/web/xfoil/ (last access: 7 February 2017), 2013.

12. Eriksen, P. E.: Rotor wake turbulence – An experimental study of a wind turbine wake, Doctoral thesis at NTNU, 34, ISBN 978-82-326-1408-0, 2016.

13. Frandsen, S., Barthelmie, R., Pryor, S., Rathmann, O., Larsen, S., Højstrup, J., and Thøgersen, M.: Analytical modelling of wind speed deficit in large offshore wind farms, Wind Energy, 9, 39–53, doi:10.1002/we.189, 2006.

14. Hallanger, A. and Sand, I. Ø.: CFD Wake modelling with a BEM wind turbine sub-model, Modeling, Identification and Control, 34, 19–33, ISSN 1890–1328, 2013.

15. Hsu, S. A., Meindl, E. A., and Gilhousen, D. B.: Determining the power-law wind-profile exponent under near-neutral stability conditions at sea, J. Appl. Meteorol., 33, 757–765, doi:10.1175/1520-0450, 1994.

16. Jensen, N. O.: A note on wind generator interaction, Technical Report, Risø, RISØ-M-2411, available at: www.orbit.dtu.dk/fedora/objects/orbit:88807 (last access: 7 February 2017), 1983.

17. Kocer, G., Mansour, M., Chokani. N., Abhari, R. S., and Müller, M.: Full-Scale Wind Turbine Near-Wake Measurements Using an Instrumented Uninhabited Aerial Vehicle, J. Sol. Energ. Eng., 133,041011, doi:10.1115/1.4004707, 2011.

18. Kumer, V. M., Reuder, J., Svardal, B., Sætre, C., and Eecen, P.: Characterisation of Single Wind Turbine Wakes with Static and Scanning WINTWEX-W LiDAR Data, Energy Procedia, 80, 245–254, doi:10.1016/j.egypro.2015.11.428, 2015.

19. Krogstad, P. Å. and Eriksen, P. E.: "Blind test" calculations of the performance and wake development for a model wind turbine, Renew. Energ., 50, 325–333, doi:10.1016/j.renene.2012.06.044, 2013.

20. Krogstad, P. Å., Sætran, L., and Adaramola, M. S.: Blind Test 3 calculations of the performance and wake development behind two in-line and offset model wind turbines, J. Fluid. Struct., 52, 65–80, doi:10.1016/j.jfluidstructs.2014.10.002, 2015.

21. Larsen, G. C., Madsen, H. A., Larsen, T. J., and Troldborg, N.: Wake modeling and simulation, Technical Report, Risø-R-1653(EN), available at: www.orbit.dtu.dk/fedora/objects/orbit:80992 (last access: 7 February 2017), 2008.

22. Ning, S. A.: A simple solution method for the blade element momentum equations with guaranteed convergence, Wind Energy, 17, 1327–1345, doi:10.1002/we.1636, 2014.

23. Maal, G. T.: Parameter study of electric power production in wind farms – experiments using two model scale wind turbines, Master's thesis NTNU, available at: www.brage.bibsys.no/xmlui/handle/11250/2350000 (last access: 7 February 2017), 2014.

24. Medici, D. and Alfredsson, P. H.: Measurements on a Wind Turbine Wake: 3-D Effects and Bluff Body Vortex Shedding, Wind Energy, 9, 219–236, doi:10.1002/we.156, 2006.

25. Mendonça, F., Baris, O., and Capon, G.: Simulation of Radial Compressor Aeroacoustics Using CFD, ASME Turbo Expo 2012, Turbine Technical Conference and Exposition, Copenhagen, Denmark, 8, 1823–1832, Paper No. GT2012-70028, doi:10.1115/GT2012-70028, 2012.

26. Ostovan, Y., Amiri, H., and Uzol, O.: Aerodynamic Characterization of NREL S826 Airfoil at Low Reynolds Numbers, RUZGEM Conference on Wind Energy Science and Technology, METU Ankara Campus, Ankara, Turkey, 2013.

27. Pierella, F., Krogstad, P. Å., and Sætran, L.: Blind Test 2 calculations for two in-line model wind turbines where the downstream turbine operates at various rotational speeds, Renew. Energ., 70, 62–77, doi:10.1016/j.renene.2014.03.034, 2014.

28. Prytz, E., Huuse, Ø., Müller, B., Bartl, J., and Sætran, L.: Numerical Simulation of Flow around the NREL S826 Airfoil at Moderate Reynolds numbers Using Delayed Detached Eddy Simulation (DDES), AIP Conference Proceedings 07/2017; vol. 1863(1):560086, 2017.

29. Sætran, L. and Bartl, J.: Invitation to the 2015 "Blind test 4" Workshop, Technical document NTNU, available at: www.sintef.no/globalassets/project/nowitech/events/bt4_invitation2015.pdf, (last access: 7 February 2017) 2015.

30. Sagmo, K. F., Bartl, J., and Sætran, L.: Numerical simulations of the NREL S826 airfoil, J. Phys. Conf. Ser., 753:082036, doi:10.1088/1742-6596/753/8/082036, 2016.

31. Sanderse, B., van der Pijl, S. P., and Koren, B.: Review of computational fluid dynamics for wind turbine wake aerodynamics, Wind Energy, 14, 799–819, doi:10.1002/we.458, 2011.

32. Sarmast, S. and Mikkelsen, R.: The experimental results of the NREL S826 airfoil at low Reynolds numbers, Technical Report, available at: www.urn:nbn:se:kth:diva-120583 (last access: 7 February 2017), 2013.

33. Sarmast, S., Dadfar, R., Mikkelsen, R. F., Schlatter, P., Ivanell, S., Sørensen, J. N., and Henningson, D. S.: Mutual inductance instability of the tip vortices behind a wind turbine, J. Fluid Mech., 755, 705–731, doi:10.1017/jfm.2014.326, 2014.

34. Schepers, J. G., Boorsma, K., and Snel, H.: IEA Task 29 MexNext: analysis of wind tunnel measurements from the EU project Mexico, Proceedings of The Science of Making Torque from Wind, 169–178, 2010.

35. Schepers, J. G., Boorsma, K., and Munduate, X.: Final Results from Mexnext-I: Analysis of detailed aerodynamic measurements on a 4.5 m diameter rotor placed in the large German Dutch Wind Tunnel DNW, J. Phys. Conf. Ser., 555, 012089, doi:10.1088/1742-6596/555/1/012089, 2014.

36. Schümann, H., Pierella, F., and Sætran, L.: Experimental Investigation of Wind Turbine Wakes in the Wind Tunnel, Energy Procedia, 35, 285–296, doi:10.1016/j.egypro.2013.07.181, 2013.

37. Somers, D.M.: The S825 and S826 Airfoils, Technical Report NREL/SR-500-36344, available at: www.wind.nrel.gov/airfoils/Documents/S825,S826_Design.pdf (last access: 7 February 2017), 2005.

38. Sørensen, J. N. and Shen, W. Z.: Numerical modeling of wind turbine wakes, J. Fluid Eng., 124, 393–399, doi:10.1115/1.1471361, 2002.

39. Talmon, A. M.: The wake of a horizontal-axis wind turbine model, measurements in uniform inflow and in a simulated atmospheric boundary layer, TNO Data report, available at: www.publications.tno.nl/publication/100176/YosHZP/85-010121.pdf, (last access: 7 February 2017) 1985.

40. Trujillo, J. J., Seifert, J. K., Würth, I., Schlipf, D., and Kühn, M.: Full-field assessment of wind turbine near-wake deviation in relation to yaw misalignment, Wind Energ. Sci., 1, 41–53, doi:10.5194/wes-1-41-2016, 2016.

41. Van Leer, B: Towards the ultimate conservative differencing scheme II: Monotonicity and conservation combined in a second–order scheme, J. Comput. Phys., 14, 361–370, 1974.

42. Wagner, R., Cañadillas, B., Clifton, A., Feeney, S., Nygaard, N., Poodt, M., St. Martin, C., Tüxen, E., and Wagenaar, J. W.: Rotor equivalent wind speed for power curve measurement – comparative exercise for IEA Wind Annex 32, J. Phys. Conf. Ser., 524, 012108, doi:10.1088/1742-6596/524/1/012108, 2014.

43. Wheeler, A. J. and Ganji, A. R.: Introduction to engineering experimentation, Third edition, Upper Saddle River, NJ, USA, Pearson/Prentice Hall, XI, ISBN-13:987-0-13-511314-1, 2004.

PAPER 6

Performance of the NREL S826 airfoil at low to moderate Reynolds numbers: A reference experiment for CFD models

Jan Bartl, Kristian Sagmo, Tania Bracchi, Lars Sætran

Original version in review in
European Journal of Mechanics - B/Fluids

PAPER 6

Performance of the NREL S826 airfoil at low to moderate Reynolds numbers: A reference experiment for CFD models

Jan Bartl, Kristian Sagmo, Tania Bracchi, Lars Sætran

Department of Energy and Process Engineering, Norwegian University of Science and Technology, 7491 Trondheim, Norway

In review in European Journal of Mechanics - B/Fluids

Submitted on 21 December 2017, in review

Summary. Lift, drag and surface pressure measurements are performed on a wing section of the NREL S826 wind turbine airfoil at eight Reynolds numbers ranging from 0.5×10^5 to 6.0×10^5. Alongside with the measurements two types of Reynolds averaged Navier-Stokes (RANS) simulations are performed, one of which includes a laminar to turbulent transition model. The lift and drag characteristics are observed to be dominated by low Reynolds number effects for $Re < 0.7 \times 10^5$, related to the presence of laminar separation bubbles (LSBs) on the suction side of the profile. For $Re \geq 0.7 \times 10^5$ the airfoil's performance is rather independent of the Re-number for the present free stream turbulence intensities, while significantly higher peak lift is measured than in earlier experiments on the same airfoil. At high angles of attack, strong three-dimensional spanwise surface flow distribution reminiscent of a single stall cell is observed. The RANS simulations in a two-dimensional domain including the Langtry-Menter $\gamma - Re_\theta$ transition model accurately predict lift and drag coefficients as long as the flow is fairly attached. Further, the $\gamma - Re_\theta$ model simulations are observed to predict the location and average size of the LSBs in this region.

1 Introduction

With the advance of computational fluid dynamics (CFD) in all fields of engineering aerodynamics, well-defined experimental data sets for the validation of computational setups are needed. The objective of this combined experimental and computational study is twofold.

The first objective is to provide experimentally obtained airfoil polars at low to medium Reynolds numbers for the NREL S826, which serve as important input data for Blade Element Momentum (BEM) or Actuator Line (ACL) simulations of wind turbine rotors. The BEM approach is the most commonly used method in the design process of wind turbine rotors, having the big advantage of a very fast simulation of the rotor's aerodynamic performance [23]. As an input, BEM simulations require aerodynamic polars for the Reynolds number range the blade elements are operating in. The NREL S826 airfoil was originally designed for mid-scale wind turbines at the National Renewable Energy Laboratory (NREL). A detailed description of the airfoils characteristics is given in [22]. Therein, the geometry is specified and the performance characteristics for chord length based Reynolds numbers from $Re_c = 1.0 \times 10^6$ to 3.0×10^6 are assessed. Since 2011, four blind test experiments on the performance and wake development behind model wind turbines of a rotor diameter of $D = 0.90\,m$ have been carried out at the Norwegian University of Science and Technology [6, 15, 7, 1]. The model turbines rotors were designed based on the NREL S826 airfoil, however, much smaller Reynolds numbers of the magnitude $Re_{c,tip} = 1.0 \times 10^5$ were prevailing for these model experiments. It was concluded that some of the uncertainty in the prediction of turbine performance and wake data could be subscribed to different sets of airfoil polars used in the simulations. Therefore, two experimental studies on the airfoils performance at low to moderate Reynolds numbers have been conducted in the wake of the blind test workshops. Sarmast et al. [21] and later Sarlak et al. [20] performed experiments on a two dimensional S826 wing section of the chord length c_L =0.10 m at Denmarks Technical University (DTU). They observed abrupt separation effects at low angles of attack already at $Re_c < 1.0 \times 10^5$. Another experimental set of S826 airfoil data is available by Ostovan et al. [14] realized at the Middle East Technical University (METU) in Turkey. They measured lift and drag coefficients from $Re_c = 0.72 \times 10^5$ to $Re_c = 1.45 \times 10^5$ on a wing section of a chord length of c_L=0.20 m. No indications of abrupt separation effects at the lowest Reynolds numbers were observed in this experiment, although a much lower peak lift than in the DTU experiments was measured.

The measured lift and drag data are aimed to serve as input data for BEM and ACL simulations of small-scale wind turbines, such as the blind test experiments. In particular, the polars should give an accurate account of the airfoils performance characteristics under the specific flow conditions achieved at the NTNU wind tunnel.

A related challenge for CFD simulation methods is to accurately predict the point of transition between the laminar and turbulent boundary layer on the blade surface. For the investigated low to moderate Reynolds numbers in this experiment the initial boundary layer on the airfoil surface develops typically laminar. The laminar boundary layer separates when exposed to a large adverse pressure gradient and forms a LSB. Further downstream, the laminar shear layer destabilizes and undergoes a transition to turbulent flow [13]. Due to a high momentum transport perpendicular to the airfoil surface the shear layer is able to re-attach. According to Kerho and Bragg [5] this happens as soon as turbulent mixing has eliminated the reverse near-surface flow. Hence, the second objective is that the present data shall serve as a reference experiment for state-of-the-art CFD modeling. The numerical computations reported here builds up on a previous study presented by Sagmo et al. [18], in which a initial experimental dataset was used for reference. The present study includes the final, repeated experimental dataset and also adds computations using the $\gamma - Re_\theta$ laminar to turbulent transitional model presented by Langtry and Menter [9]. An updated set of fully turbulent simulations using the Realizable $k-\epsilon$ turbulence model is included for direct comparison. Other numerical simulations of the NREL S826 airfoil were performed by Sarlak et al. [20] as well as Cakmakcioglu et al. [2]. Cakmakcioglu et al. carried out simulations in a 2D and 3D domain using a Langtry-Menter ($\gamma - Re_\theta$) transition model as well as a Delayed Detached Eddy Simulation (DDES) in the stall region. As expected, they observed increased accuracy at stall with 3D simulations. At stall, DDES did not give improved results compared to 3D-transitional modeling, but was computationally more expensive. Sarlak et al. [20] performed three-dimensional Large Eddy Simulations on a S826 wing and compared them to DTU's experimental results. The LES simulations resulted in higher lift predictions compared to experimental results, especially at the onset of stall. They furthermore discussed hysteresis effects while changing the angle of attack as well as three dimensional flow effects at stall [19]. Early experiments related to the 3D flow effects on a rectangular plan-form wing beyond stall were conducted by Winkelmann and Barlow [27], as well as Weihs and Katz [25]. A more recent comprehensive study was conducted by Manolesos et al. [12] which combined experimental and computational investigations. Manolesos found inherently unstable stall cells on the wing's suction side (aspect ratio AR=2) at higher angles off attack and managed to reproduce experimental results computationally. Furthermore, the study indicated a strong interaction of the stall cell vortices with the trailing edge line vortices, which caused a inward deflection and consequently a strong spanwise variation of the force coefficients. In a continuation of this work, Manolesos and Voutsinas [11] also investigated the influence of Reynolds number, aspect ratio and angle of attack on the formation of stall cells.

The presented set of experimental data shall thus serve as a well-documented reference experiment for validation of CFD tools, offering a detailed database of the flow fea-

Table 1. Turbulence Intensity levels (TI) and Integral turbulent length scales (L_{uu}) at the test rig location for all Reynolds numbers.

Re_c [−]	U_{ref} [m/s]	TI [%]	L_{uu} [m]
0.5×10^5	1.47	0.71	0.0078
0.7×10^5	2.36	0.70	0.0072
1.0×10^5	3.17	0.70	0.0066
2.0×10^5	6.82	0.44	0.0214
3.0×10^5	9.91	0.32	0.0575
4.0×10^5	14.32	0.30	0.0867
5.0×10^5	18.30	0.27	0.1276
6.0×10^5	22.27	0.26	0.2828

tures around the NREL S826 airfoil. In this paper, we give an example on steady state RANS modeling of transitional effects such as laminar separation bubbles as well as three-dimensional flow effects at the onset of stall. The capability of predicting transitional effects by the Langtry-Menter $\gamma - Re_\theta$ transitional model is tested and the influence on the airfoil performance analyzed.

2 Experimental setup

2.1 Wind tunnel & inflow conditions

The experimental data of this study are measured in the closed-loop wind tunnel at NTNU in Trondheim. The rectangular test section of the wind tunnel is 2.71 m broad, 1.81 m high and 11.15 m long. The wind tunnel inlet speed is controlled by an inlet contraction, which is equipped with static pressure holes at the circumferences at two defined cross sections. The wind tunnel is driven by a $220kW$ fan located downstream of the test section being able to generate maximum wind speeds of up to $U_{max} \approx 25\,m/s$.
In order to assess the turbulence intensity level and integral turbulent length scale in the inflow, hot-wire measurements in the empty wind tunnel were performed at the wing position for all inflow Reynolds numbers. Table 1 shows the turbulence intensity levels measured in the empty tunnel for the whole Reynolds number range. Outside the wind tunnel boundary layers, the mean velocity in the empty tunnel was found to be uniform within 0.6% for all Reynolds numbers. The boundary layer thickness at wind tunnel walls is measured to be y_{BL}=0.220 m for a Reynolds number of $Re_c = 3.0 \times 10^5$ from the wind tunnel floor at the wing position.

2.2 Geometry and test rig setup

The NREL S826 airfoil was originally designed by Somers [22] at the National Renewable Energy Laboratory to be used at the blade tip of horizontal-axis wind turbines of a rotor

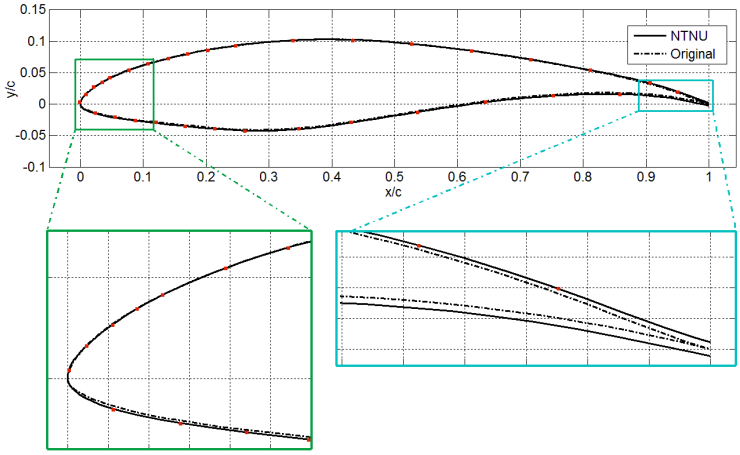

Fig. 1. Comparison of the physically produced airfoil coordinates (NTNU) with the original design coordinates as designed by NREL (Original). The red points indicate the locations of the pressure taps around the circumference at mid-span.

diameter of $20 - 40m$. The primary objective was to obtain a maximum lift coefficient $C_L > 1.40$ at $Re = 1.0 \times 10^6$, low sensitivity to roughness and low profile drag. The airfoil was designed for high Reynold numbers $Re \geq 1.0 \times 10^6$, but was then utilized for Reynolds numbers one magnitude lower in NTNU's Blind test experiments. This discrepancy in Reynolds number then motivated the investigation of the airfoil's characteristics in transitional flow regimes.

The physical geometry of the airfoil for this experiment is CNC-milled from the synthetic polyurethane based board material called ebaboard 1200. Several layers of black gloss paint are thereafter laid on the raw material. A surface roughness measurement confirms a hydraulically smooth surface, i.e. the mean roughness depth of the surface is within the viscous sublayer and thus not affecting the boundary layer profile or skin friction.

The cross-section is based on the original NREL S826 profile coordinates. As it was not possible to produce an infinitely thin trailing edge, a trailing edge thickness of $d_{TE} = 2\,mm$ was defined, to which the produced profile is converging to. Figure 1 shows a comparison of the original profile as designed by NREL and the actually produced profile at NTNU. The actual surface coordinates of the model were measured by a high-resolution digitizing arm. Furthermore, the location of the 32 pressure taps on the wing surface at midspan are indicted in Figure 1. The S826 wing test rig is set up vertically in the test section and has a chord length of $c = 0.45\,m$ and a total height of $h_{total} = 1.78\,m$. In Figure 2 the test rig is set up in the wind tunnel is shown. The wing consists of three main parts. The main mid-section is connected through rods in the inside of the wing to a 6-components force balance located underneath the wind tunnel floor. Additionally, there are two dummy wing

Table 2. Geometrical measures of the S826 wind test rig.

Airfoil chord length	$c_L = 0.45\,\mathrm{m}$
Total wing height	$h_{total} = 1.78\,\mathrm{m}$
Mid-section height	$h_{main} = 1.18\,\mathrm{m}$
Dummy height	$h_{dummy} = 0.30\,\mathrm{m}$
Gap between dummies and main part	$\Delta h_{gap} = 0.002\,\mathrm{m}$
Pressure taps location	$h_{taps} = 0.89\,\mathrm{m}$
Total wing aspect ratio	$AR = 3.95$

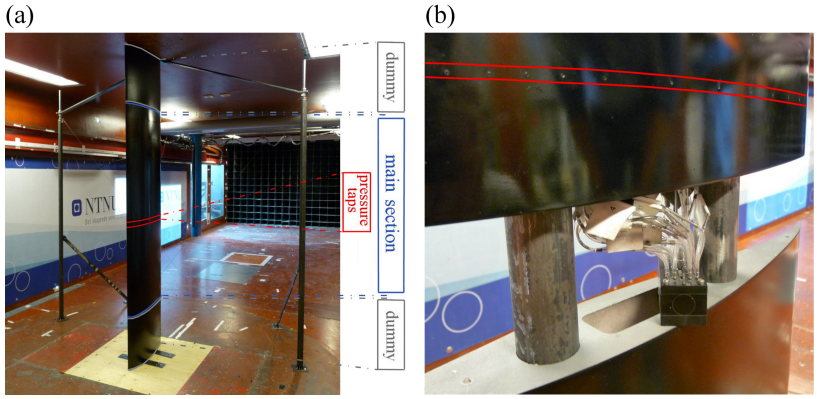

Fig. 2. (a) The S826 test rig set up in wind tunnel test section. The rig consists of three parts: the main part in the center and two dummy parts at the wind tunnel floor and roof. **(b)** Detail: The pressure taps (marked between the red lines) and the 32-channel pressure transducer inside the opened wing.

sections near the floor and roof of the tunnel. As there is a gap of about $2mm$ between main and dummy parts, these dummies do not touch the main wing section nor the force balance. The dummy parts are designed in order to cancel out interaction of the central wing section with the boundary layer flow near the test section's roof and floor.
At mid-span the wing is equipped with 32 pressure taps around the circumference as indicated in Figure 2. All important geometrical measures are summarized in Table 2.

2.3 Velocity, force and pressure measurements

A Pitot-static probe installed $x = 1\,m$ upstream of the test rig is used to obtain the free-stream velocity. The density of air is calculated from the temperature measured by a thermocouple inside the wind tunnel and the ambient pressure measured by a mercury manometer.
The mean and fluctuating surface pressure is measured by 32 pressure taps which are located around the wing's mid-span. The taps are connected to a Electronically Scanned Pressure (ESP) transducer of the type DTC Initium mounted inside the wing as shown in Figure 2 (b). The sensors of the DTC Initium pressure scanner are made of piezo-

resistive silicon which are sensitive to thermal variation, which is compensated for by digital temperature compensation in the system. The pressure scanners were periodically reset to minimize zero voltage drift. Thus, errors in pressure within ±0.03% of the full scale pressure range are ensured. Measurements are sampled for $t_{sample} = 60\,s$ with a sampling rate of $f_{Sample} = 500\,Hz$. From the measured surface pressure, distributions the normalized pressure, lift, drag were calculated by the following equations:

$$C_p = \frac{p}{\frac{1}{2}\,\rho\,U^2}, \tag{1}$$

$$C_{L,p} = \frac{f_L}{\frac{1}{2}\,\rho\,c_L\,U^2}, \tag{2}$$

$$C_{D,p} = \frac{f_D}{\frac{1}{2}\,\rho\,c_L\,U^2}. \tag{3}$$

Lift characteristics are measured by six-components force balance, on which the wing was mounted. Measurements were taken over a t_{sample} =60 s time interval and sampling rate of f_{Sample}=500 Hz. Automatic rotation of the force balance provided angle of attack in the range α=−15° to +30°. Measured lift forces were normalized by the following equation:

$$C_{L,fb} = \frac{F_L}{\frac{1}{2}\,\rho\,c_L\,h\,U^2}. \tag{4}$$

A wake rake measuring total pressure was placed at $x = 0.7c$ distance downstream of trailing edge to measure pre-stall drag. 20 probes with a uniform spacing of $\Delta z = 10\,mm$ across the wake at the same height as the pressure taps. It has to be noted that the method of momentum deficit integration is more reliable than direct force measurements, but not considered to be reliable when the profile is stalled as the pressure probes are not capable of capturing the three-dimensional motions of the wake. Alternatively, the drag calculated from surface pressure integration or direct force measurement can be used for $\alpha > 15°$. For these high angles the pressure drag becomes dominant and is thus deemed to give a more accurate drag estimation. The static Pitot-probe upstream of the wing is used as reference pressure for the wake rake probes:

$$C_{D,wr} = \frac{F_D}{\frac{1}{2}\,\rho\,c_L\,h\,U^2}. \tag{5}$$

2.4 Statistical measurement uncertainties

Uncertainties in the lift- and drag measurement were calculated according to the methods described in [26]. Lift uncertainties were calculated from a systematic error estimate in velocity and force cell calibration as well as precision errors assessed from standard deviations in the single measurements. The resulting uncertainties were observed to rise in stalled conditions were plotted as errorbars in Figure 6. At its highest the total uncertainty in lift was calculated to be 3.5%. For the calculation of uncertainties in drag a minor decrease in static pressure along the wing tunnel had to be taken into account when assessing the wake momentum loss. Due to higher wake pressure fluctuations, larger uncertainties were computed for stalled angles of attack. Consequently, a significantly higher relative uncertainty of up to 20% was measured for the drag coefficient. The angle of attack could be adjusted with a measured accuracy of approximately $\Delta\alpha$=$\pm$0.25°. The angle subtended by the mid chord line due to the trailing edge thickness of $2mm$ adds a $\pm$0.125° uncertainty in the angle of attack.

3 Computational methods

3.1 Numerical models

The implementation and calibration of $\gamma - Re_\theta$ transition model into StarCCM+ is described in the paper by Malan et al. [10]. The Realizable $k - \epsilon$ turbulence model was run with a two-layer approach, which blends the two-equation model into the one equation model formulated by Wolfshtein [28] near the wall. The selected segregated flow solver was of second order, with an up-wind convection scheme implemented by a SIMPLE-like algorithm [3]. Moreover, the model settings assumed an isothermal, compressible and ideal gas.

3.2 Computational domain and grid

An illustration of the grids used is presented in Figure 3. The numerical study includes computational results on both a 2D and 3D grid. The 3D grid is essentially an extrusion of the 2D grid profile. An o-type mesh is used around the wing profile, with tangential wall normal extrusion layers extending 10 mm outwards to cover the boundary layer. A total of 42 to 62 wall layers were used. The bulk mesh was made up of trimmed, hexagonal cells, with multiple control volumes to contain cell growth. In order to facilitate the use of the $\gamma - Re_\theta$ transition model, all grids were designed to have wall $y^+ < 1$ over the airfoil surface. The grids were designed for a wall normal cell layer growth rate of 1.1, as it is recommended in [8]. The wing surface was modeled as hydraulically smooth, as justified by surface roughness measurements on the model used in the experiment. Both 2D and 3D

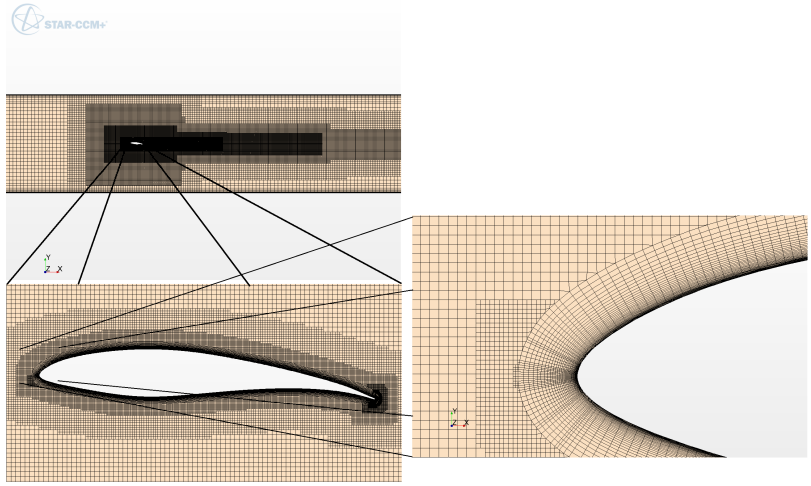

Fig. 3. Illustration of grid cell distribution for mid-span x-y-plane used for most simulations, both 2D and 3D. Simulations for $\alpha = 12°$ required a finer stream wise spacing of cells near the leading edge than shown here, due to a small laminar separation bubble.

Table 3. Different surface cell sizes in percentage of the chord length. δ_{span} and δ_{chord} denote the span-wise and chord-wise cell spacing. $\delta_{w.cell}$ denotes the cell size in the wake behind the airfoil, stretching four chord lengths downstream. $\#_{tot}$ denotes the total cell count for each grid and $\triangle_{CPU}$ denotes the accumulated CPU time per iteration in seconds, referred to $\gamma - Re_\theta$ simulations. y^+_{max} denotes the maximum y^+ value of the first wall grid layer.

Grid	y^+_{max}	δ_{span}	δ_{chord}	$\delta_{w.cell}$	$\#_{tot}$	$\triangle_{CPU}$
2D coarse	0.595	-	(0.0129-0.35)%	(0.086-2.73)%	$6.88 \cdot 10^4$	1.17 s
2D medium	0.604	-	(0.0032-0.36)%	(0.043-1.39)%	$1.15 \cdot 10^5$	1.59 s
2D fine	0.614	-	(0.0020-0.17)%	(0.043-0.67)%	$3.04 \cdot 10^5$	4.82 s
3D medium	0.590	(0.087-0.35)%	(0.0013-0.35)%	(0.022-1.38)%	$5.33 \cdot 10^7$	1160 s

grids are designed to match the exact dimensions of the NTNU wind tunnel test section used in the experiments. Simulations using the $\gamma - Re_\theta$ transition model requires a finer mesh resolution of the wing boundary layer compared to fully turbulent simulations. In order to facilitate this, all 3D simulations were run using a half domain, imposing symmetry conditions along the mid-span location. A summary of some key grid parameters is shown in Table 3. Another discrepancy worth pointing out was that the gap modeled between the airfoil measurement section and the wall dummies was exaggerated to 4 mm in the simulations, so that a impact estimation could be made. Results comparing lift and drag coefficients computed from both continuous and split airfoil test section geometries are included in Table 6, Section 4.4.

3.3 Boundary conditions & wall treatment

The turbulence intensity (TI) and turbulence length scale (L_{uu}) are specified at the domain inlet in Star-CCM+. For this study the measured TI and L_{uu} values as listed in Table 1 were set at the inlet rather than the wing location. Due to the decay of turbulence a small error in the TI at the wing position is generated. However, for the present simulations the error generated was found to be small as shown in a sensitivity study included in Section 4.3, Table 5. The parameters turbulent kinetic energy k, turbulent dissipation rate ϵ and the specific turbulent dissipation rate ω are derived from TI and L_{uu} by the following relations:

$$k = \frac{3}{2}(TIv)^2, \tag{6}$$

$$\epsilon = \frac{C_\mu^{3/4} k^{3/2}}{L_{uu}}, \tag{7}$$

$$\omega = \frac{\sqrt{k}}{L_{uu}(\beta^*)^{1/4}}. \tag{8}$$

Here, v is the turbulent velocity scale (set to $\approx$3.17 ms^{-1} for $Re = 1.0 \times 10^5$), and C_μ and β^* are model coefficients. A dynamic pressure outlet of one atmosphere was set on the rear wall boundary. A previous investigation of the sensitivity of the downstream position of the pressure outlet using 2D simulations showed negligible effect on the overall drag and lift coefficients [18].

All the present simulations were shown to have wall y^+ <1, both for 2D and 3D. This induced a wall treatment similar to a low y^+ treatment. The low wall y^+ treatment in STARCCM+ makes no explicit modeling assumptions, and sets the the velocity distribution in the viscous sub-layer as $u^+_{laminar} = y^+$ [3]. The velocity distribution in the logarithmic layer is set to

$$u^+_{turbulent} = \frac{1}{\kappa} ln(Ey^+), \tag{9}$$

in which the von Karman constant is set to $\kappa = 0.42$, while E is set to the default constant $E = 0.9$. The definition of the dimensionless u^+ and y^+ stems from the usual *law of the wall* [24].

Table 4. Gradual grid refinement computed in the 2D $\gamma - Re_\theta$ simulations. E_f represents the relative error compared to the fine grid solution. GCI_m denotes the medium grid-convergence index, relative to the fine grid solution values.

	$\alpha = 4°$				$\alpha = 8°$			
Grid	C_D	C_L	E_{f,C_D}	E_{f,C_L}	C_D	C_L	E_{f,C_D}	E_{f,C_L}
coarse	0.0240	0.953	0.53%	-0.79%	0.0322	1.307	4.20%	-1.44%
medium	0.0234	0.960	-2.04%	-0.01%	0.0305	1.325	-1.20%	-0.14%
fine	0.0239	0.960	-	-	0.0309	1.327	-	-
GCI_m[%]	3.27	0.02	-	-	1.93	0.23	-	-

3.4 Iterative errors and grid discretization error estimation

All 2D simulations were run until a flat-lining of normalized model residuals below 10^{-5} was displayed. 3D simulations were generally observed to converge with slightly higher orders of 10^{-3} in normalized residuals. As a first estimate for an iterative error, results were compared to values obtained at a large number of excessive iterations. The relative differences were usually well below 1% for the 3D simulations and lower than 0.001% for the 2D simulations. An exception for the 3D simulations was found for the prediction of drag coefficients at $\alpha = 10°$ and 12°, where the solution value varied with as much as 5% over the course of 2000 iterative steps. To give some estimate on the numerical discretization errors the procedure presented in the paper by Celik et al. [4] was followed. The method for reporting the so-called grid convergence indicator (CGI) is based on Richardson Extrapolation for discretization error estimation and also introduces a safety factor F_s. The mesh dependency study was conducted using 2D grids with three steps of varying resolution. These are referred to as the coarse, medium and fine grids. For $\alpha = 0°$, 4°, and 8° a slightly less refined wing surface mesh was used compared to the simulations at $\alpha = 12°$. This was due to a small leading edge separation bubble being predicted at $\alpha = 12°$, which required additional curvature refinement and wall normal cell layers to be properly resolved. In an effort to ensure that results converge for all setups, the stream wise grid spacing over the airfoil was not allowed to exceed a certain limit. Failing to resolve the laminar separation bubbles would result in simulations not properly converging. This restraint in grid coarsening for the airfoil boundary layer meant that, for instance, a base cell size doubling would not necessarily lead to a 1/4 times reduction in total cell count. See Table 4 for a presentation of force coefficient results for different grid sizes using the Menter SST $k-\omega$ $\gamma - Re_\theta$ model. Not all target values showed asymptotic behavior and due to small relative differences between the grid solutions a good estimate for the observed numerical order could not be computed. Instead, an assumed numerical order p=2 was chosen while the presented medium grid-convergence index was computed relative to the fine grid solution with a safety factor of $F_s = 1.25$ as recommended by Roache [17].

4 Results

In this section lift, drag and surface pressure distributions are presented. First, the experimental results for the lift and drag coefficients are given for all eight Reynolds numbers. Thereafter, the simulation results of three different simulation setups are compared to the experimental results. All pressure distributions are evaluated at mid-span. Special attention is given to transitional effects at selected angles of attack and the capability of the implemented transition models to capture these effects. Furthermore, three-dimensional flow effects at the onset of stall are investigated in detail.

4.1 Experimental results

The lift and drag coefficients of the NREL S826 wing were measured at eight different Reynolds numbers ranging from 0.5×10^5 to 6.0×10^5. The lift coefficients are obtained by direct force measurement on the mid-wing section, which was connected to the six-component force balance. The drag coefficients were calculated from the momentum loss measured in the wake behind the wing at mid-span. Figure 4 (a) shows the experimental lift results for all investigated Reynolds numbers. It should be noted that the inflow turbulence intensity and length scales vary according to the values given in Table 1. It is observed that the Reynolds number has a minor influence on the lift coefficient and drag coefficients for $Re \geq 0.7 \times 10^5$. The average lift curve slope in the linear lift region between α =-8° $-$ 10° is about 0.1 units C_L per degree. The maximum lift coefficient is found around $\alpha \approx 13°$, with a peak value of $C_{L,max} = 1.56$.

Smaller deviations in lift are found for $\alpha < 7°$ for the lower Reynolds numbers 0.7 and 1.0×10^5, while the deviations are very small with α approaching $C_{L,max}$. In the deep-stall region for $\alpha > 15°$ the differences between the Reynolds numbers are observed to be slightly bigger again, indicating a somewhat later full flow separation with increasing Reynolds numbers. As an example, the lift coefficients range between $C_{L,20°,Re70k} = 1.17$ and $C_{L,20°,Re400k} = 1.30$ at $\alpha = 20°$.

The lift characteristics measured at $Re = 0.5 \times 10^5$, however, are observed to be significantly different. For positive angles of attack between $\alpha = 2°$ and 8°, the lift curve collapses intermediately before reaching a lift level similar to that observed for higher Reynolds numbers at α $8°to10°$. For $\alpha \geq 11°$ an almost linear drop in lift is observed, resulting in considerably lower lift coefficient values compared to those measured for higher Reynolds numbers. A further subsequent drop in lift at $\alpha \approx 15°$ indicates a complex flow over the wing at $Re = 0.5 \times 10^5$.

The drag results obtained from the integrated momentum loss in the wake at mid span are presented in Figure 4 (b) for the entire Reynolds number range. In the pre-stall region measurement results for $Re > 1.0 \times 10^5$ are well aligned. However, the drag coefficients

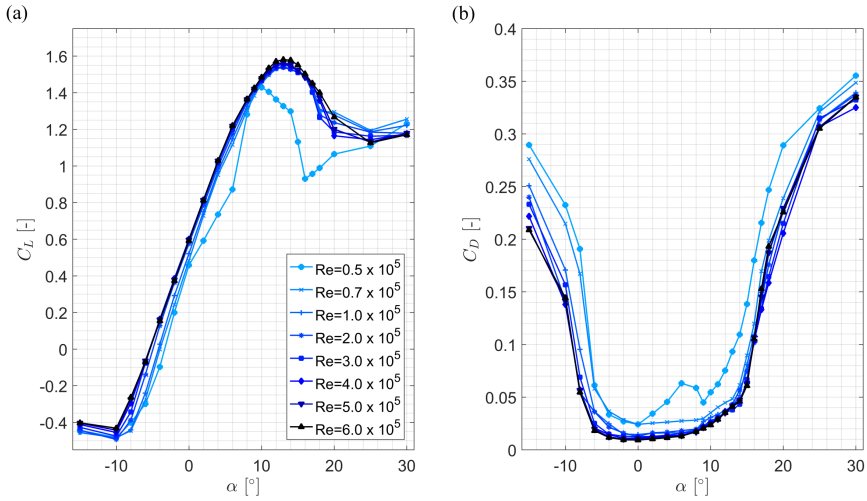

Fig. 4. **(a)** Lift and **(b)** drag coefficients measured from $Re = 0.5 \times 10^5$ to $Re = 6.0 \times 10^5$. Lift coefficient results shown are obtained from direct force measurements in the wake. Drag coefficient results are calculated from the momentum loss in the wake at mid-span.

are in general observed to further decrease with increasing Reynolds number. A minimum in drag is found at $\alpha = 0°$ for all Reynolds numbers. Measurements for Reynolds numbers $Re \leq 1.0 \times 10^5$ result in a larger drag for the whole pre-stall region. At $\alpha = 0°$, for instance, the drag coefficients for $Re = 0.5 \times 10^5$ is measured to be $C_{D,0°,Re50k} = 0.0236$, while it is almost 50 % smaller for $Re = 2.0 \times 10^5$ only amounting $C_{D,0°,Re200k} = 0.0125$ respectively. As α approaches 14° the portion of separated flow on the upper airfoil surface increases, making the drag coefficient rise significantly for all Reynolds numbers. As previously observed for the lift characteristics, also the drag coefficients for $Re = 0.5 \times 10^5$ show a different trend. A local rise in drag is already observed between $\alpha = 2°$ and 8°, corresponding to a local collapse in lift. At this low Reynolds number local re-circulation zones are suspected to cause a lift decrease and drag increase at certain angles of attack, which will be analyzed in more detail in the following sections. In Figure 5 the mean surface pressure distributions at mid-span at $\alpha = 0$, 4, 8 and 12° are presented for a range of different Reynolds numbers. Due to a very high uncertainty in the results of $Re = 0.5 \times 10^5$, this Reynolds number is not plotted. Note that surface pressure distributions for $Re = 1.0 \times 10^5$ are included in Figure 7 and hence omitted in Figure 5 for clarity. For $Re = 0.7 \times 10^5$ substantial deviations are observed compared to higher Reynolds numbers. At all angels of attack the extent of laminar separation bubbles is considerably larger in this low Reynolds number regime. For example at α=4° the separation bubble occurs at both pressure and suction side. For $Re \geq 2.0 \times 10^5$ the pressure distributions generally match very well.

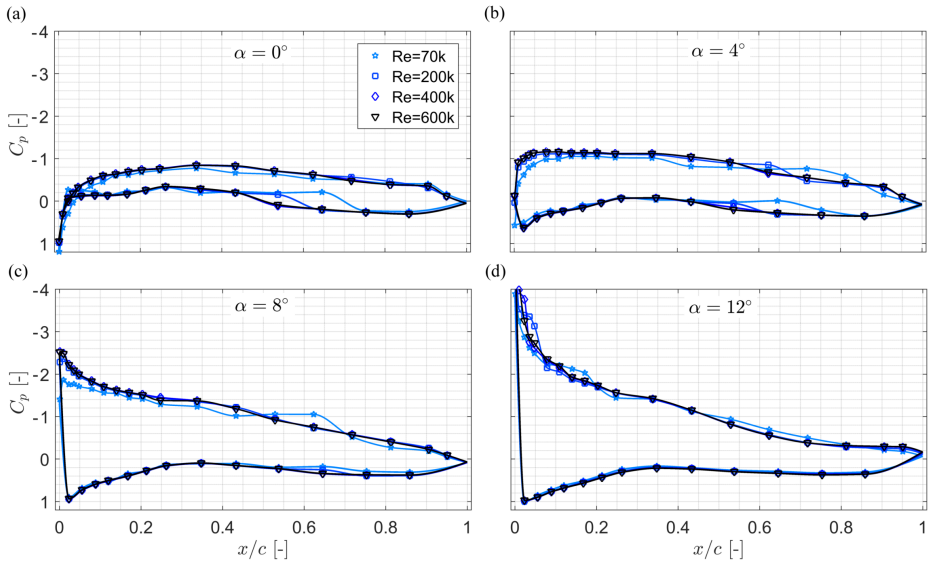

Fig. 5. Comparison of mid-span surface pressure at **(a)** $\alpha = 0°$ **(b)** $\alpha = 4°$ **(c)** $\alpha = 8°$ and **(d)** $\alpha = 12°$ for $Re_c = 0.7 \times 10^5$, $Re_c = 2.0 \times 10^5$, $Re_c = 4.0 \times 10^5$ and $Re_c = 6.0 \times 10^5$.

Smaller separation bubbles are still observed for $Re = 2.0 \times 10^5$ at α=0° and α=0°.

4.2 Model predictions

In this section, the model predictions are compared to the experimental results at Re=1.0 $\times$ 10^5. In Figure 6 the model predictions at $\alpha = 2°, 4°, 8°, 10°$ and 12° are compared to the experimental lift and drag results. In addition to the results obtained from direct force measurements and wake momentum loss integration, lift and drag were calculated from surface pressure measured around the airfoil circumference at mid span. The lift characteristics from surface pressure thus give an indication about the local flow conditions at mid span and indicate the significant three-dimensional flow effects occurring at stall, which are commented on in more detail in the following section. In order to help evaluate the two-dimensionality of the experimental setup the $\gamma - Re_\theta$ is used for a 2D computational domain as well as a full 3D discretization of the model setup. As shown in Figure 6 (a) all three models utilized predict the lift coefficient in the linear region between $\alpha = 0 - 8°$ quite accurately. At the onset of stall at $\alpha = 12°$, however, the model predictions show a significant spread and the 2D $\gamma - Re_\theta$ model predicts a slightly lower value than the corresponding 3D simulation. Although it is incapable of predicting such transitional effects as laminar separation bubbles, the lift level predicted by the Realizable k-ϵ model's coincidentally matches the experimental results closer compared to the other

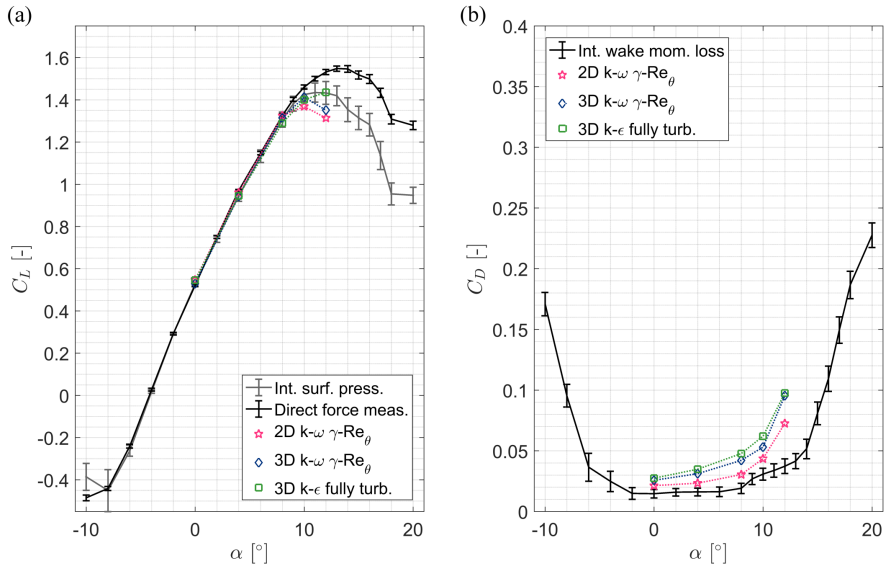

Fig. 6. Comparison of **(a)** Lift and **(b)** drag coefficients at $Re = 1.0 \times 10^5$.

two models at $\alpha = 12°$. Due to their considerably lower magnitude, the drag coefficients are more sensitive to quantify. The predictions by all three models are observed to slightly over-predict compared to the total drag measured by the momentum loss in the wake at mid span. The deviations for $\alpha = 0, 4$ and $8°$ are acceptably small, while the mismatch at $\alpha = 12°$ is considerably larger giving values almost twice as high as the experimental value. Almost no influence of the modeling of transitional effects compared to the fully turbulent boundary layer simulations is observed in the 3D simulations. The drag results of the 2D model are seen to give slightly lower values than the corresponding 3D simulations.

A closer analysis of the pressure distributions reveals further details of the simulations as presented in Figure 7. Herein, the pressure coefficient C_P is compared for all four investigated angles of attack. The error bars given with the experimental curves are quantifying the standard deviation of the measured pressure fluctuations at mid-span. The experimental pressure distribution at $\alpha = 0°$ indicates local separation bubbles both at the pressure and suction side. While the pressure side bubble occurs around $x/c = 0.5 - 0.6$, the suction side bubble is located closer to the trailing edge at $x/c = 0.8 - 0.9$. With increasing angle off attack the suction side bubble is observed to move upstream. At $\alpha = 12°$ it is located very close to the leading edge around $x/c = 0.05 - 0.10$ causing a significant jump in suction side pressure. For angles of attack $\alpha > 16°$ transition is observed to occur directly at the leading edge with the flow not being able to re-attach (not shown in graph). On the pressure side the separation bubble moves further downstream at increasing angle of attack and is eventually disappearing around $\alpha \geq 6°$. The surface pressure

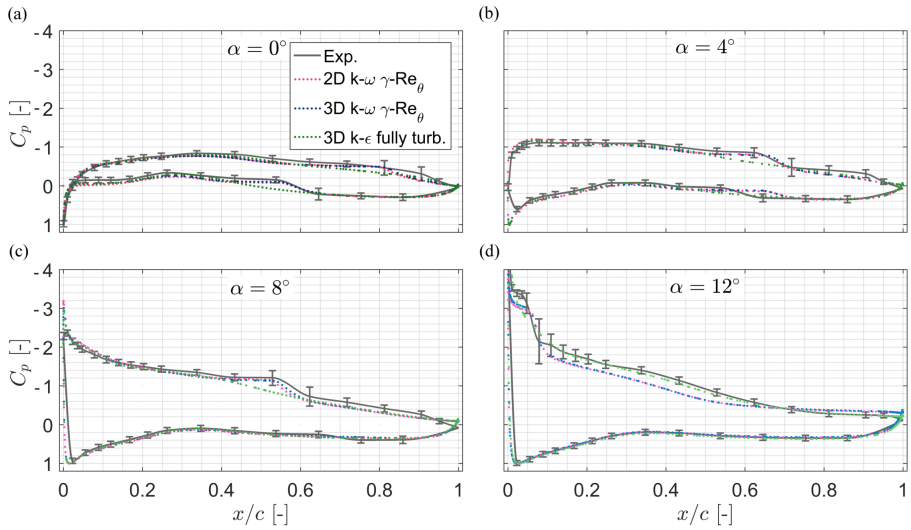

Fig. 7. Comparison of mid-span surface pressure at **(a)** $\alpha = 0°$ **(b)** $\alpha = 4°$ **(c)** $\alpha = 8°$ and **(d)** $\alpha = 12°$ for $Re_c = 1.0 \times 10^5$.

prediction by the $\gamma - Re_\theta$ model is observed to be comparable to the experimental results for $\alpha = 0 - 8°$, both in the 2D and 3D setup. The resulting surface pressure magnitudes and locations of the separation bubble are well predicted. The 2D and 3D simulations results are more or less congruent. At the onset of stall at $\alpha = 12°$, however, the suction side pressure predictions are observed to be considerably differing from the experimental values. Although the location of the separation bubble matches well with the experimental location, the suction side pressure level is predicted too high for a significant portion of the chord from $x/c = 0 - 0.60$. This also causes the separation point to move upstream in the $k - \omega$ simulation relative to the k-ϵ simulation, and might be the main reason for the aforementioned under prediction in lift coefficient $C_{L,12°}$ at the same angle. Considering the relatively close agreement between the fully turbulent k-ϵ and the transitional $k - \omega$ simulations for $\alpha = 0 - 8°$ the effect of the LSB's on the lift and drag values are observed to be small in this range. At $\alpha = 12°$ the experimentally measured suction side pressure level is well matched by the Realizable k-ϵ model in contrast to the predictions by the $\gamma - Re_\theta$ model after the boundary layer transitions. As a consequence the lift coefficient computed by the k-ϵ simulation gives a closer approximation of the experimental value. A visualization of the turbulent kinetic energy (TKE) and mean velocity distributions around the airfoil simulated with the $3D\,\gamma - Re_\theta$ model at $Re_c = 1.0 \times 10^5$ is presented in Figure 8. At $\alpha = 8°$ and $\alpha = 12°$ the presence of laminar separation bubbles on the suction side is clearly observed. These are indicated by a local mean velocity drop and re-increase further downstream. The turbulent kinetic energy is observed to reach local

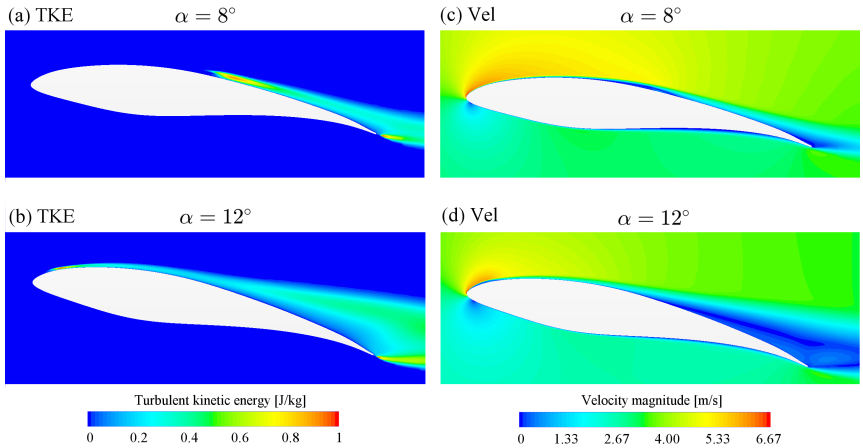

Fig. 8. $3D\,\gamma - Re_\theta$ simulations at the mid-section symmetry plane at $Re_c = 1.0 \times 10^5$. **(a)** and **(b)** show the turbulent kinetic energy around the airfoil at $\alpha = 8°$ and $\alpha = 12°$ respectively. **(c)** and **(d)** show the corresponding velocity magnitude distributions at $\alpha = 8°$ and $\alpha = 12°$ respectively.

maxima around the location of re-attachment. These locations corresponds well with the maximum pressure fluctuations measured near the reattachment location of the LBS as previously shown in Figure 7. At $\alpha = 8°$ the LSB originates at $x/c \approx 0.4$ and extends almost 0.2 chord-lengths downstream, while it originates right after the leading edge for $\alpha = 12°$ and only measures about half the size. The TKE plots in Figure 8 (a) and (b) clearly show that the flow manages to re-attach in both cases. The flow is observed to fully separate around $x/c \approx 0.9$ for $\alpha = 8°$ and at $x/c \approx 0.5$ for $\alpha = 12°$. The boundary layer on the pressure side is observed to remain laminar for both angles of attack.

4.3 Sensitivity to inflow turbulence level

In order to quantify effects of inflow turbulence an additional computational sensitivity study was conducted, quantifying the effect of three different inflow turbulence levels on lift ans drag at $Re = 1.0 \times 10^5$. Table 5 shows the results for lift and drag coefficients for three angles of attack $\alpha = 8$, 10 and 12° at three different inlet turbulence intensities $TI_{2 \cdot c} = 0.71$, 0.56 and 0.22%. The investigated angles are chosen to be around the airfoil's stall point. The different inflow turbulence intensity levels are observed to significantly influence the resultant lift and drag coefficients. When decreasing the inflow turbulence considerably smaller lift and larger drag coefficients were simulated. As indicated by the computed standard deviation σ in the last row of Table 5, the variations in lift related to inflow turbulence increase with increasing angle of attack. Note that for the lowest inflow turbulence level the simulation for $\alpha = 12°$ displayed oscillatory convergence with normalized residuals in the order of 10^{-3}, possibly indicating that a proper steady state

Table 5. Lift and drag coefficients at $Re = 1.0 \times 10^5$ as a function of different inlet turbulence intensities computed by 2D simulations with the $\gamma - Re_\theta$ model. The turbulent length scale was set according to Table 1.

		$\alpha = 8\ ^\circ$		$\alpha = 10\ ^\circ$		$\alpha = 12\ ^\circ$	
TI_{inlet} [%]	$TI_{2\cdot c}$ [%]	C_L	C_D	C_L	C_D	C_L	C_D
0.94	0.71	1.330	0.02990	1.378	0.04305	1.324	0.07161
0.71	0.56	1.325	0.03049	1.370	0.04361	1.314	0.07263
0.25	0.22	1.309	0.03334	1.355	0.04525	1.277	0.07685
Standard deviation σ		0.01097	0.00184	0.01167	0.00114	0.02476	0.00277

solution does not exist, and an accurate result may require a transient analysis.

4.4 Three-dimensional flow effects

As shown in Figure 6 (a) the lift coefficient results obtained from direct force measurements differ significantly from those obtained from mid-span surface pressure integration as soon as the wing is partly stalled at $\alpha \approx 10°$. This indicates that the local flow conditions at mid-span cannot be assumed to be representative for all span-wise wing cross sections, and the flow can no longer accurately be described as two-dimensional. On the contrary, considerable three-dimensional flow effects are observed as soon as the flow separates from the suction side surface. The surface flow of the non-stalled, partly-stalled and fully-stalled wing section is compared in Figure 9. For this purpose tufts of a length of $2.5cm$ have been taped to the suction side of the wing in the experiment, while iso-line of constant surface pressure are extracted from the $3D$ Realizable $k - \epsilon$ simulation. This allows only a very qualitative comparison, but the three-dimensionality of the flow becomes apparent at $\alpha = 15°$ both in the experiment and the simulation. While the flow is still fairly attached at $\alpha = 8 - 10°$ as indicated by aligned tufts in the experiment and parallel isobars in the simulation, the surface flow clearly separates for $\alpha = 14 - 15°$. A big part of the tufts are observed to begin fluttering. At the wing's mid-span the separation is seen to happen in the first half of the wing's chord. With increasing distance from the mid-section the flow separation is observed to occur further downstream, which is indicated by the approximated red line. The 3D simulation supports this observation by the means of surface pressure isobars. At the partly-stalled $\alpha = 15°$ significant 3D flow establishes indicating a faster pressure increase at mid-span than further from the center. A complex flow is simulated on the wing dummy sections close to the wall boundary layers of the wind tunnel domain. The gap between the wing's main section and the dummies was assessed not to have a significant qualitative influence on the flow structures [18] although vortex shedding is predicted as is illustrated in Figure 10 (a). The earlier separation at the wing's mid-section is assumed to be an effect of so-called stall cell vortices, which is

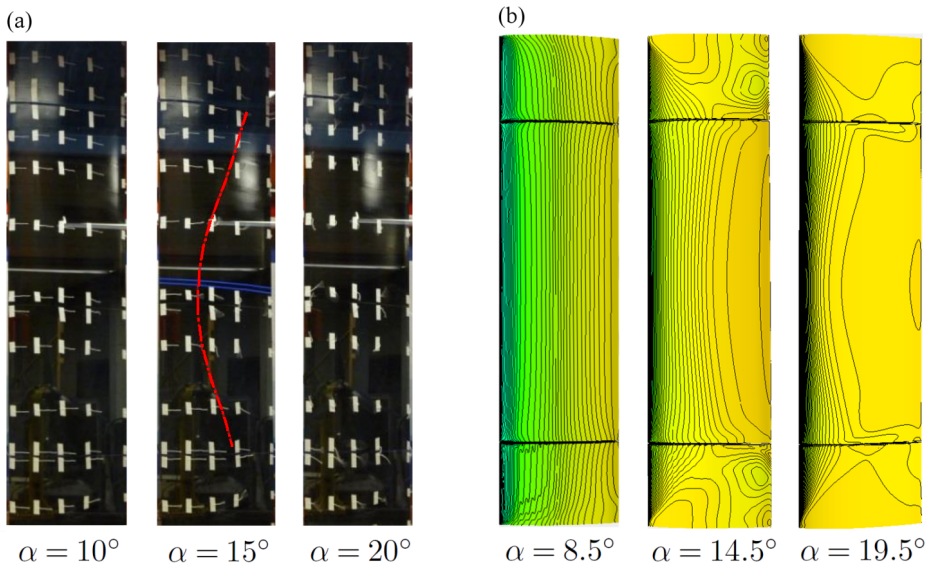

Fig. 9. **(a)** Flow visualization on the suction side surface with tufts in the experiment. The red line approximates the locations of flow separation. The blue lines indicate the location of the mid-span pressure taps. **(b)** Iso-lines of constant pressure on the suction side surface from the 3D k-ϵ fully turbulent simulation.

assumed to interact with the separation line vortex as described in [11]. At $\alpha = 19-20°$ the complete wing section is fully-stalled. While the gap separating the wing wall dummies and the measuring section may not have an adverse effect on the pressure distribution, skin-friction is clearly affected as shown in Figure 10 (a). These observations are reflected in the values presented in Table 6, cases A and C, comparing force coefficients for computational domains, in which the gaps are resolved to ignore the gaps. Moreover, the lift and drag coefficients for a wall-to-wall measurement are included (B). In general, a relatively small impact on the computed lift coefficients of less than 0.8% is observed. As expected, the lift coefficients are consistently lower when including the wall boundary layers, especially for higher angles of attack. Comparing cases B and C, a difference in lift coefficients of about 6.5% is observed. Noticeably, also the computed drag coefficients are roughly 10-25% lower in case C, as secondary flows from the gaps and drag inducing wall effects are not taken into account in this case. This quantification largely explains the excessive values obtained for the drag coefficient from the 3D simulations, relative to the measured values at mid-span and the 2D simulation results.

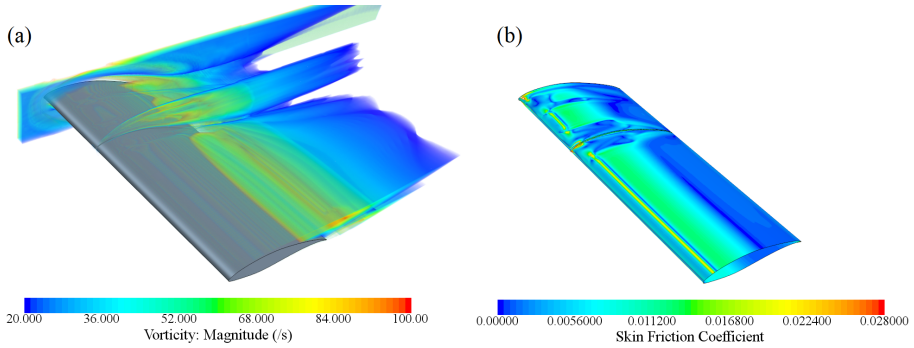

Fig. 10. Visualizations of 3D flow for $\alpha = 12°$: **(a)** A volume render of vorticity. **(b)** Skin friction coefficient.

Table 6. Results from 3D simulations with the Realizable $k - \epsilon$ turbulence model. Lift and drag coefficients were computed in three different ways: A - summation of surface forces on the main wing section (without dummy sections); B - summation of surface forces wall-to-wall for a split blade geometry (including dummy sections); C - summation of surface forces on a virtual central measuring section computed on a continuous blade geometry (no splits).

	$\alpha = 4$ °		$\alpha = 10$ °		$\alpha = 12$ °	
case	C_L	C_D	C_L	C_D	C_L	C_D
A	0.948	0.0350	1.370	0.0694	1.436	0.0976
B	0.926	0.0349	1.296	0.0737	1.308	0.1062
C	0.958	0.0308	1.396	0.0574	1.424	0.0903

5 Discussion

The presented experimental lift and drag results show a relatively stable performance for all assessed Reynolds numbers of $Re \geq 0.7 \times 10^5$. At the lowest measured Reynolds number $Re = 0.5 \times 10^5$, transitional effects are observed to significantly influence the airfoils performance. This is in agreement with the measurements performed by Ostovan et al. [14] at METU, who do not observe any clear low Reynolds numbers effects on the performance at $Re \geq 0.715 \times 10^5$. In contrast to that, measurements by Sarmast and Mikkelsen [21] at DTU found a clear Reynolds number dependent performance for $Re \leq 0.8 \times 10^5$. These differences are considered to stem from the considerably lower turbulence level of $TI_{DTU} < 0.2\%$ at such low Reynolds numbers in DTU's facilities compared to what is achieved in METU's ($TI_{METU} < 0.6\%$) and NTNU's ($TI_{NTNU,Re=70k} = 0.7\%$) wind tunnels. As can be observed in Figure 11 the experimental results at $Re = 1.0 \times 10^5$ match well with earlier experiments presented by Sarlak et al. [20] and Ostovan et al. [14] as long the flow is largely attached. However, significant differences are found as soon as stall kicks in between α=8° and α=16°. Both METU's and DTU's experiments show a significantly lower maximum lift coefficient than the presented NTNU data. METU's measurements

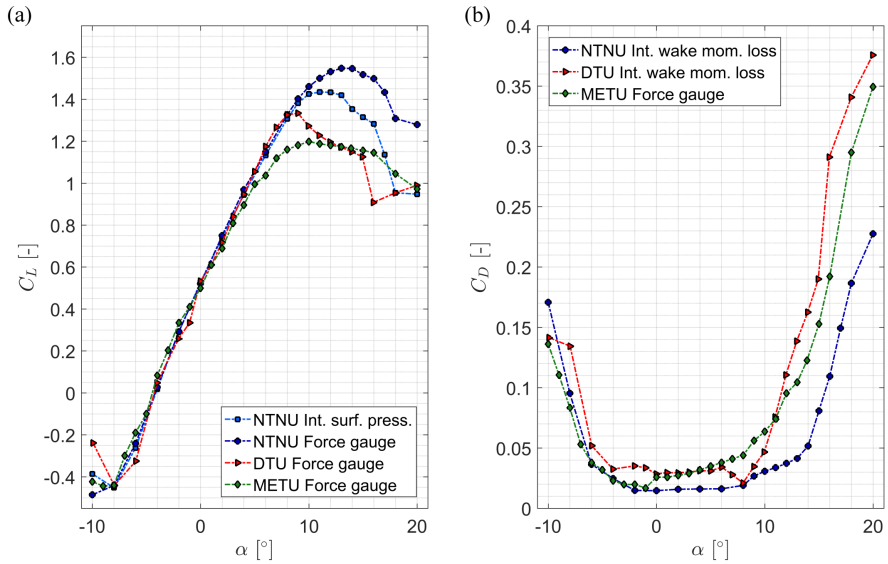

Fig. 11. Comparison of the lift and drag coefficients of three different experimental data-sets measured at NTNU, DTU and METU at $Re = 1.0 \times 10^5$.

indicate the onset of stall already around $\alpha = 6 - 7°$, while reaching a maximum lift of $C_{L,max,METU} = 1.2$ and remaining at that level until α=16°. In the case of DTU's measurements flow separation on the suction side flow begins around α=8°, similar to the present NTNU measurements, but is much more abrupt. The considerably lower inflow turbulence level in DTU's experiments could explain the sudden drop in lift, compared to NTNU's results measured at an about three times higher inflow turbulence intensity. As seen in Figure 8 the LSB for α=8° is positioned on the ridge of the suction side of the airfoil, and moves gradually upstream as the angle of attack is increased. If the turbulent mixing is not high enough to sufficiently energize the boundary layer the flow will not re-attach and an abrupt stall could occur. Moreover, the different test rig setups could possibly influence the different lift coefficient results. While the lift was measured on the entire wing spanning over the whole wind tunnel width/height in DTU's and METU's setup, NTNU's setup aimed to cancel out wall interaction effects by dummy sections close to the walls. The lift force was only measured on the mid-section of the wing, which is not affected by lift-reducing wall effects. The effects of the gaps between the wing measuring section and the wall was, as noted in Section 4.4, simulated to be much less detrimental to the evaluation of the lift coefficient than the effect of wind tunnel wall boundary layers and blockage.

The variation in the different drag coefficient results is large also for attached flow conditions. Although a comparable drag coefficient of $C_{D,min,METU} = 0.017$ is measured at

α=-1° in METU's experiments, the drag seems to jump to a much higher level for $\alpha = 0$-$-6°$, relative to the present measurements. The opposite trend is observed in DTU's drag results, where the minimum drag of $C_{D,min,DTU} = 0.021$ is measured at α=8° right before stall occurs. However, the drag level is considerably higher from $\alpha = -4° - 7°$, which is in accordance with separated flow and the abrupt loss in generation of lift. In comparision the NTNU results from wake momentum loss integration show a consistently low drag coefficient of $C_{D,NTNU} = 0.015 - 0.016$ from $\alpha = -2° - 6°$. As reflected in the gradual decrease in the measured lift, flow separation at the onset of stall seem to be much more docile in the present measurements. The drag first increases only slightly around $\alpha = 9°$ before rising strongly around $\alpha = 15°$. Note however that due to three-dimensional effects, the wake momentum deficit measured at mid span is not expected to give accurate results for the drag-coefficient beyond an angle of attack of $\alpha = 10°$.

Comparison with previous numerical simulations performed on the S826 airfoil seem to confirm a higher maximum lift coefficient relative to previous measurements in the present Reynolds number range, although the numerical prediction of stalled flow is still observed to be difficult. LES computations by Sarlak et al. [20] resulted in a maximum lift of $C_{L,max,DTU,LES} = 1.54$ at $\alpha = 12°$ ($Re = 1.0 \times 10^5$). Also, computations by Cakmakcioglu et al. [2] at the same Reynolds number indicate a significantly higher lift coefficient level than in METU's experiments. In a Delayed Detached Eddy Simulation (DDES) they find a maximum lift coefficient of $C_{L,max,METU,DDES} = 1.38$ and their $2D$ realizable $k - \epsilon$ model results in a lift of $C_{L,max,METU,k-\epsilon} = 1.44$, both computed at $\alpha = 10°$.

In summary, it has been observed that different experimental setups of the same airfoil resulted in different performance characteristics, especially for separated flow and low Reynolds regimes. The different inflow turbulence intensity levels are considered to be main reason for these variations. As observed in Table 5, the resulting values indicate smaller lift and larger drag coefficients with decreasing inflow turbulence. This finding in general supports the different trends in C_L and C_D measured at DTU, METU and NTNU, although the authors suggest transient simulations be carried out in the stall region to verify this trend. In addition to the above discussed discrepancies the influence of the wing's aspect ratio (AR) on three-dimensional effects at the onset of stall might have a notable effect on the measured lift and drag coefficients. As shown by [11, 27, 25], the wing's AR influences the relative stall cell (SC) area. For lower ARs the relative SC area was observed to be higher. The model used at DTU and METU had an aspect ratio $AR_{DTU} = AR_{METU} = 5.0$, while NTNU's setup features a smaller ratio of about $AR_{NTNU} \approx 4.0$.

6 Conclusions

A combined experimental and numerical study on a wing section of the NREL S826 airfoil at low to moderate Reynolds numbers was realized. The lift and drag characteristics is observed to be strongly affected by transitional effects for Reynolds numbers lower than $Re < 0.7 \times 10^5$. Also, at larger Reynolds numbers, smaller laminar separation bubbles are seen to appear on the airfoils pressure and suction side. The influence of these bubbles on the lift and drag characteristics is observed to decrease with increasing Reynolds number. Lift characteristics calculated from pressure measurements at the wing's mid-span position significantly differ from force measurements on the entire wing measuring section as soon as the wing begins to stall. This is in accordance with three-dimensional flow effects at the onset of stall. For large angles of attack a 3D flow structure reminiscent of a single stall cell is observed, in agreement with previous findings, considering the low aspect ratio of the wing used in the present measurements.

In both 2D and 3D computational setups the capability to predict laminar separation bubbles by the transitional $\gamma - Re_\theta$ model by Langtry-Menter has been tested. The model was able to accurately predict the location and the resulting mean surface pressure variations of laminar separation bubbles, in the linear lift range. In partly stalled flow conditions both turbulence models utilized in the 3D computational domain numerical models showed a tendency to under-predict the generated lift at the measuring section of the wing. The differences might be alleviated by obtaining a closer match between the measured and modeled free-stream turbulence intensities at wing, as indicated by the turbulence intensity study presented. Furthermore, the effects of two- versus three-dimensional computational domains was investigated showing differences as soon as the effects of three-dimensional flow are observable at an angle of attack $\alpha \approx 10°$. Hence, 2D simulations are not expected to give an accurate account of the airfoils lift and drag coefficient above this angle of attack for the present Reynolds number range. Judging by the grid discretization error estimated and the uncertainty range in the experiments, the 2D simulations can be said to give good estimates for both the lift and drag coefficients. For future comparison with the measured drag coefficients, it is recommenced that the coefficients are calculated at mid-span also for 3D simulations, analogous to the measurements. For the measurement of the lift coefficients the wall dummies appear to be effective in mitigating the boundary layer and blockage effects from the tunnel walls. The gaps between the force measuring section of the wing and wall dummies are simulated to have a relatively small effect on the measured lift coefficient, compared to a wall-to-wall analogous approach.

A comparison to earlier experiments realized on the same airfoil at DTU and METU showed a good agreement in the linear lift region. Significant differences are observed in both lift and drag coefficients at the onset of stall, with the presented NTNU data resulting in considerably higher maximum lift. The present combined experimental and numerical

investigation suggests that these discrepancies in the stall region can be largely explained by the difference in the free stream turbulence intensity affecting the formation and extent of the laminar separation bubbles, as well as dictating the subsequent turbulent reattachment and separation.

Acknowledgements

The authors would like to acknowledge Nikolai Yde Aksnes for the great effort in designing the wing and conducting the first set of experiments. Arnt Egil Kolstad is acknowledged for the assistance in design and assembling of the wing model. Thomas H. Hansen is acknowledged for his initial ideas and input to the design of this project. SIEMENS is acknowledged for providing an academic license and support for StarCCM+. This research was supported with computational resources at NTNU provided by NOTUR.

Appendix: Experimental lift and drag data

The lift coefficients C_L and drag coefficients C_D for all measured Reynolds numbers are listed in Tables 7 and 8 respectively. The tabulated profile coordinates of marginally modified NREL S826 profile and all data for the presented pressure coefficients C_P are available on request to the corresponding author.

Table 7. Lift coefficients obtained from direct force measurements at the main section of the wing for all investigated Reynolds numbers.

α [°]	$Re = 50k$	$Re = 70k$	$Re = 100k$	$Re = 200k$	$Re = 300k$	$Re = 400k$	$Re = 500k$	$Re = 600k$
-15	-0.4443	-0.4557	-0.4538	-0.4420	-0.4268	-0.4116	-0.4038	-0.4021
-10	-0.4815	-0.4828	-0.4851	-0.4929	-0.4747	-0.4545	-0.4423	-0.4313
-8	-0.4011	-0.4451	-0.4408	-0.3871	-0.3429	-0.2941	-0.2745	-0.2630
-6	-0.2992	-0.2761	-0.2399	-0.1397	-0.0761	-0.0698	-0.0640	-0.0704
-4	-0.0964	-0.0009	0.0275	0.1287	0.1595	0.1640	0.1611	0.1549
-2	0.1998	0.2423	0.2926	0.3632	0.3828	0.3857	0.3782	0.3734
0	0.4585	0.4839	0.5217	0.5758	0.5944	0.6003	0.5969	0.5921
2	0.5923	0.7285	0.7506	0.7866	0.8054	0.8154	0.8141	0.8127
4	0.7357	0.9512	0.9695	0.9948	1.0144	1.0269	1.0283	1.0293
6	0.8719	1.1165	1.1478	1.1782	1.1999	1.2161	1.2185	1.2206
8	1.2814	1.3052	1.3265	1.3483	1.3594	1.3655	1.3628	1.3648
9	1.4124	1.3836	1.4028	1.4156	1.4159	1.4202	1.4205	1.4260
10	1.4290	1.4489	1.4607	1.4636	1.4655	1.4747	1.4782	1.4846
11	1.4057	1.4956	1.5005	1.5045	1.5103	1.5189	1.5243	1.5348
12	1.3637	1.5287	1.5318	1.5315	1.5359	1.5480	1.5558	1.5709
13	1.3273	1.5483	1.5483	1.5380	1.5410	1.5554	1.5635	1.5813
14	1.2984	1.5533	1.5467	1.5277	1.5306	1.5458	1.5526	1.5778
15	1.1323	1.5178	1.5179	1.5113	1.5101	1.5174	1.5226	1.5513
16	0.9309	1.4925	1.4989	1.4955	1.4907	1.4874	1.4834	1.5032
17	0.9572	1.4246	1.4333	1.4081	1.4028	1.4470	1.4429	1.4516
18	0.9893	1.2977	1.3085	1.2798	1.2658	1.3584	1.3743	1.4007
20	1.0653	1.2951	1.2793	1.2372	1.1867	1.1655	1.2011	1.2674
25	1.1090	1.1947	1.1870	1.1850	1.1627	1.1435	1.1307	1.1271
30	1.2318	1.2560	1.2224	1.1791	1.1685	1.1768	1.1794	1.1708

Table 8. Drag coefficients obtained from momentum loss calculations in the wake at midspan for all investigated Reynolds numbers.

α [°]	$Re = 50k$	$Re = 70k$	$Re = 100k$	$Re = 200k$	$Re = 300k$	$Re = 400k$	$Re = 500k$	$Re = 600k$
-15	0.2896	0.2761	0.2510	0.2401	0.2333	0.2219	0.2104	0.2089
-10	0.2324	0.2148	0.1709	0.1415	0.1568	0.1382	0.1414	0.1444
-8	0.1909	0.1673	0.0954	0.0546	0.0691	0.0571	0.0567	0.0547
-6	0.0614	0.0581	0.0365	0.0363	0.0252	0.0208	0.0197	0.0183
-4	0.0335	0.0367	0.0248	0.0216	0.0149	0.0145	0.0124	0.0118
-2	0.0271	0.0286	0.0149	0.0160	0.0131	0.0112	0.0102	0.0096
0	0.0242	0.0243	0.0147	0.0128	0.0125	0.0112	0.0105	0.0094
2	0.0344	0.0255	0.0159	0.0163	0.0128	0.0128	0.0116	0.0104
4	0.0456	0.0263	0.0161	0.0169	0.0140	0.0133	0.0124	0.0116
6	0.0632	0.0276	0.0162	0.0183	0.0159	0.0140	0.0136	0.0130
8	0.0589	0.0283	0.0191	0.0197	0.0180	0.0175	0.0170	0.0173
9	0.0450	0.0299	0.0268	0.0228	0.0217	0.0219	0.0212	0.0205
10	0.0547	0.0352	0.0308	0.0275	0.0260	0.0256	0.0247	0.0237
11	0.0624	0.0405	0.0338	0.0305	0.0308	0.0298	0.0290	0.0290
12	0.0753	0.0448	0.0374	0.0358	0.0355	0.0363	0.0351	0.0354
13	0.0934	0.0484	0.0415	0.0432	0.0380	0.0423	0.0423	0.0410
14	0.1095	0.0615	0.0517	0.0569	0.0434	0.0467	0.0473	0.0458
15	0.1384	0.0896	0.0809	0.0749	0.0669	0.0631	0.0632	0.0610
16	0.1799	0.1198	0.1095	0.1015	0.1035	0.1035	0.1067	0.1054
17	0.2156	0.1697	0.1495	0.1418	0.1341	0.1333	0.1453	0.1530
18	0.2469	0.1988	0.1867	0.1757	0.1645	0.1587	0.1871	0.1933
20	0.2892	0.2389	0.2277	0.2273	0.2150	0.2058	0.2295	0.2258
25	0.3244	0.3210	0.3133	0.3132	0.3151	0.3069	0.3067	0.3052
30	0.3555	0.3486	0.3392	0.3372	0.3323	0.3251	0.3352	0.3349

References

1. Bartl, J. and Sætran, L.: Blind test comparison of the performance and wake flow between two in-line wind turbines exposed to different turbulent inflow conditions, Wind Energy Science, 2, 5576, doi:10.5194/wes-2-55-2017, 2017.

2. Cakmakcioglu, S. C., Sert, I. O., Tugluk, O., and Sezer-Uzol, N.: 2-D and 3-D CFD Investigation of NREL S826 Airfoil at Low Reynolds Numbers, J. Phys.: Conf. Series, 524, doi: 10.1088/1742-6596/524/1/012028, 2014.

3. CD-adapco: StarCCM+ user guide, code version 10.02.012.

4. Celik, I. B., Ghia, U., Roache, P. J., Freitas, C., Coleman, H., and Raad, P. E.: Procedure for Estimation and Reporting of Uncertainty Due to Discretization in CFD Applications, Journal of Fluid Mechanics; Transactions of the ASME, 130, doi: 10.1115/1.2960953, 2008.

5. Kerho, M. F. and Bragg, M. B.: Airfoil Boundary-Layer Development and Transition with Large Leading-Edge Roughness, AIAA Journal, 35, 7584, doi: 10.2514/2.65, 1997.

6. Krogstad, P.-Å. and Eriksen, P.E.: Blind test calculations of the performance and wake development for a model wind turbine, Renewable Energy, 50, 325333, doi:10.1016/j.renene.2012.06.044, 2012.

7. Krogstad, P.-Å., Sætran, L., and Adaramola, M.: Blind Test 3 calculations of the performance and wake development behind two in-line and offset model wind turbines, Journal of Fluids and Structures, 52, 65 80, doi: 10.1016/j.jfluidstructs.2014.10.002, 2014.

8. Langtry, R. B.: A Correlation-Based Transition Model using Local Variables for Unstructured Parallelized CFD codes, Ph.D. thesis, University of Stuttgart, 2006.

9. Langtry, R. B. and Menter, F. R.: Correlation-Based Transition Modeling for Unstructured Parallelized Computational Fluid Dynamics Codes, AIAA Journal, 47, 28942906, doi:10.2514/1.42362, 2009.

10. Malan, P., Suluksna, K., and Juntasaro, E.: Calibrating the $\gamma - Re_\theta$ Transistion Model for Commercial CFD, in: the 47th AIAA Aerospaces Sciences Meeting, doi: 10.2514/6.2009-1142, 2009.

11. Manolesos, M. and Voutsinas, S.: Geometrical characterization of stall cells on rectangular wings, Wind Energy, 17, 13011314, doi: 10.1002/we.1634, 2014.

12. Manolesos, M., Papadakis, G., and Voutsinas, S.: Experimental and computational analysis of stall cells on rectangular wings, Wind Energy, 17, 939955, doi: 10.1002/we.1609, 2014.

13. O'Meara, M. and Mueller, T.: Laminar separation bubble characteristics on an airfoil at low reynolds numbers, AIAA Journal, 25, 10331041, doi: 10.2514/3.9739, 1987.

14. Ostovan, Y., Amiri, H., and Uzol, O.: Aerodynamic Characterization of NREL S826 Airfoil at Low Reynolds Numbers, in: Conference on Wind Energy Science and Technology-RUZGEM, 2013.

15. Pierella, F., Krogstad, P.-Å., and Sætran, L.: Blind Test 2 calculations for two in-line model wind turbines where the downstream turbine operates at various rotational speeds, Renewable Energy, 70, 6277, doi:10.1016/j.renene.2014.03.034, 2014.

16. Prytz, E., Huuse, Ø., Müller, B., Bartl, J., and Sætran, L.: Numerical Simulation of Flow around the NREL S826 Airfoil at Moderate Reynolds numbers Using Delayed Detached Eddy Simulation (DDES), AIP Conference Proceedings 1863, p. 560086, doi:10.1063/1.4992769, 2017.

17. Roache, P.: Quantification of Uncertainty in Computational fluid dynamics, Annu. Rev. Fluid. Mech. 29, 123-160, doi: 10.1146/annurev.fluid.29.1.123, 1997.

18. Sagmo, K., Bartl, J., and Sætran, L.: Numerical simulations of the NREL S826 airfoil, Journal of Physics: Conference Series, 753, 082 036, doi:10.1088/1742-6596/753/8/082036, 2016.

19. Sarlak, H.: Large Eddy Simulation of Turbulent Flows in Wind Energy, Ph.D. thesis, DTU Wind Energy, 2014.

20. Sarlak, H., Mikkelsen, R., Sarmast, S., and Sørensen, J. N.: Aerodynamic behaviour of NREL S826 airfoil at Re=100 000, J. Phys.: Conf. Series, 524, doi:/10.1088/1742-6596/524/1/012027, 2014.

21. Sarmast, S. and Mikkelsen, R.: The experimental results of the NREL s826 airfoil at low Reynolds numbers, Tech. Rep. urn:nbn:se:kth:diva-120583, KTH, 2013.

22. Somers, D. M.: The S825 and S826 Airfoils, Tech. Rep. SR-500-36344, NREL, url: wind.nrel.gov/airfoils/Documents/S825,S826-Design.pdf, 2005.

23. Sørensen, J. N.: General Momentum Theory for Horizontal Axis Wind 5 Turbines, vol. 4 of Research Topics in Wind Energy, Springer International Publishing Switzerland, 1 edn., doi:10.1007/978-3-319-22114-4, 2016.

24. Versteeg, H. K. and Malalasekera, W.: An Introduction to Computational Fluid Dynamics, Pearson Education, Harlow, 2 edn., 2007.

25. Weihs, D. and Katz, J.: Cellular patterns in poststall flow over unswept wings, AIAA Journal 21 (12), 1757-1759, doi: 10.2514/3.8321, 1983.

26. Wheeler, A. and Ganji, A.: Introduction to Engineering Experimentation, Pearson Education, 3 edn., 2004.

27. Winkelmann, A.E. and Barlow, J.B.: Flowfield model for a rectangular planform wing beyond stall, AIAA Journal 18 (8), 1006-1008, doi:10.2514/3.50846, 1980.

28. Wolfshtein, M.: The velocity and temperature distribution in one-dimensional flow with turbulence augmentation and pressure gradient, International Journal of Heat and Mass Transfer, 12, 301318, doi: 10.1016/0017-9310(69)90012-X, 1969.